Demonstration of Quantum Gate Operations and Quantum Sensing on a Scalable System Based on Neutral Atoms

Demonstration von Quantengatteroperationen und Quantensensorik in einem skalierbaren System aus neutralen Atomen

Vom Fachbereich Physik der Technischen Universität Darmstadt zur Erlangung des Grades eines Doktors der Naturwissenschaften (Dr. rer. nat.) genehmigte Dissertation von Tobias Schreiber aus Bensheim

Tag der Einreichung: 13.11.2024, Tag der Prüfung: 18.12.2024

1. Gutachten: Prof. Dr. G. Birkl
2. Gutachten: Prof. Dr. T. Walther

Darmstadt, Technische Universität Darmstadt

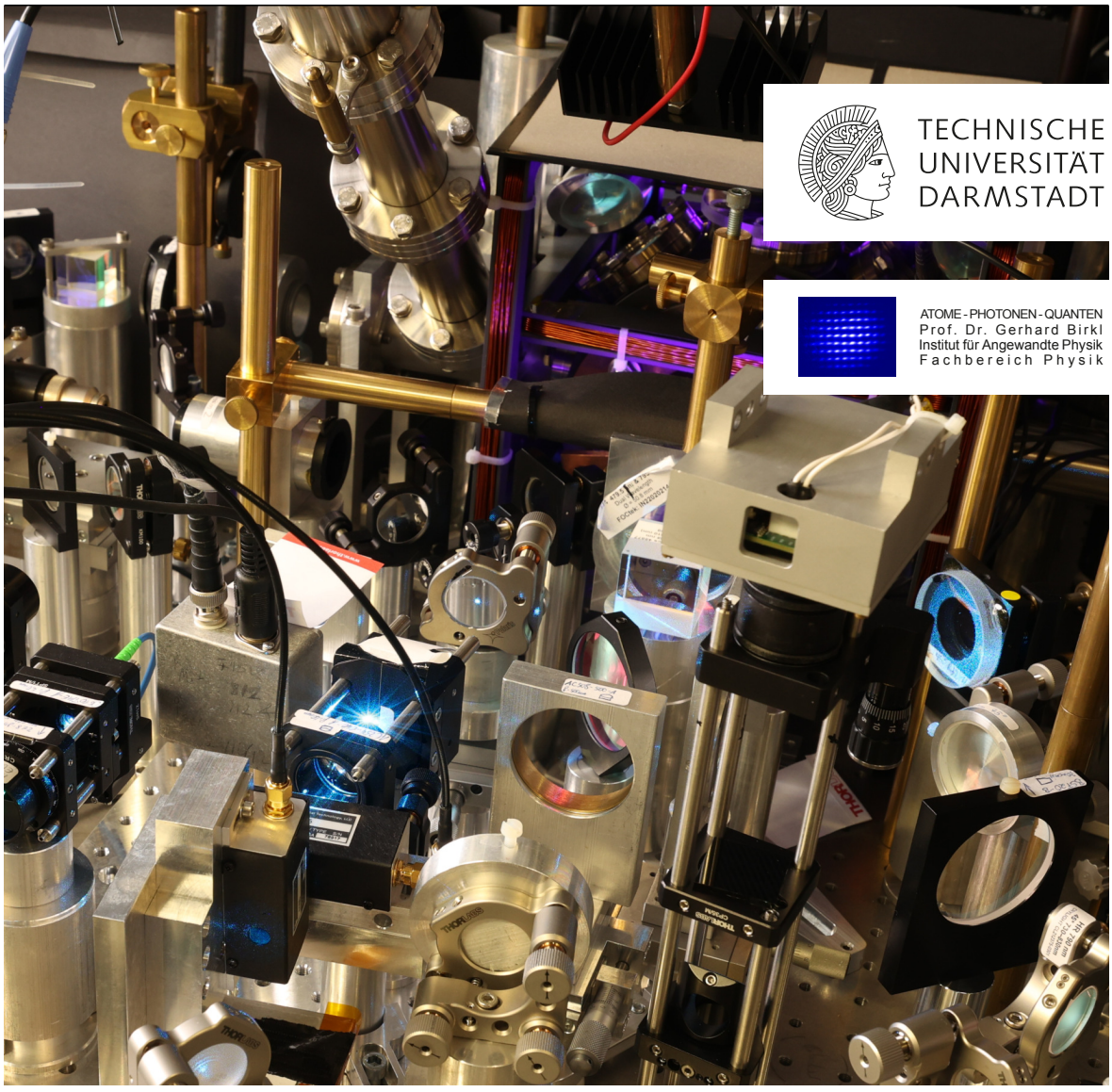

Demonstration of Quantum Gate Operations and Quantum Sensing on a Scalable System Based on Neutral Atoms
Demonstration von Quantengatteroperationen und Quantensensorik in einem skalierbaren System aus neutralen Atomen

Accepted doctoral thesis by Tobias Schreiber

1st reviewer: Prof. Dr. G. Birkl
2nd reviewer: Prof. Dr. T. Walther

Date of submission: 13.11.2024
Date of thesis defense: 18.12.2024

Darmstadt, Technische Universität Darmstadt

Jahr der Veröffentlichung der Dissertation auf TUprints: 2025

Bitte zitieren Sie dieses Dokument als:
URN: urn:nbn:de:tuda-tuprints-293345
URL: http://tuprints.ulb.tu-darmstadt.de/29334

Dieses Dokument wird bereitgestellt von tuprints,
E-Publishing-Service der TU Darmstadt
http://tuprints.ulb.tu-darmstadt.de
tuprints@ulb.tu-darmstadt.de

Front cover: Photography of the science chamber in the Quips-B experiment with enabled laser light at 480 nm, used for experiments with Rydberg atoms, and activated UV LEDs.

To Fanny,
To Jürgen and Martina,
To Peter and Elisabeth

Abstract

Neutral atoms in registers of optical tweezers have established themselves as a versatile platform for timely investigations in quantum physics. This applies in particular to the access to new orders of magnitude in metrology and the development of quantum computers. The research into quantum physics, which has been ongoing for less than a hundred years, shows potential for numerous further discoveries.
This work demonstrates the application of neutral atoms in optical tweezer arrays as quantum sensors and as quantum processors in the same experimental setup. In the field of quantum sensing, a magnetic field resolution of $98(29)$ nT is demonstrated with a spatial resolution of a few micrometers. A sensitivity of the sensor of $25\,\mu\mathrm{T}/\sqrt{\mathrm{Hz}}$ is achieved. Using the magnetic field measurement, one component of a quadrupole field with a range from -2μT to $7\,\mu$T is probed. The Ramsey spectroscopy used here is not limited to the measurement of magnetic fields, but allows the measurement of any field that causes a sufficient shift in the energy levels of the atoms.
For the application of neutral atoms as a quantum processor, this work shows the demonstration of 1-qubit rotations, virtual-Z rotations and a restricted controlled NOT (CNOT) operation. The clock states in the hyperfine structure of individual rubidium atoms, known for their long coherence times, are used as qubit basis states. For the selected parameters, an inhomogeneous coherence time of $T_2^* = 340(26)\,\mu$s is demonstrated with a perspective to a homogeneous coherence time of several milliseconds. Manipulations of the qubit states are performed on the basis of two-photon transitions. By varying the reference phase of an optical phase-locked loop, virtual-Z rotations on superpositions of these basis states are demonstrated. The interaction between the atoms is controlled using Rydberg states. The excitation of these states is studied in detail and typical limitations are addressed and partly associated with the generation of electrostatic fields. These fields are supposed to originate from rubidium atoms ab- and desorbed at the surfaces of the vacuum housing. To the author's knowledge, an optical phase-locked loop is used for the first time to stabilize a laser on the transmitted light of a highly stable optical resonator with a Finesse larger than $30\,000$.
The application of these operations to the atoms are explicitly designed to allow a scaling of the operations. A key feature is the controlled addressing of individual sites of the atom arrays, which is implemented for both the 1-qubit and the restricted CNOT operation. This represents a new approach in contrast to other quantum processors, which achieve the scaling of their quantum gates by moving the atoms in the optical registers. Addressing with light offers the prospect of an operation that is 100 times faster than the movement of the atoms allows.

Zusammenfassung

Neutrale Atome in Registern von optischen Pinzetten haben sich als vielfältige Plattform für die Erforschung aktueller Fragestellungen der Quantenphysik etabliert. Dies betrifft insbesondere die Erschließung von neuen Größenordnungen in der Metrologie und die Entwicklung von Quantencomputern. Die seit weniger als einhundert Jahren andauernde Erforschung der Quantenphysik zeigt Potential für zahlreiche weitere Entdeckungen auf diesen Gebieten.
Diese Arbeit demonstriert die Anwendung von neutralen Atomen in Registern von optischen Pinzetten als Quantensensoren und als Quantenprozessoren in dem selben experimentellen Aufbau. Auf dem Feld der Quantensensorik wird eine Magnetfeldauflösung von $98(29)$ nT demonstriert mit einer räumlichen Auflösung von wenigen Mikrometern. Eine Sensitivität des Sensors von $25\,\mu\mathrm{T}/\sqrt{\mathrm{Hz}}$ wird erreicht. Mithilfe der Magnetfeldmessung wird eine Komponente eines Quadrupolfeldes mit einer Spanne von -2µT bis 7 µT vermessen. Die dabei verwendete Technik der Ramsey-Spektroskopie ist hierbei nicht nur auf die Messung von magnetischen Feldern limitiert, sondern erlaubt die Messung jedes Feldes, das eine ausreichende Verschiebung der Energieniveaus der Atome bewirkt.
In der Anwendung als Quantenprozessor zeigt diese Arbeit die Demonstration von 1-Qubit Rotationen, virtuellen-Z Rotationen und einer eingeschränkten *Controlled NOT* (CNOT) Operation. Als Qubitbasiszustände werden die für ihre langen Kohärenzzeiten bekannten Uhrenzustände in der Hyperfeinstruktur von einzelnen Rubidiumatomen verwendet. Eine inhomogene Kohärenzzeit von $T_2^* = 340(26)$ µs wird für die verwendeten Parameter demonstriert mit einem Ausblick auf eine homogene Kohärenzzeit von mehreren Millisekunden. Manipulationen von Qubitzuständen werden auf der Basis von Zwei-Photonen-Übergängen vorgenommen. Mittels Variation der Referenzphase einer optischen Phasenregelschleife werden hierbei auch virtuelle-Z Rotationen auf Superpositionen dieser Basiszustände demonstriert.
Eine Wechselwirkung zwischen den Atomen wird durch die Verwendung von Rydbergzuständen gesteuert. Die Anregung dieser Zustände wird ausgiebig untersucht und typische Limitierungen behoben, die teilweise mit der Erzeugung von elektrostatischen Feldern in Zusammenhang gebracht werden. Es wird vermutet, dass diese Felder von Rubidiumatomen erzeugt werden, die an den Oberflächen der Vakuumaperatur ab- und desorbiert werden. Nach Kenntnis des Autors wird erstmals eine optische Phasenregelschleife angewendet, die einen Laser auf das transmittierte Licht eines hochstabilen optischen Resonators mit einer Finesse größer als $30\,000$ regelt.
Die Umsetzung dieser Operationen auf den Atomen ist explizit so aufgebaut, dass sie eine Skalierung der Operationen erlaubt. Eine Schlüsseltechnologie stellt dabei die gesteuerte Adressierung von einzelnen Plätzen der atomaren Register dar, die sowohl für die 1-Qubit- wie auch für die eingeschränkte CNOT-Operation implementiert wird. Dies stellt einen neuen Ansatz im Gegensatz zu anderen Quantenprozessoren dar, die die Skalierung ihrer Quantengatter durch die Bewegung der Atome in den optischen Registern erreichen. Eine Adressierung mit Licht stellt dabei eine 100-fach schnellere Operation in Aussicht als es die Bewegung der Atome zulässt.

Contents

1. Introduction

Since the first idea of simulating quantum physics with quantum systems that follow an equivalent Hamiltonian but are better accessible, proposed by Richard Feynman [1], many quantum mechanical systems have been investigated for the realization of this task. The recent developments in quantum computing are dominated by superconducting circuits, reaching from first claims of quantum advantage in 2019 [2] to further demonstrations [3] and applications of utile quantum computing in the limits of the *Noisy Intermediate-Scale Quantum* (NISQ) era in 2024 [4]. These systems have already passed the frontier from demonstrating single physical effects, like preparing quantum states and Rabi oscillations, to performing calibrated gates that allow the investigation of complex algorithms.
For an application of a quantum system as quantum computer, the criteria by DiVincenzo must be satisfied [5]. Also for the systems competing with superconducting qubits, the fulfillment of these criteria has been demonstrated meanwhile [6, 7]. One of the competing concepts is the use of neutral atoms as a platform for quantum computing. Among them, the *Quantum Information Processing System* (Quips) at Technische Universität Darmstadt investigates the utilization of ^{85}Rb as a platform for quantum technologies. Starting from a moderate number of ensembles of rubidium atoms in version Quips-A [8], it has been developed to a world-leading system for trapping neutral atoms in defect-free structures in version Quips-B [9].
For the demonstration of coherent operations on quantum states, Rabi floppings of the states in the hyperfine structure of the atoms have been demonstrated using two-photon transitions in this experiment [8]. This thesis attempts to demonstrate the next milestones on the path to quantum computation in Quips which is the demonstration of a universal set of quantum gates. The universal set of gates requires the demonstration of 1-qubit rotations, virtual-Z rotations and a CNOT operation.
One of the keys to a universal set of quantum gates with neutral atoms is the controlled interaction between a pair of single atoms via the Rydberg blockade. The foundation of this field of atomic physics, describing atoms with one electron excited to a state with high principal quantum number, dates back before the discovery of quantum physics. Nevertheless, this research is not old-fashioned but an active field [10, 11, 12, 13, 14] as it is bridging the gap between semi-classical and quantum mechanical descriptions of the dynamics of an atom [15]. Modern setups allow the experimental exploration of the many implications Rydberg atoms and their interactions give.
The field of high-precision experiments in atomic physics was opened by the developments in cold atom physics and laser physics. With the invention of the laser [16], the doorway to quantum mechanical operations on atoms was opened. Also in recent experiments, lasers are often one of the keys to new experimental demonstrations and improvements in any parameter of the laser, e. g. power, wavelength, linewidth, or long-term stability, instantly offer new applications. Some milestones on this path are the first optical dipole trap in 1986 [17], but also the magneto-optical trap (MOT) [18] in 1987, and coherent manipulations of quantum states with a two-photon process in 1996 [19]. As one of the last fields in atomic physics, the controlled excitation to a defined Rydberg state was achieved in 1998 [20], driven by the development of lasers at short wavelengths with extremely narrow linewidth. And still, this

technique often defines the limit of experiments with Rydberg atoms which is therefore also addressed in this thesis.
Apart from quantum computing, also quantum sensing is one of the keystones defining the second quantum revolution [21]. With the high degree of control gained for the demonstration of tasks of quantum computation, this field can be accessed, too. Quantum sensors, among others, are explicitly interesting in the fields of magnetic and inertial sensing. Using the same setup and techniques developed for quantum computing, quantum sensing is demonstrated in this work.
This thesis is organized as follows:
In **Chapter 2**, concepts for quantum computing are presented in the context of DiVincenzo's criteria [5]. Among other systems, neutral atoms are assessed as a promising candidate for the demonstration of these criteria and basic conditions for the construction of such a system are concluded.
Chapter 3 describes the optical setup that is used in order to demonstrate DiVincenzo's criteria. The chapter starts with the physics that governs the trapping of individual atoms, the preparation of quantum states and the behavior of Rydberg atoms. Then, the basic techniques used with the trapped atoms are presented, like the initialization into a specific quantum state, the measured decoherence, and the imaging. Finally, the requirements for the construction of gate operations in this experiment are concluded.
Chapter 4 characterizes the laser systems that have been built or improved in the course of this thesis and are used for the demonstration of gate operations. This includes the use of optical phase-locked loops for the locking of one laser to another and for the locking of lasers to the light transmitted through a highly stable optical resonator.
In **Chapter 5**, the demonstration of quantum gate operations is described, showing 1-qubit rotations, virtual-Z rotations and a restricted controlled NOT (CNOT) operation that relies on postselection. This chapter therefore includes the results of Rabi and Ramsey experiments on the qubit basis states, the demonstration of site-selective and coherent Rydberg excitation and its improvements regarding shifts of the resonance frequency induced by light pulses at short wavelengths, and the controlled inversion of the quantum state of one atom controlled by the state of a neighboring atom.
Chapter 6 shows that the same setup can also be applied as a quantum magnetic field sensor, demonstrating its unique properties as versatile platform for quantum technologies.
In **Chapter 7**, a discussion of the demonstrated results is given with perspectives for future optimizations.

2. Concept of quantum computing with neutral atoms

Quantum computing with neutral atoms requires to fulfill DiVincenzo's criteria [5]. These are:

1. A scalable physical system with well characterized qubits
2. The ability to initialize the state of the qubits to a simple fiducial state
3. Long relevant decoherence times
4. A universal set of quantum gates
5. A qubit-specific measurement capability

In the following, these criteria are discussed in detail.

2.1. A scalable physical system with well characterized qubits

Many quantum systems have been proposed to fulfill the first of DiVincenzo's criteria. Among them are trapped ions, superconducting circuits, specialized crystals, single photons and neutral atoms.
The first demonstrations of quantum computation were performed in ion traps, showing that quantum mechanical systems are able to perform calculations as known from classical computers [6]. These results were produced with a very limited number of qubits that allowed classical computers to simulate the outcome of the experiment exactly. But the aim of quantum computing is to reach quantum advantage [22].
The platforms based on ion traps show strong interactions that are not promising to scale these systems up towards the system sizes that are supposed to reach quantum advantage. Starting from a qubit number of 50 qubits, a quantum computer is expected to outperform classical computers [23].
First results that claimed to demonstrate quantum computation beyond quantum advantage were produced on superconducting systems [2]. Further developments claim to demonstrate a systems with utile application [4]. According to a recent roadmap, a limit of 127 qubits and $100 - 1000$ gates is foreseen for one processor, planning modular extension for a further scaling [24].
In the recent years, systems based on neutral atoms broke one benchmark after the other, especially regarding the number of qubits [25] but also regarding gate fidelities [7]. Among the systems using neutral atoms, the variety of used species is still very large [26, 27, 28, 29]. Due to their different quantum numbers, also the performance regarding each of DiVincenzo's criteria varies. On the one hand, none of these systems was able to outperform the alternatives in each discipline yet. On the other hand, none of these systems showed intrinsic limitations that restrain neutral atoms from reaching quantum advantage.

For the scaling of qubit numbers, optical dipole traps were used in geometries that involve all dimensions of space [28, 9, 30]. As an illustration, one string of atoms, a plane and three dimensional structures have been demonstrated as visualized in Fig. 2.1. In this thesis, a platform for quantum technologies based on neutral atoms using the isotope ^{85}Rb is chosen to be upgraded in order to fulfill all of DiVincenzo's criteria. The rubidium atoms especially showed excellent capabilities for scaling the number of atoms [31]. Furthermore, each of DiVincenzo's criteria has already been demonstrated for its own on rubidium [32].
An open question is still the scalability of quantum operations. Most of the gate procedures shown so far operate on a limited number of qubits [33]. As all techniques for gate operations have been demonstrated for rubidium, this species is taken to remain a good candidate to engineer a gate operation that allows a scaling with the number of qubits.

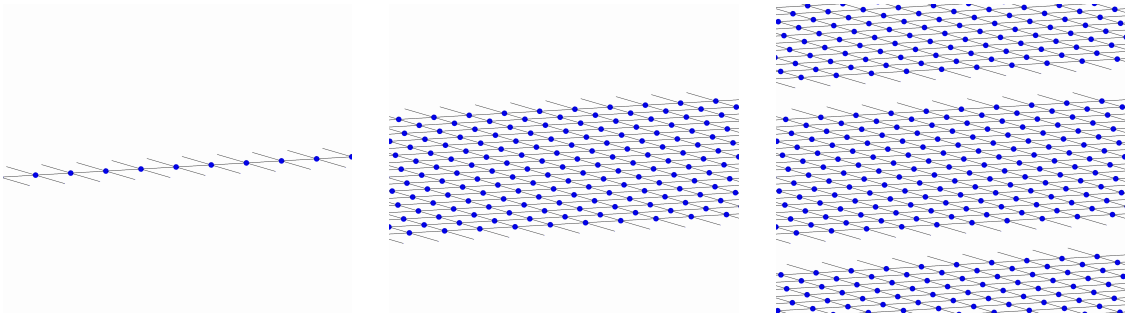

(a) (b) (c)

Fig. 2.1.: Examples of geometries for the scaling of atoms in spatial dimensions. Black lines connecting the schematic atoms are drawn to convey the drawn perspective.

2.2. Ability to initialize the state of the qubits to a simple fiducial state

The use of atoms as qubits begins with the choice of levels in the energy structure of the respective physical system. In neutral atoms, electronic states [27], magnetic states [29] and hyperfine states [7] have been used as qubit states. In recent research, even the use of transitions in the manifold of the nuclear spin has been discussed [34, 29].
These options differ in the used energy splitting that forms the qubit. Whereas electronic states can use an energy splitting on the order of electron volts, the energy splitting between hyperfine states is only one millionth of an electron volt. In magnetic states, the energy splitting is again a factor of thousand smaller.
These differences in the energetic scales have direct implications for the preparation of one of such a state as fiducial state and for its lifetime. One of the most convenient options for preparation offer electronic states as they can be prepared by optical pumping. But due to the limited lifetime of excited electronic states, alkaline metal atoms do not offer excited states with long lifetimes. In contrast, earth-alkaline atoms offer singlet and triplet states that allow the encoding of long-living electronic qubits [35, 27]. The use of magnetic qubits is limited by the stability of the magnetic bias field [36, 37].
For all used types of qubits, the degeneracy in the magnetic quantum number must be lifted in order to define the desired qubit state. Therefore, a magnetic bias field ("quantization field")

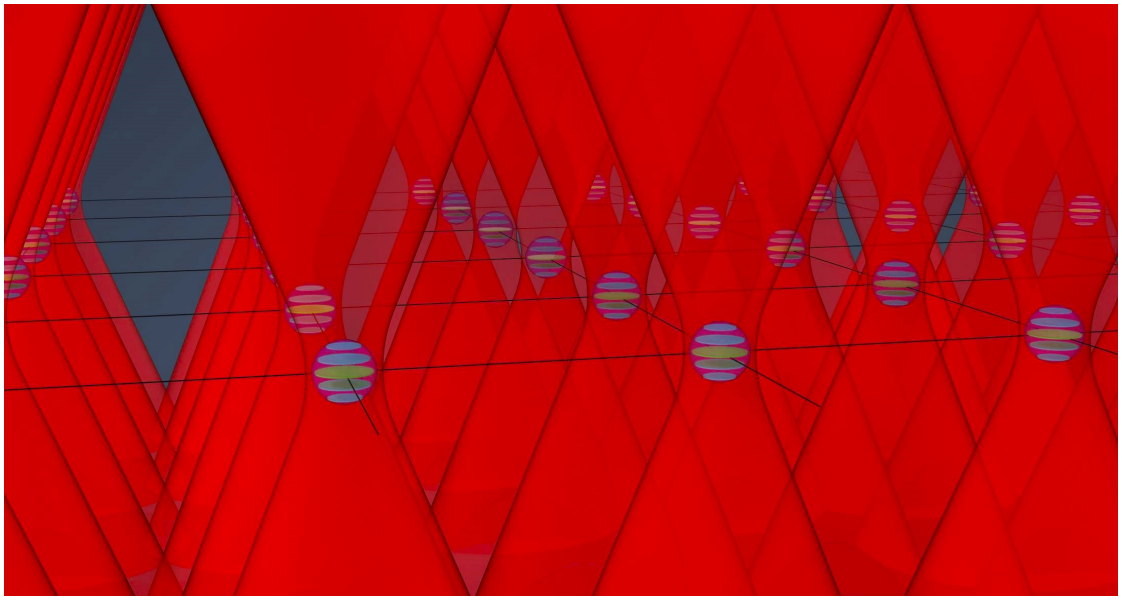

Fig. 2.2.: Visualization of a two-dimensional array of atoms in optical dipole traps with a schematic representation of m_F states ranging from -2 to $+2$. As the most promising m_F state, the state $m_\mathrm{F} = 0$ is highlighted in green. Black lines connecting the schematic atoms are drawn to convey the drawn perspective.

is applied to the atoms. As a drawback, the stability of the qubit is connected to the stability of the quantization field. As an illustration, the loss of this field (e. g. due to experimental failure) would lead to a loss of the quantum information. The noise on the respective components of the quantization field can become a limitation for decoherence times, as discussed in the next section.

When a fiducial state is chosen, it needs to be prepared. Starting from atoms in optical dipole traps, optical pumping is applied in all cases. Depending on the chosen basis states, this task shows different complexity. For states in the respective hyperfine structure manifold with extreme values of the F quantum number and maximum $|m_\mathrm{F}| = \mathrm{F}$, optical pumping on a cycling transition is an extremely efficient process that allows error rates well beyond one percent.

But these states are not very promising for quantum computing due to their large sensitivity to magnetic fields following the Zeeman effect [38]. The more promising choice are the "clock states" meaning states with a quantum number $m_\mathrm{F} = 0$. Following the linear scaling of the Zeeman effect with m_F, these states do not show a dependency on the magnetic field strength in first order, offering long coherence times as discussed in the next chapter. The preparation of these states is much more difficult and still a field of active research. Optical pumping on dipole-forbidden transitions [39] and its optimizations [40] are the mostly applied techniques. A drawback is, that the cooling of the clock states is not compatible with sideband cooling so far. Typical qubit basis states used are the states with $m_\mathrm{F} = 0$ and different F quantum number, like the states $|0\rangle = |5^2\mathrm{S}_{1/2}, \mathrm{F} = 2, m_\mathrm{F} = 0\rangle$ and $|1\rangle = |5^2\mathrm{S}_{1/2}, \mathrm{F} = 3, m_\mathrm{F} = 0\rangle$ of ^{85}Rb.

2.3. Long relevant decoherence times

In order to achieve long relevant decoherence times, the choice of the quantum states and the quality of isolation from any perturbations are crucial. For quantum computing, its concept has to be constructed with superpositions of states that are created by an electro-magnetic field with frequency ω_{light}. All operations after the initialization of the qubits must be constructed to be used on a superposition state $|\Psi\rangle = a\,|0\rangle + b\exp^{(i\theta)}\,|1\rangle$. Then, for the time evolution of the phase θ, it holds [41]:

$$\theta = \left(\omega_{\text{light}} - \omega_{\text{atom}}\right) t. \tag{2.1}$$

This means, that any quantum mechanical operation that changes the frequency of the transition ω_{atom} will imprint a time-dependent phase on the result of the quantum operation. This way, many mechanisms can cause changes of the phase like light shifts, magnetic fields, and electric fields.

A major limitation for the coherence of neutral atoms in dipole traps are the traps themselves. The scattering of the trapping light causes depolarization. Choosing the right parameters (see Sec. 3.1.1) allows to achieve depolarization times on the order of milliseconds and up to seconds [42, 7].

Regarding the magnetic field, the Zeeman effect describes an energy splitting ΔE in an external magnetic field B following

$$\Delta E = m_{\text{F}}\, g_{\text{F}}\, \mu_{\text{B}}\, B \tag{2.2}$$

using the hyperfine Landé g-factor g_{F} and the Bohr magneton μ_{B}. As the effect scales with the m_{F} quantum number, the clock states are the typical choice for qubit basis states. However, higher orders of the Zeeman effect can cause a shift for the levels of the clock states as well (see Sec. 3.2).

The influence of a electric field $\mathbf{E}$ on the energy levels of neutral atoms scales with the polarizability α following [43]

$$\Delta E = -\frac{1}{2}\alpha\,|\mathbf{E}|^2\,. \tag{2.3}$$

As the polarizabilities for the ground states are on the order of $h \times 0.08\,\text{Hz}\,\text{cm}^2\,\text{V}^{-2}$ [43], electric fields are negligible for the decoherence of these states. Highly excited atoms though can exhibit polarizabilities that are many orders of magnitude larger (see Sec. 3.1.5). Quantum information stored in such highly excited states can therefore show much fast decoherence times due to electric fields.

2.4. Qubit-specific measurement capability

A qubit-specific and state-sensitive measurement capability is provided in many experiments with a combination of a highly-sensitive camera [44] with adequate resolution and a lossy state projection. The state projection is performed by a resonant excitation of one of the qubit basis states. The concept is to induce loss of the atoms in one of the basis states and to take a fluorescence image of the atoms that are left-over [45, 46]. Though lossless detection schemes have been presented on single atoms [47, 48, 49], the state-specific readout of a large number of atoms is still an open discussion.

The process of state projection in the manifold of hyperfine and m_{F}-states is subject to a

method of optical pumping. The problem here is, that the resonant light needs to deliver enough energy to atoms that are supposed to be lost, but must leave the atoms in the other state in the trap with very high fidelity.
The main problem stays in providing a high fidelity for the detection of individual atoms. This task incorporates the physics of the light inducing the fluorescence in parameters of intensity and detuning, the settings of the camera but moreover robust software. For inducing the fluorescence of the atoms, the same light as used for cooling is used but with different parameters. The choice of parameters is a trade-off between scattering of atoms out of the traps, for instance with too much intensity or a too less detuning, and long exposure times. As the reached level of fluorescence is highly dependent of multiple beam pointings, changes in the level of fluorescence can occur. The software evaluating the fluorescence images therefore needs to be tolerant against changes of the fluorescence levels.
The time for the qubit-specific measurement is a cost regarding the decoherence time. Two timescales are important: The timescale for state projection and the timescale for imaging. The quantum nature of the experiment ends with applying the state projection. So, this operation must be placed well within the decoherence time, which can mean only a few hundred microseconds for a $1/e$ decoherence time of one millisecond. After the state projection, the presence of the atoms in the traps indicate their final state after the quantum experiment. So, the timescale for imaging is the lifetime of the atoms in the traps, which is limited for instance by the vacuum pressure and the trap depth. Therefore, timescales of up to 100 ms can be used until the imaging starts and also long exposure times can be used. Smaller timescales would be preferable nevertheless for improved rates of experimental cycles.

2.5. Universal set of quantum gates

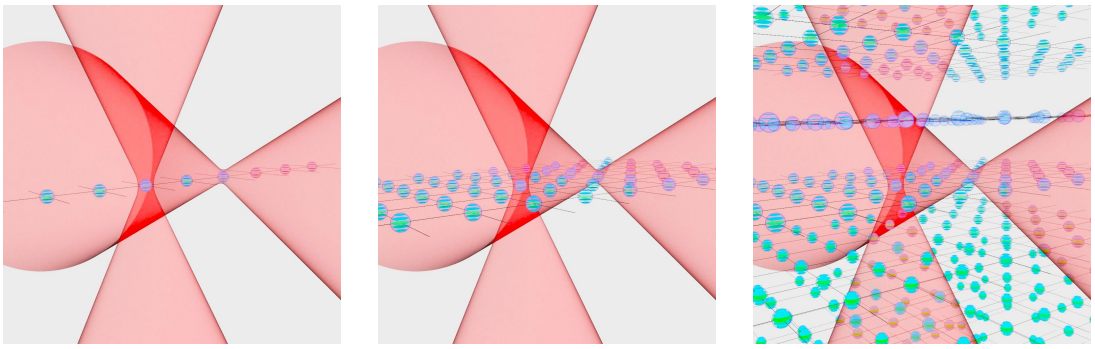

(a) (b) (c)

Fig. 2.3.: Visualizations of addressing individual atoms with laser beams inducing gate operations for different geometries of atom arrays from (a) one line to (b) a two-dimensional array and (c) and cubic arrangement. The higher the dimension used for storing atoms is chosen, the less options stay for single-site addressing with laser beams without interacting with unaddressed atoms. Black lines connecting the schematic atoms are drawn to convey the drawn perspective.

A universal set of quantum gates can be built out of a set of 1-qubit gates allowing the creation of all possible superposition states of the qubit basis and an interaction via a CNOT-gate [50]. For both types of gates, operations on subsets of the stored atoms are required in order to realize a quantum circuit. As depicted in Fig. 3.18, addressing with laser beams naturally sets

limits to the geometry used for the storage of atoms. As a good trade-off, a two-dimensional array of atoms is seen as a promising starting point for the discussion. In this concept, the 1-qubit gate is discussed firstly and then the CNOT gate.

2.5.1. Properties of the 1-qubit gate

The 1-qubit gate is an operation that manipulates the superposition of the qubit states for wach qubit independently. In alkali metal atoms, operations on hyperfine qubits coupled by microwave radiation [51, 52] or two-photon transitions [8, 53] have been demonstrated. These works show a good trade-off between technical complexity and coherence times.
The 1-qubit gate aims to writing information into the system. As this usually involves very specific information that cannot be encrypted in some kind of uniform starting point, it is expected that the manipulation of single qubits is needed for this gate. Due to the aim of manipulating single qubits, the microwave operation is not appropriate, as the resolution of a microwave field is limited [54].
There are demonstrations that show single-site addressing by the use of a globally applied light field (or a microwave field) and a locally acting light field that implies a light shift on one atom which shifts the resonance of the atom to match the frequency of the global light field (or the microwave) or to shift the resonance explicitly away from the frequency of the global light field (or the microwave) [55, 30, 56]. In this thesis, such a technique is not used as it seems straightforward that both ways of operation imperil the coherence either of the addressed qubit or of the unaddressed qubits.
The only technique that is trusted to perform local operations is a geometric localization of the light field in form of a steerable, tightly focused laser beam. For operations on the clock states, this requires two co-propagating light fields in circular polarization (see Sec. 3.1.2).
Due to the limited decoherence time, the time for one operation of this gate is limited. This involves two timings: The pulse itself and the switching from one qubit to another.
Producing light pulses in the regime of microseconds is state-of-the-art. In order to reach even lower pulse timings, more advanced techniques need to be used [57]. In contrast, the switching from one qubit to another is still an open discussion in the field [58]. Regarding the decoherence time of several $100\,\mu s$ and a perspective of performing up to 100 gates [4], a gate time shorter than $10\,\mu s$ is crucial. This involves addressing a qubit or a set of qubits and performing the relevant light pulses. Therefore, a switching time from one qubit to another of $1\,\mu s$ is desired.

2.5.2. Properties of the CNOT gate

With the CNOT gate, the mathematical operation on the quantum information is defined. Therefore, an addressed operation is needed for this gate, too.
A switching time from one qubit to another in the order of $1\,\mu s$ and a total gate time of less then $10\,\mu s$ are required following the same argument as stated for the 1-qubit gate.
For realizing a CNOT gate on neutral atoms, the Rydberg blockade is discussed to be the most promising option [58]. This task is not trivial and it is still an open discussion how this can be achieved in the best way with the recent laser techniques. The competing ideas involve using a single-photon UV-transition [26], a two-photon transition [59] or even three-photon transitions. The two-photon and three-photon processes hereby allow the compensation of the Doppler effect (two-photon) and recoil energies (three-photon) [60]. A complete investigation, which laser system should be used for optimal results is discussed in other works and

is not the scope of this thesis.
In order to use a two-photon transition, the two involved light fields need to drive a so called ”ladder scheme”. Regarding the influence of the Doppler effect, a co-linear, counter-propagating operation of the two beams is desired in order to reduce the influence of the Doppler effect. Nevertheless, the Doppler effect cannot be suppressed completely if light fields with different wavelengths are used in the ladder scheme.
Apart from these benefits, the process chosen for the Rydberg excitation is irrelevant for the gate operation. But regarding the functionality as a CNOT gate, the wave function of the final Rydberg state is relevant. As shown also in this experiment, the Rydberg blockade depends on the angular momentum quantum number of the used Rydberg states [39]. In order to keep the CNOT logic as simple as possible, an isotropic Rydberg blockade is desired. Therefore, an $|nS\rangle$-state is preferred over P- or D-states. From the choice of using an $|nS\rangle$-state as final state and having the $|5S\rangle$-state as initial state, a transition without a change in angular momentum is needed. This requires that the Rydberg light fields are circularly polarized.
Combining the Rydberg blockade with the other DiVincenzo criteria is difficult. The scalability of a Rydberg excitation is one of the major problems. In quantum simulation, some experiments show a Rydberg blockade on arrays consisting of hundreds of atoms using a global addressing [13, 12]. Depending on the scope of the experiments, the laser power and the required Rabi frequencies are the only limit. But the techniques used in simulation are only in part applicable to the construction of a CNOT gate using an addressed operation.
Demonstrations of gate operations using the Rydberg blockade include the Hadamard-controlled-Z (H-C_Z) and the amplitude swap (ASWAP) protocol [33] and the “Levine-Pichler” gate [32, 7]. The latter operation is also named as symmetric gate in other publications [10, 29]. As the Levine-Pichler gate requires full control over the light frequencies and phases, it is not in the scope of this thesis.
Scalability for the gates can be used in at least two contexts here. The more sophisticated context of scalability means the operation on multiple qubits in parallel at the same time. Approaches for this are formulated in the gate protocols using the Levine-Pichler gate. But even with this gate, the number of different patterns where a gate can be performed could be limited due to the switching time from one pattern to the next. Therefore, a weaker context of scalability is in focus of this thesis which is the number of array sites where a gate can be performed. Basically, the optical setup is supposed to perform a Rydberg excitation in 100 different array sites with no other limit than measurement time.
All in all, individual rubidium atoms in arrays of optical dipole traps are expected to deliver a quantum system that allows the demonstration of the DiVincenzo criteria. Experiments with rubidium can demonstrate long enough decoherence times, all types of gate operations and the scalability of qubit numbers. In the following, the technical realization of all of these concepts is described, including an approach for the scalability of gate operations with rubidium.

3. Technical realization

From the many proposed techniques that are supposed to allow quantum computing, a promising subset is chosen and its technical details and developments during this project are presented. This chapter starts with an introduction to the formula that define optical dipole traps and coherent operations that allow to use neutral atoms as carriers of quantum information. Next, a detailed analysis of the subsystems of the experimental apparatus of Quips-B is given following again DiVincenzo's criteria. Therefore, the properties of the qubit basis are discussed regarding the used basis states in ^{85}Rb. Afterwards, the initialization of a defect-free array of atoms in the $|5^2\mathrm{S}_{1/2}, \mathrm{F} = 2, m_\mathrm{F} = 0\rangle$ state is described. In the following, the coherence times of the qubits in the dipole traps are demonstrated before discussing the readout. Finally, the geometric configuration of the qubits and laser beams used for quantum operations in this setup is presented.

3.1. Overview of the physics of trapping and coherent manipulation of neutral atoms

The most relevant formula defining the processes used in this project are described. Most of these mechanism are derived in textbooks or in preceding theses and only their results are summarized in this section.

3.1.1. Optical dipole traps

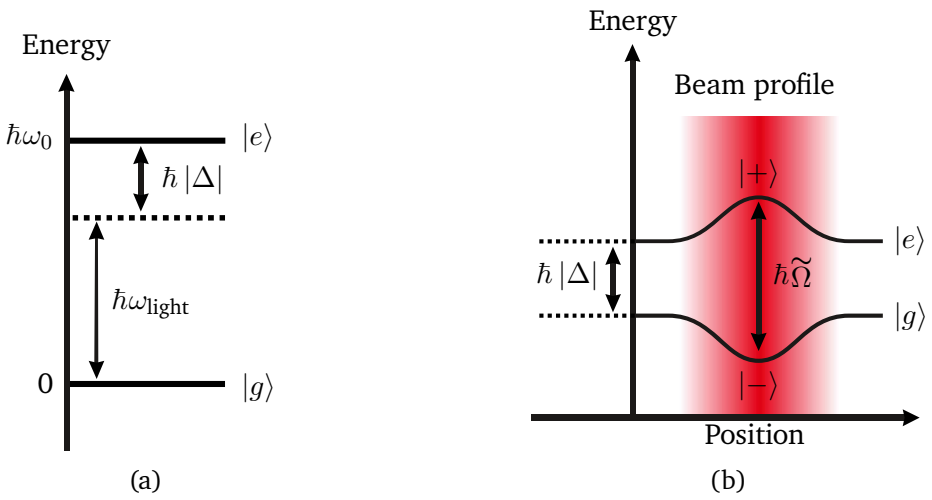

Fig. 3.1.: (a) Level scheme assumed for an ideal two-level system. (b): Scheme of the shift of the energy eigenstates in an optical dipole trap, modified from [61].

For the demonstration of gate operations, neutral atoms in optical dipole traps are used. Their dominant properties regarding quantum operations are the scattering rate and the trap depth

which define the coherence times and lights shifts for the gate operations. The equations for these two properties are motivated here. A complete derivation of the interaction between the light field and the (simplified) atom in this experiment is described in [59, 62].
The optical dipole traps in the discussed experiments operate with large detunings relative to an optical transition (compared to the linewidth of the transition) between two states $|g\rangle$ and $|e\rangle$. Following the derivation in [59], the two states are coupled and perform Rabi oscillations with the Rabi frequency Ω_0 given by

$$\Omega_0 = \frac{\langle g| \hat{\boldsymbol{\epsilon}} \cdot \mathbf{d} |e\rangle \cdot E_0}{\hbar}. \tag{3.1}$$

with the unit vector $\hat{\boldsymbol{\epsilon}}$ marking polarization vector of the linearly polarized electrical field $\mathbf{E}$ with amplitude E_0 and the dipole moment of the atom $\mathbf{d}$. The light field oscillates at a frequency ω_L which can be detuned with respect to the atomic resonance by $\Delta = \omega_0 - \omega_\mathrm{L}$ as shown in Fig. 3.1 (a). The coupling of the states of the atom lead to a shift of their energy eigenvalues by:

$$E_\pm = -\frac{\hbar\Delta}{2} \mp \frac{\hbar\Omega}{2} \tag{3.2}$$

with

$$\Omega := \sqrt{\Omega_0^2 + \Delta^2}, \tag{3.3}$$

where Ω is the generalized Rabi frequency. For the typically large detuning of the optical dipole traps, this reduces to:

$$\Delta E = \frac{\hbar\Omega_0^2}{4\Delta}. \tag{3.4}$$

This shift of the energy eigenvalues leads to an effective potential for atoms in the ground state given by:

$$U_\mathrm{dip}(\mathbf{r}) = \frac{3\pi c^2}{2\omega_0^3}\frac{\Gamma}{\Delta} I(\mathbf{r}) \tag{3.5}$$

The dependency of the potential depth against the detuning is plotted for two states of ^{85}Rb in Fig. 3.3 (a). The rate of scattering is then given by:

$$\Gamma_\mathrm{SC} = \frac{3\pi c^2}{2\hbar\omega_0^3}\left(\frac{\Gamma}{\Delta}\right)^2 I(\mathbf{r}), \tag{3.6}$$

where $I(\mathbf{r}) = \epsilon_0 c\,|\mathbf{E}(r)|\,/2$ and the spontaneous decay rate Γ of the excited state is also known as natural linewidth [63], c is the speed of light and ϵ_0 the vacuum permittivity. The exact values of Γ for ^{85}Rb together with other relevant parameters are given in Fig. 3.2. A plot of the dependency of the scattering rate against the detuning for two states of ^{85}Rb is shown in Fig. 3.3 (b).

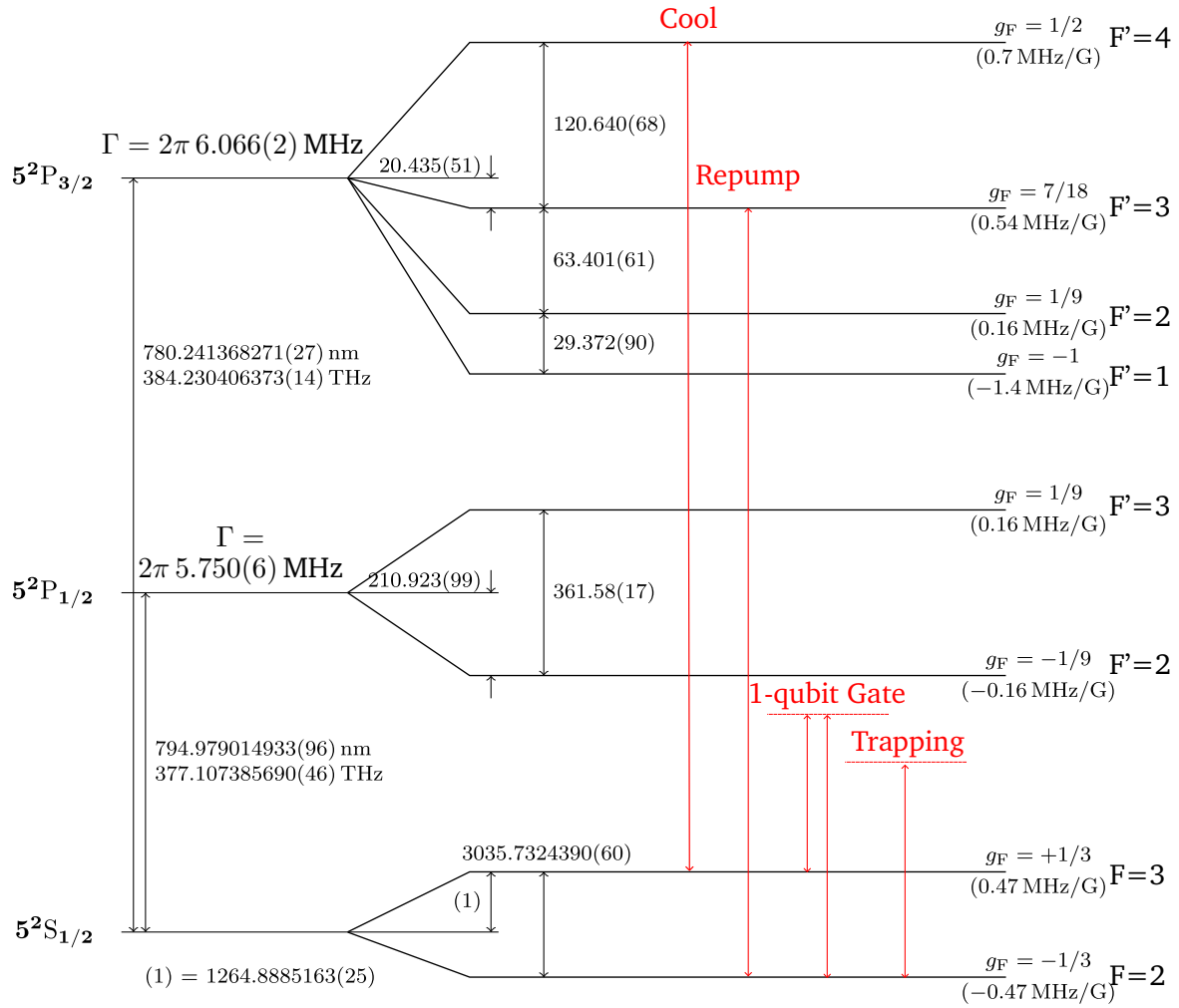

Fig. 3.2.: Partial level scheme of ^{85}Rb and the transitions used for cooling, trapping, and 1-qubit operations. The F-quantum number of the excited states 5^2P are written as F' to differentiate these states from the ground states 5^2S. Energy is drawn not to scale. (Modified from [43].)

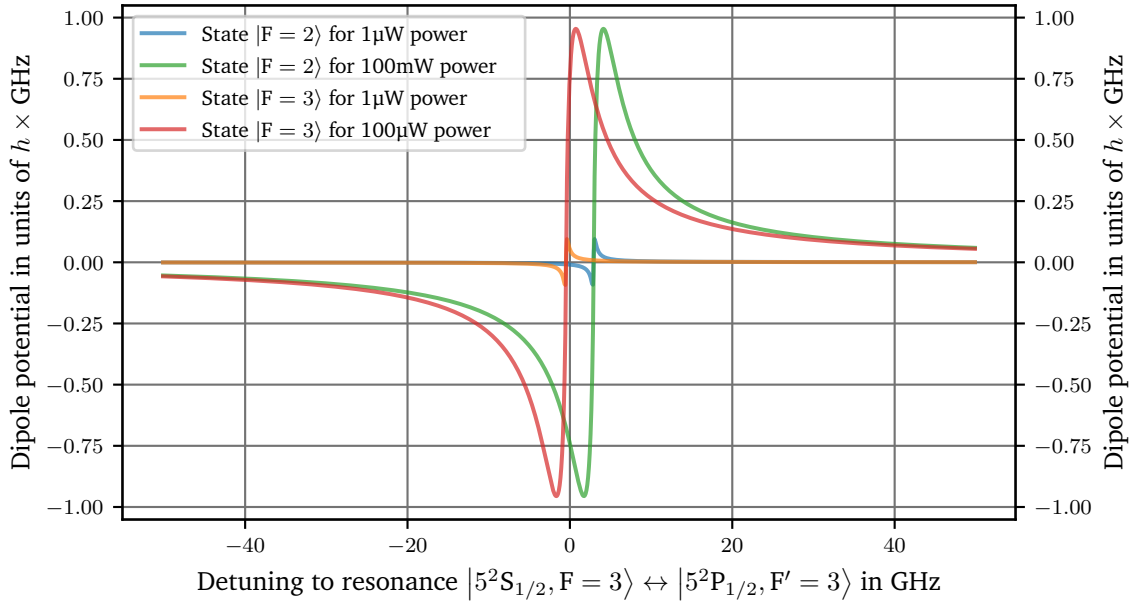

(a)

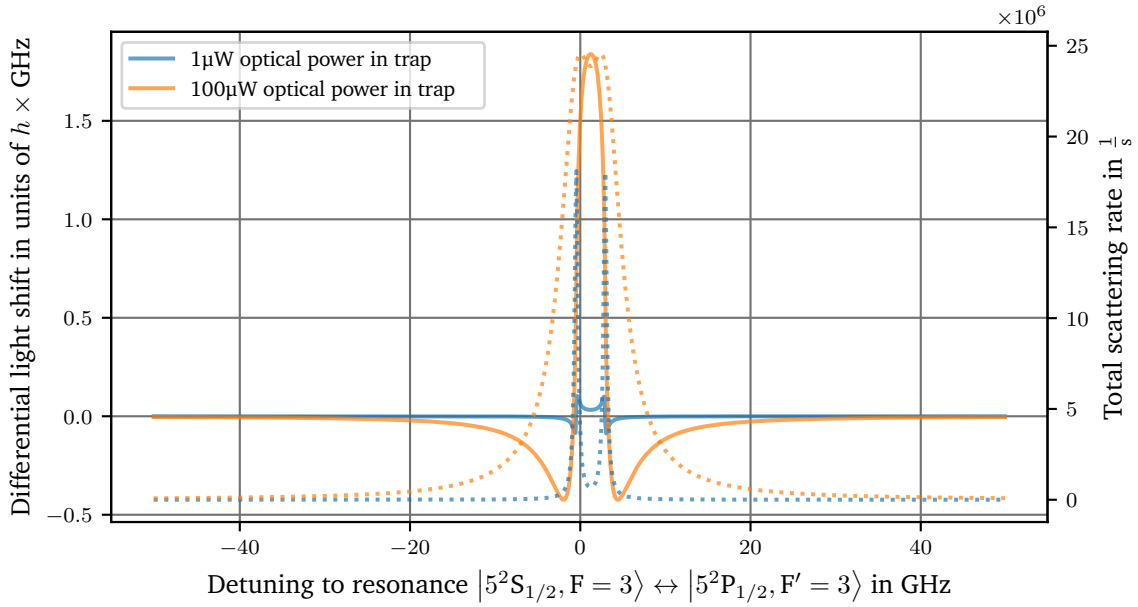

(b)

Fig. 3.3.: (a) Plot of (3.5) for the case of ^{85}Rb. (b) For this isotope, two hyperfine states offer two close transitions for which the formula can be applied individually, resulting in a differential light shift (solid line), see (3.10). Between the two states, the high scattering rate (dotted) following (3.6) is a challenge for coherent operations. Only the ground states with $m_F = 0$ are taken into account.

3.1.2. Two-photon processes

In ^{85}Rb, the hyperfine structure offers wide applications for quantum information processing. Hereby, two-photon processes are widely used. Such transitions are described in terms of a three-level system, consisting of two states $|0\rangle$ and $|1\rangle$ with a small energy splitting of Δ_{hfs} and one state $|i\rangle$ with a large energy difference to these states. This system, also known as "Λ-scheme" is visualized in Fig. 3.4 (a). Two coherent light fields are used in this system with the angular frequencies ω_1 and ω_2, which couple the states $|0\rangle \leftrightarrow |i\rangle$ and $|1\rangle \leftrightarrow |i\rangle$ respectively. A detuning $\Delta_{\mathrm{i,1}}$ to the resonances with the state $|i\rangle$ is used which is large compared to the Rabi frequencies Ω_1 and Ω_2 that define the transitions $|0\rangle \leftrightarrow |i\rangle$ and $|1\rangle \leftrightarrow |i\rangle$. Then, the state $|i\rangle$ is adiabatically eliminated and the system can be reduced to an effective two-level system between the states $|0\rangle$ and $|1\rangle$ [65]. The Rabi oscillation in this system is then given by the two-photon Rabi frequency following [64]

$$\Omega_{2\mathrm{P}} = \frac{\Omega_1^* \Omega_2}{2\Delta_{\mathrm{i}}}. \tag{3.7}$$

In this effective two-level system, the detuning for the resulting Rabi oscillation is defined by

$$\delta = \omega_1 - \omega_2 - \Delta_{\mathrm{hfs}}. \tag{3.8}$$

When applying the light fields, the states become dressed states with an energy shift according

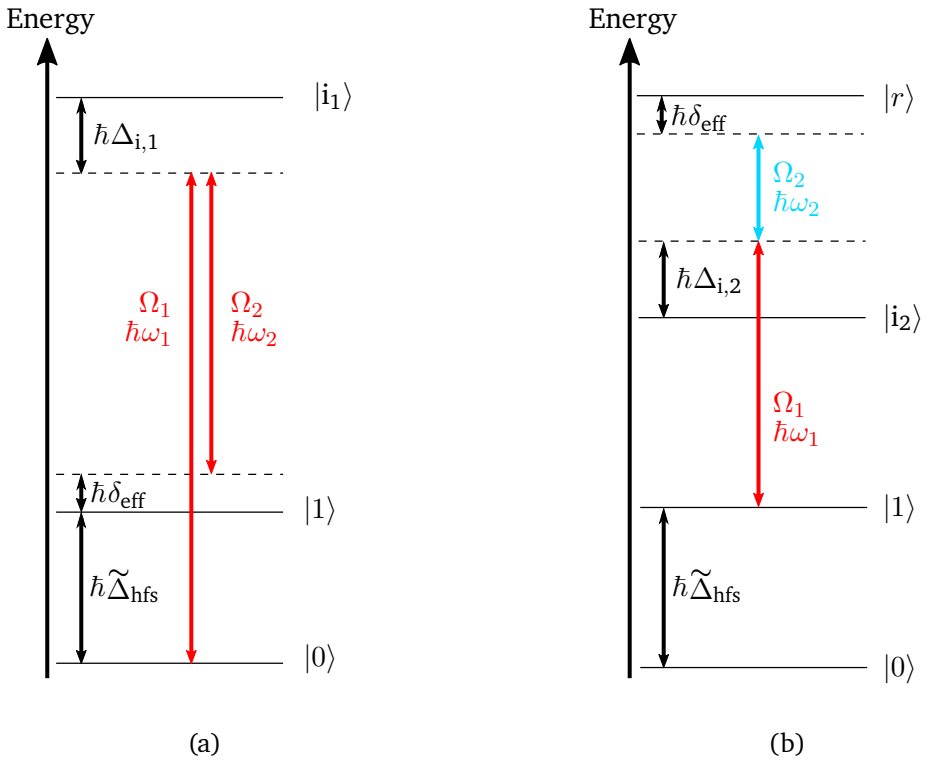

Fig. 3.4.: (a) Level scheme of a two-photon process in Λ-configuration, from [61], modified from [64]. (b) Level scheme of a two-photon process in ladder configuration.

to (3.4). As both states are shifted, the differential light shift is given by:

$$\delta^{\mathrm{AC}} := \frac{\Delta E_{|0\rangle\leftrightarrow|\mathrm{i}\rangle} - \Delta E_{|1\rangle\leftrightarrow|\mathrm{i}\rangle}}{\hbar} \tag{3.9}$$

$$= \frac{\left(\Omega_1^2 - \Omega_2^2\right)}{4\Delta_{\mathrm{i},1}}. \tag{3.10}$$

A plot of this effect is given in Fig. 3.3 (b). With these definitions, an effective Rabi frequency $\sim\Omega$ of the two-photon process for a present light shift can be defined in analogy to (3.3) by

$$\widetilde{\Omega} = \sqrt{|\Omega_{2\mathrm{P}}|^2 + (\delta^{\mathrm{AC}} - \delta)}. \tag{3.11}$$

In the typical experimental procedure, the effective Rabi oscillation is measured including all shifts. It is therefore handy to define the energy splitting of the lower states including the light shifts $\widetilde{\Delta}_{\mathrm{hfs}}$ and the effective detuning δ_{eff} also including this shift to

$$\widetilde{\Delta}_{\mathrm{hfs}} = \Delta_{\mathrm{hfs}} + \delta^{\mathrm{AC}} \tag{3.12}$$

$$\delta_{\mathrm{eff}} = \omega_1 - \omega_2 - \widetilde{\Delta}_{\mathrm{hfs}}. \tag{3.13}$$

This effective Rabi frequency holds for atoms in a light field as drawn in Fig. 3.1 (b). Including a damping γ of the driven oscillation and an optional time shift t_0 relative to the start of the interaction between the atom and the light field, the population in the upper state of the two-level system is given by [66]:

$$P_{\mathrm{Rabi}}(t) = \frac{\Omega^2}{\gamma^2 + 2\Omega^2}\left[1 - \exp^{\left(\frac{-3\gamma(t-t_0)}{4}\right)}\left(\cos(\widetilde{\Omega}(t-t_0)) + \frac{3\gamma}{4\widetilde{\Omega}}\sin(\widetilde{\Omega}(t-t_0))\right)\right]. \tag{3.14}$$

The same formalism described here can also be used in the context of a "ladder" scheme as shown in Fig. 3.4 (b). Such a scheme is used for the coherent excitation from one of the qubit basis states to the Rydberg state via a two-photon process.

3.1.3. Ramsey experiment

The evolution of a quantum mechanical phase of a superposition state as mentioned in (2.1) is motivated. This effect is tested in a Ramsey experiment. The two-level system is defined with two quantum-mechanical states $|0\rangle$ and $|1\rangle$ that are split by an energy $E = \hbar\omega_0$ as shown in Fig. 3.5 (a). Here, the initial state is defined to $|0\rangle$. An electro-magnetic field of the form

$$\mathbf{E}(t) = \mathbf{E_0}\exp^{i\left(\omega_0 + \delta_{|0\rangle\leftrightarrow|1\rangle}\right)t} + c.c. \tag{3.15}$$

is used to couple the two states with a Rabi frequency $\widetilde{\Omega}$. Here, $\delta_{|0\rangle\leftrightarrow|1\rangle}$ is used to describe a detuning of the driving field relative to the unperturbed transition frequency ω_0.
In a representation on the Bloch sphere [50] as drawn in Fig. 3.5 (b), a pulse of the driving field with duration $\tau = 4/\widetilde{\Omega}$ results in a rotation of the state vector of $\pi/2$ around the **x**-axis. Therefore, this operation is called a $\pi/2$ pulse.
A typical experiment starts with the preparation of a two-level system in one of its basis states

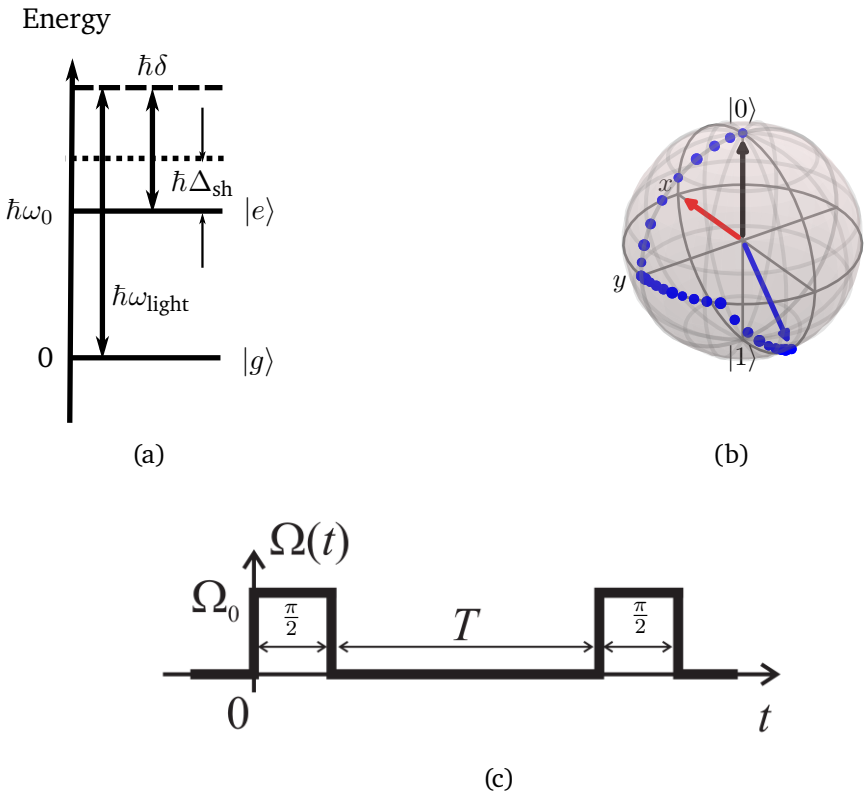

Fig. 3.5.: (a) Scheme of the energy shifts occurring in a Ramsey experiment including light shifts, modified from [41]. (b) Scheme of the evolution of the quantum state during a Ramsey experiment starting in the $|0\rangle$ state with a rotation over $\pi/2$ in the equatorial plane [67]. (c) Scheme of the pulse sequence used for a Ramsey experiment, modified from [41].

and follows the pulse sequence drawn in Fig. 3.5 (c) A $\pi/2$ pulse couples the two basis states and prepares a superposition that can be described by

$$|\Psi\rangle = \underbrace{a\exp^{(i\xi)}}_{=:\alpha}|0\rangle + \underbrace{b\exp^{(i\zeta)}}_{=:\beta}|1\rangle \tag{3.16}$$

with a polar representation of the complex amplitudes α and β by the variables $a,\ b,\ \xi,\ \zeta \in \mathbb{R}$. The variables ξ and ζ act as global phases, but only the relative phase can be detected [50]:

$$\theta = \xi - \zeta. \tag{3.17}$$

The experiment must be understood as an individual evolution of the phase θ of the superposition state, according to the energy splitting between the states $|0\rangle$ and $|1\rangle$, and of the phase of the driving field that couples the states. The accumulated differences of these evolutions are measured with a second $\pi/2$ pulse after a time of evolution T. In absence of further effects and for a set detuning $\delta_{|0\rangle\leftrightarrow|1\rangle} \neq 0$, the light field accumulates a phase offset according to $\left(\delta_{|0\rangle\leftrightarrow|1\rangle}T\right)$ relative to the evolution of the state. This motivates (2.1) under the assumption $\delta_{|0\rangle\leftrightarrow|1\rangle} = \left(\omega_{\mathrm{light}} - \omega_{\mathrm{atom}}\right)$

$$\theta = \left(\omega_{\mathrm{light}} - \omega_{\mathrm{atom}}\right) T.$$

In real experiments, many effects contribute to the effective frequency of the phase evolution. For instance, the AC Stark effect [68] can cause shifts of the transition frequency ω_{atom} to

$$\omega_{\mathrm{atom}} = \omega_0 + \Delta_{\mathrm{sh}} + \delta_{\mathrm{p}}. \tag{3.18}$$

Here, shifts that are present only during the time of free evolution T are described by Δ_{sh} whereas shifts that are present in addition to that during the pulses of the driving field are described by δ_{p} [41]. For instance, atoms stored in optical dipole traps experience the light shift of the traps (Δ_{sh}) during the time of free evolution and experience a light shift from the light fields driving the clock transition via a two-photon process (δ_{p}) during the pulses in addition to the traps . These effects need to be discussed individually for the respective experiments.

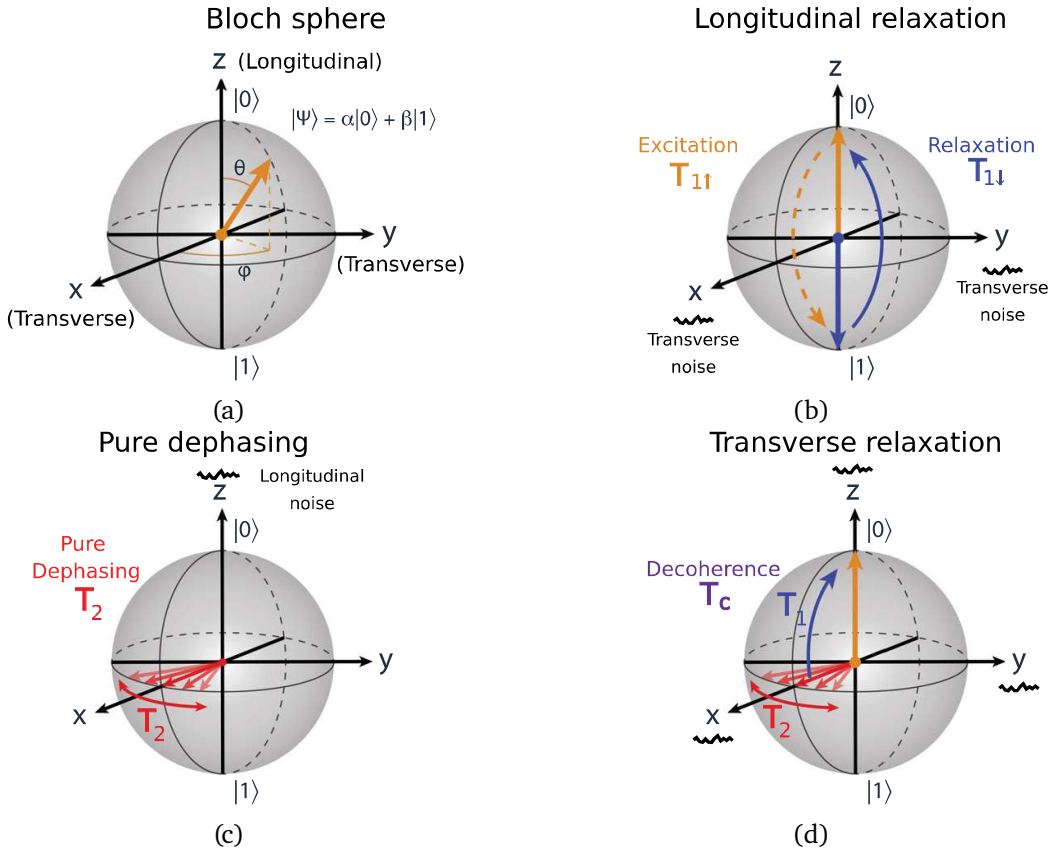

Fig. 3.6.: Scheme of the different mechanisms of decoherence of quantum states, taken from [67].

In addition, effects that cause a damping of the measured oscillation need to be taken into account. These effects can be separated into the longitudinal relaxation and the transverse relaxation as visualized in Fig. 3.6. Longitudinal relaxation is visualized in Fig. 3.6 (b) and is given by the energy exchange of the two-level system with the environment in terms of excitation and relaxation. These two effects are characterized by the times $T_{1\uparrow}$ and $T_{1\downarrow}$. The relaxation is then described by a damping time T_1 following [67]

$$\frac{1}{T_1} = \frac{1}{T_{1\uparrow}} + \frac{1}{T_{1\downarrow}}. \tag{3.19}$$

Transverse relaxation is split into two effects for quantum experiments using multiple qubits,

a homogeneous dephasing and an inhomogeneous dephasing. This is characterized by damping times T_2, T_2' and T_2^* following [69]

$$\frac{1}{T_2} = \frac{1}{T_2'} + \frac{1}{T_2^*}. \tag{3.20}$$

The homogeneous part of dephasing results from noise in the energy splitting of the states. As a result, noise η_h is added to the phase θ of the qubit to $\theta + \eta_h$. This will diffuse the phase of one qubit in the equatorial plane of the Bloch sphere as shown in Fig. 3.6 (c). The time constant of this diffusion is characterized by T_2'.
When averaging over multiple measurements of quantum systems, the different realizations will differ from each other, mainly due to classical effects like a finite temperature of the atoms. This causes the inhomogeneous dephasing when systems are averaged that are not completely comparable. For an atom in an optical dipole trap, the effective trap depth varies from shot to shot due to different temperatures of the atom. After the averaging, atoms with different precession speed will be taken into account, leading to a measured dephasing characterized by T_2^*. As this shot-to-shot dephasing is given by noise at rather slow frequencies, it can be compensated by unitary operations of the qubit, e. g. dynamical decoupling [70, 71]. Therefore, the inhomogeneous dephasing is considered to be reversible [67].
Typically in experiments with neutral atoms without compensation of inhomogeneous dephasing, the inhomogeneous dephasing time T_2^* is the major contribution to the dephasing and the longitudinal relaxation can be neglected (see Sec. 3.5). In this case, the probability to measure the two-level system in the state $|1\rangle$ at the end of the Ramsey experiment is given by $P_{\text{Ramsey}}(t)$ following [69, 72]

$$P_{\text{Ramsey}}(t) = C + \alpha(t, T_2^*)\frac{A}{2}\cos\left[\left(\omega_{\text{light}} - \omega_{\text{atom}}\right)t + \kappa(t, T_2^*) + \phi\right] \tag{3.21}$$

with

$$\alpha(t, T_2^*) = \left(1 + \left(\exp^{(2/3)} - 1\right)\left(\frac{t}{T_2^*}\right)^2\right)^{(-2/3)} \tag{3.22}$$

$$\kappa(t, T_2^*) = -3\arctan\left(\frac{t}{T_2^*}\sqrt{\exp^{2/3} - 1}\right) \tag{3.23}$$

$$\tag{3.24}$$

where A, C and ϕ are free fit parameters to adapt for errors in contrast (A) and offset (C) due to preparation errors and detection errors, as well as a phase offset (ϕ).

3.1.4. σ and π transitions

The orientation of the quantization field defines the required directions of propagation and polarization of the light inducing operations on the atoms. A classical visualization of this relation is drawn for the emission of light in Fig. 3.7. In the picture of the electron forming a classical electrical dipole oriented along the magnetic axis, three cases of its motion are defined. In the case of a classical oscillation along the dipole axis, the movement of the electron induces electro-magnetic waves oscillating along the orientation of the magnetic fields. This

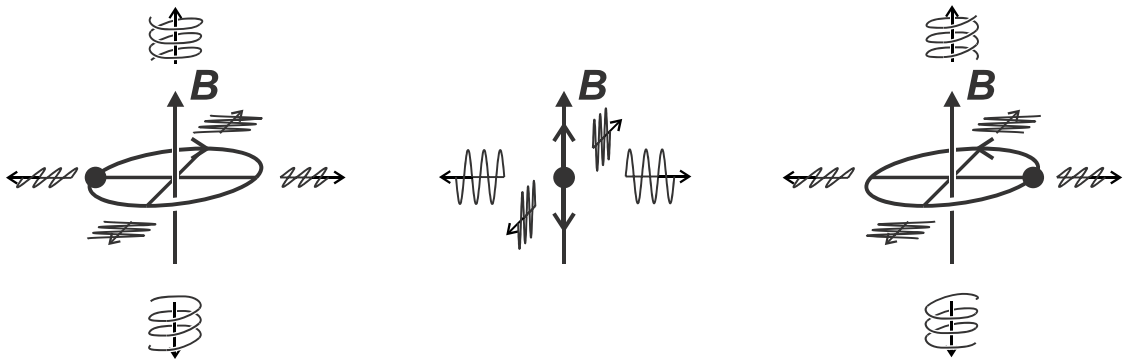

Fig. 3.7.: Classical visualization of light emission of atoms in a magnetic field **B**. ΔM_J stands for the angular-momentum components of the emitted photons in the direction of the magnetic field. (Modified from [73].)

is linear polarized radiation with an angular momentum which has no component along the magnetic axis, defined as $\Delta M_\mathrm{J} = 0$. Due to the conservation of angular momentum, this can originate only from transitions between m_F-states with $\Delta m_\mathrm{F} = 0$. Following a common naming for the polarization of light, this is called a "π transition" in this thesis, adapting the naming from [43].
A more complex situation holds for an electron rotating around the magnetic axis. In a projection perpendicular to the magnetic axis, emitted radiation is also linearly polarized but in a plane perpendicular to the orientation of the magnetic axis. In a perspective along the magnetic axis, this radiation is circularly polarized, corresponding to $\Delta M_\mathrm{J} = \pm 1$. This angular momentum originates from transitions between m_F-states with $\Delta m_\mathrm{F} = \pm 1$. In contrast to the π transition, this is called a "σ transition" in this thesis.
This naming is useful for the discussion of the stimulation of these transitions. Following the invariance of time, light irradiated in the respective direction is able to drive transitions between the respective m_F-states. But in contrast to the typical naming of σ polarization for circularly polarized light, also linearly polarized light can drive a σ transition if its polarization plane is oriented perpendicularly to the magnetic field. This is a limitation for optical pumping using π transitions, as any error in the orientation of the linearly polarized light regarding the direction of propagation and the polarization plane stimulates σ transitions (see Sec. 3.4.3).

3.1.5. Rydberg blockade

An atom is called a "Rydberg atom" if the binding energy of one of its electrons follows the Rydberg formula

$$E = -\frac{R_y^*}{n^2}. \tag{3.25}$$

With the Rydberg energy $R_y^* \approx 13.6\,\mathrm{eV}$ and the principal quantum number n, this formula holds for the hydrogen atom. Other species with one electron excited to sufficiently high

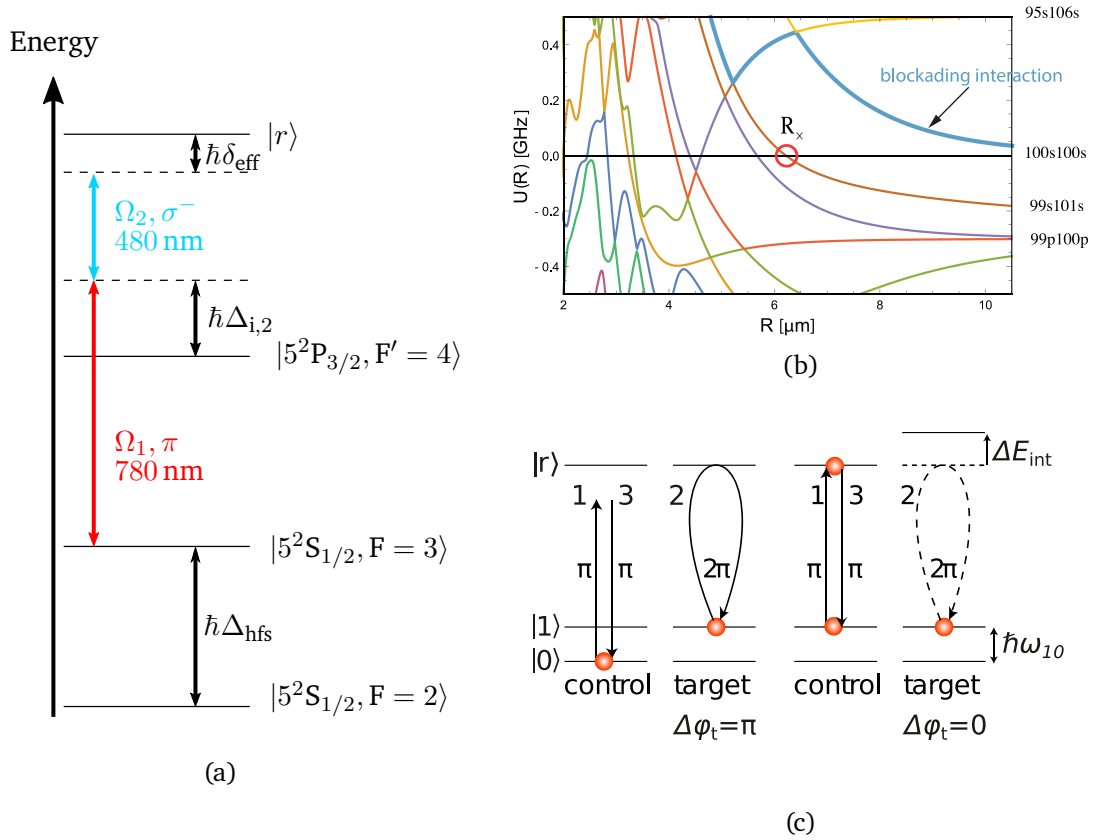

Fig. 3.8.: (a) Transition scheme for a two-photon excitation of a Rydberg state in ^{85}Rb. (b) Dependence of the energy shift induced by the interaction of two neighboring Rydberg atoms in the $100s$ state visualized on the slope labeled "blockading interaction". For closer approximation than 7 µm, molecular resonances with other Rydberg states dominate the interaction. The position of the outer-most resonant molecular potential crossing $R_\times$ is marked with a red circle. The energy scale is centered about the $100s + 100s$ dissociation limit for two Rb atoms. (Taken from [74].) (c) Scheme of a controlled phase operation mediated by the Rydberg blockade.

enough values of n that they behave comparable to a hydrogen atom are also called a Rydberg atom using the effective principal quantum number n^* that takes the field of the inner electrons into account. In the field of neutral-atom quantum computing, a "Rydberg state" is assumed to have $n > 30$ [77, 59].

Due to the large principal quantum numbers, the excitation of an alkali atom into the Rydberg state requires very short wavelengths. An alternative is a two-photon transition following the ladder scheme (see Sec. 3.1.2). For ^{85}Rb, a typical excitation of a Rydberg state via the intermediate state $|5^2\text{P}_{3/2}, \text{F}' = 4\rangle$ is shown in Fig. 3.8 (a). For such an excitation scheme, two lasers with wavelengths of 780 nm and 480 nm are applied. Corresponding to their visual appearance, the lasers are called the blue Rydberg laser (480 nm) and the red Rydberg laser (780 nm).

Following Bohr's semi-classical atomic model, the atomic radius of a Rydberg state scales as

$$r = (n^*)^2 \times a_0 \tag{3.26}$$

with the Bohr radius $a_0 = 0.529\,\text{Å}$ [59]. This intense scaling with the principal quantum number allows the interaction between atoms over large distances via van-der-Waals interactions.

Tab. 3.1.: Scaling laws as a function of the effective principle quantum number n^* for the most important properties of Rydberg states. Adopted from [75, 76].

Property	Quantity	Scaling law
Binding energy	E_{n^*}	$(n^*)^{-2}$
Level spacing	$\lvert E_{n^*} - E_{n^*+1}\rvert$	$(n^*)^{-3}$
Radius	$\langle r\rangle$	$(n^*)^2$
Polarizability	α	$(n^*)^7$
Radiative lifetime	τ	$(n^*)^3$
Transition dipole moment $\lvert g\rangle \leftrightarrow \lvert nl\rangle$	$\lvert\langle nl\rvert - er\lvert g\rangle\rvert$	$(n^*)^{-3/2}$
Transition dipole moment $\lvert nl\rangle \leftrightarrow \lvert nl'\rangle$	$\lvert\langle nl\rvert - er\lvert nl'\rangle\rvert$	$(n^*)^2$
Resonant dipole-dipole interaction coefficient	C_3	$(n^*)^4$
van der Waals interaction coefficient	C_6	$(n^*)^{11}$

For quantum computing based on neutral atoms, this allows to implement controlled interactions between atoms that are well isolated from the environment when they are not in a Rydberg state.
The scaling of this interaction strength and other parameters is shown in Tab. 3.1. The van-der-Waals interaction can be scaled large enough to construct the "Rydberg blockade". For two interacting atoms that are fixed at a distance R_b, this describes a shift of the energy eigenvalues of the Rydberg states that is large enough to suppress an excitation of both atoms. The shift of the energy eigenvalues via induced dipole moments between two equal Rydberg states follows [38]

$$\Delta E = -\frac{C_6}{R^6} \tag{3.27}$$

with the van-der-Waals coefficient C_6 and the distance R. If the shift of the double excitation is large enough to dominate the Rabi frequency Ω, this excitation is suppressed. Due to the strong dependence on the distance, the "blockade radius" is used to describe the situation where the atoms are close enough to exhibit a Rydberg blockade following [58]

$$R_\mathrm{b} = \frac{C_6}{\hbar\Omega}. \tag{3.28}$$

For ^{85}Rb and principal quantum numbers $n > 60$, typical values for the blockade radius R_b are $(5 - 15)\,\mu\mathrm{m}$. The regime of Rydberg blockade is hereby also limited towards extremely small distances due to molecular resonances that induce avoided level crossings ("spaghetti regime") as shown in Fig. 3.8 (b) [74].
In the regime of Rydberg blockade, this mechanism can be used in the context of quantum information as shown in Fig. 3.8 (c). Hereby, one qubit is called the "control" and the other the "target" suggesting their functions in the gate and referring to the pulse sequence that first couples the control qubit to the Rydberg state with a π pulse, then the target qubit with a 2π pulse and lastly again the control qubit with a π pulse.
For two qubits with two qubit basis states $|0\rangle$ and $|1\rangle$, the excitation to the Rydberg state is specific for the respective basis state. This makes the occurrence of the Rydberg blockade dependent on the initial configuration of states. Following the notation in [78], the initial configurations of pure states for each qubit are $|00\rangle$, $|01\rangle$, $|10\rangle$, $|11\rangle$. With a Rydberg excitation coupling the state $|1\rangle$ and $|r\rangle$, the Rydberg blockade allows only one atom to occupy Rybderg

state, transferring the initial states to the states $|00\rangle \rightarrow |00\rangle$, $|01\rangle \rightarrow |0r\rangle$, $|10\rangle \rightarrow |r0\rangle$, $|11\rangle \rightarrow |r1\rangle$. This operation acts as a controlled phase gate for the target qubit as its wavefunction accumulates a phase shift of π dependent on the state of the control qubit.
Further details on the Rydberg state used in this experiment are named in the context of those experiments in Sec. 5.3.1.

3.1.6. Canonical quantum gates

Operations on qubits are performed with so called quantum gates. From the perspective of quantum physics, a gate is a Hermitian operator. In the representation of the Bloch sphere, any rotation $\hat{R}(\theta, \phi)$ following

$$\hat{R}(\theta, \phi) = \begin{pmatrix} \cos(\theta/2) & -i\exp^{(-i\phi)}\sin(\theta/2) \\ -i\exp^{(i\phi)}\sin(\theta/2) & \cos(\theta/2) \end{pmatrix} \tag{3.29}$$

of the Bloch vector is a valid gate as it fulfills $\hat{R}^\dagger = \hat{R}$. In the perspective of computer science, special rotations are abbreviated for instance X, Y, and Z for rotations through an angle of π around the x-, y-, or z-axis of the Bloch sphere respectively. For rotations by an angle of $\pi/2$, an index can be set to the respective operation, for instance $X_{\pi/2}$. An intuitive visualization of these and other common quantum gates is presented in [67]. Furthermore, the Hadamard gate H is a specialized operation that includes a rotation around the x-axis of the Bloch sphere by π together with a rotation around the y-axis of the Bloch sphere by $\pi/2$. As the definition of the x- and y-axis of the Bloch sphere is only a matter of a relative phase, this operation can be realized by virtual-Z rotations $H = Z_{\pi/2}X_{\pi/2}Z_{\pi/2}$ [78, 67].

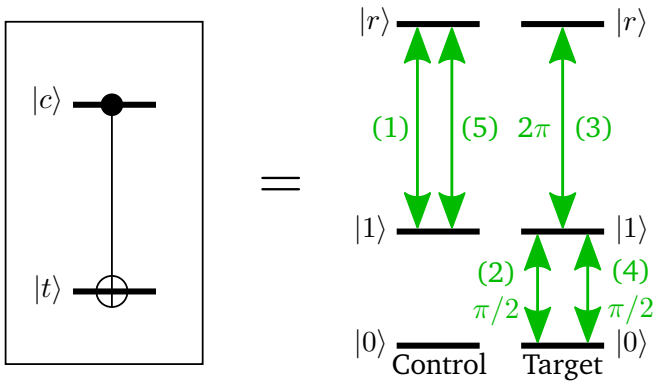

Fig. 3.9.: Scheme of the pulse sequence for a H-C_Z gate on neutral atoms with one light field coupling the $|1\rangle$ and the $|r\rangle$-state and one local 1-qubit gate coupling the two qubit basis states, following [33].

For the discussion of 2-qubit gates, the same notation as for 1-qubit gates is used with the prefix “C” to indicate, that the respective operation on one qubit is controlled by another qubit. For instance, the controlled phase gate C_Z executes a Z gate on one qubit controlled by a second qubit. For a universal set of quantum gates, a CNOT gate is required and can be constructed from Hadamard gates and the C_Z gate.
For neutral atoms, the CNOT gate can be demonstrated using the Rydberg blockade with the H-C_Z protocol [33] shown in Fig. 3.9. This protocol requires single-site controlled operations on two qubits which are named after their functions in the gate as the “control” and the

"target" qubit. The concept utilizes a Rydberg state $|r\rangle$ which offers a Rydberg blockade, see Sec. 3.1.5. The protocol assumes, that a first ground-to-Rydberg state rotation by π on the control qubit couples this qubit to the Rydberg state (pulse (1) in Fig. 3.9). On the target qubit, a $\hat{R}(\pi/2, 0)$ rotation on the qubit basis states is performed (2) prior to a ground-to-Rydberg state rotation by 2π (3), adding a phase shift of π to the phase of the superposition. Whether this phase shift happens or not is determined by the state of the control atom. A successful Rydberg excitation of the control qubit suppresses the Rybderg excitation of the target according to the Rydberg blockade. The last pulses serve for a consistent outcome of the experiment. The $\hat{R}(\pi/2, 0)$ rotation on the qubit basis states of the target qubit (4) defines the gate logic to invert the target state, if the control qubit is not excited to the Rydberg state. A final ground-to-Rydberg state rotation by π (5) on the control qubit de-excites the population in the Rydberg state back to the basis state $|1\rangle$.

3.2. A scalable system with well characterized qubits

Starting again with DiVincenzo's criteria, the quantum system that is used to encode the qubits is presented. In the project Quips-B, the isotope ^{85}Rb is used. A scheme of the transitions used in this experiment is shown in Fig. 3.2.
The hyperfine states $|0\rangle = |5^2\mathrm{S}_{1/2}, \mathrm{F} = 2, m_\mathrm{F} = 0\rangle$ and $|1\rangle = |5^2\mathrm{S}_{1/2}, \mathrm{F} = 3, m_\mathrm{F} = 0\rangle$ are used as qubit basis. As an advantage, the integer F-quantum number of ^{85}Rb allows for using clock states with quantum number $m_\mathrm{F} = 0$. These states show much longer coherence times than the magnetic sensitive states with $m_\mathrm{F} \neq 0$ in this experiment too, as discussed in Sec. 3.5. As a drawback, the high F-quantum numbers produce a large manifold of m_F substates. According to the Zeeman effect, this leads to an energy splitting in an external magnetic field B following

$$\Delta E = m_\mathrm{F}\, g_\mathrm{F}\, \mu_\mathrm{B}\, B \tag{3.30}$$

using the hyperfine Landé g-factor g_F and the Bohr magneton μ_B. In this experiment, a quantization field with a field strength of $720(1)\,\mu\mathrm{T}$ is used, which leads to an energy splitting of $6.8\,\mathrm{MHz}$ between adjacent m_F substates. When testing the frequency of the transition $|0\rangle \leftrightarrow |1\rangle$ ("clock transition"), the quadratic Zeeman effect needs to be taken into account which scales with [43]

$$\Delta\omega_\mathrm{clock} = 2\pi \times 0.129398\, \frac{\mathrm{Hz}}{\mu\mathrm{T}^2}\, B^2. \tag{3.31}$$

For operations that involve the excited states $|5^2\mathrm{P}_{1/2}\rangle$ and $|5^2\mathrm{P}_{3/2}\rangle$ like trapping and two-photon transitions, state mixing and spontaneous Raman scattering [79] must be taken into account. As the hyperfine splitting in the excited state manifold $\left(|5^2\mathrm{P}\rangle\right)$ is only in the range of $100\,\mathrm{MHz}$ and for the ground state manifold $\left(|5^2\mathrm{S}\rangle\right)$ in the range of $3\,\mathrm{GHz}$, the energy splitting is rather small. Using ^{87}Rb, which shows a Zeeman splitting on the same order of magnitude, but offers a double splitting between adjacent F-substates, e. g. approximately $6.8\,\mathrm{GHz}$ for the qubit states [80], the larger energy splitting would reduce the coupling of the qubit states to other states.
In order to prepare the ^{85}Rb atoms as qubits, they need to be laser cooled and trapped. The cooling of rubidium atoms has been described in the literature and preceding theses [62, 72, 39] and is not discussed here in detail. The cooled atoms can then be trapped by optical dipole traps following the effects shown in Sec. 3.1.1.

The results of applying (3.5) for the trapping potential and (3.6) for the scattering rate to the parameters of ^{85}Rb are plotted in Fig. 3.10. For this calculation, a light field with a detuning of few nanometers relative to the D1 line $(795\,\mathrm{nm})$ is assumed. Only the $m_\mathrm{F} = 0$ states are taken into account as these are the relevant states for the qubit operations. Plots for the different m_F states can be found in [72]. The linear dependence of the trapping potential on the inverse of the detuning against the resonance frequency is directly visible in form of attraction for negative detuning (larger wavelength) and repulsion for positive detuning (smaller wavelength). As the scattering rate decreases faster with detuning than the dipole potential by one order in the detuning, it is possible to reduce the scattering for any given dipole potential.

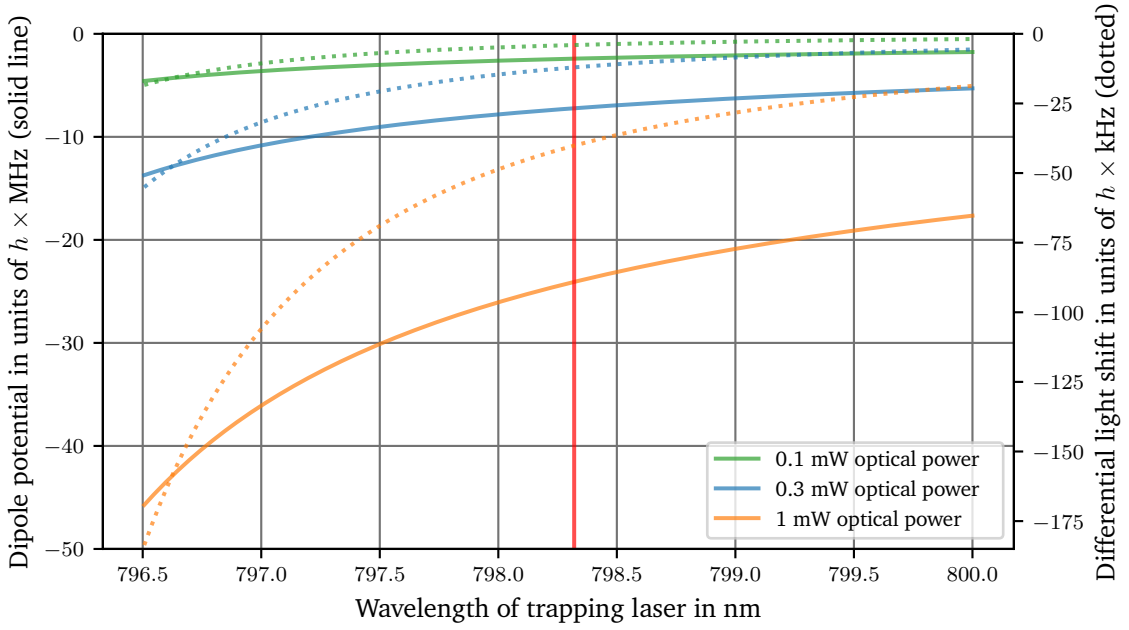

(a)

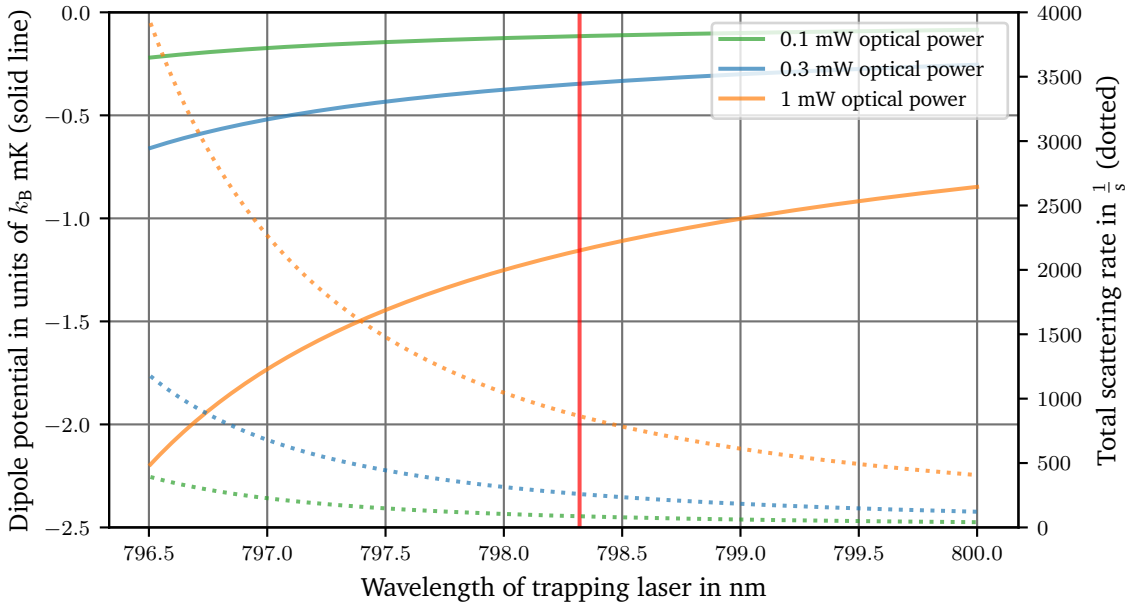

(b)

Fig. 3.10.: (a) Calculated potential following (3.5) and differential light shift following (3.10) for the regime of the used dipole traps. (b) The same data of the calculated potential but scaled in units of $k_B\times$ millikelvin and the scattering rate following (3.6). The powers represent the situations used for loading the atoms into the dipole traps (1 mW in the central trap), for the experiments with gate operations (0.3 mW in the central trap), and for magnetic field sensing (0.6 mW in the central trap). Only the ground states with $m_F = 0$ are taken into account. The typical wavelength used for the gate experiments is highlighted by the red line.

3.3. Qubit-specific measurement capability

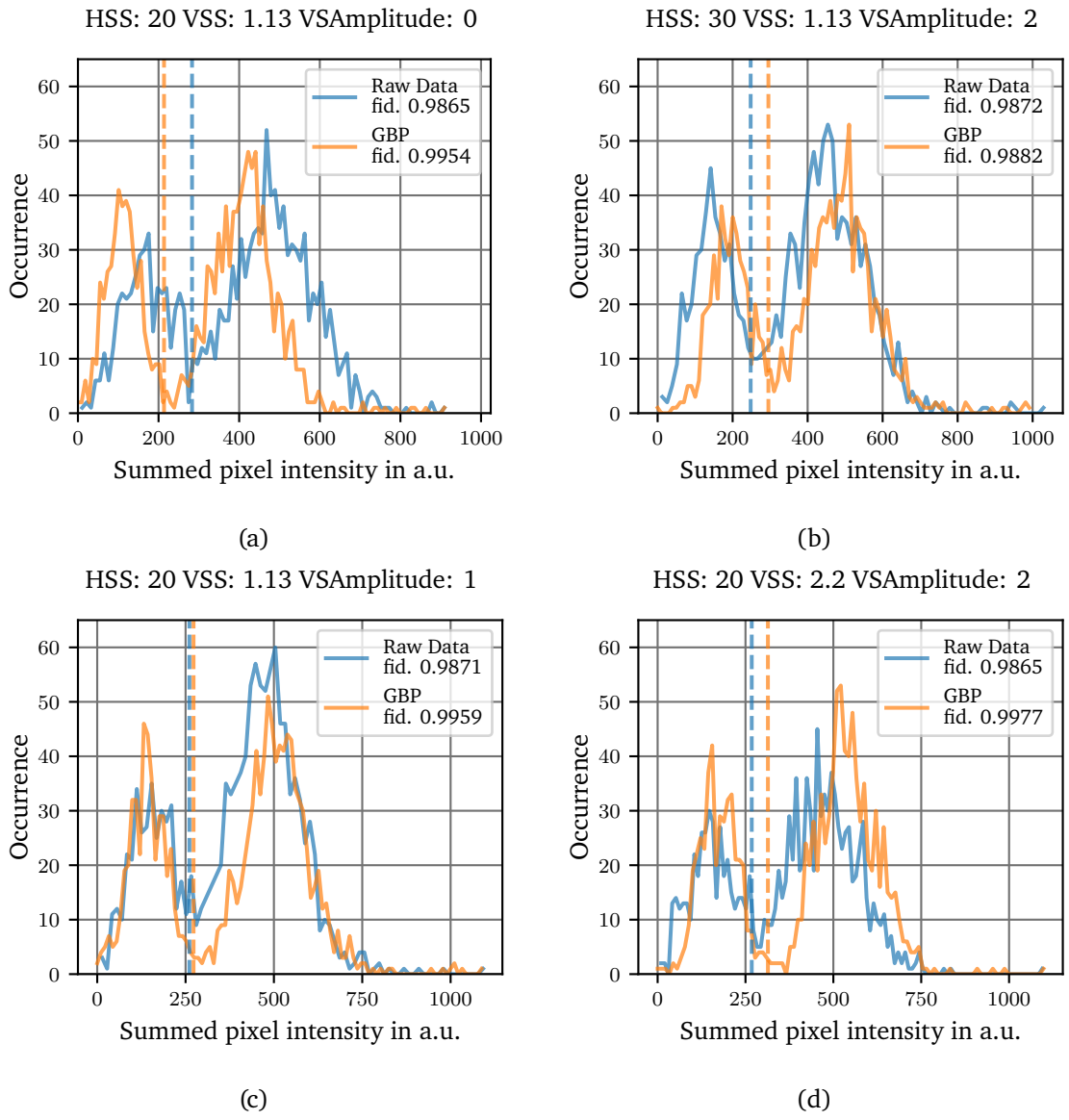

Fig. 3.11.: Overview of the influence of multiple camera settings on the detection quality for a central trap (10,10). The tested parameters are the VSS, the HSS and the VSAmplitude. A Gaussian band pass filter (GBP) is used on 5 x 5 pixels of the raw data of each trap with a spatial high pass corner frequency of 3 pixels and a spatial low pass corner frequency of 0.5 pixels. The thresholds used for the discrimination between a filled trap and an empty trap is drawn as dashed line.

The result of a quantum operation needs to be detected. For this task, techniques for the detection of individual atoms and for the measurement of their states are required.
Imaging of individual atoms is performed by fluorescence detection. A CCD camera, equipped with an electron-multiplying (EM) amplifier, allows the detection of single photons. The used camera is an Andor iXon Ultra 888 with a pixel size of 13 µm x 13 µm [44].
The fluorescence of the atoms is stimulated by irradiating the cooling and repumping light

that are used to create the MOT and the optical molasses.
In order to perform an optimal imaging, the detuning and the power of the cooling light and the settings of the camera must be optimized. Basically, the detuning of the cooling light should be decreased to an acceptable limit that offers detection with high fidelity but with low atom loss. If the detuning of the cool light is too small, the atoms are heated out of the traps.
The optimization of the camera settings is a matter of experiment specific properties and relies on statistical evaluation. The influence of different camera parameters is presented in Fig. 3.11 for one central trap (index (10,10)) of the array. A statistics of 1300 experiment runs is evaluated for each setting. The settings HSS, VSS, and vertical shift amplitude (VSAmplitude) are varied. The EM gain is set to 300 a. u., the exposure time is 100 ms, the detuning of the cool light is chosen to -35 MHz.
The images taken are evaluated trap-specific with an array of 5 x 5 pixels for each trap. These pixels can be evaluated with two different techniques. The (legacy) technique is a summation of the intensities detected in this square [81]. A newer evaluation implemented by Marcel Mittenbühler uses a two-dimensional Gaussian band pass filter (GBP) first followed by an image convolution [82]. The spatial corner frequencies of this filter is set to a high pass for features smaller than 3 pixels and a low pass for features larger than 0.5 pixels. The resulting intensities are evaluated in a histogram plotting the occurrence of the summed pixel intensity in a number of 100 bins.
The histograms show a bimodal distribution corresponding to events with an atom occupying the trap (peak at high intensities, right) and an empty trap (peak at low intensities, left). Events at higher intensities than the right peak would indicate the occurrence of two atoms in one trap. For the detection of the result of the quantum experiment, a threshold for the summed pixel intensity is calculated. If the summed pixel intensity exceeds this threshold, the trap is considered filled. With these thresholds, a fidelity for a correct detection given these distributions is calculated.
As shown in the different histograms, the shapes of the distributions vary with the camera settings. Even with simple summation, the fidelity of atom detection is nearly constant around a level of (98.68 ± 0.04) %. Using the GBP, the fidelity is increased in all cases with an optimum of $99.77(1)$ %.
A general conclusion of this evaluation cannot be drawn as an evaluation of all traps of the array needs to be considered. However, the camera setting with the maximum detection fidelity of HSS$=\ 20$, VSS$=\ 2.2$ and VSAmplitude$=\ 2$ has not been considered an optimum before. This is especially due to higher noise at high spatial frequencies resulting from the maximum setting of 2 for the VSAmplitude. As this noise is filtered efficiently by the GBP, a further analysis of camera settings using the GBP is recommended.
As a result, atoms in both the $|0\rangle$ and the $|1\rangle$ qubit basis state are imaged. In order to create a state-selective measurement, loss of atoms in the $|1\rangle$ state is stimulated by a resonant light field. This is achieved by a light field that drives the atoms in the $|1\rangle$ state from their superposition state into a cycling transition where they cannot decay to the other qubit state [45, 46]. For rubidium, only the $|5^2\mathrm{S}_{1/2}, \mathrm{F} = 3, m_\mathrm{F} = \pm 3\rangle$-states offer a cycling transition together with the states $|5^2\mathrm{P}_{3/2}, \mathrm{F}' = 4, m_{\mathrm{F}'} = \pm 4\rangle$. The state projection is basically the only point in this discussion where the two qubit states are not equivalent as there is no option for a cycling transition from the $|5^2\mathrm{S}_{1/2}, \mathrm{F} = 2\rangle$ manifold. It is not possible to perform this operation via the D1 line at 795 nm.
A limit for state projection is that the $m_\mathrm{F} = 0$ state is used as a qubit state but that the cycling transition is given for extreme m_F-states. As a result, an atom that is supposed to be

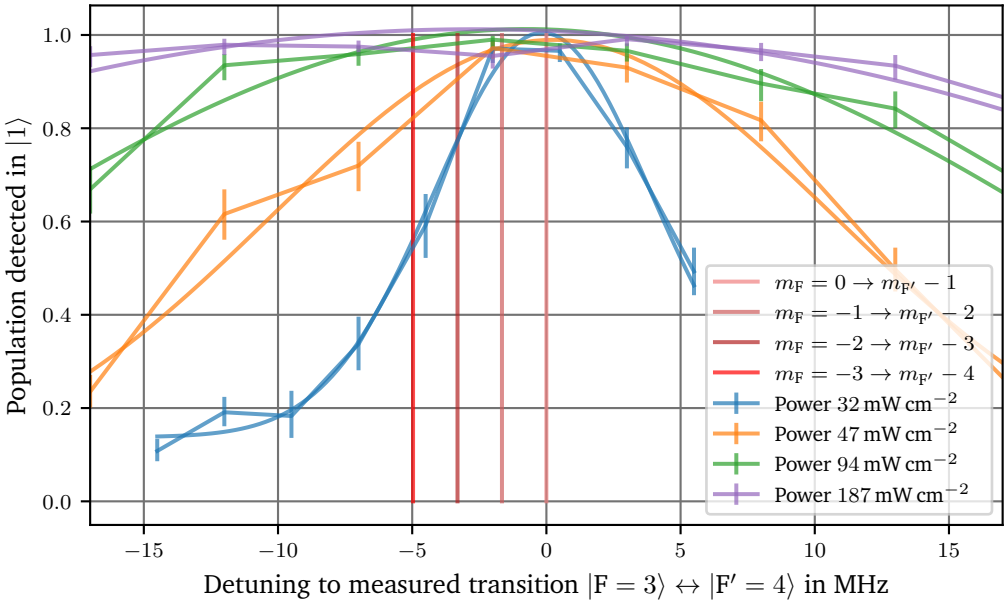

Fig. 3.12.: Test of the state projection with different intensities of the light driving the cycling transition. A saturation broadening is observed. The Zeeman splitting for the different transitions $|5^2\mathrm{S}_{1/2}, \mathrm{F}=3, m_\mathrm{F}\rangle \leftrightarrow |5^2\mathrm{P}_{3/2}, \mathrm{F}'=4, m_{\mathrm{F}'}\rangle$ in the quantization field of $0.720(1)$ mT is drawn as red lines assuming σ^- transitions. The Zeeman splitting is on the order of the natural linewidth of $2\pi \times 6.066(2)$ MHz [43].

pushed away must be pumped through the states $m_\mathrm{F} = \pm 1$ and $m_\mathrm{F} = \pm 2$ towards one of the extreme states. In order to keep the chance for a bit flip as small as possible, a perfect circular polarization of the light inducing the state projection is needed. If this light contains any other polarization, the chance increases to have transitions that do not pump the state of the atom towards the cycling transition. Therefore, this beam needs to propagate along the quantization field in circular polarization in order to reach an optimum qubit-specific measurement.

Another aspect of an optimum state projection is the absolute power and pulse duration of the light driving the cycling transition. In the recent setup, an optical power of up to $32(2)$ µW and a beam waist of $105(13)$ µm are applied at the atom plane. Tests with lower intensities and longer pulse durations of the light inducing the state projection resulted in lower fidelities of the state projection of up to 3 %. It is expected that this is given by a partially resolved Zeeman splitting of the D2 line. This is motivated by the comparison of the measured saturation broadening and calculated Zeeman splitting shown in Fig. 3.12. For the D2 line of ^{85}Rb, the saturation intensity is $1.669\,32(35)$ mW cm^{-2}. The red lines indicate the calculated splitting of the σ^- transitions used for the state projection. For the state $|5^2\mathrm{P}_{3/2}, \mathrm{F}'=4, m_{\mathrm{F}'}\rangle$, a splitting proportional to $2\pi\, m_{\mathrm{F}'} \times 7.0\,\mathrm{MHz\,mT^{-1}}$ in a magnetic field is known (see Fig. 3.2). The state $|5^2\mathrm{S}_{1/2}, \mathrm{F}=3, m_\mathrm{F}\rangle$ shows a splitting proportional to $2\pi\, m_\mathrm{F} \times 4.7\,\mathrm{MHz\,mT^{-1}}$. In the quantization field of $0.720(1)$ mT, a difference of up to $2\pi \times 4.968(2)$ MHz between the resonance frequencies of the σ^- transitions is expected. Hereby, the measured transition is assigned to the transition $|m_\mathrm{F}=0\rangle \rightarrow |m_{\mathrm{F}'}-1\rangle$ which has an offset of $2\pi \times 5.040(2)$ MHz to the transition without quantization field. The range of resonance frequencies is comparable to the natural linewidth of the transition of $2\pi \times 6.066(2)$ MHz [43]. A saturation broadening that dominates

the Zeeman splitting of the σ transitions seems to be preferable for a high-fidelity state projection. Therefore, the state projection is performed with light pulses at maximum intensity of $187\,\mathrm{mW\,cm^{-2}}$ and minimum duration of typically $7\,\mu\mathrm{s}$.

3.4. Initialization of the state of the qubits to a simple fiducial state

The deterministic preparation of a defect-free structure of initialized qubits is a prerequisite for the investigation of interactions between the qubits. It is shown here, how a two-dimensional array of dipole traps is created and filled with individual atoms in a defect-free configuration as described in [39, 61, 9]. Then the options for the initialization of the qubits are presented and the reached quality of preparation is shown.

3.4.1. Preparation of a two-dimensional array of individual atoms

The optical setup that creates an array of dipole traps uses the microlens array type 19-00021 by SÜSS Micro Optics. This microlens array offers a pitch of $75\,\mu\mathrm{m}$ and a focal length of the microlenses of $1.101\,\mathrm{mm}$. The foci of the microlenses are reimaged into the vacuum chamber by the relay optics described in Tab. 3.2 which demagnifies the focal plane of the microlenses by a factor of $10.6(1)$.
As a result, an array of optical dipole traps for ^{85}Rb is created with a separation of $7.0(2)\,\mu\mathrm{m}$ between the individual trap sites and a waist of the traps of $1.45(10)\,\mu\mathrm{m}$ [39, p.11].
The microlens array is illuminated with a Gaussian beam with a waist of $1.32\,\mathrm{mm}$ [83] originating from a Titanium:Sapphire (TiSa) laser [84]. Therefore, a Gaussian envelope in the light intensity is superimposed on the created spot pattern, resulting in varying trap depths declining towards the outer regions. The calculations shown in the previous chapter are performed for the central trap, resulting in lower values for trap depth and scattering rate for the outer traps. Techniques to avoid this variation in trap intensities have been demonstrated in other theses [85, 86, 87]. As a result, an array with a usable number of 19 rows and 19 columns is created bearing 361 trap sites. Following the established labeling convention, the traps are labeled in tuples naming the row trap index (y) first and the column trap index (x) second in the form (y, x) with both indices starting from 0. Following this logic, the center trap is labeled (9,9) [39].
Due to the Talbot effect [31], additional planes with trap arrays are created in front and behind the focal plane of the objective [88]. As these Talbot planes are able to trap atoms as well as the focal plane, these additional atoms offer the opportunity to act as additional qubits. The spacing of these planes is $61(4)\,\mu\mathrm{m}$ which is not addressable by the gate operations. To avoid a high background in the fluorescence images used for the readout, the atoms in the Talbot planes outside the focal plane are removed by a resonant light field. This light field is irradiated parallel to the Talbot planes with a structured beam leaving the focal plane dark.

3.4.2. Atom-by-atom assembly of defect-free patterns

When loaded from the optical molasses, a fraction of approximately $50\,\%$ of the traps is loaded with one atom due to the collisional blockade mechanism [59]. This results in an array with statistically filled sites.
A movable optical tweezer controlled by a pair of acousto-optical deflectors (AODs) (DTSXY,

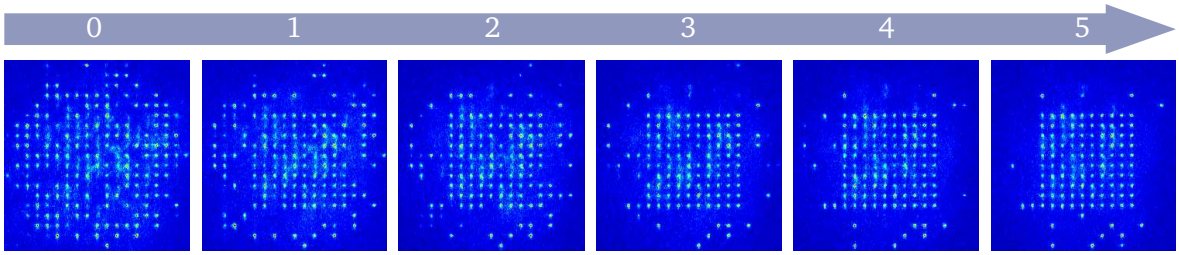

Fig. 3.13.: Fluorescence images taken from the atom distribution in the atomic array during the sorting sequence. Here, an array of 10x10 traps is filled with individual atoms. Starting from a stochastically loaded atom array, a defect-free cluster is generated by a sequence of 5 arrangements. (Modified from [61].)

AA Opto-Electronics) is used to sort the atoms to defect-free structures, that is prerequisite for a reliable demonstration of next neighbor interactions. One example of a sequence sorting a completely filled array of 10x10 sites is shown in Fig. 3.13. The target structure is defined at the beginning of each sorting step. In order to assign trap sites that are filled but are supposed to be empty (reservoir traps) and vice-versa (target traps), a fluorescence image of the initial structure is taken, i. e. step 0 in Fig. 3.13. A heuristic sorting algorithm then calculates paths that efficiently connect reservoir traps with target traps [81]. By the use of two fast programmable DDS, the AODs move the tweezer spot in order to execute these paths including loading an atom from the reservoir trap into the movable tweezer and placing the atom in the target trap [39].
In Quips-B, a single step efficiency of up to 70 % is reached. As a result, the target structure is not completely filled at the end of the first step. This is tested with a following fluorescence image shown in step 1 in Fig. 3.13. Based on this image, the next iteration of the sorting sequence is executed. In the shown case, a sequence of 5 steps created a completely filled array of 10x10 atoms. The record regarding the prepared number of atoms in a defect-free pattern in Quips-B is 111 atoms [9]. Further advances demonstrated a record of 441 atoms in a defect-free pattern based on this technique [25].

3.4.3. State preparation by Raman-assisted pumping

After the creation of a defect-free structure, the atoms must be prepared in one of the qubit states to act as a fiducial initial state. Two techniques for the preparation can be used in this experiment: Optical pumping into a dark state utilizing a dipole-forbidden transitions or Raman-assisted pumping. The first technique uses that the transition $|5^2\mathrm{S}_{1/2}, \mathrm{F}=3, m_\mathrm{F}=0\rangle \leftrightarrow |5^2\mathrm{P}_{1/2}, \mathrm{F}'=3, m_{\mathrm{F}'}=0\rangle$ is dipole-forbidden, leaving the state $|5^2\mathrm{S}_{1/2}, \mathrm{F}=3, m_\mathrm{F}=0\rangle$ as a dark state. This technique is explained in full detail in the literature [38, 39].
A limit of this preparation scheme is given by the degree of imperfection in driving only π-transitions (see Sec. 3.1.4 and [40]). In order to overcome this limit, the Raman-assisted pumping scheme as described in [32, 78] is used for the experiments in chapter 5. The technique uses multiple cycles of coarse pumping of atoms in all m_F-states in the $|5^2\mathrm{S}_{1/2}, \mathrm{F}=2\rangle$ manifold using a light field in circular polarization that is resonant to the $\left|5^2\mathrm{S}_{1/2}, \mathrm{F}=3\right\rangle \leftrightarrow \left|5^2\mathrm{P}_{1/2}, \mathrm{F}'=3\right\rangle$ transition. During a pulse length of several microseconds of this light, repeated π pulses of the global 1-qubit gate are applied to all states of the $|5^2\mathrm{S}_{1/2}, \mathrm{F}=2\rangle$ manifold with

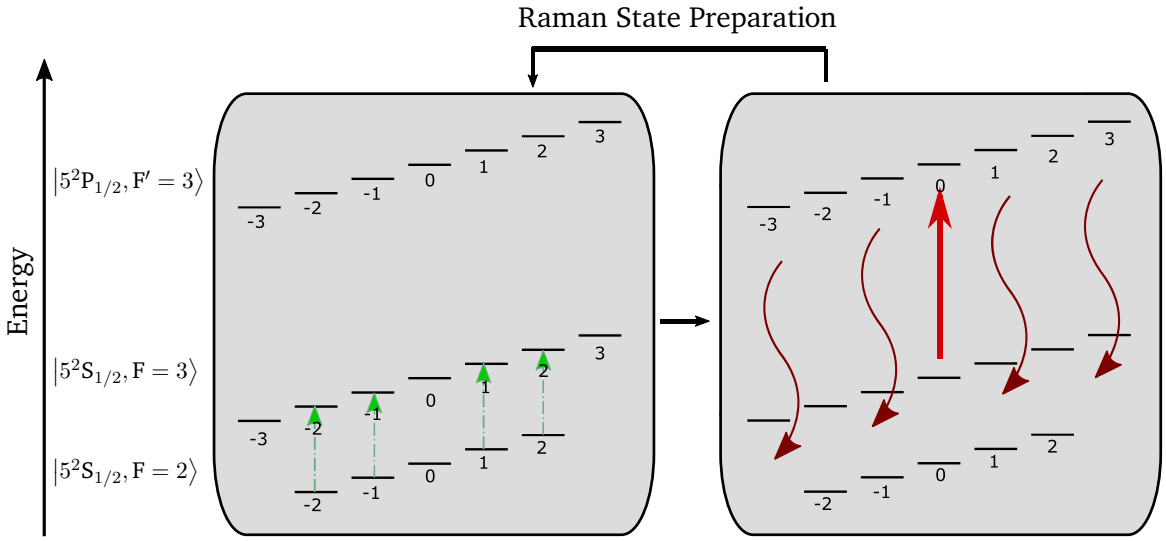

Fig. 3.14.: A schematic representation of the Raman-assisted pumping sequence used for state preparation. A coarse pumping with a transition from the $|5^2S_{1/2}, F = 3\rangle$ to the $|5^2P_{1/2}, F' = 3\rangle$ manifold (light red arrow, right) is used for a dissipative decay to the $|5^2S_{1/2}, F = 2\rangle$ manifold (dark red arrows, right). From there, only qubits states $m_F \neq 0$ are pumped in the $|5^2S_{1/2}, F = 3\rangle$ manifold by state-selective global Raman π pulses (green arrows, left) such that qubits in the wrong state perform further decays to the $|5^2S_{1/2}, F = 2\rangle$ manifold. Only the target state $|5^2S_{1/2}, F = 2, m_F = 0\rangle$-state is left as a dark state that accumulates the population. (Modified from [32].)

$m_F \neq 0$. As a result, the $|5^2S_{1/2}, F = 2, m_F = 0\rangle$-state is not addressed in this sequence and sums up population decaying from the $|5^2P_{1/2}, F' = 3\rangle$ manifold. Using a number of 45 cycles consisting of four π pulses for the m_F states to be pumped, a probability of $93\,\%$ to find the atoms in state $|5^2S_{1/2}, F = 2, m_F = 0\rangle$ is reached as shown in Fig. 3.15 using a detuning of $17\,\text{GHz}$ relative to the $|5^2S_{1/2}, F = 3\rangle \leftrightarrow |5^2P_{1/2}, F' = 2\rangle$ transition.

A limit of this pumping scheme is given by the time needed to perform a sufficient number of pumping cycles. A visualization of the relevant timings is shown in Fig. 3.16. Here, the sequence of pulses with the light inducing the global 1-qubit gate and the error signal of the frequency stabilization (see Sec. 4.1.1) is shown. In the error signal, a repeating pattern of four plateaus is visible. These plateaus correspond to the four different frequencies the laser has to settle in order to drive the four different transitions $|F = 2, m_F = -2\rangle \leftrightarrow |F = 3, m_F = -2\rangle$, $|F = 2, m_F = -1\rangle \leftrightarrow |F = 3, m_F = -1\rangle$, $|F = 2, m_F = +1\rangle \leftrightarrow |F = 3, m_F = +1\rangle$, and $|F = 2, m_F = +2\rangle \leftrightarrow |F = 3, m_F = +2\rangle$ as shown in Fig. 3.14.

As can be seen in Fig. 3.16 and in more detail in Sec. 4.1.2, stabilizing one frequency needs up to $10\,\mu\text{s}$ until the fast gradient in the signal settles. Including some headroom, $15\,\mu\text{s}$ of time are reserved for the frequency stabilization. A residual slow drift within the plateaus shows the interplay of the two regulators explained in Sec. 4.1.1 and [89] and does not describe a frequency error. This is experimentally tested, as the preparation works as soon as the plateau is settled but not if the steep slope is still present during the pulse.

After settling one frequency, a π-pulse with a length of $12\,\mu\text{s}$ is performed. In total, one pumping cycle has a duration of $108\,\mu\text{s}$, resulting in a time of $8.1\,\text{ms}$ for a sequence of 75 cycles used with a detuning of $38\,\text{GHz}$ relative to the intermediate state $|i_1\rangle$. This time scale is long enough such that scattering of the light of the 1-qubit gate (during the pulses) and of the

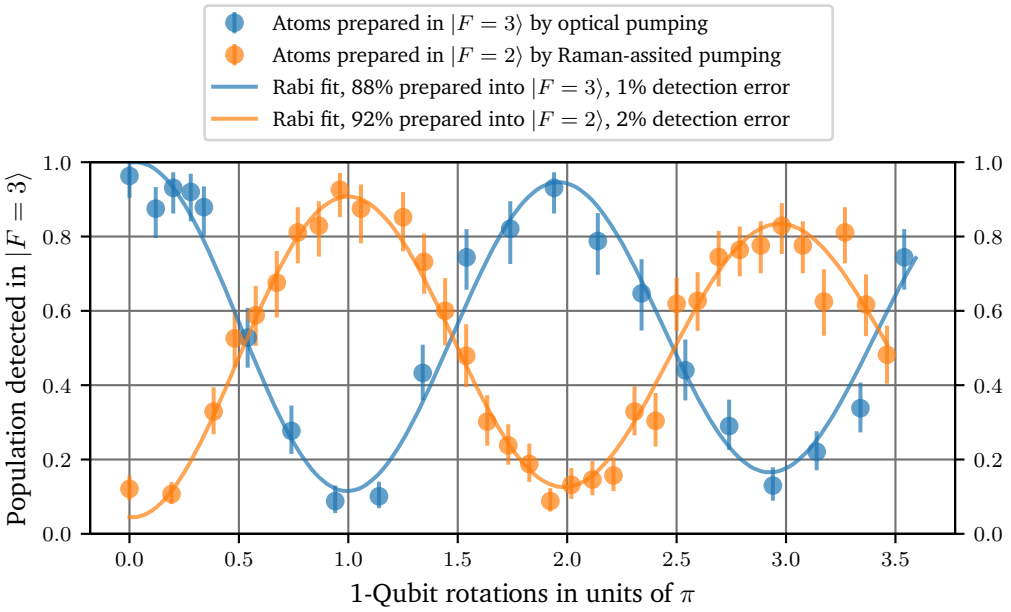

Fig. 3.15.: Rabi oscillations driven by the global 1-qubit gate demonstrating the quality of state preparation. In blue, the best reached state preparation of state $\left|5^2\mathrm{S}_{1/2}, \mathrm{F} = 3, m_\mathrm{F} = 0\right\rangle$ using a magnetic field, the light inducing the 1-qubit gate, and the light inducing the state projection along the **x**-axis. In this setup, optical pumping exploiting the dipole-forbidden transition $\left|5^2\mathrm{S}_{1/2}, \mathrm{F} = 3, m_\mathrm{F} = 0\right\rangle \leftrightarrow \left|5^2\mathrm{P}_{1/2}, \mathrm{F}' = 3, m_{\mathrm{F}'} = 0\right\rangle$ with π-polarized light reached a population of $88(2)\,\%$ in $|\mathrm{F} = 3, m_\mathrm{F} = 0\rangle$. In yellow, a typical state preparation using the Raman-assisted pumping scheme is shown. In this setup, the magnetic field, the light inducing the 1-qubit gate, and the light inducing the state projection are aligned along the **z**-axis. With the Raman-assisted pumping, a population of at least $92\,\%$ in state $\left|5^2\mathrm{S}_{1/2}, \mathrm{F} = 2, m_\mathrm{F} = 0\right\rangle$ is achieved. From this plot, a baseline loss of $8\,\%$ is read out and an error for state detection of $2\,\%$.

trapping light (during the whole sequence) become effective.
One option to reduce the scattering of the 1-qubit light is using a larger detuning relative to the $\left|5^2\mathrm{S}_{1/2}, \mathrm{F} = 3\right\rangle \leftrightarrow \left|5^2\mathrm{P}_{1/2}, \mathrm{F}' = 2\right\rangle$ transition. Experiments with a larger detuning soon reached a limit of $10\,\mathrm{ms}$ for the whole sequence which is given by the control electronics explained in Sec. 4.3.2. If the reached preparation becomes a limit in future work, this technique allows further improvements which is the major advantage in comparison with the preparation by optical pumping alone. An outlook for a laser system that would allow to increase the detuning by two orders of magnitude and to reduce the scattering by four orders of magnitude while reducing the time for the preparation scheme by a factor of two is discussed in Sec. 4.1.2.
For the following experiments, a baseline loss of $8(2)\,\%$ and a detection error of $2(1)\,\%$ is extracted from these experiments.

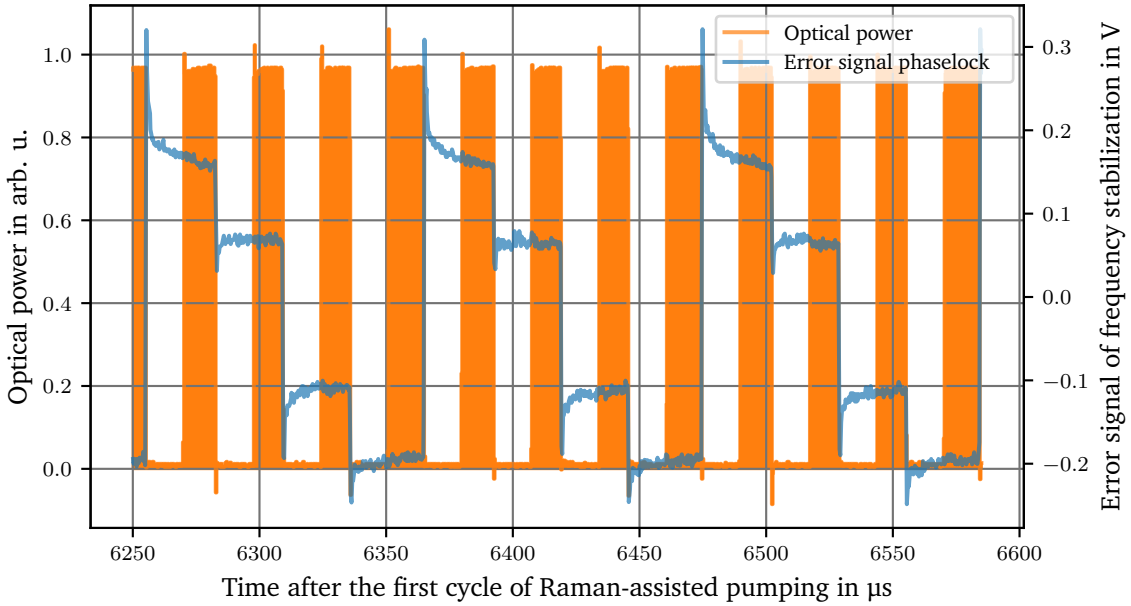

Fig. 3.16.: Plot of three randomly chosen cycles of the Raman-assisted pumping scheme. In total, 75 cycles are performed is this configuration. The optical power of the light inducing the 1-qubit gate is shown in yellow to mark the pulses and the error signal of the frequency stabilization of the respective laser system (see Sec. 4.1.1) is drawn in blue to demonstrate the changes in the laser frequency. The first pulse in this data is discussed in detail in Fig. 4.2 regarding the settling of a frequency and the technical details of the laser system.

3.5. Long relevant coherence times

Previous work has already given much insight into the effects dominating the dephasing and the decoherence of the trapped and state-prepared atoms [39, 61]. This chapter summarizes some of these results and presents the recent achievements. In Quips-B, the times T_1, T_2' and T_2^* (see Sec. 3.1.3) can be measured by different types of experiments. For testing the relaxation time T_1, atoms in an initialized m_F-state are stored in the optical dipole traps and after a variable wait time, the state is probed. The homogeneous dephasing time T_2' was investigated in a spin-echo experiment described in [8]. The experiment to measure the inhomogeneous dephasing time T_2^* is a Ramsey-type experiment as described in Sec. 3.1.3 performed with the global 1-qubit gate operation.

In this thesis, the relaxation time T_1 could be increased by a reduction of scattering processes (see (3.6)). Starting from the initialization of the qubits, the relaxation time is a limit for the duration of the experimental sequence until the final state projection. In this case, it is a maximum time for the Raman-assisted pumping, the quantum gate operations or quantum sensing experiments and the state projection. For such a procedure, several tens (for gate operations) or even hundreds of microseconds (for sensing) are needed. As shown in Fig. 3.17 (a), typical $1/e$ decay time constant of 30 ms can be observed in this setup, enabling basic quantum operations.
If highly complex sequences are to be investigated, the following improvement is proposed: An improvement of the relaxation time can be achieved with a higher power of the trapping

light, see Sec. 3.2. For the creation of the optical dipole traps, a Titanium:Sapphire (TiSa) laser by Sirah Lasertechnik is used [84]. In the experiments shown here, only $2\,\mathrm{W}$ of optical power can be used to create the dipole traps due to thermal instabilities in the fiber optic coupler. With this optical power, a detuning to the D1 line of only $3.2\,\mathrm{nm}$ can be achieved with a sufficient trap depth. The laser used is able to produce $4.8\,\mathrm{W}$ in a spatial mode that can be coupled into a fiber. Using large mode area fibers and suitable couplers would give the option to use the full power of this laser system and therefore allow for at least a doubling of the detuning. As a result, a reduction of the scattering rate by a factor of 4 is possible which should increase the relaxation time by the same factor.

For the demonstration of quantum gates, the relaxation time is not the limit but rather the inhomogeneous dephasing time T_2^*. In Fig. 3.17 (b), the dephasing of a Ramsey-type experiment is shown. The experiment tested the evolution of the phase of a prepared superposition state from the initialization up to a maximum time of free evolution of $760\,\mu\mathrm{s}$. Within this period of time, groups of length $40\,\mu\mathrm{s}$ are tested with a sampling rate of 4 points within $10\,\mu\mathrm{s}$. These groups test the times $0\,\mu\mathrm{s} - 40\,\mu\mathrm{s}$, $80\,\mu\mathrm{s} - 120\,\mu\mathrm{s}$ and starting from $200\,\mu\mathrm{s}$ with gaps of $80\,\mu\mathrm{s}$ between each group. A fit following (3.21) results in a T_2^* time of $340(26)\,\mu\mathrm{s}$. This time is sufficient for the demonstration of a gate sequence and for quantum sensing as aimed for in this work.
If this time constants needs to be improved in the future, the following effects must be investigated further: the phase noise of the laser system used for the 1-qubit gate operations, the temperature of the atoms, long-term drifts of the properties of the traps and the pointing of the light inducing the 1-qubit gate, and long-term drifts of the stabilization electronics. A starting point of this discussion is given in [90] stating that the phase noise of the laser system is not expected to be the limiting effect based on an electronic measure of the phase noise and a simulation taking only this phase noise into account. A framework of the influence of mechanical drifts can be found in [91].

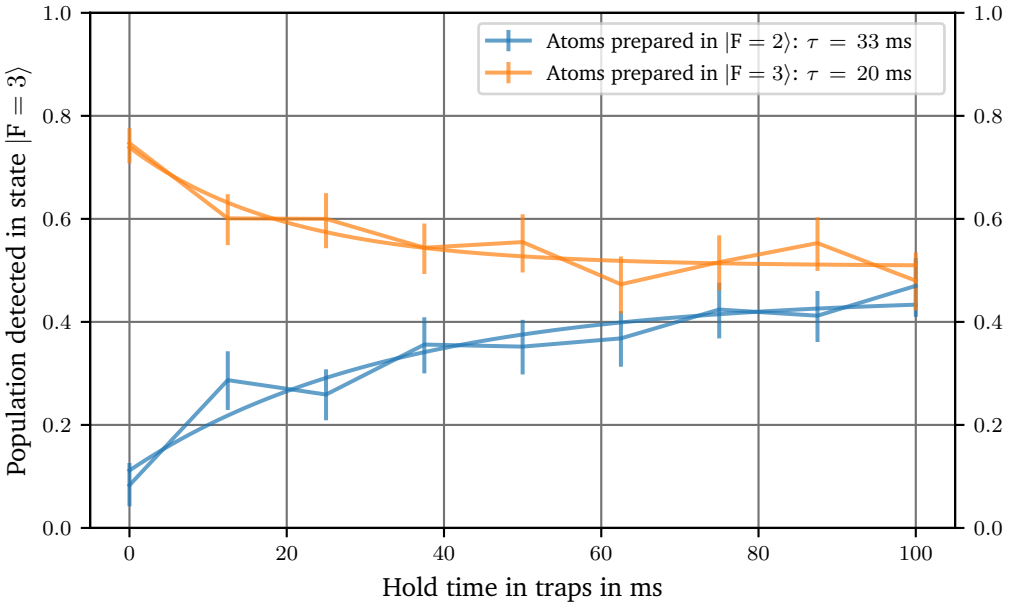

(a)

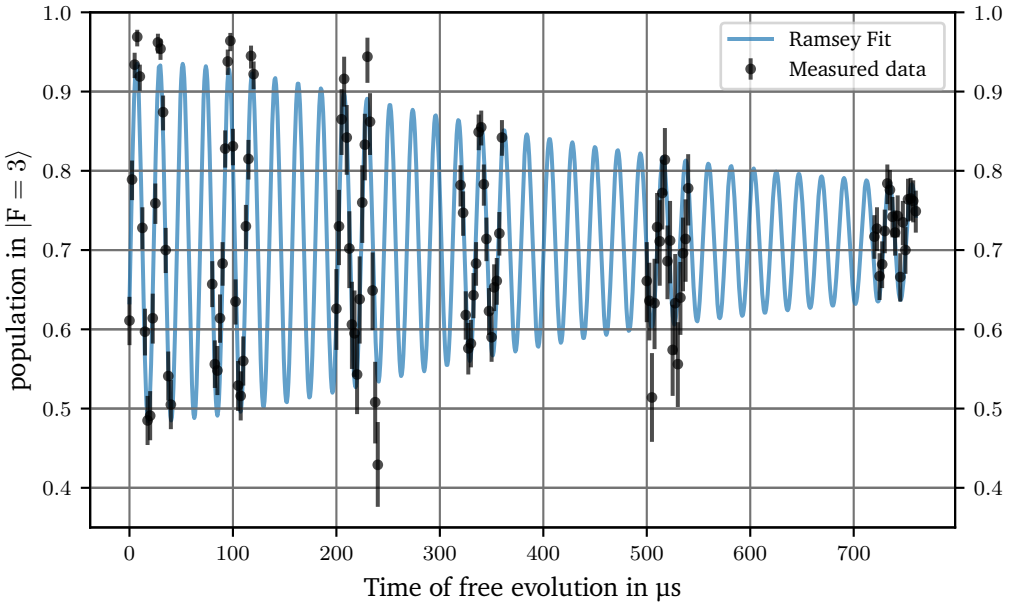

(b)

Fig. 3.17.: (a) Measurement of the relaxation (see Fig. 3.6 (b)) of a prepared $|F\rangle$-state for holding the atoms in the dipole traps for a configuration as used in the quantum experiment. A square of 3x3 of the central traps is averaged. As the initial state is prepared by optical pumping, static losses of $18\,\%$ for the state $|F = 3\rangle$ and $28\,\%$ for the state $|F = 2\rangle$ during the pumping sequences are corrected. As only the decay constants are of interest, a perfect initial preparation of the states is not optimized. (b) A Ramsey-type experiment demonstrating the inhomogeneous dephasing (see Fig. 3.6 (c)) of the quantum state of atoms stored in the dipole traps. A square of 3x3 of the central traps is averaged.

3.6. Implementation of the set of quantum gates

This chapter serves to discuss the technical progress made in order to implement a universal set of quantum gates in a configuration described in Sec. 2.5. Besides technical details and absolute numbers, technical improvements are discussed to advance the experiment in the future by lifting some limitations in the design.

3.6.1. Geometric layout of the science chamber and light fields

The orientation of the quantization field defines the geometry of the light fields used for coherent operations. The superposition of these beams for the different operations must be aligned with respect to the quantization field (see Sec. 3.1.4). The isotope ^{85}Rb and its transitions dictate some of the required wavelengths and beam parameters as discussed here. It follows that operations like the state detection, cooling and imaging require light at $780\,\mathrm{nm}$ while the wavelengths used for the excitation of the Rydberg state are given by the laser system using both $780\,\mathrm{nm}$ and $480\,\mathrm{nm}$ [90].

These requirements can be summarized as follows:

1. For gate operations circularly-polarized light fields are needed, namely the counter-propagating Rydberg light fields at $780\,\mathrm{nm}$ and $480\,\mathrm{nm}$ and the co-propagating light fields inducing 1-qubit gates.

2. Both, the laser beams for the CNOT-gate and for the 1-qubit gate need to be single-site addressed on 25 atoms.

3. These two beams need to be movable over 25 atoms.

4. A homogeneous magnetic field along the laser beams inducing the gate operations must be applied.

5. Optical access for trapping the atoms in linearly polarized dipole traps and cooling the atoms via laser cooling is needed.

6. The light inducing the state projection at $780\,\mathrm{nm}$ needs global access to all traps with circular polarization.

7. The cooling system at $780\,\mathrm{nm}$ is also used to stimulate emission for the imaging of the atoms.

8. For imaging, a highly sensible camera needs visible access to the atoms with a high-NA objective in order to resolve single atoms.

9. All light fields must have vanishing influence on the phase evolution mentioned in (2.1) unless desired.

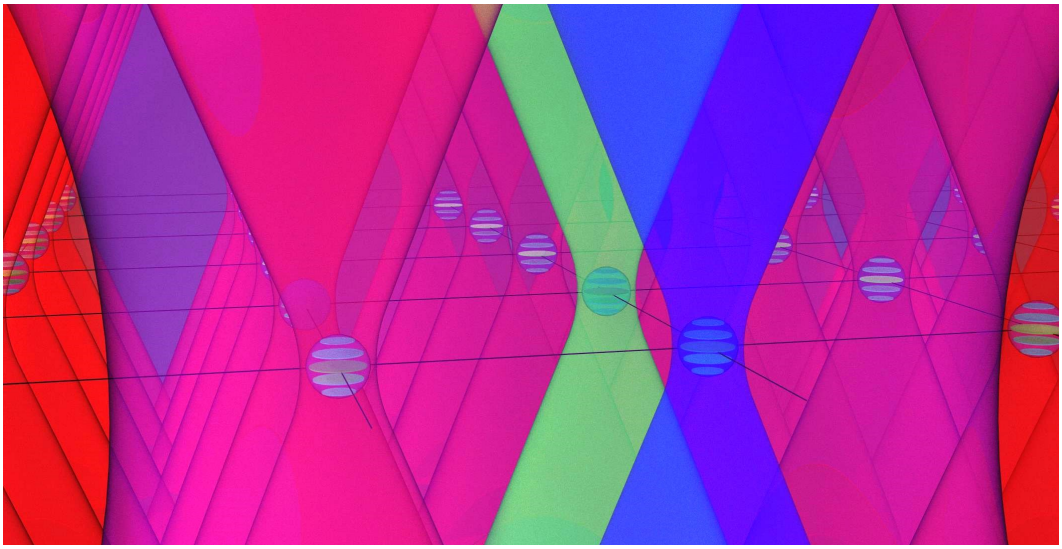

Fig. 3.18.: Schematic representation of the plane of atoms with the single-site addressed blue Rydberg light (blue) and the globally addressed red Rydberg light (purple), the trapping light (dark red) and light inducing the local 1-qubit operation (green). The atoms are drawn as blue balls with a visualization of five m_{F}-substates.

3.6.2. Geometric layout of the light fields

Using the constraints above allows discussing the required geometry. For this work, an array of individual atoms is instrumental in demonstrating a set of quantum gates. This atom plane defines the **x** and **y** directions of the setup. This leaves the **z** direction for optical access of the individual sites and the single-site addressed gate operations, as in the **x** and **y** directions there is no clear line of sight to all individual atoms.
In order to resolve and address single atoms, high-NA objectives [92] are used from both sides along the **z** direction. The high resolution of these objectives is used for trapping and for imaging the single atoms on the EMCCD camera as well as for single-site addressed gate operations. To visualize the beam configuration in the experiment, Fig. 3.18 can be used. There, the trapping light is focused by the objectives to form an array of optical dipole traps (dark red) that allow the preparation of single-atoms (blue balls). Additionally, a beam for a single-site addressed 1-qubit gate is visualized by the green beam in the center. Next to this spot, single-site addressed Rydberg excitation is shown with the blue beam. From above, the blue Rydberg light at $480\,\mathrm{nm}$ is focused on a single trap, whereas from below, the red Rydberg light is irradiated globally (purple). Similar to the red Rydberg light, the light for state projection is irradiated globally (not drawn).
For constructing the gate operations, the polarization of the beams need to meet the requirements given by the transitions they are supposed to induce (see Sec. 3.1.4). The gate operations and the light for state projection need to drive σ transitions with circular polarization. This requires the quantization field to be collinear to these beams along the **z** direction. This is a challenge for the engineering of these beams due to aligning the beams with high precision on the traps and superposing the five beams in different polarizations. A complication added to this challenge is the desire to minimize losses of laser power. This issue can be solved by discriminating the laser beams in the wavelength domain.
The setup therefore uses the D1 line at $795\,\mathrm{nm}$ for trapping and 1-qubit gate operations, while

using the D2 line at $780\,\mathrm{nm}$ for imaging and for state projection. Dichroic filters are then used to superpose the beams [93] to achieve a situation as shown in Fig. 3.18. The light at $795\,\mathrm{nm}$ for the 1-qubit gate is superimposed with the light at $480\,\mathrm{nm}$ for the Rydberg excitation and both are irradiated to the atoms from the same direction. Both light fields need to be circularly polarized. This polarization is produced by a custom-made dual-wavelength quarter-wave plate [94] .A dichroic mirror (DMSP650L) that reflects $795\,\mathrm{nm}$ and transmits $480\,\mathrm{nm}$ is used to superimpose the blue Rydberg light with the light inducing the 1-qubit gate [95], see Sec. 3.6.4.
Couter-propagating the beams named before, the trapping light and the different applications of light at $780\,\mathrm{nm}$ (state projection, red Rydberg and imaging) are irradiated. The light fields at different wavelengths are superimposed by a Semrock "RazorEdge" FDi03-R785 filter [96] that reflects $780\,\mathrm{nm}$ and transmits $795\,\mathrm{nm}$. The required polarizations are created through the filter itself as discussed in detail in Sec. 3.6.4.

3.6.3. Science chamber

The science chamber in Quips-B is based on a spherical octagon (Kimball MCF600-SO200800-A) shown in Fig. 3.19 [97]. It offers two large view ports opposite of each other with a usable diameter of $100\,\mathrm{mm}$ as shown in Fig. 3.19 (a). Together with custom-made vacuum windows, the science chamber offers a total length along the $\mathbf{z}$ direction of $64.49\,\mathrm{mm}$. This allows the use of two objectives with a focal length of $37.5\,\mathrm{mm}$ located on both sides of the chamber in a confocal configuration as shown in Fig. 3.19 (b). Additionally, the chamber also needs to support an ultra-high vacuum environment and the optical access to produce a MOT with ^{85}Rb atoms. The realizations of this starting point is described in the preceding theses to this project [39, 61, 72, 98]. In the coordinate system defined in the previous section, this involves beams for the MOT in the $\mathbf{x}+\mathbf{y}$ and $\mathbf{x}-\mathbf{y}$ directions that are irradiated into the chamber via ports with a diameter of $40\,\mathrm{mm}$. The third pair of beams for the MOT is irradiated along the $\mathbf{z}-\mathbf{x}$ direction through the main view ports with an angle-of-incidence of approximately $45°$ as shown in Fig. 3.19 (b).
The chamber offers four additional ports with a size of $40\,\mathrm{mm}$ that are used for monitoring the MOT with a camera that is placed in the $+\mathbf{y}$ direction and for the selection of one specific atom plane with a beam in circular polarization propagating in the $+\mathbf{x}$ direction. The port in the $-\mathbf{y}$ directions was previously used for an early version of state preparation as discussed in [61].
Along the $-\mathbf{x}$ direction, the red Rydberg light is irradiated globally on the side of the atom plane in p-polarization. Do note that this orientation is suboptimal as discussed in Sec. 3.6.1. This orientation is owed to the fact that a high power light field in this direction could easily destroy the EMCCD camera. Using the red Rydberg light along the $\mathbf{z}$ direction would need a power in excess of $1\,\mathrm{W}$, requiring a suppression of more that $60\,\mathrm{dB}$ to meet the damage threshold specification of the camera [44]. This risk was deemed unacceptable. If future developments can sufficiently solve this issue, the desired configuration with the red Rydberg light propagating in the $+\mathbf{z}$ direction should be exploited.

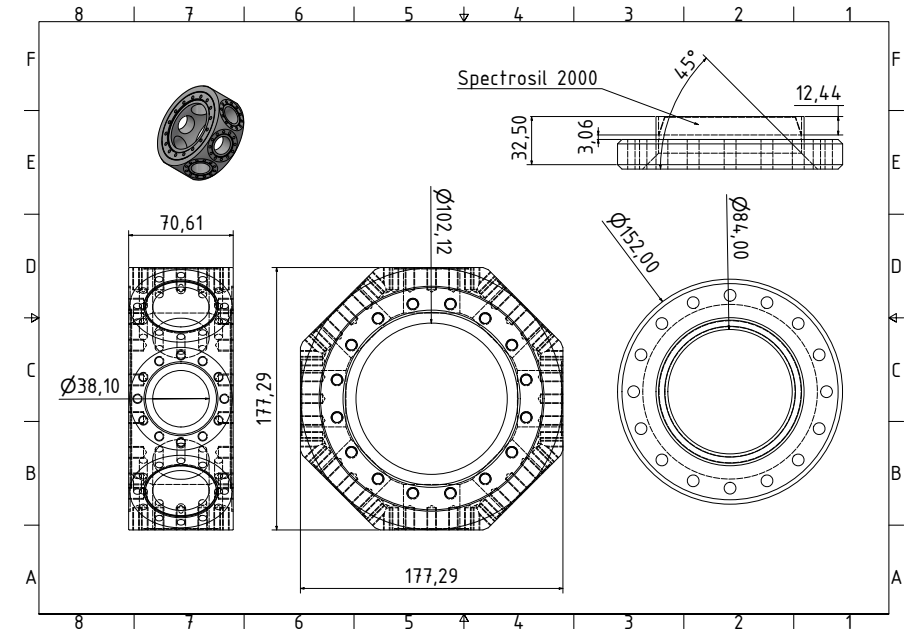

(a)

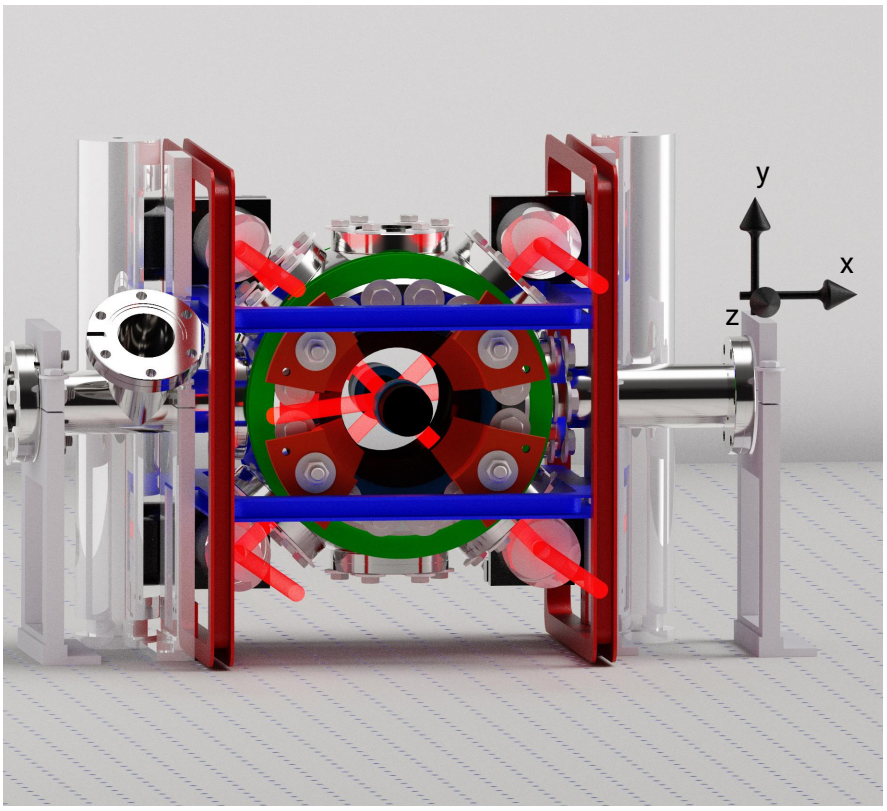

(b)

Fig. 3.19.: (a) Technical Drawing of the innermost parts of the vacuum system. On the left, the science chamber is shown [97], on the right the custom-made CF100 windows. (b): Render graphics of the science chamber, showing the beams for cooling and trapping the atoms in a MOT in red and the high-NA objectives at the center of the two CF100 windows in black. Laser beams are not drawn to scale.

3.6.4. Optical layout of the experiment table

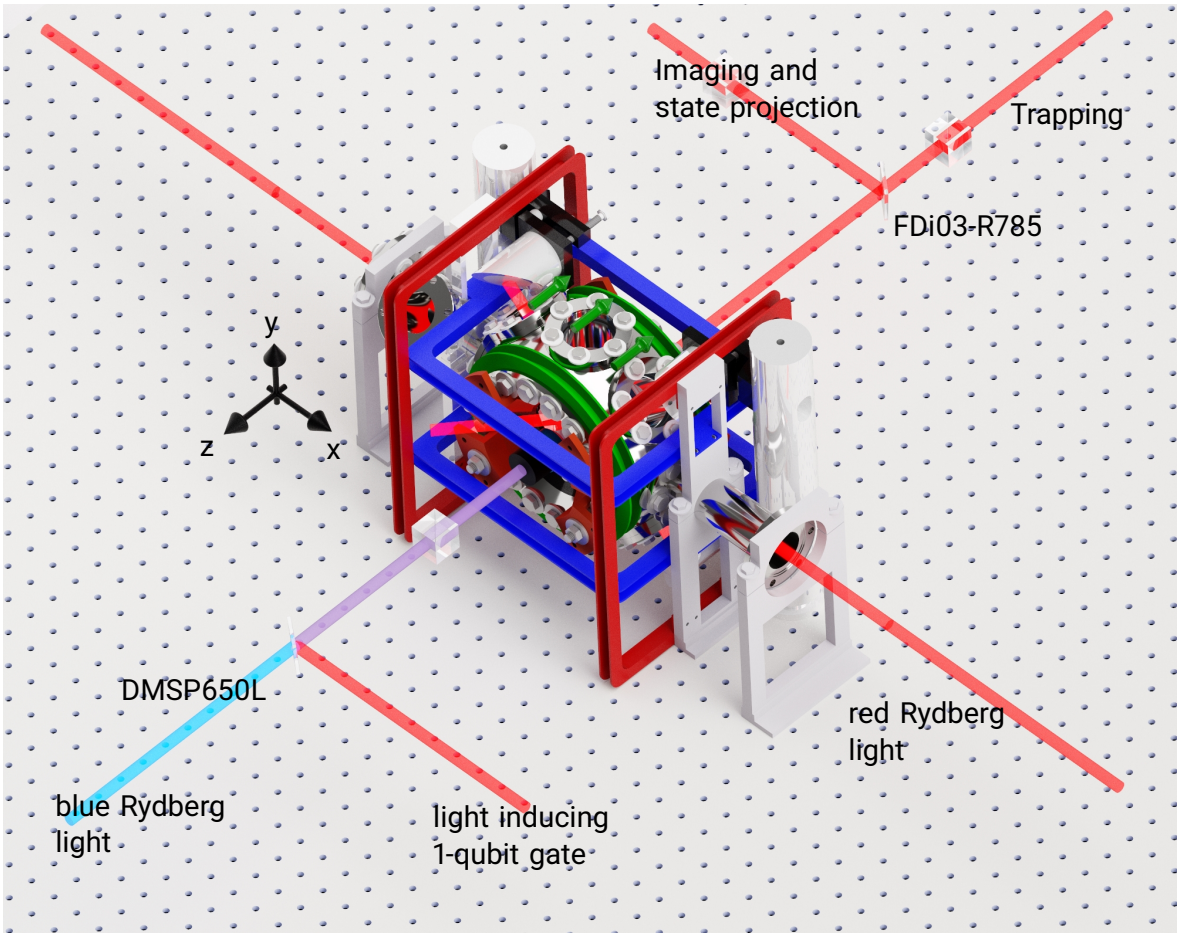

Fig. 3.20.: Render graphic of the vacuum chamber with a schematic visualization of the most import beams: The single-site addressed blue Rydberg light in blue is superimposed with the light inducing the 1-qubit gate in the front; the trapping light is superimposed with the beam paths for imaging and light inducing the state projection in the back. The magnetic field defining the $|m_F\rangle$-states is oriented along the $-\mathbf{z}$ as indicated by the green arrows. Laser beams are not drawn to scale.

As discussed in Sec. 3.6.2, the technical challenge of using the **z** direction for both gates, trapping and qubit-specific detection bears many complexities. These beam paths are structured by four functions: Imaging and state projection of the atoms using the EMCCD camera (Imaging and state projection), creation of the trap array (trapping), the light inducing the local 1-qubit gate and addressing with the blue Rydberg light. Two pairs of each of the four beams must be superimposed and irradiated through one of the high-NA objectives. As discussed, dichroic beam splitters are used for the superposition of each pair. The combinations of beams and dichroic beam splitters is visualized in Fig. 3.20. In the case of the superposition of the light inducing the local 1-qubit gate and the blue Rydberg light, the used wavelengths $795\,\mathrm{nm}$ (for inducing the local 1-qubit gate) and $480\,\mathrm{nm}$ (for the blue Rydberg light) are very far apart from each other. A standard dichroic beam splitter (Thorlabs DMSP650L) [95] is used to transmit the light at $480\,\mathrm{nm}$ and reflect the light at $795\,\mathrm{nm}$. In this case, polarizations are nearly irrelevant for the dichroic mirror as the behavior of the coating does not vary for

the different polarizations at the respective wavelengths. The $480\,\text{nm}$ light is transmitted in p-polarization whereas the $795\,\text{nm}$ is reflected in s- and p-polarization without any distortion observed. This allows the $795\,\text{nm}$ light not only to be used as addressed 1-qubit gate operations (p-polarized component) but also to be used as global 1-qubit gate operation (s-polarized component). Both components of the light at $795\,\text{nm}$ are focused differently such that they produce different beam sizes at the atom plane. More details on this specialized optics is given in Sec. 4.1.3.

After the superposition of the light inducing the local 1-qubit gate and the blue Rydberg light, a polarizing beam splitter (PBS) (Edmund optics 48877) [99] is used to clean the polarization of the $480\,\text{nm}$ light. Behind this PBS, the dual-wavelength quarter-wave plate is used to create the circular polarization for both wavelengths that is supposed to interact with the atoms.

The superposition of the imaging path and the trapping path requires an in-depth discussion as different polarizations are required to interact with the atoms. For the trapping light, strict linear polarization with minimal circular components is crucial for trapping the atoms. Circular components in the trapping light would lift the degeneracy of the m_F-states [100] which leads to additional losses during the loading of the traps for this experiment. But in the imaging path, the light for the state projection is irradiated in circular polarization.

The wavelengths for the different functions are $780\,\text{nm}$ (imaging and state projection) and $798\,\text{nm}$ (trapping). Therefore, a dichroic beam splitter with a much steeper edge in the spectral behavior than the one used for $480\,\text{nm}$ and $780\,\text{nm}$ is needed. A dichroic beam splitter with a steep edge and sufficient optical quality ($\lambda/10$) was found in the RazorEdge filter FDi03-R785 [101]. But due to the small difference in wavelengths, this filter has a strong dependency on the polarizations of the transmitted and reflected light. It is therefore impossible to reflect light at $780\,\text{nm}$ that is already circularly polarized. One solution is to use another dual-wavelength wave plate that acts as a quarter-wave plate for $780\,\text{nm}$ and as a $1\,\lambda$-wave plate for $797\,\text{nm}$ behind the dichroic beam splitter. But it turned out that the linear polarization for the trapping light is not well enough transmitted through this wave plate to allow efficient trapping. In a test with the trapping light tuned to $797\,\text{nm}$, it seemed that in a region of $1\,\text{nm}$ around $797\,\text{nm}$ the extinction ratio between p- and s-polarization was still better than 500:1. But this quality of polarization was not sufficient to trap the atoms. It has not been measured in full detail but it is expected that a satisfying polarization quality for the trapping light is only maintained for a very narrow region smaller than $\pm\,0.3\,\text{nm}$ around the design wavelength. Therefore, the use of this wave plate in the trapping light is rejected.

The use of this dual-wavelength wave plate can be avoided for the light inducing the state projection and perspective red Rydberg light at $780\,\text{nm}$. In the tests for the polarization quality, it turned out, that the dual-wavelength wave plate converted light at $780\,\text{nm}$ that was reflected from the dichroic beam splitter into linear polarization for all possible settings as shown in Fig. 3.21. It is therefore expected that the dichroic beam splitter itself produces a phase shift of nearly perfect $90°$ between s- and p-polarized components of light at $780\,\text{nm}$. This allows for matching the incoming polarization such that the reflected light is circularly polarized. Fortunately, this allows for leaving out the dual-wavelength wave plate without substitution.

A visualization of the optics at the front side of the science chamber is shown in Fig. 3.22. In this three-dimensional scan, the optical constraints for imaging the trapping light and the beams for gate operations are visible. In order to focus the respective beams to spot sizes of $1.5 - 2\,\mu\text{m}$, a relay optics consisting of the objective [92] and an achromatic lens with $200 - 750\,\text{mm}$ are used in an infinity-corrected configuration. As an advantage, this configuration allows for inserting planar optics as beam splitter cubes and -plates and wave plates between the achromatic lens and the objective. As a disadvantage, the relay optics needs long

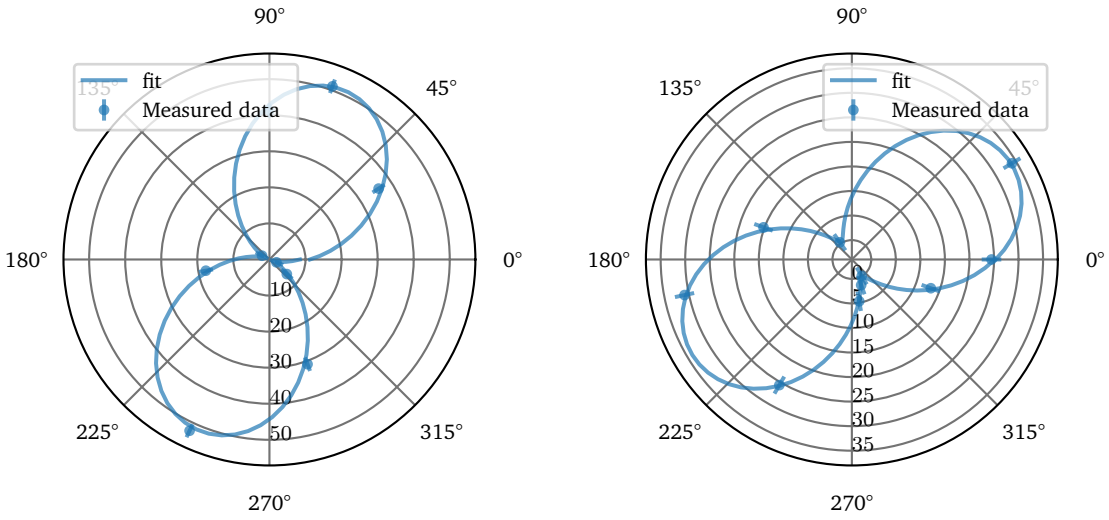

(a) (b)

Fig. 3.21.: Overview of the resulting polarizations after reflection on the dichroic beam splitter FDi03-R785. As a test setup, a PBS (Qioptiq G335726000) in front of the dichroic beam splitter produces a defined mixture of s- and p- polarization as incident light for the beam splitter. The light is then reflected off the dichroic beam splitter and passes through the dual-wavelength $\lambda/4$-wave plate. A second PBS behind the wave plate is used for analyzing the resulting light together with an optical power meter (Newport 1815). (a) Incoming light consisting of s- and p-polarization at the dichroic beam splitter with the dual-wavelength wave plate behind the beam splitter. The measured light is linearly polarized with an extinction ratio of $850:1$. (b) A mixture of s- and -p polarized light after a rotation of the first PBS for $35°$. The measured light behind dichroic beam splitter an wave plate is linearly polarized with an extinction ratio of $22:1$.

beam paths which are limited by the available space on the optical table.
The optics used for imaging the different beams into the science chamber are listed in Tab. 3.2. Further details on the experimental realizations of the subsystems are discussed separately for the respective functions in the next chapter.

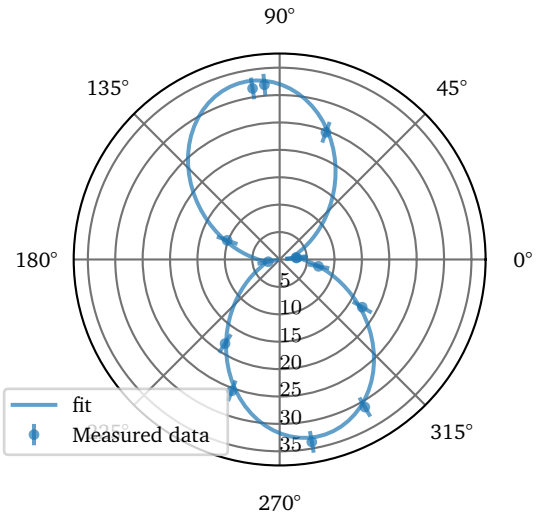

(c)

Fig. 3.21 (continued): (c) The setup is changed by placing the dual-wavelength wave plate in front of the dichroic beam splitter. Circularly polarized light is now incident on the beam splitter. The measured light behind the beam splitter is linearly polarized with an extinction ratio of $15.3:1$.

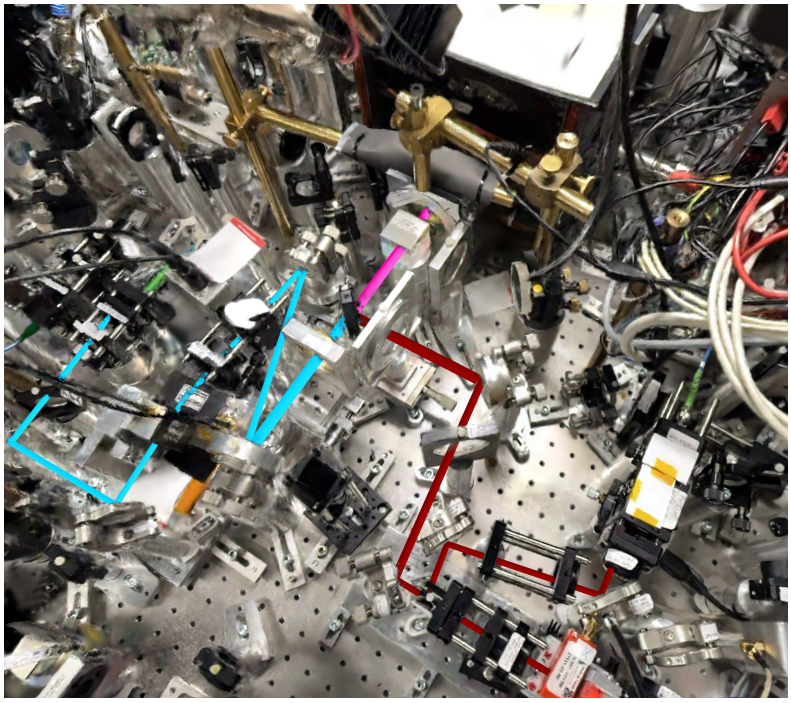

Fig. 3.22.: A three-dimensional visualization of the front window of the science chamber used for the laser beams of the 1-qubit gate and the blue Rydberg light. The perspective is chosen to match the view in the render graphics Fig. 3.20. The dual-wavelength wave plate and the PBS 48877 are well visible.

Tab. 3.2.: Overview of the different beam paths irradiated via the high-NA objectives and the used components. The used optics are given and the reached spot sizes at the atom plane are given for a better understanding. The addressing system for the light inducing the local 1-qubit gate is described in detail in Sec. 4.1.3 and the addressing with the blue Rydberg light in Sec. 4.2.4. The resolution of the imaging at the atom plane is estimated from the spot size of single atoms detected on the camera.

System	Resolution at atom plane in µm	Focal length objective in mm	Focal length of achromatic lens in mm	Calculated magnification	Spot Size in image plane in µm
Trapping Light	1.45	37.5	400	10.66	15.5
Imaging on EMCCD camera	2.3	37.5	750	20	39
local 1-qubit gate	2.2	37.5	300	8	22
blue Rydberg light	2.1	37.5	500	13.33	18

4. Optical systems for the implementation of a universal set of quantum gates

For the operations planned in the previous section, laser systems at wavelengths of $480\,\mathrm{nm}$, $780\,\mathrm{nm}$, and $795\,\mathrm{nm}$ are needed. This section describes the laser systems build or improved during this thesis. This involves the generation of light with the required properties in specialized laser systems as well as the optical systems used for the beam paths into the science chamber.
First, the laser systems at $795\,\mathrm{nm}$ used for the 1-qubit operations are presented. Then, the laser systems at $480\,\mathrm{nm}$ and $780\,\mathrm{nm}$ used for the Rydberg excitation are described with the focus on the single-site addressing and the application of an optical phase-locked loop (OPLL) to these laser systems. As the addressing systems for both gate operations use AODs controlled by RF-frequencies, an FPGA-based system for agile frequency synthesis and the control of laser pulses is introduced finally.

4.1. Laser systems for 1-qubit operations

The laser system for 1-qubit operations aims to drive a two-photon transition on the D2 line of ^{85}Rb at $795\,\mathrm{nm}$. The generation of this light by two phase-locked lasers is described first, then the addressing system build for 1-qubit operations on individual atoms is presented. As the same light is used for the state preparation by Raman-assisted pumping, an extension of this setup optimized for state preparation is proposed finally.

4.1.1. Phase-stabilized ECDL system

For the coherent manipulation of the qubits encoded in the hyperfine states, a pair of phase-locked external cavity diode lasers (ECDL), emitting light at $795\,\mathrm{nm}$, are used. The setup is shown in Fig. 4.1. One laser, referred to as master, is stabilized in its absolute light frequency by a Fizeau-based wavemeter (WS6-600, High Finesse). From a range of several hundred gigahertz, set by the laser parameters, an arbitrary frequency can be chosen with a resolution down to $20\,\mathrm{MHz}$ and an absolute accuracy of $600\,\mathrm{MHz}$. A second laser, referred to as the slave, is locked with an OPLL relative to the master using a fast current source in the laser head, as described in [90].
The two lasers beams are superposed via a PBS generating one main output with approx $95\,\%$ of the laser power and one auxiliary output that is used to monitor the wavelength and perform the OPLL. To achieve the lock, the light in the auxiliary output is detected with a fast photodiode (G4176, Hamamatsu) [102]. The photodiode measures a beat note of the difference frequency of the lasers. This beat note is compared, with respect to phase and frequency, to the reference frequency with the phase-frequency detector HMC439 [103]. As reference frequency, either a DDS with a fast frequency control (f_0) or a synthesizer (SMB100A, Rohde&Schwarz) with an option for a phase modulation (ϕ) can be chosen.

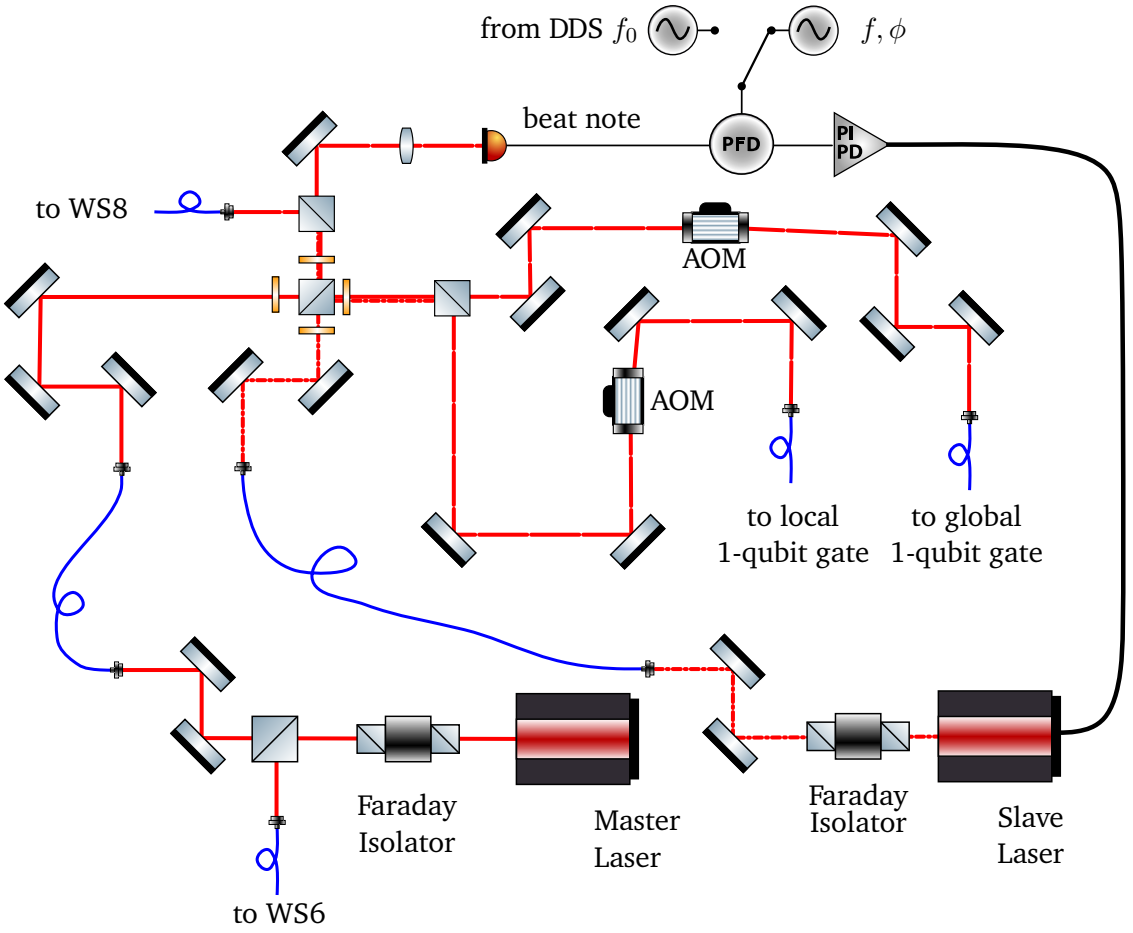

Fig. 4.1.: Scheme of the optical phase locked loop used for coherent manipulation of the qubit states. Laser light is drawn in red, electrical wires in black and optical fibers in blue. The light from the two ECDL (master laser and slave laser) is drawn in different line styles (solid and slash-dotted) up to the PBS from where they propagate indistinguishably in the same polarization and direction (long slashes). The proportional-integral (PI) and proportional-differential (PD) regulators are explained in detail in [89].

A two-stage proportional-integral-differential controller is used to match the beat note signal with the reference frequency. A slow digital controller based on the "STEMlab" platform [104] acts as an proportional-integral controller to match the difference frequencies of the two lasers to the reference frequency. This slow controller can act on the laser current driver and the piezo of the ECDL. A fast analog proportional-differential controller is used to keep the phase of the beat note synchronous to the phase of the reference signal. Together, both regulators reach a control bandwidth of $2.8\,\mathrm{MHz}$ and a phase noise of $123\,\mathrm{mrad}$ [89].
The main output of this system is split into two beams that contain both light fields in the same polarization. Both channels can be switched by acousto-optical modulators (AOMs) and are coupled into polarization-maintaining fibers guiding the light to the experiment. One channel is supposed to act as the local 1-qubit gate, the second channel is supposed to act as the global 1-qubit gate.

4.1.2. Future optimizations of the 1-qubit laser system

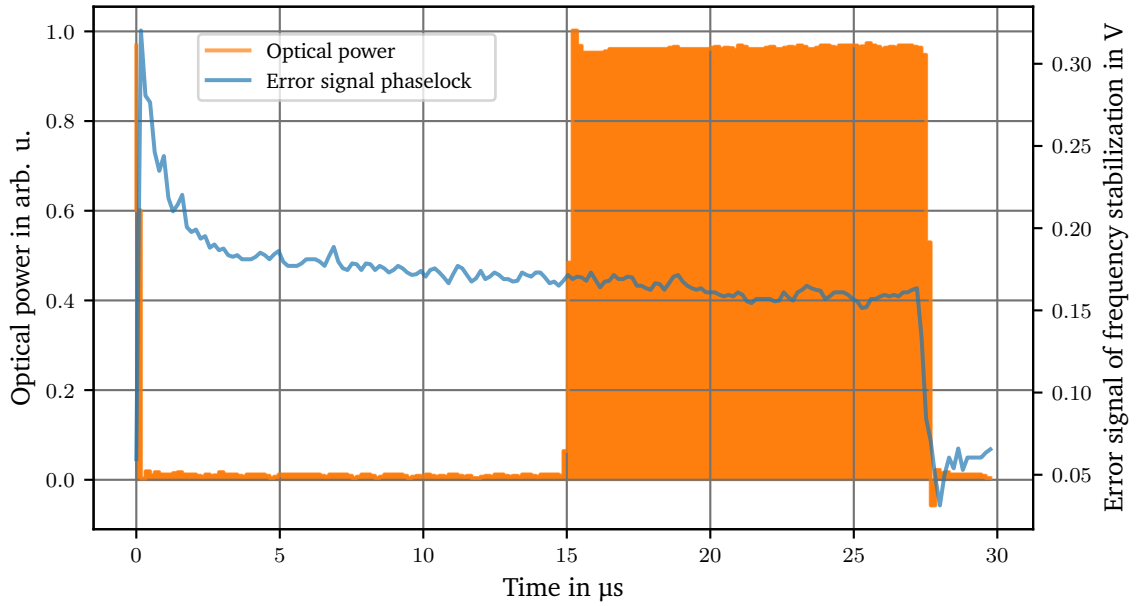

Fig. 4.2.: Detailed view on the first pulse in Fig. 3.16, taken in a randomly chosen cycle of the Raman-assisted pumping scheme. At the start of the shown data, the reference frequency is switched over approximately 28 MHz from a two-photon resonance for the $|\mathrm{F}=2, m_\mathrm{F}=+2\rangle \leftrightarrow |\mathrm{F}=3, m_\mathrm{F}=+2\rangle$-transition to a resonance for the $|\mathrm{F}=2, m_\mathrm{F}=-2\rangle \leftrightarrow |\mathrm{F}=3, m_\mathrm{F}=-2\rangle$-transition. The steep edges are generated by the fast proportional-differential regulator which settles the error signal to a plateau after approximately 10 µs. The slope in this plateau shows an action of the slow proportional-integral regulator reducing the offset of the error signal. A pulse of this laser light is given after a time of 15 µs taking a safety margin into account. This wait time is one limit for the preparation by the Raman-assisted pumping described in Sec. 3.4.3.

The Raman-assisted pumping using the global 1-qubit gate is limited by the duration required for the whole sequence yet, see Sec. 3.4.3. Both timings, the time for switching the frequency of the laser system and the duration of the π-pulses should be reduced for less scattering of the trapping light. The speed for the change of the laser frequency is limited by the laser lock. A detailed view of a frequency jump as discussed in Fig. 3.16 is shown in Fig. 4.2. As can be seen in the time constant of the first falling slope, the fast proportional-differential regulator needs up to 10 µs to settle a frequency jump on the order of 20 MHz. After that jump, a slope in the plateau of the error signal shows that the slow proportional-integral regulator reduces the offset in the error signal towards zero in order to avoid DC-offsets at the fast current source in the laser head.
In order to reduce the time for a frequency jump over a few Megahertz, a system of two stages is proposed, that generates a lock of two lasers with a frequency difference in the range of 10 GHz with the existing OPLL and an AOM-based additional difference in the laser frequency in a range of 30 MHz. An AOM-based shift would reduce the time for switching the frequency within the smaller range from 10 µs to approximately 30 ns. As an additional benefit, such a system would also allow for manipulations of the phase of the light on the same timescales. An application of this feature would be virtual-Z rotations as shown in Sec. 5.2.3 but on much

faster timescales.
The second contribution to the scattering in the Raman-assisted pumping scheme is the duration for the individual π-pulses. This duration can be reduced with more laser power. But this would also increase the scattering of the light of the 1-qubit gate. In order to avoid the scattering, a larger detuning against the intermediate state $|i_1\rangle$ is required which would also need more laser power. As both ECDLs are already driven by high-power laser diodes, a more powerful laser systems is required. Using a Ti:Sa as the master laser additionally reduces the phase noise of the system by a factor of two [89]. With a TA for the slave laser, a phase noise reduced system with an optical power of more than $4\,\mathrm{W}$ is realistic which would allow to increase the detuning by two orders of magnitude and to reduce the scattering by four orders of magnitude.

4.1.3. Addressing system for the local 1-qubit gate

The addressing of individual atoms with the light inducing the local 1-qubit gate is performed with the setup shown in Fig. 4.3. The light at $795\,\mathrm{nm}$ is coupled out of a polarization-maintaining single-mode fiber with a triplet collimator (TC06APC-780, Thorlabs) with a beam waist of $0.7\,\mathrm{mm}$. Behind a PBS filtering the polarization, an optical low-pass filter (LP02-808RE-25, Semrock / Idex) is adjusted to suppress light at $780\,\mathrm{nm}$, originating from spontaneous Raman scattering in the optical fiber [59]. Behind a beam sampler, allowing for an intensity stabilization, the light is deflected in an AOD system for two-dimensional scanning operations (DTSXY-400-800, AA OPTO-ELECTRONIC). This AOD system is placed on a four-axis alignment stage (9071, Newport) for the adjustment of maximum deflection efficiency. With a usable RF-bandwidth ΔF of $20\,\mathrm{MHz}$, the scan angle of the AOD $\delta\Theta$ is calculated to $24\,\mathrm{mrad}$ following

$$\delta\Theta = \lambda\frac{\Delta F}{v}, \tag{4.1}$$

with the wavelength λ of the 1-qubit gate light and the acoustic velocity in the AOD crystal $v = 650\,\mathrm{m\,s^{-1}}$ [105]. Following the AOD, an achromatic lens (AC254-060-B, Thorlabs) with a focal length f of $60\,\mathrm{mm}$ is used to focus the beam to a spot with a waist of $22\,\mu\mathrm{m}$ and converts the deflection angle into a lateral displacement d following [106]

$$\delta d = \arctan(\delta\Theta) f \tag{4.2}$$

resulting in a displacement of $1.46\,\mathrm{mm}$. With a reimaging by an achromatic lens with a focal length of $300\,\mathrm{mm}$ (AC508-300-B, Thorlabs) and the high-NA objective with a focal length of $37.5\,\mathrm{mm}$, a movable spot inside the science chamber with a scanning range of $180\,\mu\mathrm{m}$ is created. This allows for an addressing of 25 x 25 traps using the maximum diffraction efficiency of the AOD.
The measured spot size created by the high-NA objective is diffraction limited to a size of $2.2\,(2)\,\mu\mathrm{m}$ on purpose. The input beam to the objective does not use its full numerical aperture. A measurement of the Rayleigh range is shown in Fig. 4.4. Comparing the horizontal and the vertical dimension, an astigmatism with a separation of the foci of $10\,(2)\,\mu\mathrm{m}$ is found. In both dimensions, the Rayleigh range is measured to $24\,(2)\,\mu\mathrm{m}$ [107].
Due to the interaction with an acoustic sound wave inside the AOD, the deflected light experiences a shift of its frequency. As the local 1-qubit gate only relies on the difference frequency between master and slave laser, this shift is irrelevant for the resonance of the two-photon

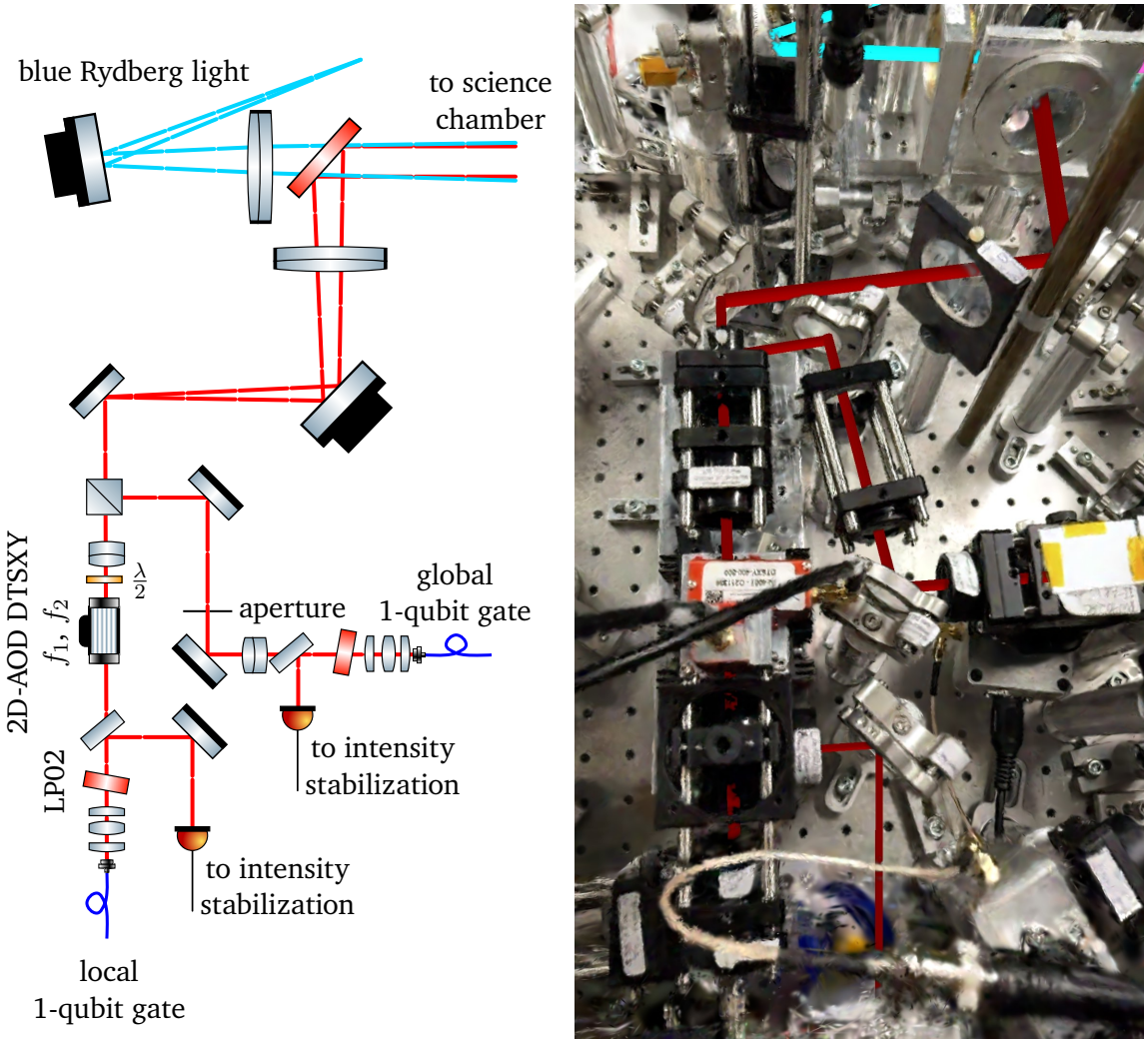

(a) (b)

Fig. 4.3.: (a) Scheme of the optical setup used to realize a local 1-qubit gate. The light from the system in Fig. 4.1 is coupled out at the three-lens collimators for the global 1-qubit gate on the right and for the local 1-qubit gate in the lower part. Optical low-pass filters LP02 are used to filter the light exiting the fibers from components at 780 nm originating from spontaneous Raman scattering in the fibers. A deflection in two dimensions is realized by the 2D-AOD system DTSXY-400-800 to create a movable spot for the local 1-qubit gate inside the science chamber. Behind the AOD, the deflected light is prepared in p-polarization with a half-wave plate. The light for the global 1-qubit gate is superposed in s-polarization with a PBS. Both light fields for the local and for the global 1-qubit gate are superimposed with the blue Rydberg light at 480 nm with the DMSP650L and pass through the dual-wavelength quarter-wave plate on the path to the science chamber (not shown here, see Fig. 4.8 (a)). The entrance into the science chamber is shown in Fig. 3.20. PBS used as polarization filters at the outputs of optical fibers are not drawn for clarity. (b) Three-dimensional visualization of the optical setup of the addressing system for the local 1-qubit gate. In the foreground, the highly compact fiber coupler used for the local 1-qubit gate is shown. In the background, the achromatic lens AC508-300-B, mounted in an aluminum mount, is shown. In the background, also the blue Rydberg light is visible.

process, see Sec. 3.1.2. A shift in the absolute frequency of the light can affect only the detuning to the intermediate state $\Delta_{i,1}$, which is on the order of several gigahertz. Therefore, a frequency variation by the AODs of up to $40\,\mathrm{MHz}$ is negligible for the 1-qubit gate operation. Additionally to the local 1-qubit gate, a globally operating 1-qubit gate is realized by a second beam superimposed with the light deflected by the AOD with a PBS. This light is focused with an achromatic lens with a focal length of $f = 40\,\mathrm{mm}$ (AC254-040-B, Thorlabs) and an aperture at the position of this focus blocks trapping light exiting the science chamber and propagating into this beam path. The position of this focus is set such that the relay optics re-images the focus far behind the atom plane. As a result, the beam has a waist of $350(25)\,\mu\mathrm{m}$ (radius) in the atom plane, allowing for a nearly homogeneous interaction with the atoms over all trap sites [108].

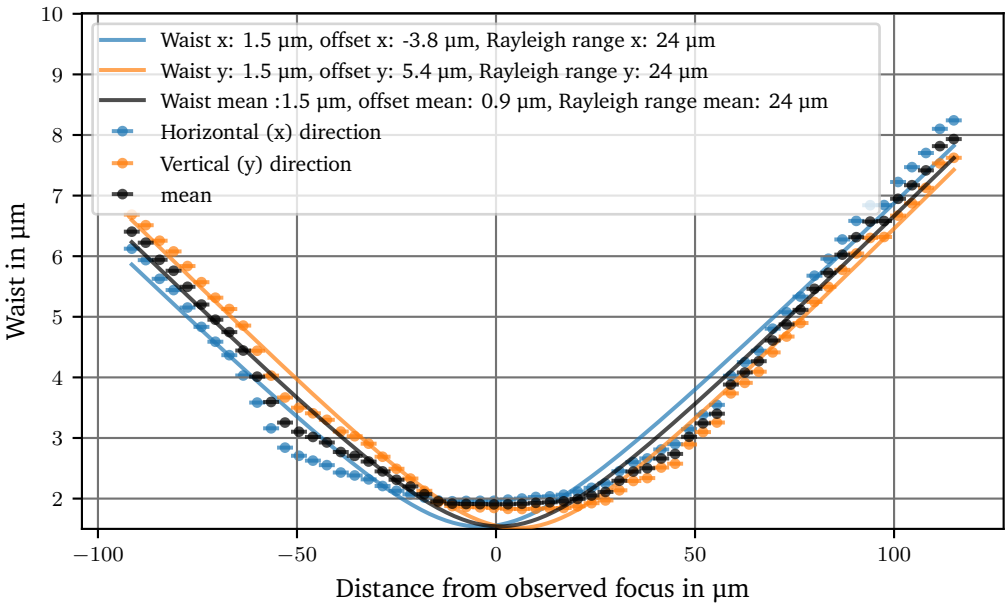

Fig. 4.4.: Measurement of the Rayleigh range of the single-site addressed light inducing the local 1-qubit gate. The data is taken in an offline setup before the installation in the Quips-B experiment, allowing for a scan through the focus of the high-NA objective with a microscope. Negative lengths correspond to a smaller distance between the high-NA objective and the focal plane of the microscope. The beam is diffraction limited as it does not use the full numerical aperture of the objective on purpose. Therefore, fits of the waist result in smaller values than the smallest measured waist of $2.2\,(2)\,\mu\mathrm{m}$. The Rayleigh range can be estimated to $24\,(2)\,\mu\mathrm{m}$ on average. For the x and y directions, the waist are fitted at different positions than the circle of least confusion (in short “offset”). This describes an astigmatism with a separation of $10\,(2)\,\mu\mathrm{m}$ between the foci in the different directions. The standard deviations of the evaluated beam widths are smaller than the marker size and therefore not drawn. The measurement uncertainty of the position arises from a calibration that is performed with the maximum used positions and interpolated for the points in between.

4.2. Laser systems for 2-qubit operations

The 2-qubit operation is implemented via the Rybderg blockade described in Sec. 3.1.5. The excitation to the Rydberg state is performed with a two-photon process using lasers at 780 nm and 480 nm which must be locked to a long-time stable reference and achieve a laser linewidths of the order of kilohertz. Both Rydberg lasers are locked via a Pound-Drever-Hall (PDH) locking scheme relative to the fringes of an ultra-low expansion cavity (ULE) (VH-6020-4, Stable Laser Systems). The technical details of these locks are presented in [90] in full details. The relevant aspects for the operation of the respective systems are given in Sec. 4.2.2 and Sec. 4.2.5. In this thesis, an extension of the locking scheme, inspired by [109] and [11], is applied and discussed in Sec. 4.2.6.

4.2.1. Rydberg excitation scheme

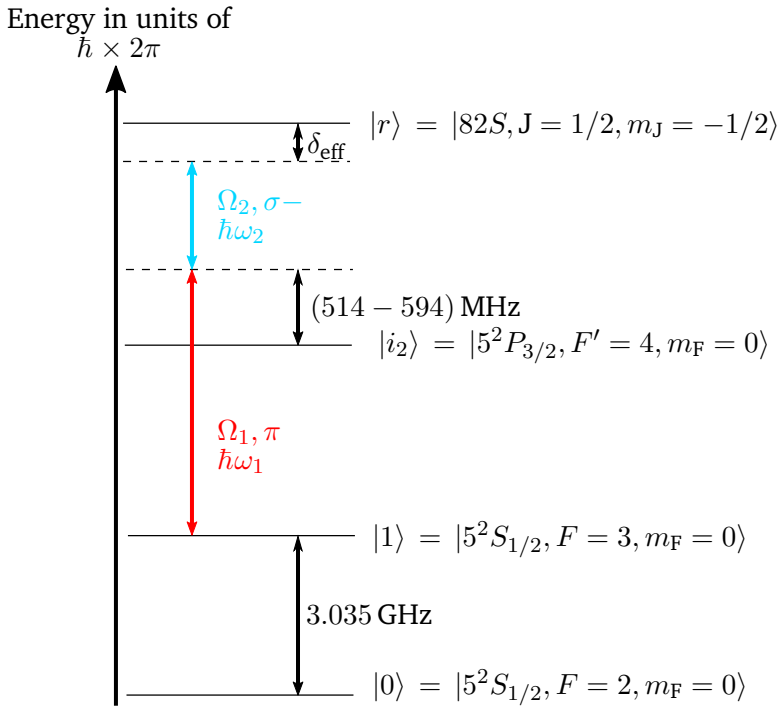

Fig. 4.5.: Scheme of the two-photon process used for the Rydberg excitation.

The excitation of the atoms to the Rydberg state is performed via a two-photon process in a ladder configuration, see Sec. 3.1.2, as shown in Fig. 4.5. The state $|i_2\rangle = |5^2P_{3/2}, F' = 4, m_{F'} = 0\rangle$ is the intermediate state of this transition because the red Rydberg light is irradiated perpendicularly to the magnetic axes in linear polarization as explained in Sec. 3.6.3. This results in a reduction of the ground-to-Rydberg state Rabi frequency by a factor of 2 compared to the optimal situation of counter-propagating and circularly polarized beams.
The coupling from the qubit level $|5^2S_{1/2}, F = 3, m_\mathrm{F} = 0\rangle$ to the intermediate level is performed with a light field at 780 nm. At the atoms, a power of up to 30 mW can be stabilized

with a waist of $1.2\,\mathrm{mm}$. This results in a maximum peak intensity of $13 \times 10^{-6}\,\mathrm{mW\,\mu m^{-2}}$, whereas intensities of $(3-8) \times 10^{-6}\,\mathrm{mW\,\mu m^{-2}}$ are typically used.
For the experiments presented here, the laser is locked $74\,\mathrm{MHz}$ above the reference laser resulting in a detuning of $154\,\mathrm{MHz}$ above the transition $|1\rangle \leftrightarrow |i_2\rangle$. For the creation of fast pulses, an AOM (CT3200-121, Crystal Technologies) in double-pass configuration is used which gives an additional detuning between $(360-440)\,\mathrm{MHz}$, resulting in a total detuning of $(514-594)\,\mathrm{MHz}$ for the light interacting with the atoms. The technical details of the locking scheme itself are presented in Sec. 4.2.5.
The coupling to the Rydberg state is accomplished by adding a light field at $480\,\mathrm{nm}$ whose frequency is matched to the experimentally determined resonance. A total power of $14\,\mathrm{mW}$ is irradiated into the chamber. Due to an imperfect coating of the vacuum windows, $30\,\%$ of this power is reflected. This beam is single-site addressed with a waist of $2.1\,(1)\,\mu\mathrm{m}$ by the system described in Sec. 4.2.4. As a result, a peak intensity of $1.2\,\mathrm{mW\,\mu m^{-2}}$ interacts with the atoms. Using these parameters, a Rabi frequency of $445\,\mathrm{kHz}$ is expected by calculations using the data of [43] and the ARC library [15]. Considering the single-photon coupling from the basis state $|1\rangle$ to the intermediate state $|i_2\rangle$ of the red Rydberg light, a population of the intermediate state lower than $1\,\%$ is expected.

4.2.2. 480 nm Rydberg laser

The system for the generation of the light for the blue Rydberg transition ("blue Rydberg laser") is shown in Fig. 4.6. The system is based on an ECDL emitting light at $960\,\mathrm{nm}$ which is equipped with a fast modulation option in the laser head [110] and a low-noise ultra-stable laser current driver [111]. The light of the ECDL is split into three paths: (1) seeding a tapered amplifier (TA), (2) PDH locking, and (3) phase locking.
On the first path (1), the light seeds a TA chip (EYP-TPA-0960-02000-4006-CMT04-0000, Eagleyard). This TA amplifies the light up to a power of $2\,\mathrm{W}$ which is then coupled into a polarization-maintaining fiber guiding the light to a second-harmonic generation (SHG). The SHG (SHGpro, Toptica) converts the light to a wavelength of $480\,\mathrm{nm}$. A maximum power of up to $1.1\,\mathrm{W}$ can be used at the main output of the SHG. This light is split into two paths, each controlled by an AOM (23080-2-LTD, Gooch & Housego), and is then coupled into a polarization-maintaining fiber guiding the light to the experiment. A part of the fundamental light behind the TA, that is transmitted through a dielectric mirror, is coupled into another fiber that guides the light to the Fizeau-based wavemeter (WS8-10, High Finesse).
The path for PDH locking (2) is coupled into the fiber of a fiber-coupled electro-optical modulator (EOM) (PM980, Jenoptik). This modulator produces sidebands with a tunable offset in the range $(0.1-1.7)\,\mathrm{GHz}$. For the measurements shown here, frequencies in the range of $(400-420)\,\mathrm{MHz}$ are used. After the modulator, the light passes a free-space EOM (PM7-NIR-980, Qubig, [112]) which produces an additional phase modulation with a frequency of $25.1\,\mathrm{MHz}$ that is used for the PDH locking. A scheme of the resulting light spectrum is shown in Fig. 4.7 (a). The modulated light is then guided to the ULE via a polarization-maintaining fiber that is additionally shielded against vibration and temperature fluctuations. The light is coupled into the ULE using a lens with a focal length of $300\,\mathrm{mm}$. The light field at $960\,\mathrm{nm}$ delivers an optical power of $83\,\mu\mathrm{W}$ to the front side of the ULE of which a maximum of $12\,\mu\mathrm{W}$ can be transmitted through the cavity when the laser is locked. Based on efficiencies of one third for each EOM, the spectral power density in each peak of the modulation is one ninth of the total power. This fits the measured transmission efficiency.

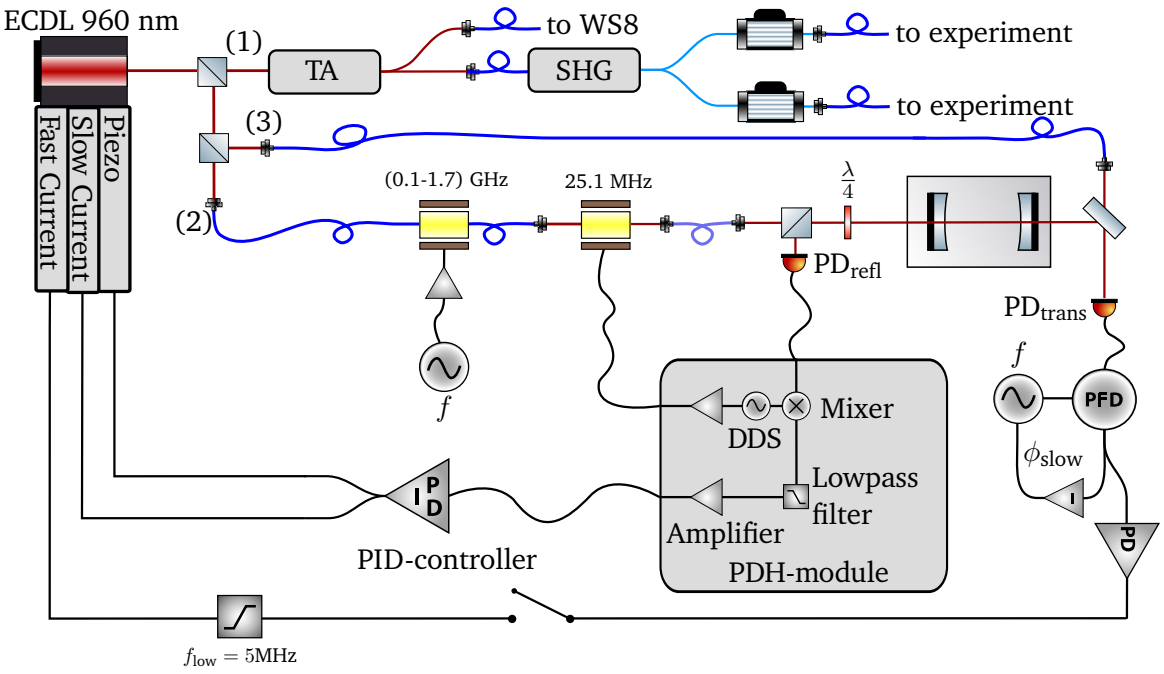

Fig. 4.6.: Scheme of the locking techniques used with the blue Rydberg laser. The light emitted from an ECDL at $960\,$nm is used for (1) seeding a TA, (2) PDH locking and (3) phase locking. The amplified light from the TA is sent to a SHG and the frequency doubled light can be switched by an AOM before being guided to the experiment via an optical fiber. For PDH locking, a fiber coupled EOM with a modulation frequency of $(0.1 - 1.7)\,$GHz is used to allow a shift of the laser frequency against the resonance of the ULE cavity. A free-space EOM working at $25.1\,$MHz is used to modulate sidebands for the PDH locking. The PDH locking is performed with the light reflected from the ULE cavity and detected with PD$_{\text{refl}}$. During the Rydberg experiments, an additional phase lock on the light transmitted through the cavity is activated with a fast switch. The transmitted light is used in a beat note with the original light from the ECDL and is detected with PD$_{\text{trans}}$. As this path also forms an optical interferometer, slow drifts in the optical path length must be compensated which is performed with a phase modulation ϕ_{slow} with a regulation bandwidth near $5\,$Hz. Lenses and PBS used as polarization filters at the input and output of optical fibers are not drawn for clarity.

The locking to the reflected light is achieved with the PDH-module described in detail in [90]. By the use of a multi-channel DDS chip with a tunable phase offset between its channels (AD9959, Analog Devices), a modulation can be imprinted on the light by the resonant EOM and the different frequency components can be tested by a reflection on the ULE. The modulation of the reflected light is detected with PD$_{\text{refl}}$ and is demodulated in a RF-mixer (SYPD-1+, Mini Circuits) to generate the error signal for PDH locking. With a fast PID regulator (FALC, Toptica) acting on the piezo and the modulation input of the laser current driver, a lock to the ULE cavity with a linewidth of $4.13\,$kHz is achieved [113].
The path for phase locking (3) couples the light into a polarization-maintaining fiber that guides the unmodulated light to the transmission side of the ULE. This path is described in detail in Sec. 4.2.6.
Via a permanent monitoring with a Fizeau-based wavemeter (WS8-10, High-Finesse), the long term stability of the laser lock an the ULE frequency reference can be estimated. In the

experiments shown here, the laser is typically locked at a frequency of $312.632323(10)$ THz.

4.2.3. Frequency scans with narrow-linewidth laser locks

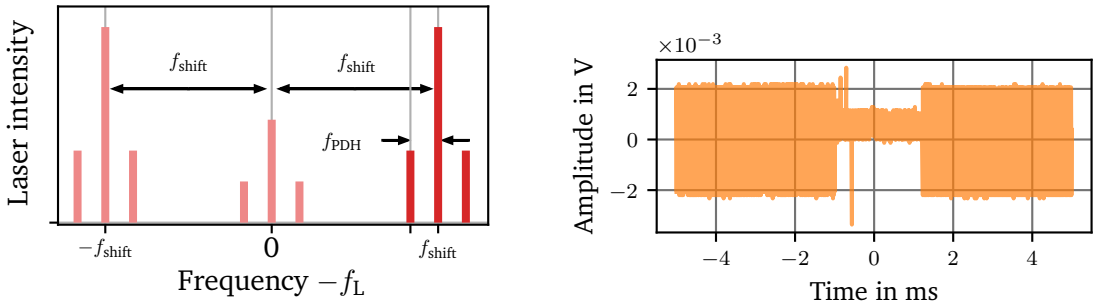

(a) (b)

Fig. 4.7.: (a) Scheme of the light spectra used for sideband locking with an ULE cavity for a frequency of the light field of f_{L}. The sidebands at f_{shift} are generated by the wideband fiber-EOMs whereas the sidebands with offset f_{PDH} are generated by resonant free-space EOMs. Frequency scans are performed by a change in f_{shift}. If the respective RF-source deactivates its output for longer than a few microseconds, the lock will fail. (b) Signal recorded for a change by 1 MHz in the output frequency of the synthesizer Siglent SSG3021X. The absolute frequencies at 412 MHz and 413 MHz are not resolved in this plot. The signal output is deactivated for several milliseconds which is unacceptable for a signal source driving the sideband frequency f_{shift}.

Scanning the laser frequency of the blue Rydberg laser system is performed by scanning the frequency f_{shift} driving the PM980 fiber EOM. A scheme of the respective light spectrum is shown in Fig. 4.7 (a). As the modulation strength of sidebands modulated by the EOM is directly proportional to the power of the high frequency applied to the modulator, the synthesizers must not vary their output power when performing a change in the output frequency. It was observed for low-end devices (SSG3021X, Siglent, [114]) that these devices do not fulfill the requirements. When performing a change in frequency, the main output is switched off completely as shown in Fig. 4.7 (b). As a result, the sideband at f_{shift} in the optical spectrum driven by this frequency vanishes and results in a flawed error signal after the PDH demodulation. For times longer than the inverse of the bandwidth of the lock, this will lead to an erratic controller output and a loss of frequency stabilization. In the Agilent E4422B, a synthesizer was found that does not drop the output power when performing changes in frequency. This synthesizer is used to perform the scans in the frequency of the blue Rydberg laser.

4.2.4. Addressing of individual atoms with the blue Rydberg light

The optical system for the addressing of individual atoms with the blue Rydberg light is shown in Fig. 4.8. The system uses an aspheric lens (C610TME-A) with a focal length of 4 mm to produce a beam with a waist of 0.35 mm. This beam is guided to a first AOD (type 4105, Crystal Technologies) which is used for a deflection in vertical direction. This AOD is adjusted to operate in the $+1$st order of deflection and therefore increases the frequency of the light. A second AOD of the same type is placed directly behind this AOD on a tip-til stage and is

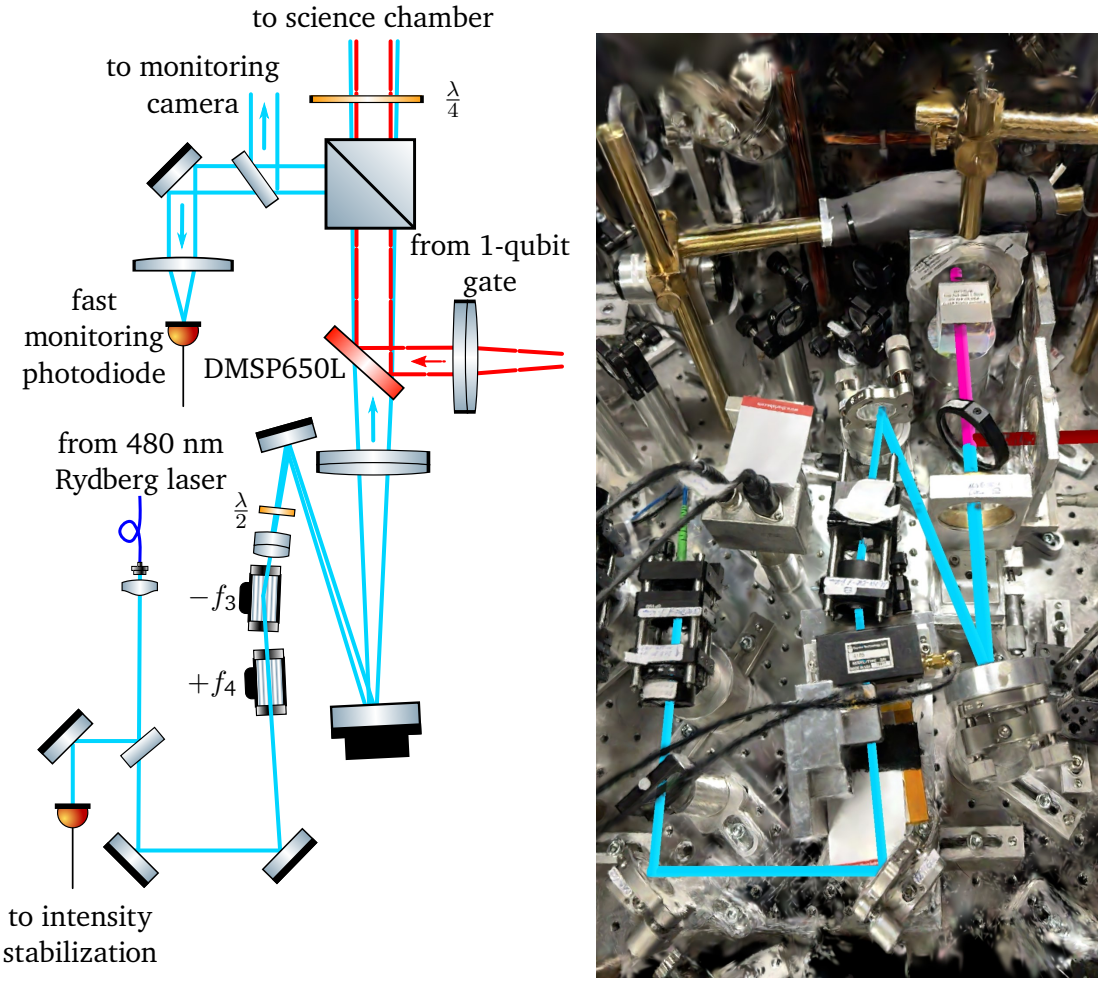

(a) (b)

Fig. 4.8.: (a) Scheme of the optical setup of the addressing of the blue Rydberg light. The light at 480 nm from the blue Rydberg laser is coupled out of an optical fiber with an achromatic lens and sent through two AODs that deflects in vertical (first, drawn in plane) and horizontal (second) direction. The system has to compensate a large refraction of the AODs with anticipating beam paths. The blue light is superimposed with the light inducing the 1-qubit gate with the DMSP650L and passes a PBS for 480 nm before both light fields become circularly polarized by a dual-wavelength quarter-wave plate. (b) A three-dimensional visualization of the optical setup. In the center, the two AODs are visible in black. From the right, the light inducing the local 1-qubit gate is superimposed.

used for a deflection in horizontal direction. The second AOD is adjusted in the -1st order of deflection and therefore decreases the frequency of the light.
The used AODs operate at a center frequency of 105 MHz. For an operation at their center frequencies, the frequency of the light would be conserved even though each AOD imprints its operation frequency on the frequency of the light. The imprinted phases of the HF-waves on the light would result in a global phase for the respective transition. The deflection axis of the AODs are aligned to the axes of the atom array which still allows for a cancellation of the HF-frequencies for operations on one diagonal axis. This, in principle allows for an application of the Levine-Pichler gate [32] in future work by using multi-tone RF signals and dynamic phase

control.
The AODs offer a usable RF-bandwidth of 35 MHz as shown in Fig. 4.9 with a total efficiency better than 55 %. Within this bandwidth, a scan angle $\delta\Theta$ of 25 mrad is achieved. Behind the AODs, the deflected beam is focused with an achromatic lens (AC254-040-A, Thorlabs) with a focal length of 40 mm to a waist of 18 µm and converts the scan angle to a displacement of 1.0 mm following (4.2). The polarization of the light is turned to p-polarization behind the AODs by a half-wave plate and then guided by two mirrors towards an achromatic lens with a focal length of 500 mm. This lens together with the high-NA objective, with a focal length of 37.5 mm, reimages the focus into the science chamber. The achromatic lens is adjusted in a way that a chromatic focus shift of the high-NA objective of 900 µm is compensated. With an external monitoring camera, a spot size at a position equivalent to the atom plane is measured to $2.1\,(2)$ µm which is consistent with an offline measurement of the Rayleigh range shown in Fig. 4.10. A scanning range of $78\,(2)$ µm in the atom plane can be used, resulting in an addressing of an atom array of 11 x 11 traps. A Rayleigh range of 25 µm is found as a mean value for both axes.
Between the achromatic lens and the high-NA objective, the light is superimposed with the light inducing the local 1-qubit gate with the dichroic mirror DMSP650L. Together, both light fields are transmitted through a polarizing beam splitter cube (48877, Edmund Optics) which filters the polarization of the light at 480 nm, but leaves the light at 795 nm unaltered. Both light fields are circularly polarized by the dual-wavelength quarter-wave plate behind the PBS and then enter the science chamber through the high-NA objective as described in Sec. 3.6.4.

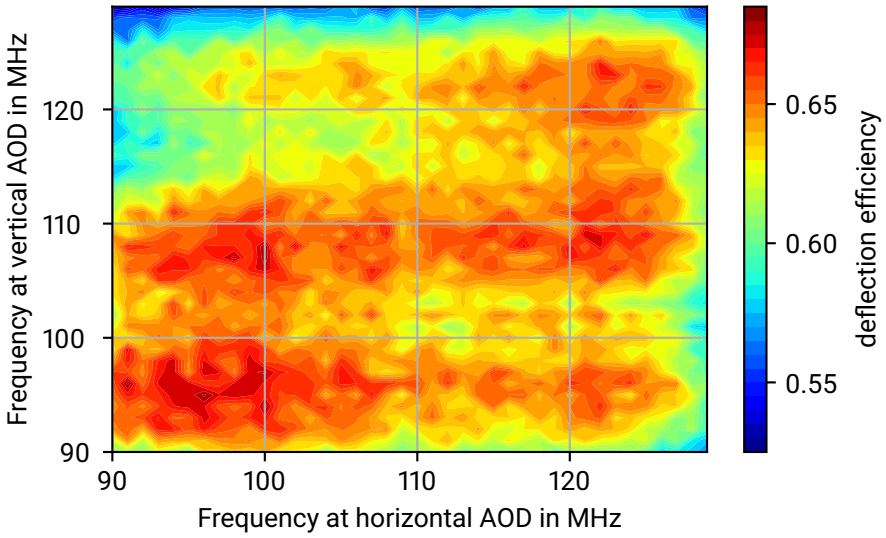

Fig. 4.9.: Total deflection efficiency of the AOD-based addressing system for the blue Rydberg light. In most regions, an efficiency above 55 % is achieved within a RF-bandwidth of 35 MHz.

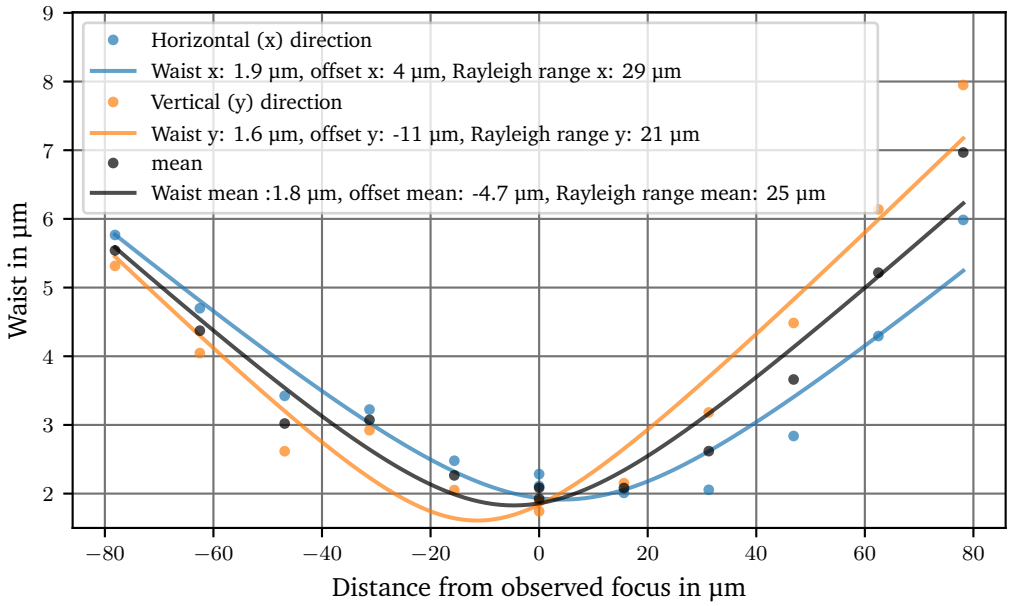

Fig. 4.10.: Measurement of the Rayleigh range of the single-site addressed blue Rydberg beam. The data is taken in an offline setup before the installation in the Quips-B experiment, allowing for a scan through the focus of the high-NA objective with a microscope. Negative lengths correspond to a smaller distance between the high-NA objective and the focal plane of the microscope. A typical behavior of this high-NA objective is found, that the beam diverges faster behind its focus and shows less variation. Therefore, fits of the waist result in smaller values than the smallest measured waist of $2.1\,(2)$ µm. The Rayleigh range can be estimated to $25\,(4)$ µm on average. For the x and y directions, the smallest waists are found at different positions than the circle of least confusion (in short "offset"). This describes an astigmatism with a separation of $15\,(2)$ µm between the foci in the different directions. The standard deviations of the evaluated beam widths are smaller than the marker size and therefore not drawn.

4.2.5. 780 nm Rydberg laser

The system generating the Rydberg light at 780 nm ("red Rydberg laser") is shown in Fig. 4.11 and based on an ECDL emitting light at 780 nm. Besides the wavelength, the ECDL is similar to the ECDL of the blue Rydberg laser, including a fast modulation option in the laser head [110] and a low-noise ultra-stable laser current driver [111]. The light of this laser is split up into four paths: (1) Seeding light for a (TA), (2) PDH locking, (3) phase locking, and (4) diagnostics via beating with a reference laser and a wavemeter (WS8-10, High Finesse, [115]). All four paths are fiber coupled in order to guarantee easy maintainability and stable operation.

The seeding light for the TA-system allows the seeding of a Coherent TA-0780-2000 [116] with up to 10 mW. After the amplification in the TA, a 7 % reflecting plate (for s-polarization) allows for an optional mixture with a second light field before passing both light fields to an AOM [117] in double-pass configuration. This AOM is used for a compensation of frequency shifts arising from the AODs in the addressing system of the blue Rydberg light described in Sec. 4.2.4. The beam is focused in the AOM with a lens with a focal length of 200 mm which results in a waist of 125 µm. A rise time of 24 ns [117] is achieved, allowing for fast pulse

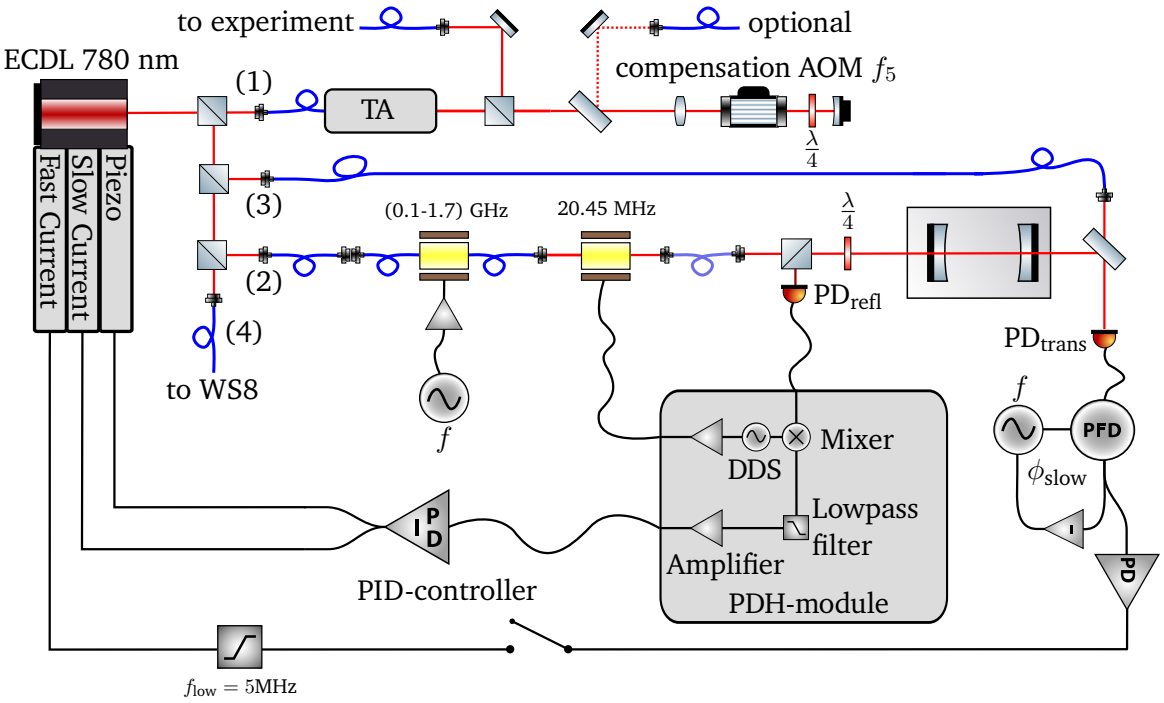

Fig. 4.11.: Scheme of the locking techniques used with the red Rydberg laser. The light emitted from an ECDL at $780\,$nm is used for (1) seeding a TA, (2) PDH locking, (3) phase locking, and (4) diagnostics. The amplified light from the TA is sent through an AOM in double pass configuration and guided to the experiment via an optical fiber. For PDH locking, a fiber coupled EOM with a working frequency of $(0.1-1.7)$ GHz is used to allow a shift of the laser frequency against the resonance of the ULE cavity. A free-space EOM working at $20.45\,$MHz is used to modulate sidebands for the PDH locking. The PDH locking is performed with the light reflected from the ULE cavity and detected with PD$_{\text{refl}}$. During the Rydberg experiments, an additional phase lock on the light transmitted though the cavity is activated with a fast switch. The transmitted light is used in a beat note with the original light from the ECDL and is detected with PD$_{\text{trans}}$. As this path also forms an optical interferometer, slow drifts in the optical path length must be compensated which is performed with a phase modulation ϕ_{slow} with a regulation bandwidth near $5\,$Hz. Lenses and PBS used as polarization filters at the input and output of optical fibers are not drawn for clarity.

modulation and in future applications also for a modulation of the light phase as used in the Levine-Pichler gate. After the double-pass, the light is coupled into a polarization-maintaining fiber guiding the light to the experiment.
The other two paths (2) and (3) are set up similarly to the system of the blue Rydberg laser besides using the specialized electro-optical components (PM780, Jenoptik, [118] and PM7-NIR-780, Qubig). The fiber-coupled phase modulator is used with a frequency of $150\,$MHz. The PDH locking uses a modulation frequency of $20.45\,$MHz at the free-space EOM produced by the PDH-module. This frequency is chosen different to the modulation frequency of the blue Rydberg laser in order to not interfere with the locking of that laser. With a Fizeau-based wavemeter (WS8-10, High Finesse) connected to path (4), the light of the red Rydberg laser at $384.229409(10)\,$THz is logged.

4.2.6. High-bandwidth locking of the Rydberg lasers via an optical phase-locked loop

Both Rydberg lasers are locked with the PDH technique on fringes of the ULE cavity. The PDH technique uses the modulations imprinted with the free-space EOMs and compares it with the modulation in the light after a reflection on the cavity. Therefore, the modulated light fields are coupled out of polarization-maintaining single-mode fibers and by the use of quarter-wave plate and a PBS, the reflected light from the ULE cavity is detected with fast photodiodes [119]. The two light fields at 780 nm and 960 nm are superimposed with a dichroic mirror (#69-221, Edmund Optics) in front of the ULE cavity as shown in Fig. 4.12. The fast photodiodes PD_{refl} for the respective wavelength detect the modulation in the light after the reflection and allow to compare this modulation in amplitude and phase with the original modulation used at the EOM in the PDH-modules [120]. The locking technique is presented in full detail in [90].

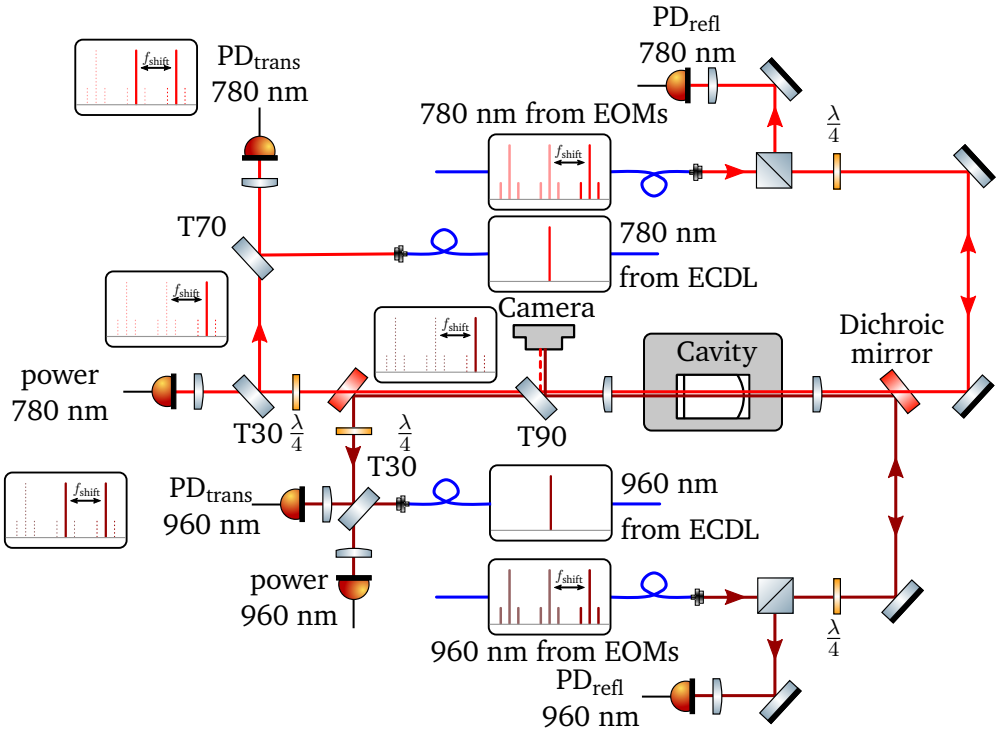

Fig. 4.12.: Scheme of the OPLL with the transmitted light oft the ULE cavity. The modulated light of each Rydberg laser (paths (2) in Fig. 4.6 and Fig. 4.11) is coupled out of polarization-maintaining single-mode fibers. The light is prepared in circular polarization by a quarter-wave plate and reflected on the ULE cavity. The reflected light passes the quarter-wave plate a second time and can be separated by a PBS from the incoming light. With the photodiodes PD_{refl}, the modulation is detected and passed to the PDH-module for demodulation and creation of the PDH error signal. The transmitted light behind the ULE cavity is detected with a camera that is able to resolve the TEM mode exiting the cavity. The light fields from of the two lasers are separated by a dichroic mirror. Each field is then split up for a measurement of the transmitted power and for a beat measurement with the unmodulated light from the respective ECDL (paths (3) in Fig. 4.6 and Fig. 4.11). The transmittance of the beam splitters are noted by the label "T" followed by the value in percent. This beat note is used for an additional phase lock to a reference synthesizer. PBS used as polarization filters at the input and output of optical fibers are not drawn for clarity.

After accomplishing the PDH lock for each of the two Rydberg lasers, an optical power of several microwatts is transmitted through the ULE cavity. This light is expected to have a very small linewidth and vanishing frequency components at higher modulation frequencies, due to the high finesse of the ULE cavity. Based on the analysis in [39], the full with at half maximum of the cavity fringes is expected to be $\Delta\nu_{780} = 47.6(4)\,\mathrm{kHz}$ for the light at $780\,\mathrm{nm}$ and $\Delta\nu_{960} = 32.1(1)\,\mathrm{kHz}$ for the light at $960\,\mathrm{nm}$. These sharp transmission windows act as spectral filters and suppress phase noise at high frequencies in the transmitted light. In terms of a frequency reference, any frequency modulation at faster frequencies than $300\,\mathrm{kHz}$ (at $780\,\mathrm{nm}$) and $200\,\mathrm{kHz}$ (at $960\,\mathrm{nm}$) is filtered because the the ring-down time for light in the cavity has been measured to $3.0 \pm 0.3\,\mu\mathrm{s}$ for the light at $780\,\mathrm{nm}$ and $5.0 \pm 0.3\,\mu\mathrm{s}$ for the light at $960\,\mathrm{nm}$ [90]. Following the argumentation in [11], phase noise above the respective corner frequencies ($300\,\mathrm{kHz}$ for $780\,\mathrm{nm}$, $200\,\mathrm{kHz}$ for $960\,\mathrm{nm}$) is suppressed by a factor of 40 and better. The cavity therefore acts as a low-pass filter for phase noise in the vicinity of its fringes. This is promising to deliver an optical frequency reference that allows for an improved locking for bandwidths above these low-pass frequencies.

In order to use this frequency reference with available techniques, a beat measurement of the light of the respective ECDL with the transmitted light from the ULE is set up for both lasers as shown in Fig. 4.12. The light transmitted through the ULE cavity is collimated with a lens with a focal length of $300\,\mathrm{mm}$ and then split up with a dirchoic mirror DMSP900 [121]. With a fraction of $30\,\%$ of the transmitted light of each wavelength, a monitoring of the transmitted power is set up. With a fraction of $70\,\%$ of the transmitted light and for each wavelength, a beat with the unmodulated light of the respective ECDL, guided via the paths (3) (see Fig. 4.6 and 4.11), is measured with fast photodiodes.

For the light at $780\,\mathrm{nm}$, a photodiode of type FDS025 is used and for light at $960\,\mathrm{nm}$, the type FGA01 is used [122]. As the beat signals are very weak, multiple low-noise amplifiers (ZX60-3018G+, Mini-Circuits and ZFL-500-HLN, Mini-Circuits as last stage) are used to generate a high-frequency beat note with a signal strength of $10\,\mathrm{dBm}$. As a result, beat spectra with center frequencies at the frequencies used for the respective fiber coupled phase modulators (e.g. $150\,\mathrm{MHz}$ and $412.03\,\mathrm{MHz}$) can be analyzed. Based on these beat spectra, the same phase locking technique based on a phase-frequency detector as used for 1-qubit gate operation, see Sec. 4.1.1, is used. Using a proportional-differential controller, the fast modulation option in the laser head controls the phase of the beat note to follow the phase of a reference synthesizer. For both Rydberg lasers, beat spectra comparing the PDH lock and the phase locked loop are shown in Fig. 4.13.

From the beat spectra, a reduction of the phase noise of $20\,\%$ for the red Rydberg laser and of $39\,\%$ for the blue Rydberg laser can be calculated. So far, this could not be tested independently due to the limited options for the analysis of laser phase noise on short time scales. The impact on the Rydberg excitation is discussed in detail in Sec. 5.3.5.

One limitation of this locking scheme is given by long-term drifts of the phase delay, mainly induced by the optical fibers. As the index of refraction of the optical fibers is highly sensible to temperature and mechanical stress, changes in both quantities will modify the phase measured in the beat note. As these effects can be clearly addressed to frequency domains smaller than $100\,\mathrm{kHz}$, a slow modulation of the phase of the reference synthesizer is used to compensate this. The controller bandwidth is set to $5\,\mathrm{Hz}$ to reduce manipulations of the light phase on the significant time scales. Additionally, a low-pass filter with a cutoff frequency of $10\,\mathrm{kHz}$ is placed at the modulation input of the reference synthesizers to avoid additional phase noise by coupling to electromagnetic interference.

As the phase deviation of the reference synthesizer is limited to a few multiples of π, but

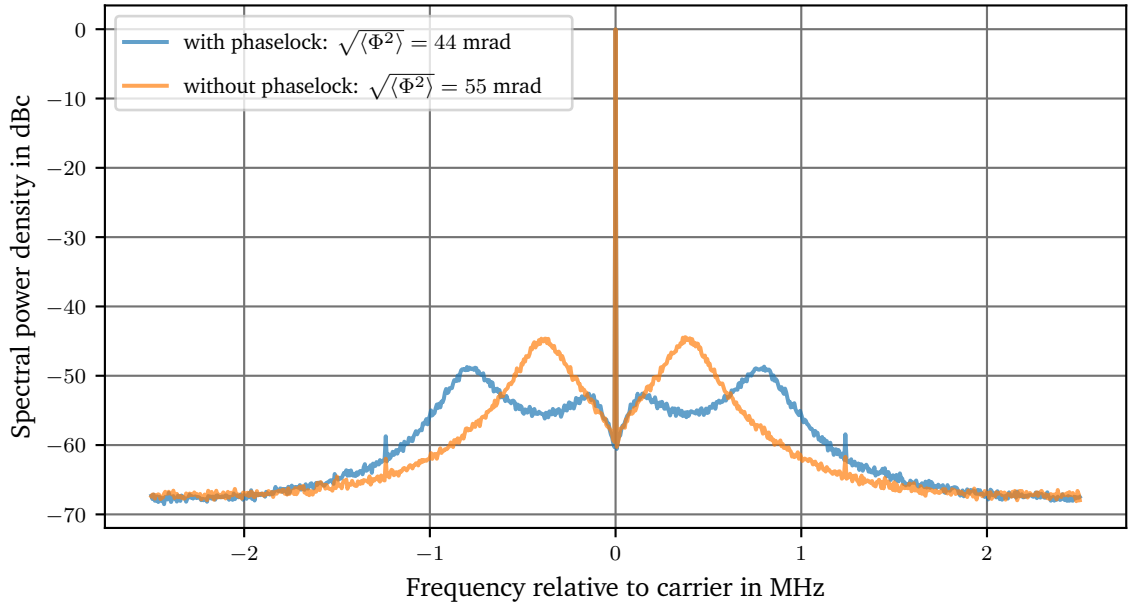

(a)

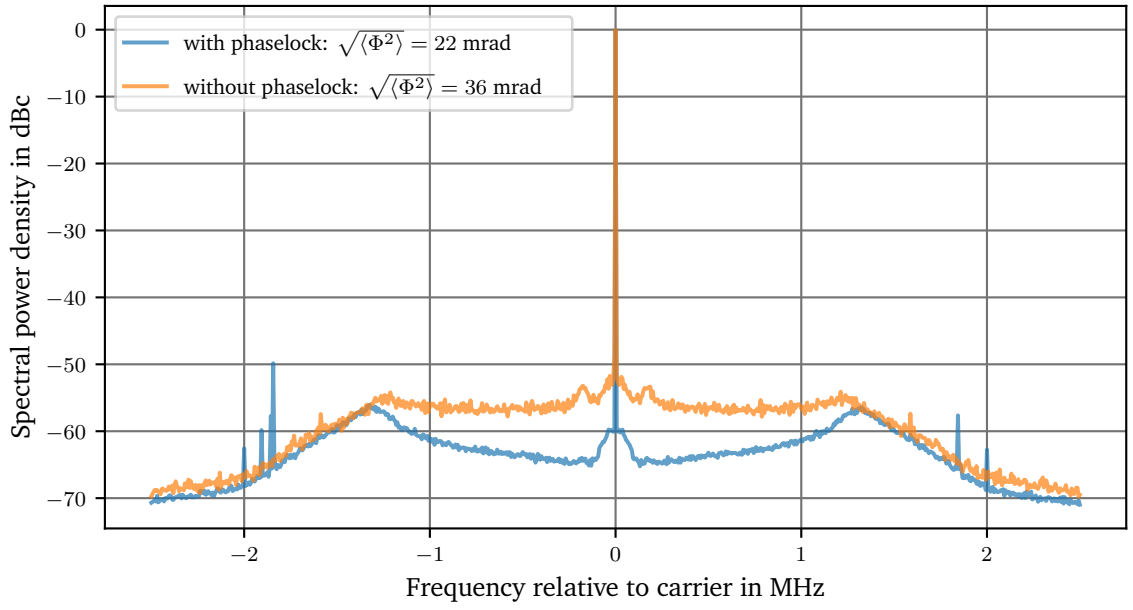

(b)

Fig. 4.13.: (a) Comparison of the phase noise of the red Rydberg laser with PDH lock only (yellow) and activated OPLL (blue). (b) The same comparison for the blue Rydberg laser measured in the fundamental light at 960 nm.

temperature drifts allow the fibers to produce a much larger phase deviation in the optical path, frequent resets of the phase offset are implemented. For a phase reset, the phase lock is deactivated in experiment slots when the light of the Rydberg lasers is not irradiated to the atoms. Then the slow controllers are reset and relocked on a new phase offset. Finally, the

phase lock of the lasers is reactivated.
Another limitation is given by the high modulation bandwidth of the fast current source in the laser head. The activation of the phase lock usually starts with a maximum output of the PD-controller given by the design of the controller. The fast current source in the laser head modulates parts of this burst on the laser diode as it can modulate frequencies of up to 150 MHz [110]. The bursts can lead to a loss of the PDH lock. In order to eliminate these extremely fast burst, low-pass filters with a cutoff frequency of 5 MHz (SLP-5+, Mini Circuits, [123]) are applied at the output of the PD controller. Using filters with good impedance matching results in a reliable operation of the phase lock with frequent resets of the phase offsets.

4.3. Agile synthesizer for Rydberg blockade mediated CNOT Gate

Due to the high sensibility of Rydberg atoms to external fields (see Tab. 5.3) and the limited options for the trapping of Rydberg atoms, experiments using these states require a very fast control over the light interacting with the atoms. The choice of AODs for the single-site addressing implies that this involves fast changes in RF-frequencies as well as triggering light pulses on timescales shorter than one microsecond. Here, an FPGA-based system is presented that allows agile changes in RF-frequencies synchronous to triggers activating the respective light fields. First, the H-C_Z sequence is described that defines the requirements for this system. Then, the technical details of the electronics are presented.

4.3.1. *H*-C_Z sequence

For an experimental realization of the H-C_Z gate (see Sec. 3.1.6), control over the position of two laser beams and a fast switching of these two beams is required. A simplified scheme of the RF- and digital channels proposed for this operation is shown in Fig. 4.14. As the addressing of the local 1-qubit gate (pulses (2) and (4) in Fig. 3.9) and the addressing of the blue Rydberg light (pulses (1), (3), and (5)) are performed with AODs, four agile RF-channels are needed, allowing frequency jumps on a timescale of at least 100 ns. These channels produce the RF-frequencies f_0 to f_4. Additionally, as the AODs in the blue addressing system shift the frequency of the light, which would create a position-dependent detuning on the Rydberg excitation, a fifth agile RF-channel is required for a compensation of this frequency shift with f_5.
The gate must operate within the coherence time of the Rydberg state of the control atom in order to reproduce its original state at the end of the sequence. This timescale is measured to a few microseconds [124]. Therefore, control over pulses shorter than microseconds is required. For the light inducing the local 1-qubit gate and at the light of least one of the two Rydberg lasers, a switching faster than this timescale is needed. This can be reached by a combination of digital signals, fast switches for RF-frequency, and AOMs. In this setup, fast digital outputs (Digital out 1 and Digital out 2 in Fig. 4.14) that operate synchronously with the agile RF-channels fulfill this requirement together with commercial fast RF-switches (ZYSWA-2-50DR+, Mini-Curcuits) and the used AOMs (CT3200-121, Crystal Technology).

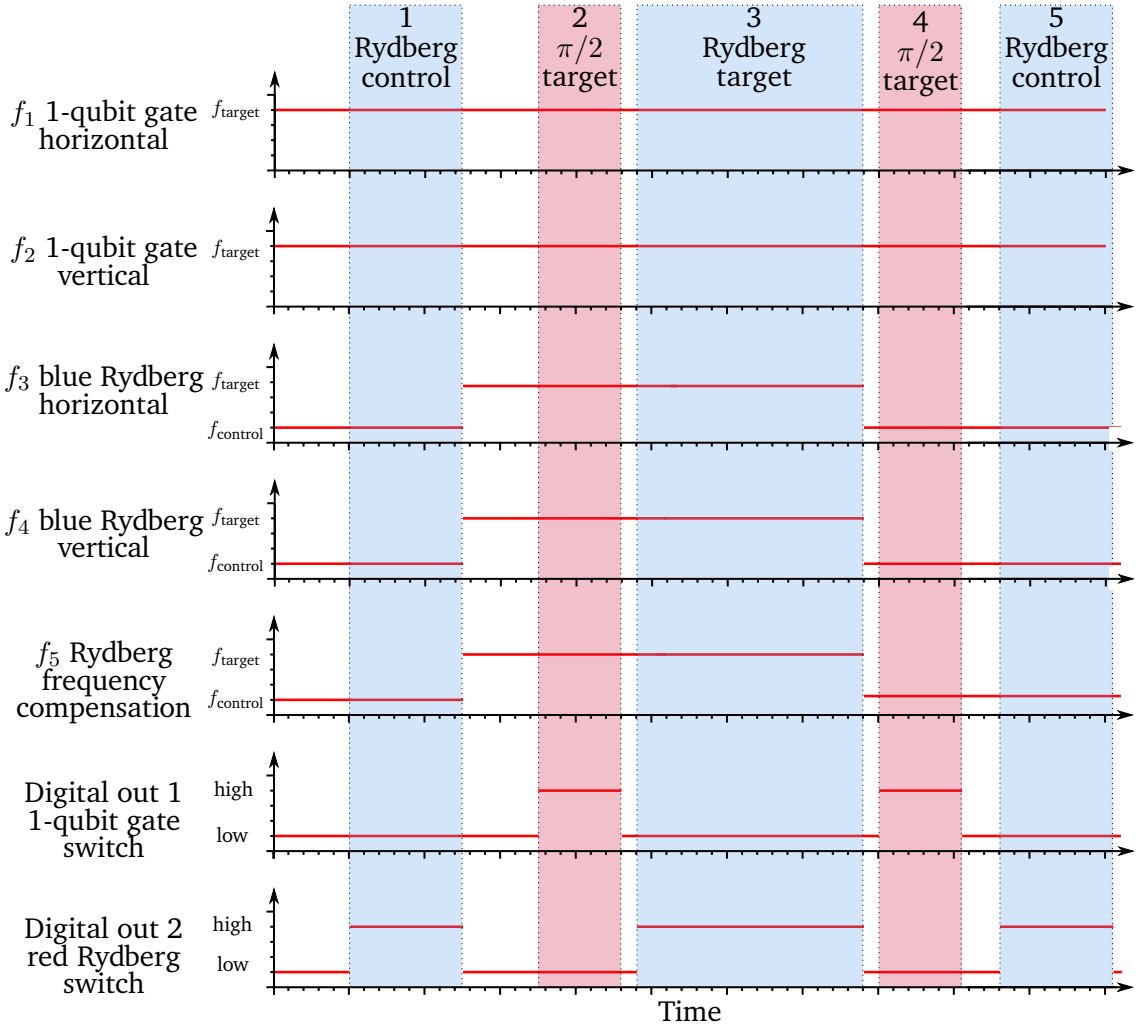

Fig. 4.14.: Scheme of the RF- and digital output channels needed for a realization of the H-C_Z gate with AOD-based addressing. Two RF-channels (f_1 and f_2) control the addressing of the light inducing the local 1-qubit gate. Two more agile RF-channels (f_3 and f_4) switch the blue Rydberg light from the control to the target qubit via AODs as indicated with the blue bars labeled “Rydberg control” and “Rydberg target”. Another agile RF-channel (f_5) is used for a compensation of the induced shift of the frequency of the blue Rydberg light. Two digital outputs activate the respective pulses of the Rydberg light and the light inducing the local 1-qubit gate. The frequencies are changed in advance of the pulses to compensate for delays in the AODs.

4.3.2. Agile frequency synthesis for AOD-based addressing

A fast control of the RF-frequencies driving the addressing systems is achieved with an FPGA- and DDS- based setup shown in Fig. 4.15. The frequency synthesis is based on DDS cards fea-

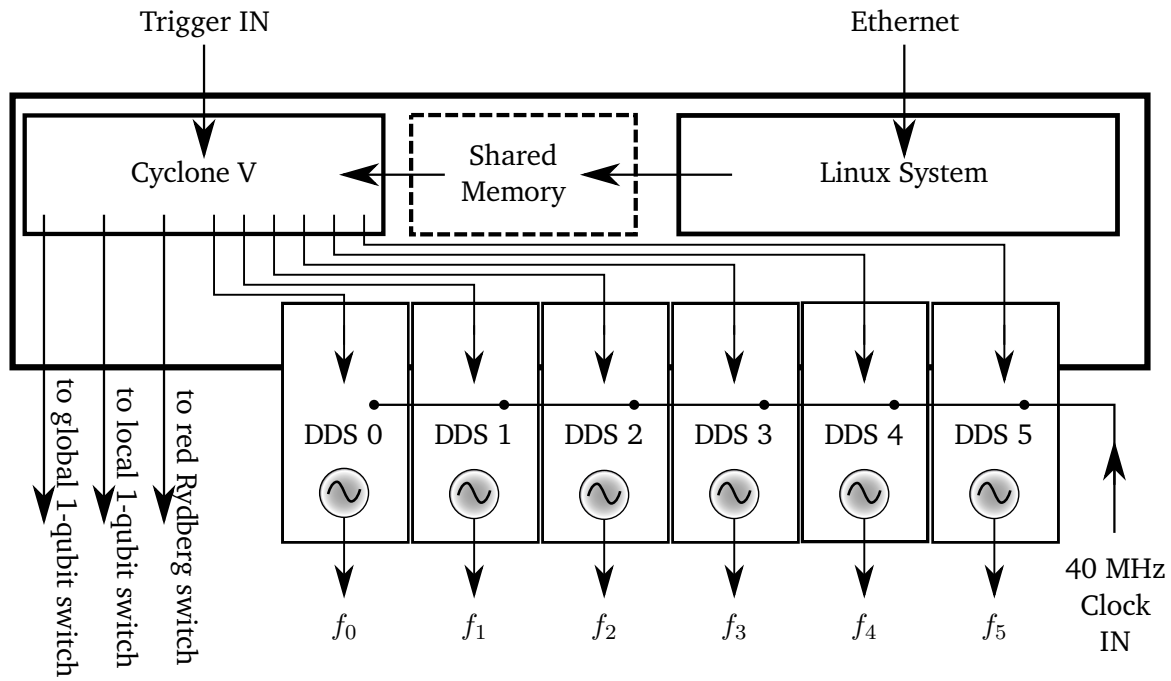

Fig. 4.15.: Scheme of the agile frequency synthesis implemented with the Terasic DE1-SOC, featuring the Cyclone V FPGA with a SoC running a Linux system with a shared memory. The shared memory is written by the Linux system with a list of operations received via ethernet. One digital input triggers the FPGA to execute the next entry in the shared memory. Controlled by to the FPGA, six DDS chips produce the frequencies f_0 to f_5. These frequencies are used in the systems drawn in Figs. 4.1, 4.3 (a), 4.8 (a), and 4.11. A common reference clock serves for a consistent frequency output. Three digital outputs are used to control the light pulses of the global 1-qubit gate, the local 1-qubit gate and the red Rydberg light via fast RF-switches.

turing an AD9910 core [125]. The fast and versatile control over the DDS cards is achieved with a System-on-Chip (SoC, DE1-SOC, Terasic), featuring a Cyclone V and an ARM Cortex-A9 dual-core processor.
Via an ethernet port, the experimental control software [126, 81] communicates with a Linux system running on the dual-core processor. This system is able to write a list of operations into a shared memory based on a first-in, first-out (FIFO) logic, which can be accessed by the Cyclone FPGA [61]. The FPGA controls 80 digital I/O pins which are programmed as one input and 79 outputs. The 79 output pins are sufficient to control six AD9910 via their (slow) serial BUS and (fast) parallel BUS. Hereby, the parallel BUS is shared among the six DDS-cards and each DDS can be addressed by triggering its individual “receive” pin. This allows for a highly efficient use of the provided pins. Three output pins are left free that are used for a fast and synchronous control over the light pulses.
The information about the frequency and the identifier of the DDS-core is saved in the FIFO memory. Additionally, the state of the three digital output pins, a time delay, and a trigger type are saved. The absolute timing of the changes in frequency are triggered by the one input pin that servers as a trigger pin (3.3 V). In the FIFO, only a few entries are defined as being triggered by this hardware pin. On timescales up to 10 ms, the FPGA can count its own clock cycles and trigger the next entry of the FIFO according to the saved delay [108]. The clock cycles of the FPGA bearing a time of 20 ns define the shortest operations that can be created.

Using this technique, a very fast control over the systems used for the gate operations is achieved. The connections of the DDS cores are labeled by the variables $f_0 - f_5$ following the indices of frequency variables in the subsystems. The frequency outputs are used in the following functions:

- f_0: agile jumps of the beat note between the two phase-locked ECDLs generating the light for the 1-qubit gate (see Fig. 4.1)
- f_1 and f_2: control the AODs deflecting the light inducing the local 1-qubit gate (see Fig. 4.3 (a))
- f_3 and f_4: control the AODs deflecting the blue Rydberg light (see Fig. 4.8 (a))
- f_5: agile frequency jumps of the compensation AOM in the red Rydberg laser (see Fig. 4.11)

The digital outputs are used to trigger pulses of the light inducing the global 1-qubit gate, the local 1-qubit gate and the red Rydberg light. Whereas the local 1-qubit gate and the red Rydberg light are used in the H-C_Z protocol described in Sec. 4.3.1, the global 1-qubit gate is used in the Raman-assisted pumping scheme described in Sec. 3.4.3.
The hardware incorporating these functions is shown in Fig. 4.16. The DE1-SOC is used as the lowest section. The digital I/O pins from the GPIO connectors of this board are distributed via an intermediate board in a spatial configuration that gives enough space for the DDS cards. These cards are mounted on top offering access to the SMA connectors with RF-cables. Via the top row of SMA connectors, the DDS cards are connected among each other and to a synthesizer producing a highly stable reference clock frequency at $40\,\mathrm{MHz}$. For a more convenient and safe use, the power supply for the DDS cores ($3.3\,\mathrm{V}$, $0.5\,\mathrm{A}$ each) is shared among the cards and delivered via the connectors from the intermediate board. A power supply of $(12 - 20)\,\mathrm{V}$ powers the intermediate section and is transformed to the required voltage of the DDS cores [127].

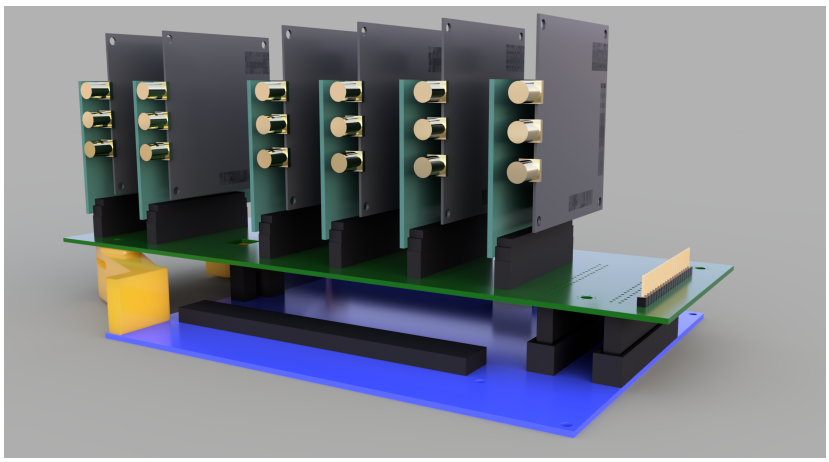

Fig. 4.16.: Render graphics of the hardware used for agile frequency synthesis. In the lower part in blue, the Terasic DE1-SOC is drawn and connected via an intermediate board to the six DDS chips on the top. In yellow, supporting structures are drawn that support the PCBs (taken from [108]).

5. Demonstration of quantum gate operations

The demonstration of a universal set of quantum gates has been the missing key to quantum computing in the Quips-B experiment for years. Parts of this task have been achieved in the course of this experiment starting from first 1-qubit rotations on ensembles of atoms [8] to experiments with single atoms [72] and sorting [61] to Rydberg excitation and interaction [14]. This thesis is the first approach to combine all parts of the puzzle. First, the experimental sequence is shown. Then, the 1-qubit operations are discussed starting with the global 1-qubit operation followed by the local 1-qubit operations which involve Rabi floppings as well as virtual-Z rotations. Next, the Rydberg excitation is discussed in full detail, with respect to the requirements for reliable experiments with Rydberg atoms in this experiment and a discussion of the performance of the Rydberg excitation. Finally, the first approach of a CNOT operation is shown.

5.1. Experimental sequence for gate experiments

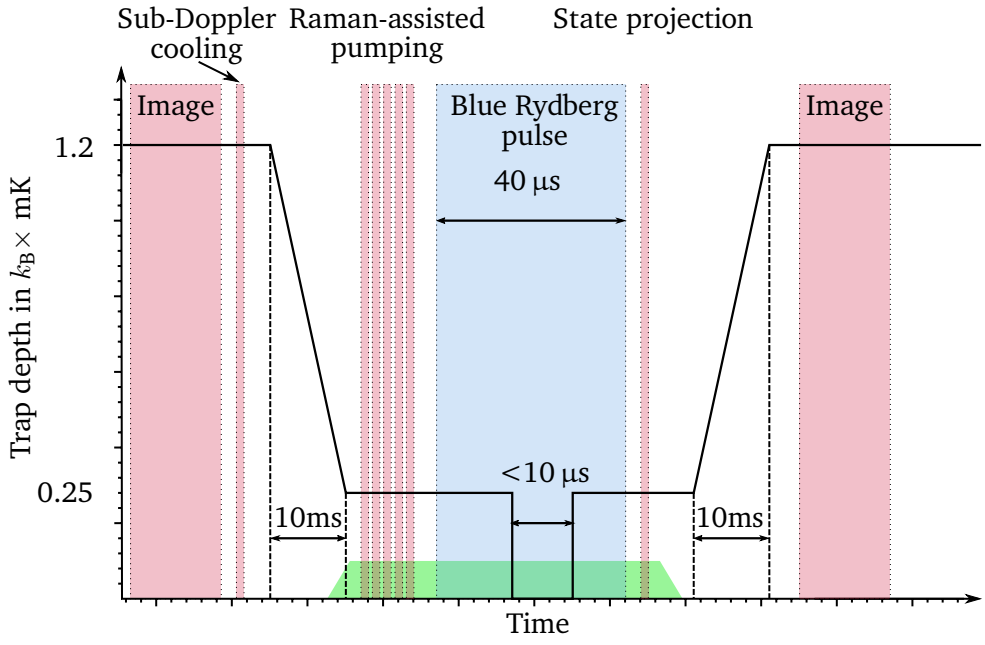

Fig. 5.1.: Scheme of the experimental sequence as trap depth over time for experiments with Rydberg atoms, 1-qubit operations, and 2-qubit operations. Time axis drawn not to scale and pulses of the Raman-assisted pumping scheme are drawn symbolically. Prominent light pulses that are applied in all experiments with quantum gates are drawn in colored boxes. As a green inlay, the activation of the quantization field is drawn.

For the demonstration of quantum gates, an experimental sequence as shown in Fig. 5.1 is used. Starting with a defect-free array of individual atoms as described in Sec. 3.4, a first fluorescence image is taken at a high trap depth of approximately $k_\mathrm{B} \times 1.2\,\mathrm{mK}$ in the center trap. A full set of trap parameters is listed in Tab. 5.1. As the imaging parameters are optimized for optimal imaging but not for cooling, a short pulse for sub-Doppler cooling follows the first imaging phase with the maximum accessible detuning of the cooling light. Next, the traps are ramped down to a trap depth of $k_\mathrm{B} \times 0.25\,\mathrm{mK}$ to reduce scattering of the trapping light.
The quantization field is activated and needs several milliseconds to reach its full strength due to the inductance of the magnetic fields coils. As described in Sec. 3.4.3, the state of the atoms is prepared to $|5^2\mathrm{S}_{1/2}, \mathrm{F} = 2, m_\mathrm{F} = 0\rangle$ by the Raman-assisted pumping scheme. From then on, 1-qubit operations can be performed at any time until the state projection. Furthermore, the blue Rydberg light is activated as explained in Sec. 5.3.3. During this pulse, the traps are deactivated for less than $10\,\mu\mathrm{s}$ as described in Sec. 5.3.2. This deactivation marks the time slot used for experiments with Rydberg atoms.
After the reactivation of the traps, the state projection can be performed as described in Sec. 3.3. For the detection of a Rydberg excitation, the state projection is not used, as it provides only information on the qubit basis states but not the Rydberg state. Finally, the traps are ramped up to the initial depth and a second fluorescence image is taken. The magnetic field must be decayed completely until the image is taken to avoid atom loss during imaging. By comparing the initial and final image of each experimental cycle, the atom loss probability (in short: loss probability) is evaluated selectively for each trap site. When using the state projection, the atom loss probability is understood as the population in the state $|1\rangle = |5^2\mathrm{S}_{1/2}, \mathrm{F} = 3, m_\mathrm{F} = 0\rangle$ with respect to the detection errors shown in Sec. 3.4.3. For experiments involving the Rydberg excitation, this is the best measure of a successful excitation as the Rydberg atoms are not attracted by the dipole traps. A detailed analysis of this process is given in [128, 39]. With the recaptured atoms, an additional cycle of rearrangement is performed and the experiment is repeated for up to nine cycles, typically.

Tab. 5.1.: Parameters of trapping light used in the different steps of the experimental cycle used for the demonstration of gate operations. The given power is the total laser power used for the generation of the trap array. The trap depth is the calculated trap depth of the central trap.

Stage in experimental cycle	Wavelength of trapping light in nm	Power of trapping light in W	Trap depth in units of $k_\mathrm{B} \times$ mK
Loading of traps	798.32	1.9	1.2
1-qubit gate experiments	798.32	0.41	0.25
Rydberg excitation	798.32	0.0	0

5.2. 1-qubit gate

The 1-qubit gates are applied in global and local operations in this experiment. The generation of the required light and the options for frequency and phase shifts are discussed in Sec. 4.1. Here, the operations that are induced by this light on the atoms are demonstrated. As a starting point, the operation with the global 1-qubit gate is discussed before the more complex discussion of the local 1-qubit gate is given.

5.2.1. Global 1-qubit gate Rabi flopping

The basis of a 1-qubit gate is a Rabi flopping of the respective qubit basis states. In words of a gate operation, the Rabi flopping coincides with a $\hat{R}(\theta, 0)$ gate for various settings of the rotation angle θ. Rabi floppings with all atoms in the array are performed with a two-photon process (see Sec. 3.1.2) and with a light beam with global access to all atoms in the atom plane via the **z**-axis (see Sec. 3.6.2).
Rabi floppings have been demonstrated within a wide range of detunings $\Delta_{\mathrm{i},1}$ to the manifold of intermediate states $|5^2\mathrm{P}_{1/2}\rangle$. Due to the Gaussian profile of the beam, a beam diameter that is larger than the edge length of the atom array of $140\,\mu\mathrm{m}$ is preferred to achieve a nearly uniform action over all atoms of the array. A beam waist of $350(32)\,\mu\mathrm{m}$ is chosen for the light inducing the global 1-qubit gate.
A significant scattering on the atoms, following (3.6), can occur for a too small detuning relative the intermediate state. The effect of scattering is shown in the Rabi floppings in Fig. 5.2 for a peak intensity of $\left(0.17(1) \times 10^{-4}\,\mathrm{mW\,\mu m^{-2}}\right)$ and a detuning of $-8\,\mathrm{GHz}$ relative to the transition $|5^2\mathrm{S}_{1/2}, \mathrm{F} = 3\rangle \leftrightarrow |5^2\mathrm{P}_{1/2}, \mathrm{F}' = 2\rangle$. The shown Rabi floppings occur at Rabi frequencies in an array of 5x5 individual atoms with a mean of $194 \pm 4\,\mathrm{kHz}$ and a range of $(164-217)\,\mathrm{kHz}$ and a $1/e$ decay time with a mean of $18 \pm 1\,\mu\mathrm{s}$ and a range of $(13-25)\,\mu\mathrm{s}$. In all traps, a trend towards a population in the $|5^2\mathrm{S}_{1/2}, \mathrm{F} = 3\rangle$ manifold with a slope of $0.5\,\%\,\mu\mathrm{s}^{-1}$ is found by irradiating the light inducing the global 1-qubit gate with a detuning of $2\,\mathrm{MHz}$ relative to the two-photon transition. By increasing the detuning of the light relative to the intermediate state from $-8\,\mathrm{GHz}$ to $-17\,\mathrm{GHz}$, the scattering could be reduced below the error rates of preparation and readout.
The Rabi floppings for the larger detuning and the same intensity of the light as before are shown in Fig. 5.3. As the detuning is increased by a factor of 2.125, the Rabi frequency is reduced by this factor following (3.11) to $91 \pm 2\,\mathrm{kHz}$ with a range of $(75 - 112)\,\mathrm{kHz}$ over the array. Owing a mean $1/e$ damping time of $83 \pm 7\,\mu\mathrm{s}$ and a range of $(43 - 153)\,\mu\mathrm{s}$, the damping tends towards a value of $50\,\%$ population on state $|1\rangle$ within the tested pulse duration.
Comparing the two damping times, the expected scaling with the inverse of the square root of the detuning following (3.6) is found.

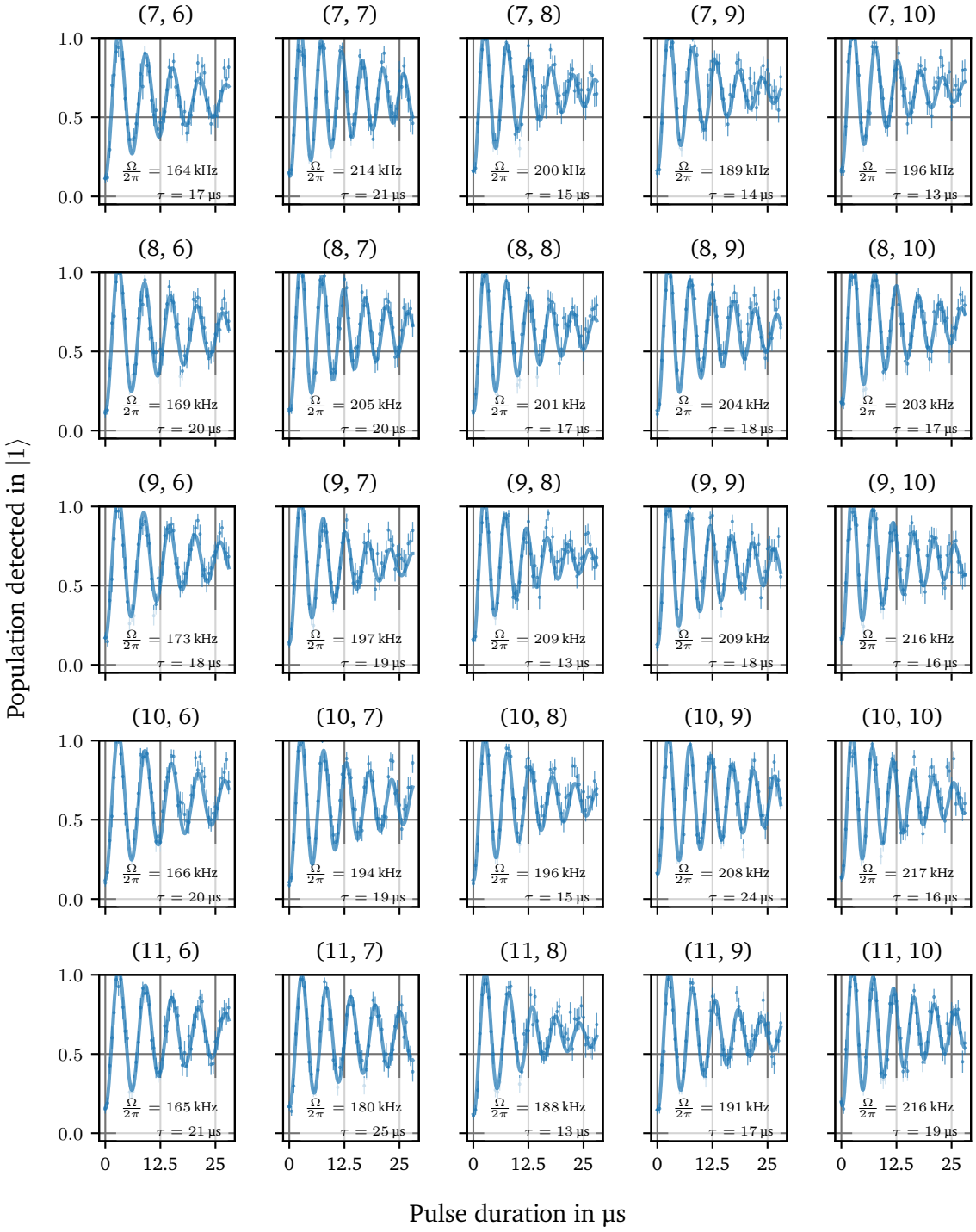

Fig. 5.2.: Site-resolved Rabi floppings driven by the light field inducing the global 1-qubit gate and a detuning of -8 GHz relative to the transition $|5^2S_{1/2}, F = 3\rangle \leftrightarrow |5^2P_{1/2}, F' = 2\rangle$. The individual traps are labeled with their vertical coordinate first and horizontal coordinate second. The curves show a mean Rabi frequency of 194 ± 4 kHz with a range of $(164 - 217)$ kHz over the array and a trend towards a population in the $|5^2S_{1/2}, F = 3\rangle$ manifold. This is evidence for a high one photon scattering rate of the light inducing the global 1-qubit gate. As a mean over all shown traps, a $1/e$ damping time of 18 ± 1 µs is calculated from a range of $(13 - 25)$ µs.

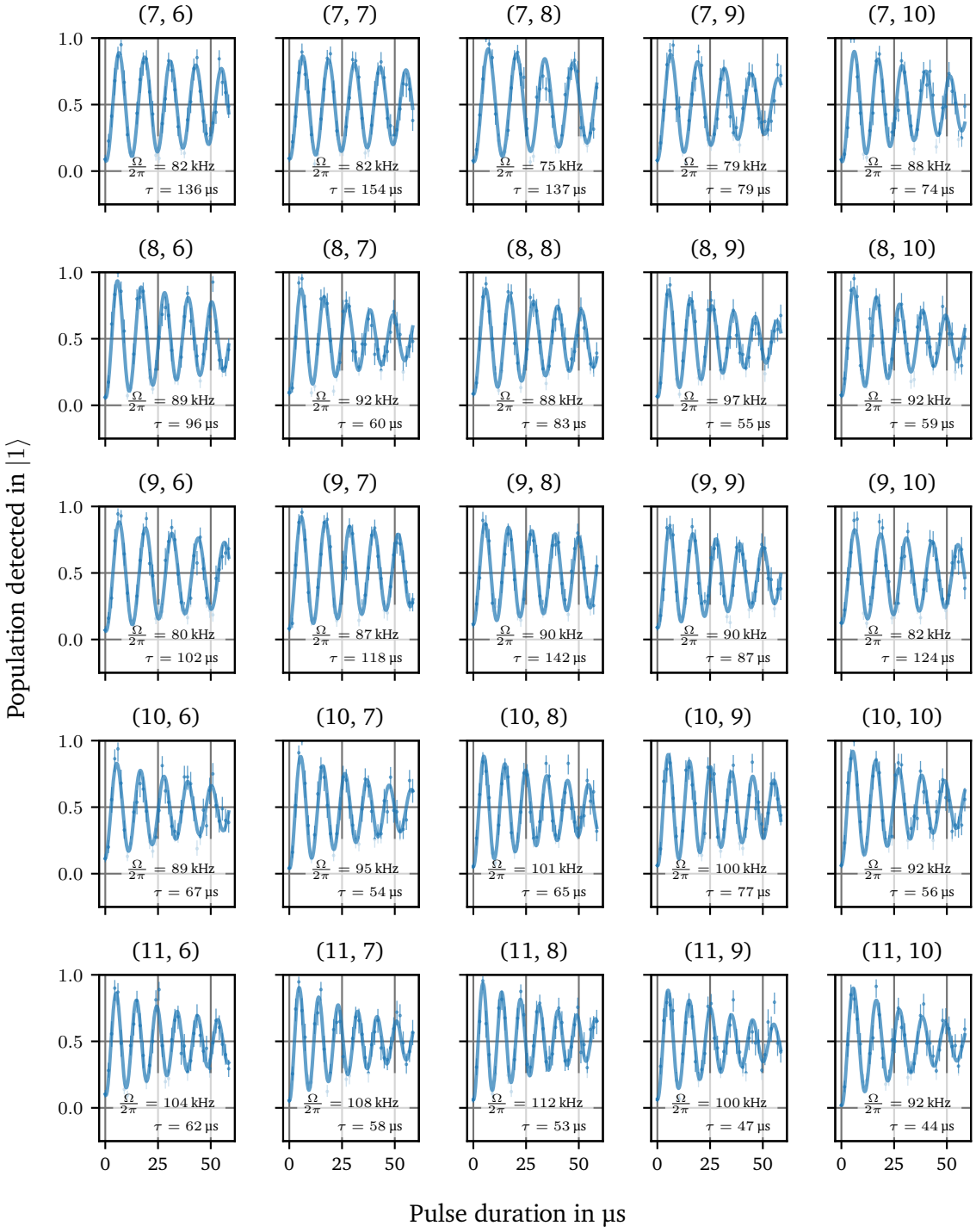

Fig. 5.3.: Site-resolved Rabi floppings driven by the light field inducing the global 1-qubit gate and a detuning of -17 GHz relative to the transition $|5^2S_{1/2}, F = 3\rangle \leftrightarrow |5^2P_{1/2}, F' = 2\rangle$. The individual traps are labeled with their vertical coordinate first and horizontal coordinate second. The curves show a mean Rabi frequency of 91 ± 2 kHz with a range of $(75 - 112)$ kHz over the array. As a mean over all shown traps, a $1/e$ damping time of 83 ± 7 µs is calculated from a range of $(43 - 153)$ µs. This data is recorded four months after the measurement shown in Fig. 5.2, with a corresponding drift of the center position of the light field inducing the global 1-qubit gate visible in a different position of the maximum Rabi frequency.

5.2.2. Local 1-qubit gate Rabi flopping

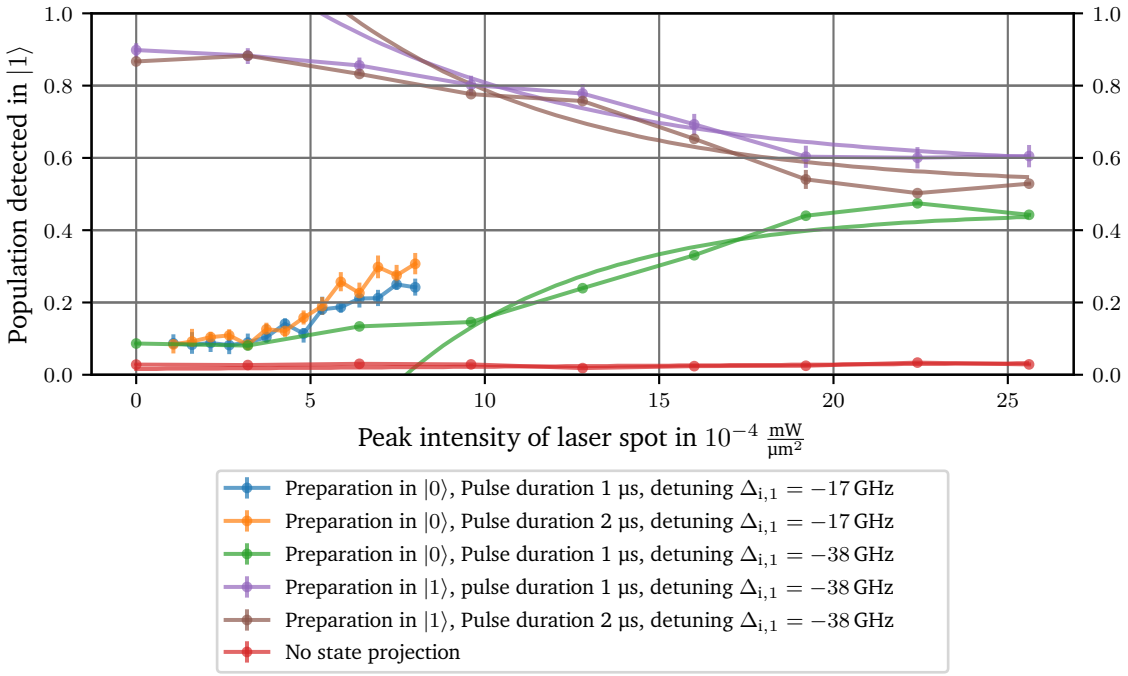

Fig. 5.4.: Depolarization driven by the high intensities of the light inducing the local 1-qubit gate for detunings $\Delta_{i,1} = -17\,\mathrm{GHz}$ and $\Delta_{i,1} = -38\,\mathrm{GHz}$ relative to the transition $|5^2\mathrm{S}_{1/2}, \mathrm{F} = 3\rangle \leftrightarrow |5^2\mathrm{P}_{1/2}, \mathrm{F}' = 2\rangle$. For the smaller detuning, the depolarization is measurable already for intensities lower than $5 \times 10^{-4}\,\mathrm{mW\,\mu m^{-2}}$ (blue). With the higher detuning, the depolarization can be sufficiently suppressed for an intensity of $8 \times 10^{-4}\,\mathrm{mW\,\mu m^{-2}}$ (green). As initial preparations in state $|0\rangle$ (blue, yellow, green) and in state $|1\rangle$ (pink, purple) both tend towards a population of $50\,\%$, depolarization of the qubit state is identified. A $1/e$ decay is fitted to values measured at intensities larger than $9 \times 10^{-4}\,\mathrm{mW\,\mu m^{-2}}$ as guide to the eye. This process does not scale directly with the pulse area as doubling the pulse length results only in a minor effect (yellow, brown). Significant loss from the traps is excluded by leaving out the state projection (red).

The local 1-qubit gate operation uses a tightly focused laser beam as described in Sec. 4.1.3. As the same optical power of $5\,\mathrm{mW}$ can be used in this system but with a spot size of $2.2(2)\,\mu\mathrm{m}$ (waist) [108], the intensity of this beam can be set four orders of magnitude larger than for the light inducing the global 1-qubit operation. In order to avoid high scattering rates and to reach a Rabi frequency of $1\,\mathrm{MHz}$, multiple ways of optical attenuation are used. Firstly, the switching AOM is driven with a very low RF-amplitude. Secondly, the respective intensity stabilization is equipped with a highly sensitive photodiode, owing a sensitivity of $0.15\,\mathrm{V\,\mu W^{-1}}$, which allows for the stabilization of a few microwatts of optical power. Thirdly, the AODs used for single-site addressing each are operated by a fraction of one tenth of their maximum efficiency only, resulting in an attenuation by a factor of 100.
As a result, Rabi frequencies of hundreds of kilohertz and above can be used with this system. But even with the used attenuation, the high intensities result in a high depolarization, as shown in Fig. 5.4. In this plot, pulse durations of $1\,\mu\mathrm{s}$ and $2\,\mu\mathrm{s}$ are tested with a peak intensity up to $26.0(3) \times 10^{-4}\,\mathrm{mW\,\mu m^{-2}}$ of the light inducing the local 1-qubit gate. In order to test non-

resonant processes stimulated by this light, a detuning of -4.5 MHz relative to the two-photon transition $|5^2S_{1/2}, F = 3, m_F = 0\rangle \leftrightarrow |5^2S_{1/2}, F = 2, m_F = 0\rangle$ is set. For a detuning of $\Delta_{i,1} = -17$ GHz to the transition to $|5^2P_{1/2}\rangle$, a significant change of the state of qubits initialized in state $|0\rangle$ towards the $|5^2S_{1/2}, F = 3\rangle$ manifold of up to $20\,\%$ can be observed (blue, yellow). In order to reduce this effect, the detuning is increased further from -17 GHz to -38 GHz (green). As shown for the respective curve, a significantly reduced change in the state of the qubits is induced for this setting, allowing to use a peak intensity of $8.0(1) \times 10^{-4}$ mW µm^{-2} for the local 1-qubit operation.
The cause for this limit is investigated by testing the behavior of atoms prepared in state $|1\rangle$ (purple, brown). A symmetric change of the state of the qubits towards a population of $50\,\%$ in state $|1\rangle$ is found, which allows to identify this effect as depolarization. Additional atom loss by heating are excluded with a measurement without state projection, showing a constant baseline loss of $2(1)\,\%$.
Using a detuning of $\Delta_{i,1} = -38$ GHz, Rabi floppings with a frequency of 1.17 ± 0.06 MHz with a range of $(0.85 - 1.36)$ MHz over the array are achieved with the local 1-qubit gate as shown in Fig. 5.5. For this measurement, the individual traps are addressed consecutively in one experimental sequence, probing the traps from left to right, line-by-line starting from the top left corner. The mean $1/e$ damping time is determined to 1.8 ± 0.2 µs with a range of $(1.08 - 3.0)$ µs. As the intensity measured for this system is the summed intensity for both light fields involved in the two-photon process, the Rabi frequency scales linear with this intensity (see (3.7)) and the scattering also scales linear with this intensity (see (3.6)). With intensities that are different by factor of 47, the same ratio is expected between Rabi frequencies and damping of the global and the local 1-qubit operation for equal detuning $\Delta_{i,1}$. For the local system, a Rabi frequency of up to $2.1(5)$ MHz and a $1/e$ damping time of $7(3)$ µs would be expected. This is evidence for additional sources of errors in this system that need further investigation. For the single-site addressing, errors in the position between positions of the atom the beam are likely regarding mechanical and thermal drifts but also the thermal motion of the atoms in the trap. Also the beam profile itself can be source of significantly lower damping times as discussed in [129].
The larger detuning also holds for the light inducing the global 1-qubit gate. The result is shown in Fig. 5.6 and an overview of the measured Rabi frequencies and damping times is given in Tab. 5.2. For the global system, the Rabi frequency decreases to 45 ± 1 kHz with a range of $(37 - 56)$ kHz over the array and $1/e$ damping times with a mean of 156 ± 87 µs with a range of $(53 - 318)$ µs. Comparing the $1/e$ damping time for the global 1-qubit operations shown for a detuning of -17 GHz with the result for -38 GHz, the quadratic scaling with the inverse of the detuning also does not fit to the results. From a damping time of 83 ± 7 µs for -17 GHz, an increase by a factor of four is expected for the higher detuning of -38 GHz. But only a factor of two is observed. Especially, the extremely long pulses of up to 100 µs could reach limits of the used sample and hold technique for the intensity stabilization [90] and probes a large range of control bandwidth of the optical phase-locked loop. Imperfections in each of the two systems could explain the shorter damping times. Though it is not a limit for the experiments shown here, this should be further investigated. Due to the low Rabi frequencies for the global 1-qubit operation, the detuning of the light inducing the 1-qubit gate is not increased further though a further suppressed depolarization would be preferred.

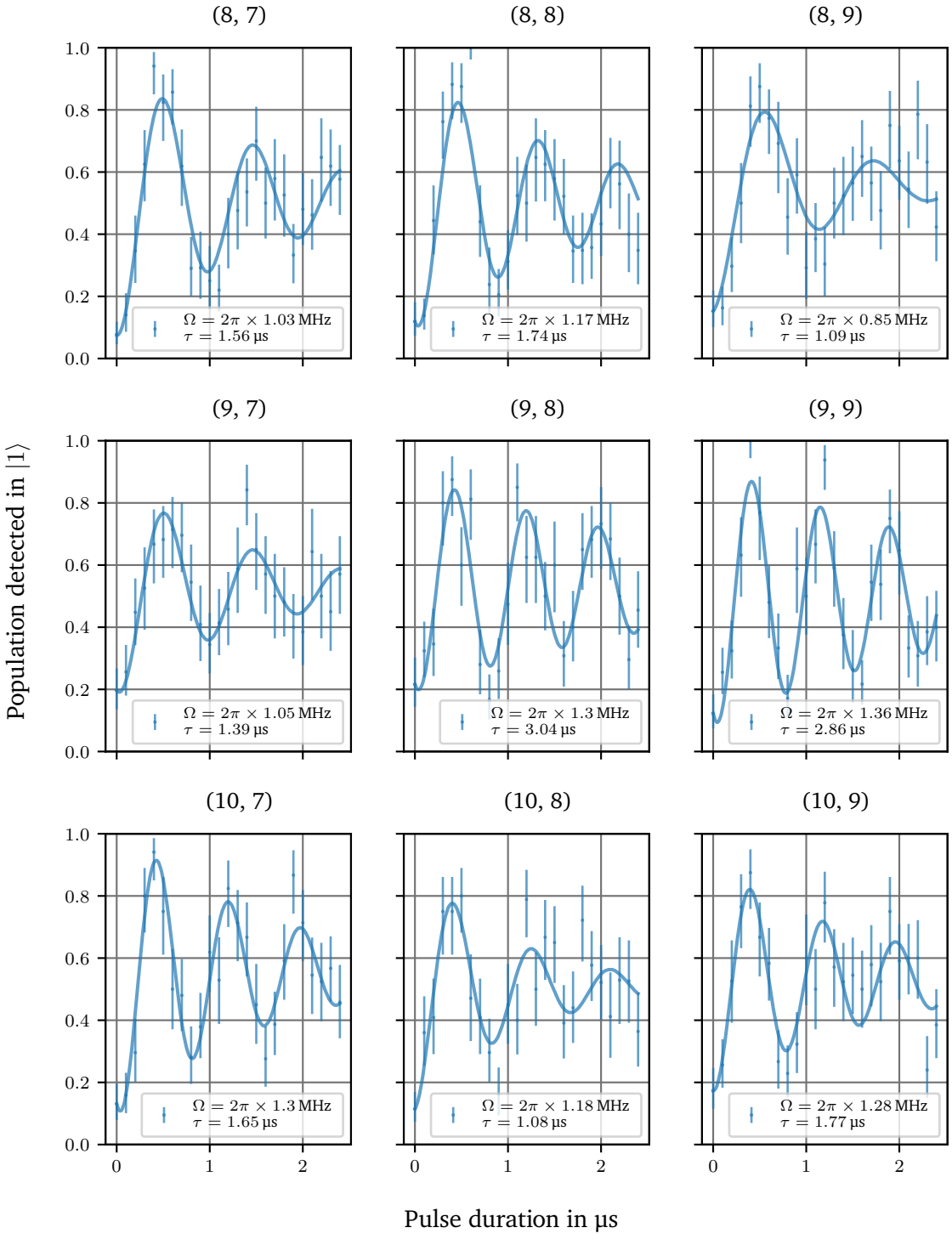

Fig. 5.5.: Site-resolved Rabi floppings driven by the light field inducing the local 1-qubit gate with a detuning of $\Delta_{i,1} = -38\,\mathrm{GHz}$ relative to the transition $|5^2S_{1/2}, F = 3\rangle \leftrightarrow |5^2P_{1/2}, F' = 2\rangle$. The individual traps are labeled with their vertical coordinate first and horizontal coordinate second. All curves show similar Rabi frequencies with a mean of $1.17 \pm 0.06\,\mathrm{MHz}$ with a range of $(0.85 - 1.36)\,\mathrm{MHz}$ over the array. As a mean over all shown traps, a $1/e$ damping time of $1.8 \pm 0.2\,\mu\mathrm{s}$ with a range of $(1.08 - 3.0)\,\mu\mathrm{s}$ is calculated.

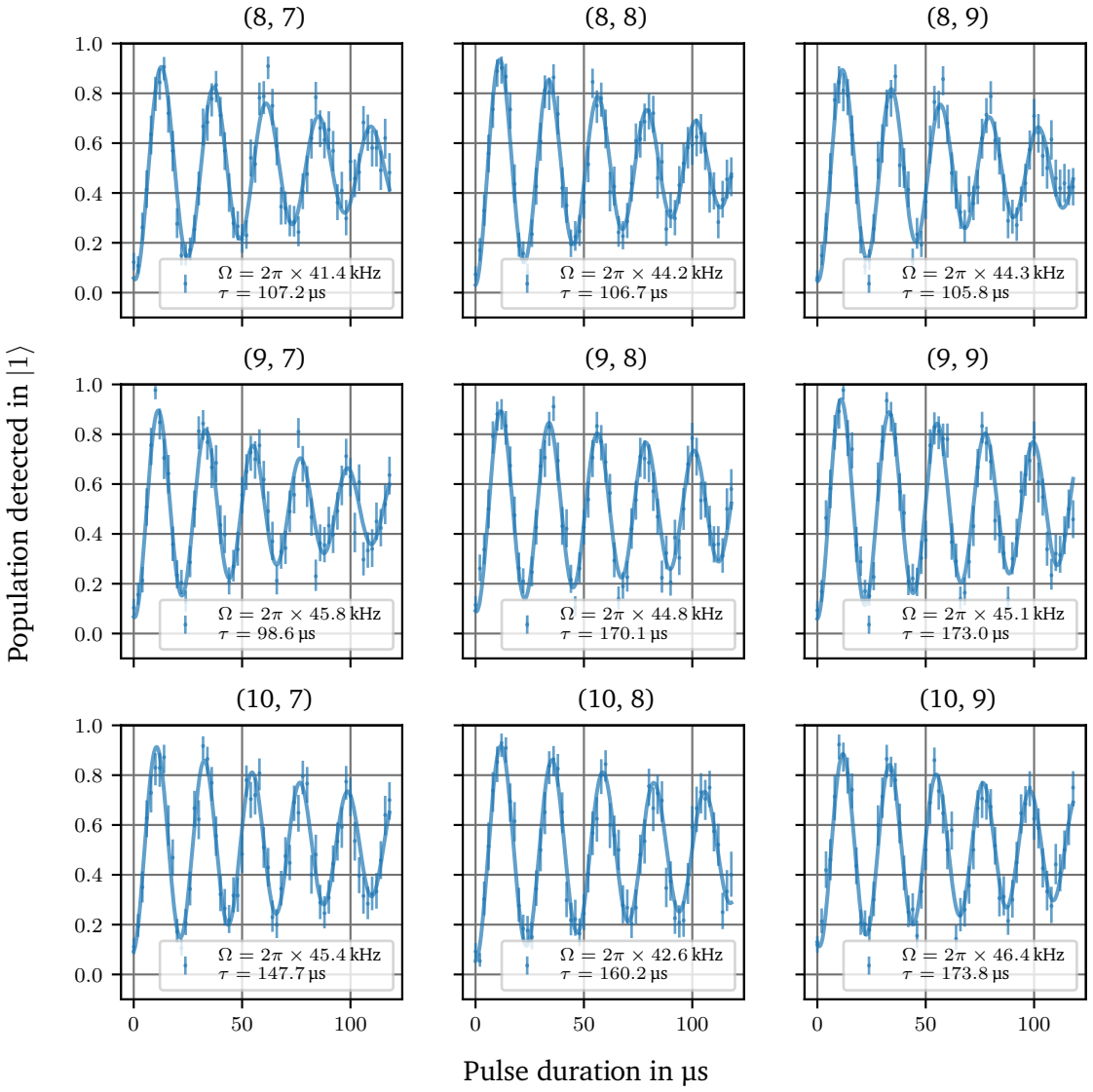

Fig. 5.6.: Site-resolved Rabi floppings driven by the light field inducing the global 1-qubit gate with a detuning of $\Delta_{i,1} = -38\,\mathrm{GHz}$ relative to the transition $|5^2S_{1/2}, F = 3\rangle \leftrightarrow |5^2P_{1/2}, F' = 2\rangle$. The individual traps are labeled with their vertical coordinate first and horizontal coordinate second. All curves show similar Rabi frequencies with am mean of $45 \pm 1\,\mathrm{kHz}$ with a range of $(37 - 56)\,\mathrm{kHz}$ over the array. As a mean over all shown traps, a $1/e$ damping time of $156 \pm 87\,\mu\mathrm{s}$ with a range of $(53 - 318)\,\mu\mathrm{s}$ is calculated.

Tab. 5.2.: Overview of the parameters of Raman Rabi floppings shown in Figs. 5.2, 5.3, 5.5, and 5.6.

Detuning in GHz	Intensity in $10^{-4}\,\mathrm{mW\,\mu m^{-2}}$	Effective Rabi frequency in kHz	$1/e$ damping time in µs
-38	8	1170 ± 60	1.8 ± 0.2
-38	0.17	45 ± 1	156 ± 87
-17	0.17	91 ± 2	83 ± 7
-8	0.17	194 ± 4	18 ± 1

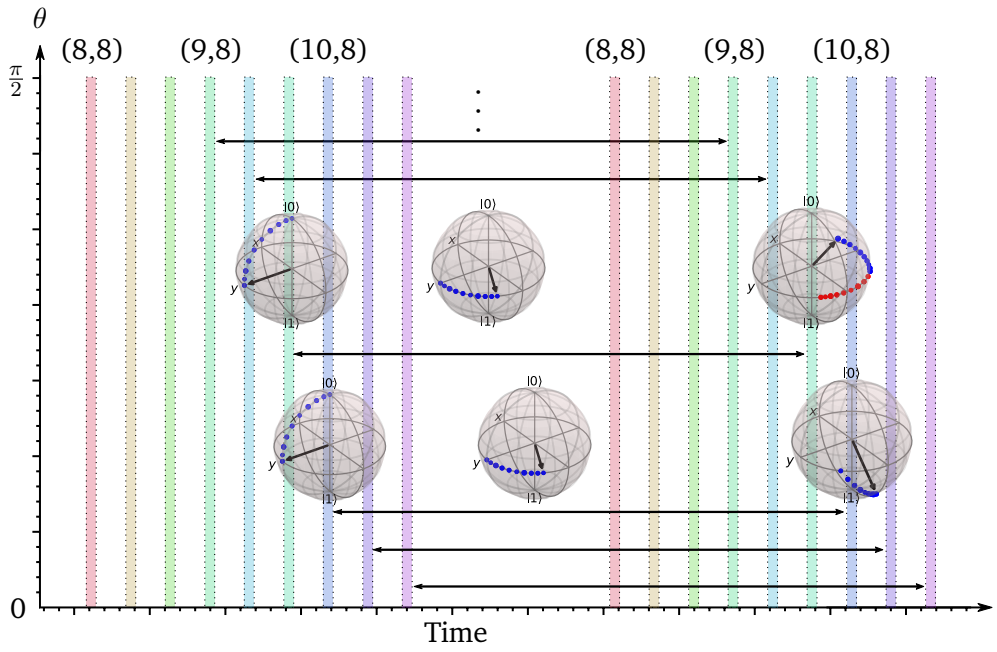

Fig. 5.7.: Pulse sequence for the demonstration of a virtual-Z rotation. For an array of 3 x 3 qubits, local $\hat{R}(\theta, \phi)$ gates are performed. The first group of nine operations forms a Ramsey experiment together with the second group. In each group, the trap sites are addressed from left to right and line-by-line, indicated by the color of the operations and the trap indices showing the addressing of the respective next line of traps. A variable phase shift by the angle ϕ for the sixth pulse of the second group demonstrates the virtual-Z rotation. A representation on the Bloch sphere is drawn with an exemplary phase shift as red trace together with a representation without the phase shift for the next pulse.

In the formulation of the CNOT gate on neutral atoms, the Hadamard gate is used, as described in Sec. 3.1.6. This gate describes rotations around the **z**- and the **x**-axis of the Bloch sphere [67]. Whereas a rotation around the **x**-axis corresponds to the Rabi floppings shown in the previous sections, the rotation around the **z**-axis can only be demonstrated with a Ramsey-type experiment.
Such Ramsey experiments are performed with the local 1-qubit gate with the sequence shown in Fig. 5.7. The experiment starts with a defect-free 5 x 5 array of individual atoms prepared in the state $|0\rangle = |5^2\mathrm{S}_{1/2}, \mathrm{F} = 2, m_\mathrm{F} = 0\rangle$. With a first series of 9 individual $\pi/2$-pulses, the atoms of the inner 3 x 3 sites are prepared in superposition states $1/\sqrt{(2)}(|0\rangle + |1\rangle)$, corresponding to a $\hat{R}(\pi/2, 0)$ gate (see Sec. 3.1.6). Between each atom addressed, a wait time of $20\,\mu\mathrm{s}$ is used, allowing for an adaption of phase and frequency of the beat note between the two ECDLs for each atom. In total, the preparation of the 3 x 3 atoms needs approximately $220\,\mu\mathrm{s}$ in this configuration. After an extra time of free evolution, a second sequence of $\pi/2$-pulses is performed. In this second sequence, the phase of the beat note is shifted by the angle ϕ for the sixth pulse via the analog phase modulation input of the synthesizer in Fig. 4.1. This corresponds to the application of a $\hat{R}(0, \phi)$ gate for the atom in trap (9,10) followed by a

$\hat{R}(\pi/2, 0)$ gate for all atoms.
This sequence allows for two experiments. The first experiment uses a fixed time of free evolution of $10\,\mu s$ between both of two pulse sequences. The measured phase evolution is therefore expected to be constant, but can assume different values for the individual traps. Only for the one atom that receives the phase-shifted pulse, an evolution corresponding to the phase shift performed on the synthesizer is expected. This result is shown in Fig. 5.8. A phase shift in the range of $\phi \in [0, 4\pi)$ in the reference frequency is performed. As can be seen in the measured phase evolution, this phase shift performs an $\hat{R}(0, \phi)$ gate on this qubit.
The second experiment varies the time of free evolution, corresponding to an evolution of the phases of the superposition states according to the effective detuning. In this experiment, the quadratic Zeeman effect is not compensated, resulting in a phase evolution with an expected frequency of $63.4\,kHz$, see Sec. 3.2. Again, trap (9,10) is addressed with a phase shift of $1/2\,\pi, 1\,\pi, 2\,\pi,$ and $3\,\pi$ in the reference frequency. The result is shown in Fig. 5.9. The measured phase evolutions demonstrate a corresponding offset in the phase evolution of trap (9,10). In all other traps, the phase evolutions are not affected.

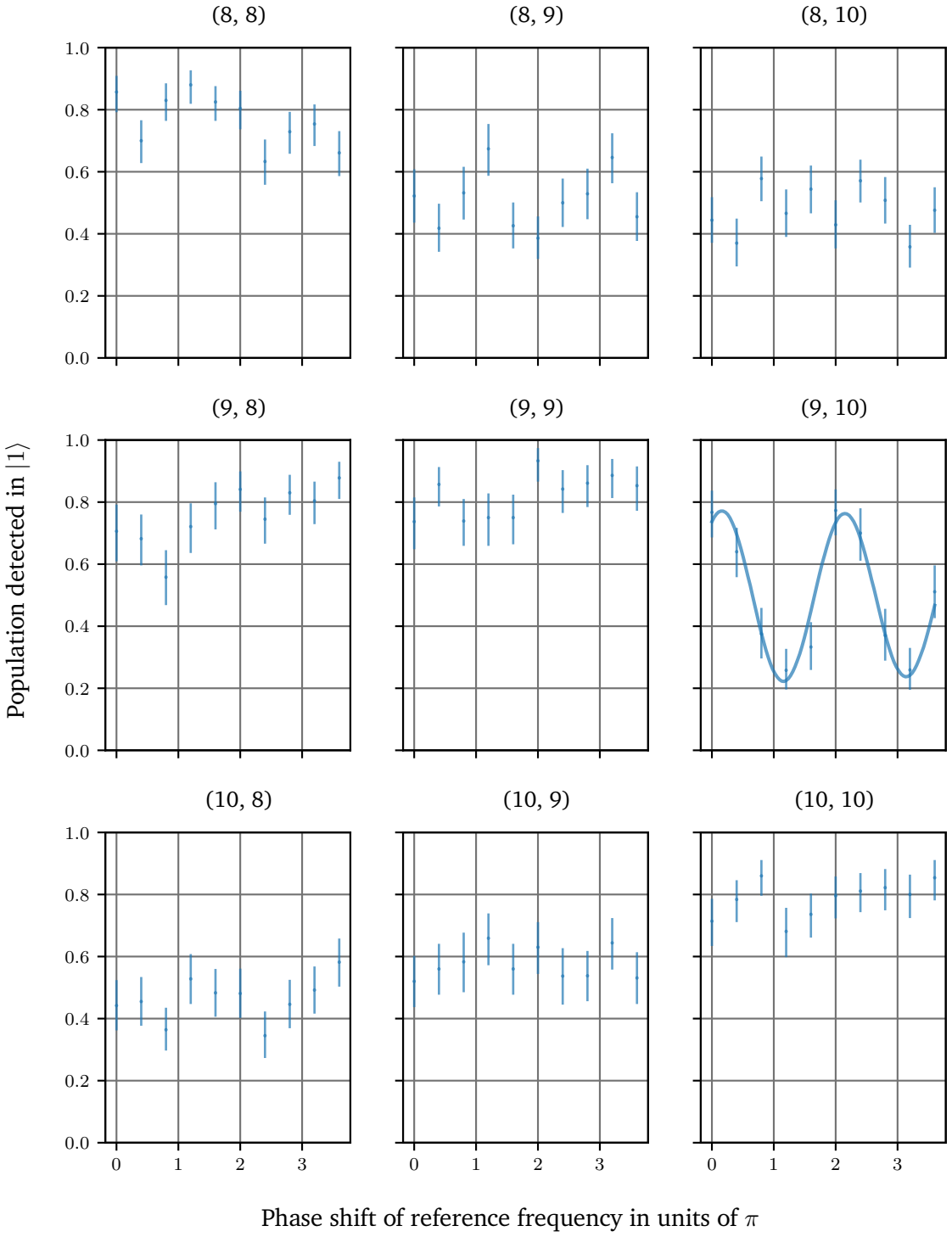

Fig. 5.8.: Virtual-Z rotations induced with a phase modulation of the reference frequency of the optical phase-locked loop described in Sec. 4.1.1. The individual traps are labeled with their vertical coordinate first and horizontal coordinate second. For trap (9,10), the phase shift is applied in the reference frequency. A corresponding Ramsey oscillation is measured whereas all other traps do not show a change in the measured phase.

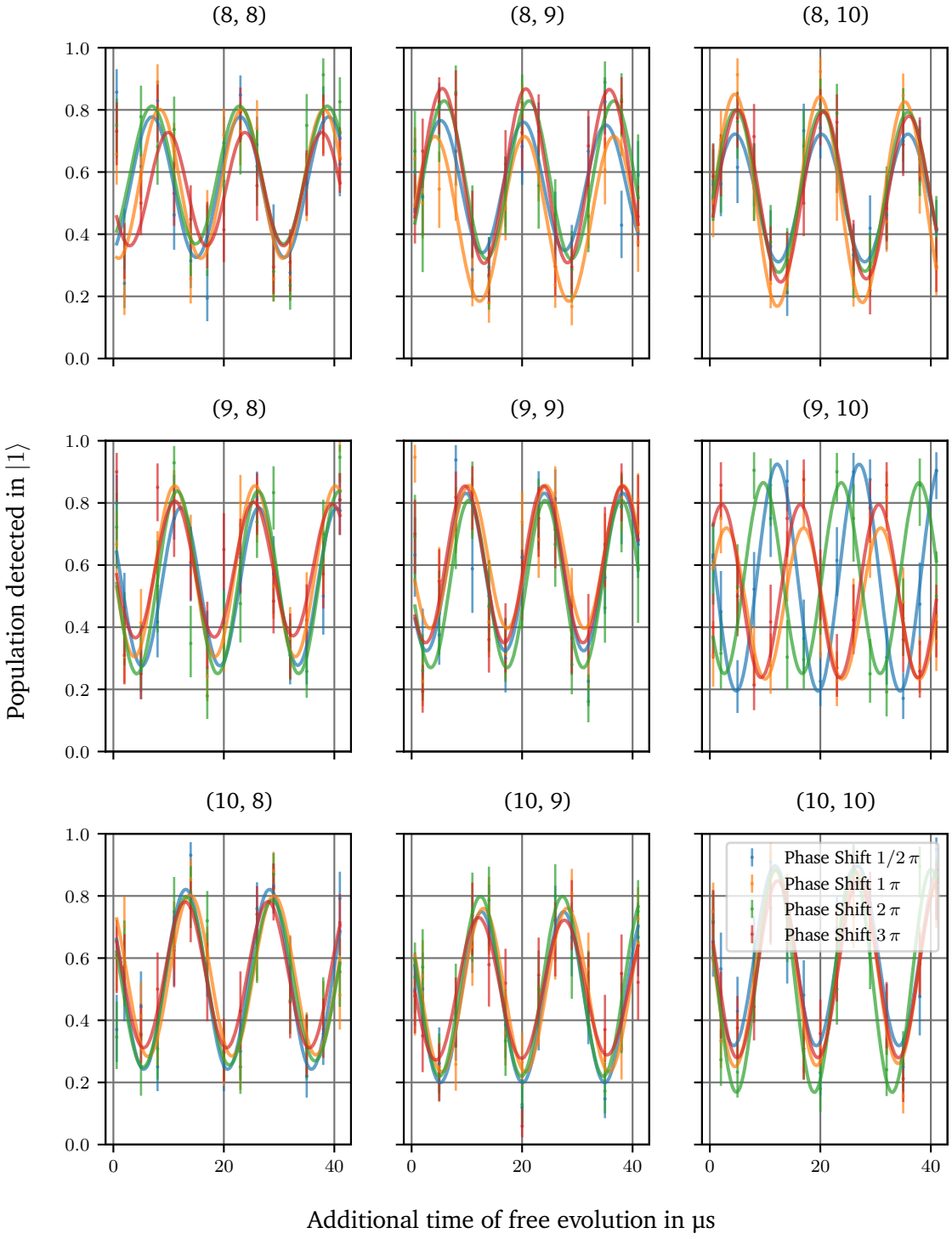

Fig. 5.9.: Ramsey oscillations demonstrating a virtual-Z rotation in trap (9,10). The individual traps are labeled with their vertical coordinate first and horizontal coordinate second. For trap (9,10), a phase shift is applied in the reference frequency. A corresponding phase shift in the Ramsey oscillation of this trap is measured whereas all other traps do not show a change in the measured oscillation.

5.3. Single-site-addressed Rydberg excitation

The excitation of individual atoms to a Rydberg state is the most promising technique for a coherent interaction between qubits stored in neutral atoms (see Sec. 2.5). This operation sets high requirements to the optical system, as the excitation to high principal quantum numbers requires high photon energies in the region of $5\,\mathrm{eV}$ and extremely narrow laser lines in the region of single kilohertz. Both requirements are still complex to maintain as discussed in the previous chapter but in general state-of-the-art. In contrast, the properties and the handling of Rydberg atoms is a field of active research.
The first section of this chapter lists known properties of some accessible Rydberg states. Then, the influence of the trapping light on the Rydberg atom is shown, resulting in limits for the trapping light. Next, a stable operation for experiments with Rydberg atoms is discussed, which gives an estimation for electric fields that need to be avoided due to the high polarizability of the Rydberg atoms. Furthermore, the interaction of the Rydberg light with the atoms is discussed regarding the two-photon and on-resonance Rabi frequencies. Finally, the differential light shift acting on the qubit basis states during the Rydberg excitation is quantified.

5.3.1. Properties of the Rydberg state

In this project, the Rydberg state $|82\mathrm{S}_{1/2}, \mathrm{J} = 1/2, m_\mathrm{J} = -1/2\rangle$ is used. This state is chosen due to a good match of its expected properties to the experimental parameters. For the optical powers of the Rydberg light fields, a Rabi frequency of $1\,\mathrm{MHz}$ is expected [61], and from the interaction strength, a blockade of next neighbors and diagonal neighbors of atoms in the array is expected. This is promising for the demonstration of a Rydberg blockade and a CNOT operation based on it. For the experiments shown here, the resonance frequency for the transition from the state $|5^2\mathrm{P}_{3/2}\rangle$, the polarizability, the C_6 coefficient, and the lifetime of the Rydberg state are relevant quantities. Calculations for some Rydberg states accessible in this experiment are shown in Tab. 5.3. For a direct application of the given resonance frequencies in this experiment, the resonance frequency for the transition from the intermediate state $|5^2\mathrm{P}_{3/2}\rangle$ to the respective Rydberg state is given as the frequency of the fundamental light at a wavelength of $960\,\mathrm{nm}$ of the blue Rydberg laser. Together with a precise wavemeter, this allows comfortably to identify the Rydberg states by their resonance frequency. As described in Sec. 4.2.2, the wavelength of the fundamental light is measured with a wavemeter with an accuracy of $10\,\mathrm{MHz}$.
In a resonant process with atoms in dipole traps and pulses of the blue Rydberg light together with the cooling light, a resonance at $312.63263(5)\,\mathrm{THz}$ was found and assigned to the state $|82\mathrm{S}_{1/2}\rangle$. Compensated for the involved switching AOM and AODs, this is a discrepancy to the calculated resonance frequency of $100(10)\,\mathrm{MHz}$ (in the blue light), but still allows a discrimination against the other Rydberg states which should be separated by more than $13\,\mathrm{GHz}$ (in the blue light).
For the two-photon process used for the gate sequence, a frequency of the fundamental light of the blue Rydberg laser in the vicinity of $312.632323(2)\,\mathrm{THz}$ is used with minor changes due to optimizations of the frequency of the red Rydberg light. A direct measurement of the detuning of the two-photon process is not concluded from this, as the measurement of the resonant excitation from the $|5^2\mathrm{P}_{3/2}\rangle$ state to $|82\mathrm{S}_{1/2}\rangle$ includes light shifts of the intermediate state of several tens of megahertz. The detuning of the two-photon process is deduced from the properties of the red Rydberg light.

Tab. 5.3.: Parameters of Rydberg states accessible in Quips-B, calculated with the ARC library [15].

State	Resonance frequency from $5^2P_{3/2}$ for the fundamental light at 960 nm in THz	Polarizability in units of $h \times \mathrm{Hz\,m^2\,V^{-2}}$	C_6/h interaction strength in GHz µm^6	Lifetime in µs (excluding black-body loss)
$57S_{1/2}$	312.3303231	125.68	−75.11	195.7
$58S_{1/2}$	312.3507968	141.84	−92.54	206.8
$59S_{1/2}$	312.3701811	159.75	−113.57	218.4
$60S_{1/2}$	312.3885518	179.54	−138.88	230.3
$61S_{1/2}$	312.4059784	201.4	−169.21	242.7
$62S_{1/2}$	312.4225245	225.48	−205.47	255.5
$63S_{1/2}$	312.4382484	251.99	−248.66	268.7
$64S_{1/2}$	312.4532037	281.11	−299.96	282.4
$65S_{1/2}$	312.4674397	313.06	−360.7	296.6
$66S_{1/2}$	312.4810018	348.06	−431.36	311.2
$67S_{1/2}$	312.4939319	386.35	−504.27	326.3
$68S_{1/2}$	312.5062686	428.19	−605.56	341.9
$69S_{1/2}$	312.5180477	473.83	−727.25	358.0
$70S_{1/2}$	312.5293024	523.57	−862.69	374.6
$71S_{1/2}$	312.5400631	577.7	−1020.3	391.6
$72S_{1/2}$	312.5503586	636.54	−1203.7	409.2
$73S_{1/2}$	312.5602152	700.44	−1416.61	427.3
$74S_{1/2}$	312.5696574	769.73	−1663.26	445.9
$75S_{1/2}$	312.5787083	844.8	−1948.38	465.1
$76S_{1/2}$	312.5873891	926.05	−2277.3	484.8
$77S_{1/2}$	312.5957198	1013.88	−2655.99	505.1
$78S_{1/2}$	312.6037188	1108.74	−3091.14	525.9
$79S_{1/2}$	312.6114037	1211.08	−3590.22	547.2
$80S_{1/2}$	312.6187906	1321.39	−4161.55	569.2
$81S_{1/2}$	312.6258948	1440.18	−4814.46	591.7
$82S_{1/2}$	312.6327304	1567.98	−5558.98	614.8
$83S_{1/2}$	312.6393109	1705.36	−6404.95	638.5
$84S_{1/2}$	312.6456487	1852.91	−7368.93	662.8
$85S_{1/2}$	312.6517558	2011.23	−8465.5	687.8
$86S_{1/2}$	312.6576431	2180.98	−9706.62	713.3
$87S_{1/2}$	312.6633211	2362.84	−11110.38	739.5
$88S_{1/2}$	312.6687995	2557.51	−12696.41	766.3
$89S_{1/2}$	312.6740877	2765.74	−14485.81	793.7
$90S_{1/2}$	312.6791943	2988.22	−16500.92	821.8
$91S_{1/2}$	312.6841275	3226.01	−18769.76	850.5
$92S_{1/2}$	312.6888951	3479.71	−21317.87	879.9
$93S_{1/2}$	312.6935045	3750.28	−24176.86	910.0
$94S_{1/2}$	312.6979626	4038.65	−27380.24	940.7
$95S_{1/2}$	312.7022758	4345.78	−30964.32	972.2
$96S_{1/2}$	312.7064505	4672.67	−34971.46	1004.3
$97S_{1/2}$	312.7104924	5020.38	−39445.47	1037.1
$98S_{1/2}$	312.7144072	5389.99	−44434.73	1070.7

5.3.2. Influence of the trapping light on the Rydberg excitation

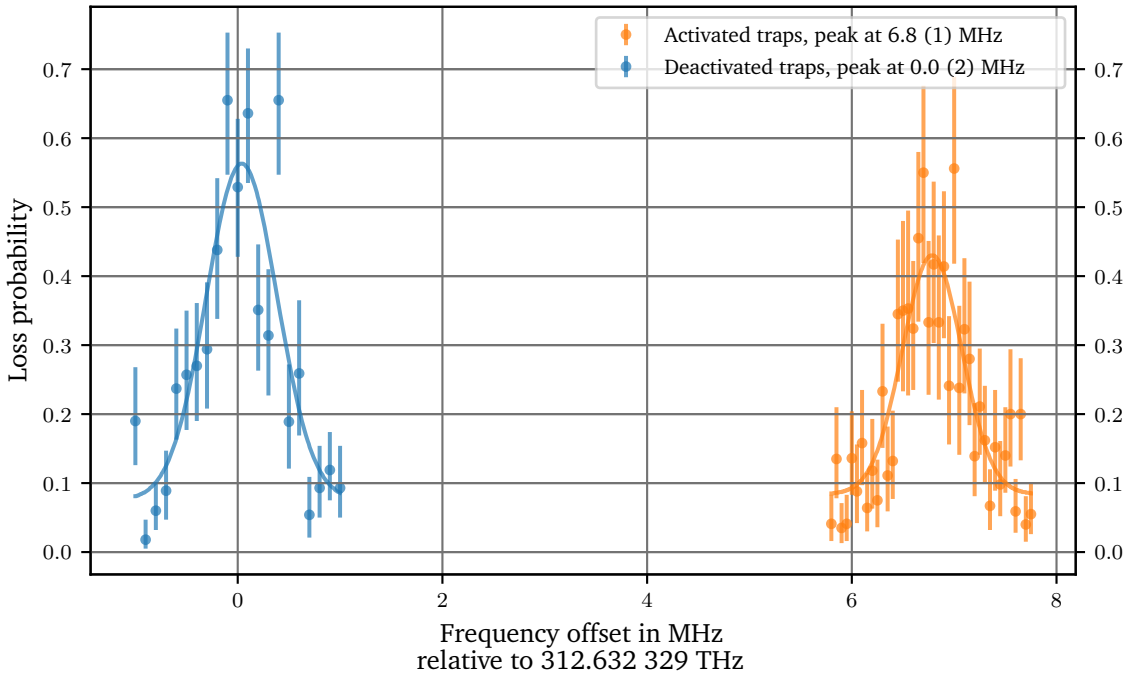

Fig. 5.10.: Test of the Rydberg resonance frequency with activated trapping light (yellow) for shallow traps of $-0.7\,\mathrm{mK}$ and an expected absolute light shift for the ground state of $-14.8\,\mathrm{MHz}$, see Fig. 3.10. In comparison, the position of the Rydberg resonance with deactivated traps is shown (blue). The measured detuning of $6.8(1)\,\mathrm{MHz}$ in the fundamental light needed with shallow traps corresponds to a detuning of the blue Rydberg light of $13.8(2)\,\mathrm{MHz}$.

The transition $|5^2\mathrm{S}_{1/2}, \mathrm{F}=3, m_\mathrm{F}=0\rangle \leftrightarrow |82\mathrm{S}_{1/2}, \mathrm{J}=1/2, m_\mathrm{J}=-1/2\rangle$ is sensitive to the absolute light shifts acting on the initial and the final states. As the trapping light creates an absolute light shift for the ground state manifold, this light affects the Rydberg excitation. A measurement of the absolute light shift induced by the trapping light is shown in Fig. 5.10. As a reference, the measured Rydberg resonance with deactivated traps is used. The two resonances show a difference in the frequency of the fundamental light of the blue Rydberg laser of $6.8(1)\,\mathrm{MHz}$. Due to the SHG that creates the blue Rydberg light, this detuning of the fundamental light takes effect with a factor of two in the blue Rydberg light, such that the resonance is shifted by $13.8(2)\,\mathrm{MHz}$.
The absolute light shift for the ground state $|5^2\mathrm{S}_{1/2}, \mathrm{F}=3, m_\mathrm{F}=0\rangle$ is calculated to $-14.8\,\mathrm{MHz}$, as shown in Fig. 3.10. This calculated light shift is larger than the measured light shift with a difference of $1.0(1)\,\mathrm{MHz}$. Previous work on this topic showed larger discrepancies of more than a factor of two [130]. The discrepancy can be explained by a lower transmittance of the trapping light on the path to the atoms, as it is subject to many surfaces and apertures which can sum up to an error of several percent. Furthermore, due to the motion of the atoms in the trap, the transition frequency becomes dependent of the position and the temperature of the atom in the trap. This leads to an effective light shift for the ground state that is smaller than the light shift in the center of the trap which is used for the calculations. Because of the statistical nature of thermal motion, a broadening of the resonance is expected. However, in

this measurement, the broadening by the Fourier components of the short pulses dominates this effect in the frequency scan.
The latter effect also affects the ground-to-Rydberg state Rabi oscillation that is needed for coherent operations. Such a Rabi oscillation with activated traps is shown in Fig. 5.11. A strong damping of the oscillation, with an $1/e$ damping time shorter than a 2π pulse, is found which is expected to be due to the different light shifts sampled in the light field of the trap.
For the experiments including excitations to the Rydberg state, this measurement provides evidence that the trapping light has to be deactivated during the Rydberg excitation. As described in [39], switching off the trapping light is possible for up to $10\,\mu s$ with nearly perfect recapture rates. This time therefore marks the maximum time that can be used for a coherent interaction with a Rydberg state. The lifetime of the Rydberg state is $614\,\mu s$ and therefore not limiting this sequence.

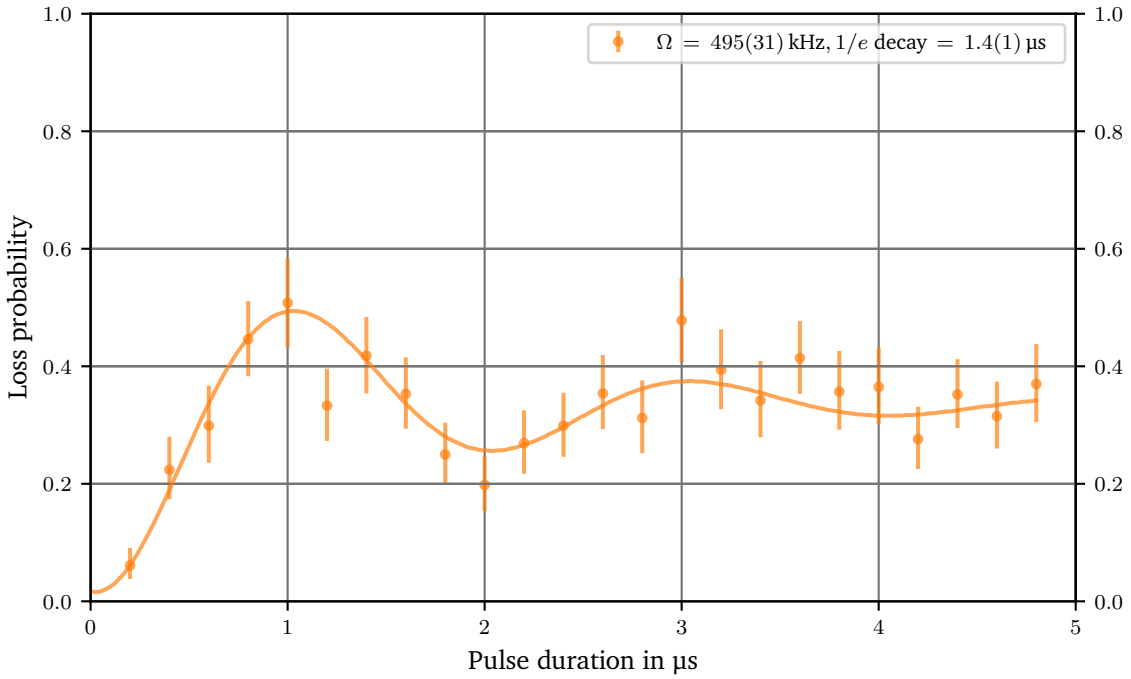

Fig. 5.11.: A ground-Rydberg Rabi flopping with activated trapping light. The strong damping is likely due to the thermal motion of the atom in the trap.

5.3.3. Stability of the Rydberg transition frequency

One of the achievements during this project is a better understanding of effects disturbing the stability of the Rydberg excitation. A reliable situation for Rydberg experiments is achieved by a frequent curing of the vacuum chamber in each run of the experiment with the blue Rydberg light and light of UV LEDs.
The evidence for a shift of the resonance frequency of the Rydberg transition induced by light pulses at these short wavelengths is shown in Fig. 5.12. In this experiment, the shift of the Rydberg resonance is tested with variable pulse durations of the blue Rydberg light. As the excitation to the Rydberg state should happen within a time of $1\,ms$ after the state preparation to avoid depolarization, an additional time slot for a pulse of the blue Rydberg light is

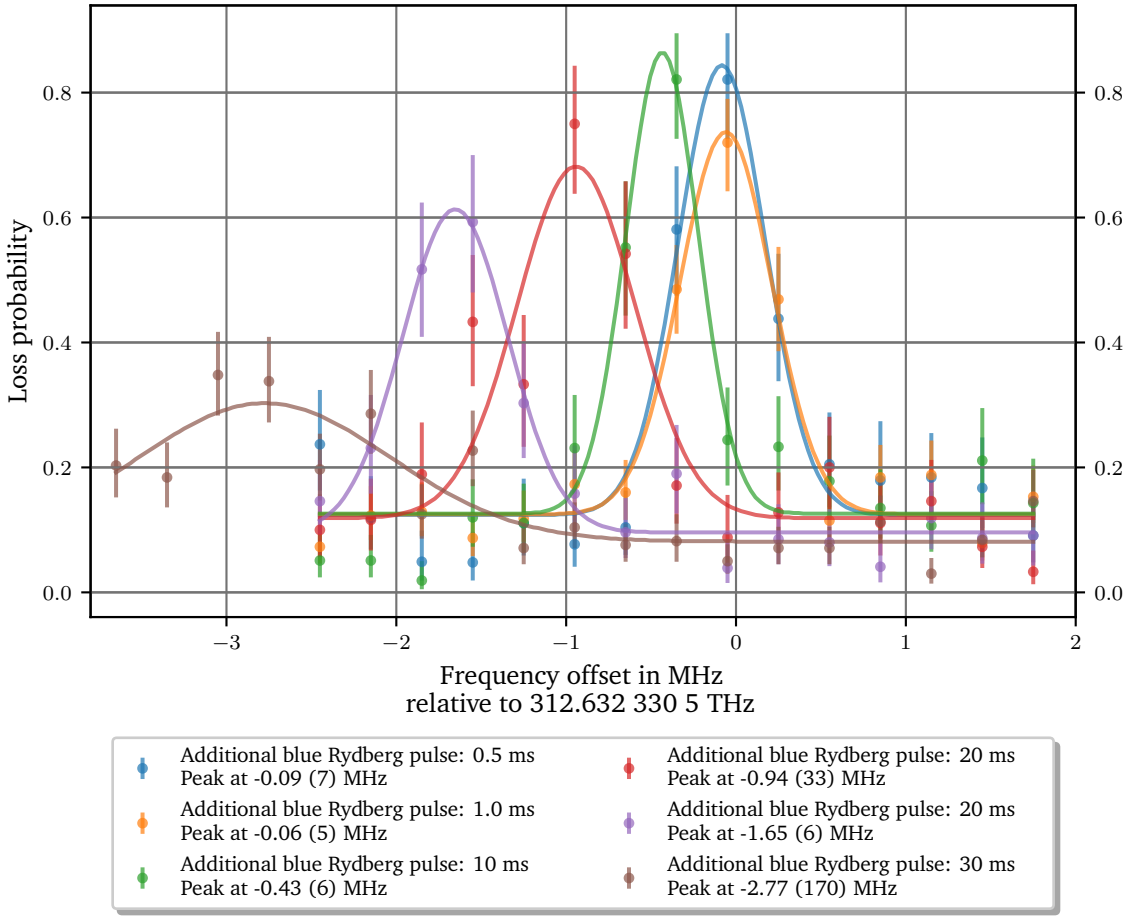

Fig. 5.12.: Shift of the Rydberg resonance in dependence of different durations of irradiation of the blue Rydberg light. A frequency offset of 1.47 MHz in comparison to Fig. 5.10 is due to a change in the frequency of the red Rydberg light.

introduced at the beginning of the experiment. Pulse durations on the order of milliseconds are tested regarding their effect on the position of the resonance.
The result of the measurement is a shift of the position of the Rydberg resonance which becomes significant from a pulse duration of 10 ms up with an intensity inside the chamber of $1.2\,\mathrm{mW\,\mu m^{-2}}$. The curves are sampled consecutively from short durations to long durations. The measurement for a pulse time of 20 ms is recorded twice and shows a temporal component as the second test of the resonance shows a larger shift of the resonance than the first. A measurement time of 20 min is needed for each of these two curves. Furthermore, the resonance broadens and looses amplitude for longer pulse durations than 20 ms, which is interpreted as a sign of processes on timescales that cannot be resolved with the averaging over the multiple realizations shown here. After this measurement, the Rydberg resonance could not be resolved over a period of more than 1 h.
A loss of the Rydberg resonance is also observed for the irradiation of the science chamber with UV light emitted by LEDs. Due to the strong reaction on light of short wavelengths that does not necessarily meet the resonance frequency of a transition, this effect is understood as light induced atomic desorption (LIAD). LIAD explains the accumulating and decaying effect and scales extremely with shorter wavelengths [131]. Also other groups have observed shifts

in the position of the Rydberg resonance that are explained by LIAD [132].
With the polarizability $\alpha = h \times 1567.98\,\mathrm{Hz\,m^2\,V^{-2}}$ of the state $82S_{1/2}$ (see Tab. 5.3), the energy shift of $\Delta E \geq 3.3\,\mathrm{MHz}$ would be explained by an electric field strength of

$$|\mathbf{E}| = \sqrt{\frac{4\Delta E}{\alpha}} \geq 0.91\,\frac{\mathrm{V}}{\mathrm{cm}}. \tag{5.1}$$

Assuming the inner sides of the windows of the science chamber as a plate capacitor with plate separation of $6.5\,\mathrm{cm}$, this would require a voltage between the windows of more than $5.9\,\mathrm{V}$.
For the transitions in the $n = 5$ manifold, an electric field of this strength would induce a level shift following the polarizability of $h \times 0.0794(16)\,\mathrm{Hz\,cm^2\,V^{-2}}$ of the ground state and a shift in the transition frequency of $h \times 0.122306(16)\,\mathrm{Hz\,cm^2\,V^{-2}}$ for the D1 transition [43]. The induced shifts on the optical transitions are not resolvable due to the line width of $5.7500(56)\,\mathrm{MHz}$.
As the LIAD can only happen if Rubidium atoms are attached to the surface of the windows, it is tried to completely desorb the population of atoms. As a consequence, the blue Rydberg light is irradiated for $100\,\mathrm{ms}$ at the beginning of each experimental run. Additionally, UV LEDs are installed near the windows of the science chamber and illuminate them during the loading of the MOT. As a result, the shown shifts of the Rydberg resonance settled after a few weeks of operation to a stable situation at the position of the resonance shown for $1\,\mathrm{ms}$.

5.3.4. Single-site addressed Rydberg excitation

With an experimental sequence using deactivated traps and the frequent curing of the vacuum windows with light of short wavelengths in each experimental cycle, the Rydberg excitation can be demonstrated reliably with single-site addressing. The results are shown in Fig. 5.13. Using the steering of the blue Rydberg light with the AOD system described in Sec. 4.2.4, individual traps are addressed in consecutive runs of the experiment. The excitation to the Rydberg state is detected by a reduced recapture probability after reactivating the trapping light.
Intensities of $1.2\,\mathrm{mW\,\mu m^{-2}}$ of the blue Rydberg light and of $4 \times 10^{-6}\,\mathrm{mW\,\mu m^{-2}}$ of the red Rydberg light achieve Rabi oscillations with a Rabi frequency of $1.0(1)\,\mathrm{MHz}$. The detuning of the red Rydberg light to the transition $|5^2S_{1/2}, F = 3, m_F = 0\rangle \leftrightarrow |5^2P_{3/2}, F' = 4, m_F = 0\rangle$ is $560(3)\,\mathrm{MHz}$.
As can be seen in the traps (8,9), (9,8), and (9,9), a single-site addressing with a crosstalk below the detectable limit is achievable. An imperfect addressing of trap (9,8) results in an additional excitation in trap (8,8), for long pulse durations.
For the addressing of the individual traps, the frequencies driving the AODs in the addressing system for the blue light are set following Tab. 5.4. For a compensation of trap-specific shifts of the frequency of the blue light induced by the AODs, the frequency driving the compensation AOM in the red Rydberg laser is changed respectively to stay in resonance for the two-photon process. The addressing of adjacent traps requires a frequency change of approximately $3.0(1)\,\mathrm{MHz}$ on the respective AOD. Following the bandwidth of the AODs (see Sec. 4.2.4) of approximately $35(1)\,\mathrm{MHz}$, a Rydberg excitation in an array of at least 10 x 10 atoms is viable with this system.

Tab. 5.4.: Combinations of frequencies used for the horizontal and vertical AODs of the blue addressing system (see Sec. 4.2.4) and the compensation AOM in the red Rydberg laser (see Sec. 4.2.5). The respective frequencies are generated by the FPGA system described in Sec. 4.3.2.

Vertical trap index	Horizontal trap index	Frequency f_3 of vertical AOD in MHz	Frequency f_4 of horizontal AOD in MHz	Frequency f_5 of compensation AOM in MHz
8	8	113.515	94.862	195.6235
8	9	113.756	91.862	194.118
9	8	110.765	94.871	197.003
9	9	110.686	91.771	195.4375

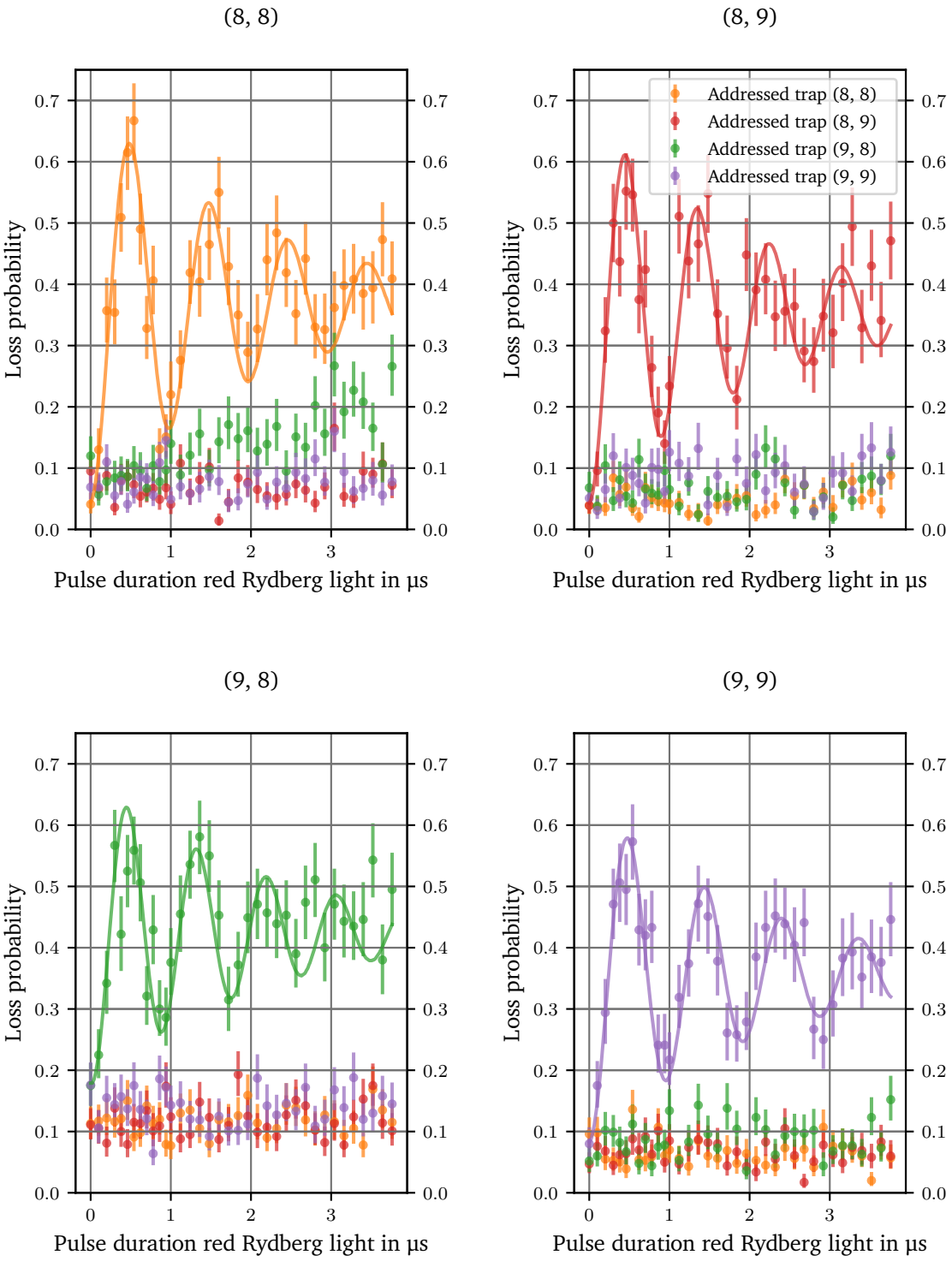

Fig. 5.13.: Overview of single-site addressed Rydberg excitations with identical Rabi frequencies in four individual traps. The individual traps are labeled with their vertical coordinate first and horizontal coordinate second. A crosstalk between traps is not resolved except for trap (8,8) and is due to a bad calibration for this trap.

5.3.5. Influence of the optical phase-locked loop in the Rydberg laser systems

This thesis presents the technique of high-bandwidth laser locking via an optical phase-locked loop on the transmitted light of an ULE cavity (see Sec. 4.2.6) firstly to the knowledge of the author and demonstrates its effect on the Rydberg excitation. As a test, ground-to-Rydberg state Rabi floppings are recorded with and without activated OPLL. For each setting of the OPLL, all pulse durations for the Rabi oscillation are sampled one after the other and then the setting of the OPLL is switched for the next experiment run. The result is shown in Fig. 5.14 (a). Though a significant reduction in the phase noise of the Rydberg lasers is demonstrated in Fig. 4.13, no significant improvement of the damping of the Rabi oscillation is found.
The benefit of the OPLL in this experiment is substantiated in Fig. 5.14 (b). In this visualization of the measurement of the Rabi oscillation, the focus is set on the convergence of the single events towards the results shown in Fig. 5.14 (a). The measurement time of $105\,\mathrm{min}$ is separated into six bins and the steps up to the given bin are averaged to an interim loss probability for each time step tested in the Rabi flopping. The deviation of this interim loss probability from the final result drawn in Fig. 5.14 (a) is plotted for each pulse duration in Fig. 5.14 (b). As a result, the convergence of the measurement with deactivated OPLL show larger deviations in the early time bins than with activated OPLL and show the same deviations than the curves with activated OPLL in the later time bins.
This behavior is evaluated further in Fig. 5.14 (c) by calculation of the standard deviations of the deviations drawn in (b). For the time bins up to $60\,\mathrm{min}$, a reduction of the standard deviation is visible. For the time bin at $21\,\mathrm{min}$ the reduction is at maximum of $30(5)\,\%$ less variation of the deviations of the interim loss probability to the final result. This can be evidence that the reduction of phase noise of the Rydberg laser systems is effective on time scales up to $60\,\mathrm{min}$. After that time scale, other effects, like drifts on longer times scales, could be the limit of the result of the Rydberg experiments, dominating the benefits of the OPLL. The improved phase noise of the OPLL therefore enables reliable experiments with Rydberg atoms on short timescales but its effect is limited by drifts on long timescales.

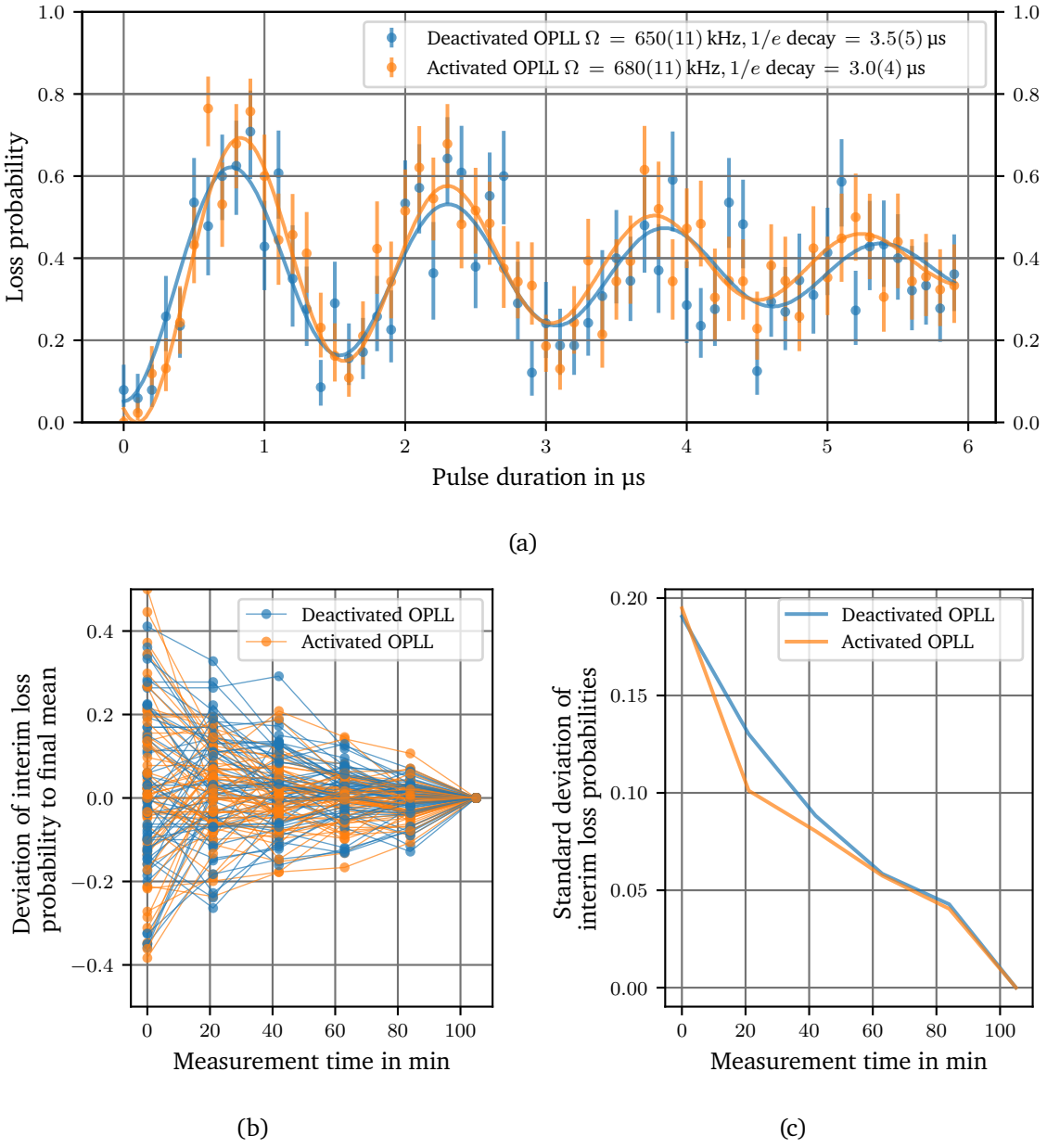

Fig. 5.14.: (a) Ground-to-Rydberg state Rabi flopping recorded with (yellow) and without (blue) activation of the phase lock system. Though no significant change in the parameters of the oscillation are found, the implementation of the phase locks allowed reliable research with Rydberg atoms on short timescales. The likely reason for this is shown in (b) depicting a time resolved convergence over the sampling period towards the points shown as Rabi flopping. For all points shown above, the difference of the interim loss probability, up to the sampling time drawn on the horizontal axis, to the final result is shown. The curves with deactivated phase locks (blue) show a wider or equal spread than the curves with activated phase locks (yellow). (c) The standard deviations of the points shown in (b) illustrate the faster convergence of experiments with Rydberg atoms with activated phase locks for medium measurement times.

5.3.6. Direct measurement of single-photon Rabi frequencies

For the optimization of the two-photon process of the Rydberg excitation, the contributions of the red and the blue Rydberg light are of interest. The contributions can be found by analysis of the light shifts induced by the respective light field. As the shifts are proportional to the inverse of the detuning to the relevant transitions, each light can be related to the states it shifts.
The red Rydberg light, driving the transition $|5^2\mathrm{S}_{1/2}, \mathrm{F}=3, m_\mathrm{F}=0\rangle \leftrightarrow |5^2\mathrm{P}_{3/2}, \mathrm{F}'=4, m_\mathrm{F}=0\rangle$, mainly shifts the states $|5^2\mathrm{S}_{1/2}, \mathrm{F}=2\rangle$, $|5^2\mathrm{S}_{1/2}, \mathrm{F}=3\rangle$, and $|5^2\mathrm{P}_{3/2}, \mathrm{F}'=4\rangle$ but not the Rydberg state $|82\mathrm{S}_{1/2}, \mathrm{J}=1/2\rangle$. The blue Rydberg light causes a shift of the energy eigenvalues for the states $|5^2\mathrm{P}_{3/2}, \mathrm{F}'=4\rangle$ and $|82\mathrm{S}_{1/2}, \mathrm{J}=1/2\rangle$, but not the $|5^2\mathrm{S}_{1/2}\rangle$ manifold.
The two-photon Rabi frequency $\Omega_{2\mathrm{P}}$ is proportional to each of the on-resonance Rabi frequencies Ω_1 (red) and Ω_2 (blue), see Fig. 4.5, following (3.7)

$$\Omega_{2\mathrm{P}} = \frac{\Omega_1^* \Omega_2}{2\Delta_\mathrm{i}}.$$

In order to identify the dominating contribution, the shift of the energy eigenvalues of the two states $|1\rangle = |5^2\mathrm{S}_{1/2}, \mathrm{F}=3, m_\mathrm{F}=0\rangle$ and $|r\rangle = |82\mathrm{S}_{1/2}, \mathrm{J}=1/2, m_\mathrm{J}=-1/2\rangle$ can be used following (3.4)

$$\Delta E_{|1\rangle} = \frac{\hbar \Omega_1^2}{4\Delta_{\mathrm{i}_2}}, \quad \Delta E_{|r\rangle} = \frac{\hbar \Omega_2^2}{4\Delta_{\mathrm{i}_2}}.$$

Following these equations, the individual contributions Ω_1 and Ω_2 of the two Rydberg lasers can be deduced from the energetic shifts of the states $|1\rangle$ and $|r\rangle$. For the ground state, the optical intensity of the red Rydberg light defines the light shift $\Delta E_{|1\rangle}$, for the Rydberg state, the optical intensity of the blue Rydberg light defines the shift $\Delta E_{|r\rangle}$.
A measurement testing the light shift of state $|1\rangle$, induced by the red Rydberg light, is shown in Fig. 5.15 (a). The complete overview of settings and results is presented in Tab. 5.5. For an optical power of the red Rydberg light of $7.55\,\mathrm{mW}$ the Rydberg resonance is found at an offset of $0.1(2)\,\mathrm{MHz}$ relative to the reference frequency of $312.632\,323\,\mathrm{THz}$. With an increased power of the red Rydberg light of $13.70\,\mathrm{mW}$, the resonance shifts to an offset of $-0.4(2)\,\mathrm{MHz}$. Due to the SHG, these frequencies take effect in the light with a factor of two, such that the shift of the resonance scales with the doubled shift of the fundamental laser frequency. Using (3.1) and (3.4), the scaling of the absolute light shift with the optical power P of the red Rydberg light is expected to follow

$$\Delta E_{|1\rangle} = \frac{\kappa P}{4\hbar \Delta_\mathrm{i}} \tag{5.2}$$

with the fit parameter κ. A linear extrapolation of the shift of the resonance using this dependency is shown in Fig. 5.15 (c). For a hypothetical excitation with vanishing power of the red Rydberg light, the resonance would shift to a frequency offset of $1.3(8)\,\mathrm{MHz}$. It must be taken into account, that a positive light shift, as it is expected for a blue detuned light field, results in a negative shift for the resonance frequency of the transition. Therefore, the two measured resonance frequencies are transformed to shifts of the state $|1\rangle$, assuming the unperturbed resonance frequency at an offset of $1.3\,\mathrm{MHz}$. According to the extrapolation, the absolute light shift of the state $|5^2\mathrm{S}_{1/2}, \mathrm{F}=3, m_\mathrm{F}=0\rangle$ follows the dependency $+h \times 150(80)\,\mathrm{kHz\,mW^{-1}}$ for

the red Rydberg light.
With this starting point, the on-resonance Rabi frequencies can be estimated. With

$$\Omega_1 = \sqrt{\frac{4\Delta E_1 \Delta_i}{\hbar}} \tag{5.3}$$

the on-resonance Rabi frequencies of the red Rydberg light are calculated. Together with the two-photon Rabi frequencies measured for these two power settings and the detuning to the intermediate state $|5^2P_{3/2}\rangle$ of $563.90\,\text{MHz}$, also an estimation of the on-resonance Rabi frequency of the blue Rydberg light Ω_2 can be calculated.
Absolute light shifts of $h \times 1.1(90)\,\text{MHz}$ and $h \times 2.10(90)\,\text{MHz}$ respectively are calculated for the state $|1\rangle$. This can be compared with the calculations shown in Fig. 5.18. For the set detuning, light shifts of $h \times 1.02(3)\,\text{MHz}$ and $h \times 1.83(3)\,\text{MHz}$ are expected which is in good agreement with this evaluation. This analysis is sufficient to prove that the contributions of the red and the blue Rydberg light do not differ by orders of magnitude. It can also be clearly seen, that the red Rydberg light is the dominant part which leads to higher scattering on the qubit basis states, compared to an equal contribution of both light fields.
Nevertheless, the resolution of this measurement is limited. The experiment is not able to test very small powers of one of the Rydberg light fields, as the duration of the π-pulse must not exceed the time of $10\,\mu\text{s}$ for which the traps can be shut off (see Sec. 5.3.2). Additionally, the requirement for short π-pulses results in a Fourier-broadening of the resonance which limits the measurement resolution for the transition frequency.

Tab. 5.5.: Evaluation of the shifts of the Rydberg transition induced by the light shift of the red Rydberg light.

Measurand	Setting 1	Setting 2
Power in mW	$7.55(5)$	$13.7(5)$
Intensity at the position of the atoms in $\frac{\text{mW}}{\mu\text{m}^2}$	$3.4(1) \times 10^{-6}$	$6.1(2) \times 10^{-6}$
Measured Rydberg resonance in MHz (fundamental) from Fig. 5.15 (a)	$0.1(2)$	$-0.4(2)$
Measured Rydberg resonance in MHz (SHG)	$0.2(4)$	$-0.8(4)$
Shift of state $\|1\rangle$ in units of $h \times$ MHz	$1.1(90)$	$2.10(90)$
Rabi frequency Ω_1 in units of $2\pi \times$ MHz (drawn in Fig. 5.15 (d))	$51(19)$	$68(19)$
Two-photon Rabi frequency Ω_{2P} in units of $2\pi \times$ MHz from Fig. 5.15 (d)	$0.55(7)$	$0.78(7)$
Rabi frequency Ω_2 in units of $2\pi \times$ MHz	$12(3)$	$13(3)$

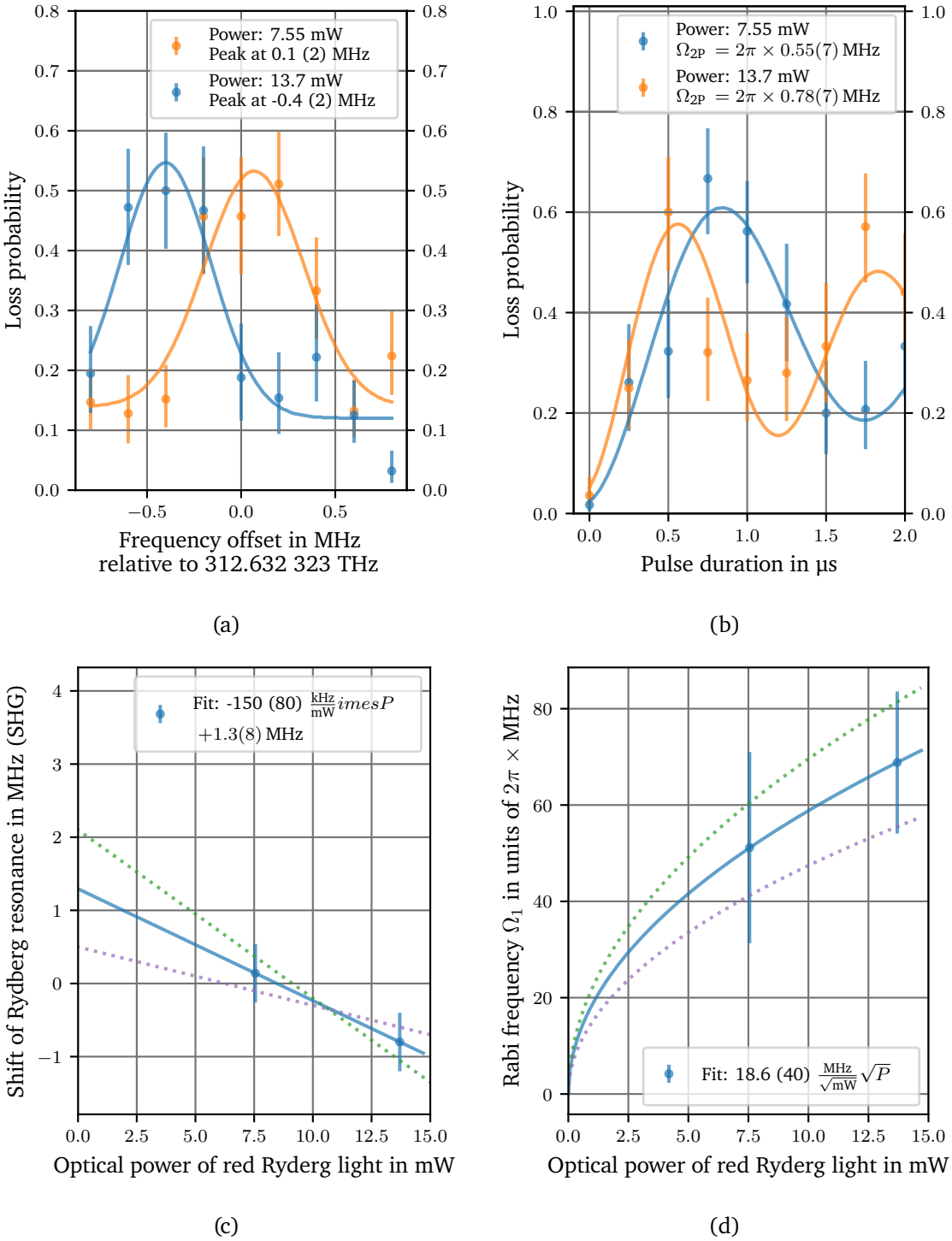

Fig. 5.15.: (a) Measured shift of the resonance of the Rydberg transition for two different power levels of the red Rydberg light. A frequency offset of 6 MHz, compared to Fig. 5.10, is due to a change in the frequency of the red Rydberg light. (d) Rabi floppings measured with the respective parameters of the two resonance in (a). (c) Extrapolation of the shift of the resonance used for the calculation of the absolute light shift of the state $|5^2S_{1/2}, F = 3, m_F = 0\rangle$. (d) Scaling of the Rabi frequency Ω_1 of the red Rydberg light with the optical power of this light. The dotted lines represent trend lines used for error estimation.

5.3.7. Differential light shift of the qubit states induced by the red Rydberg light

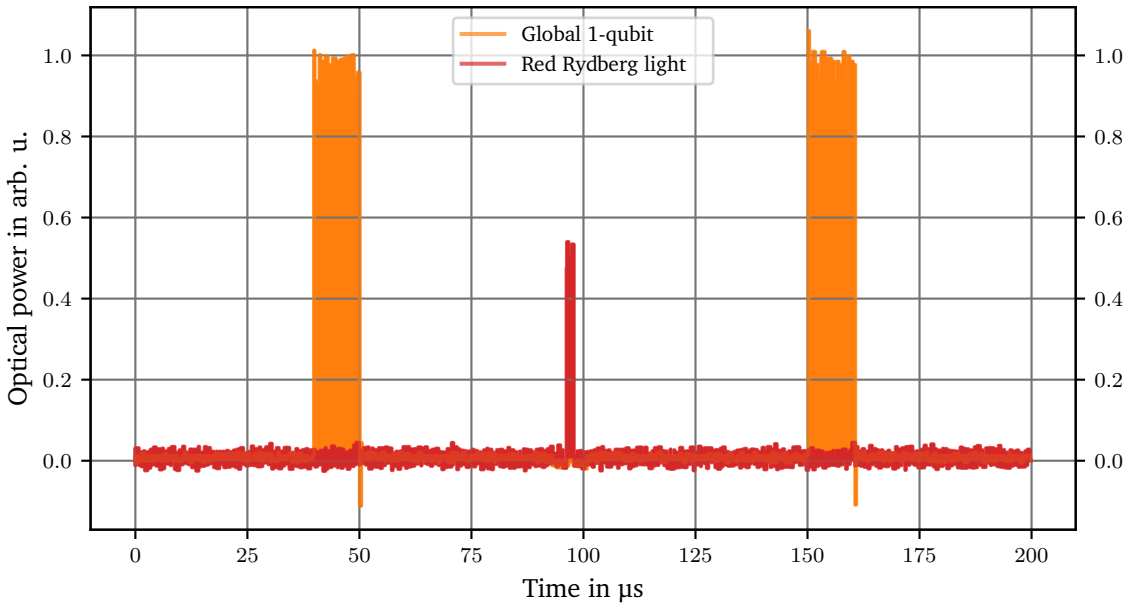

Fig. 5.16.: Sequence for the measurement of the differential light shift induced by the red Rydberg light.

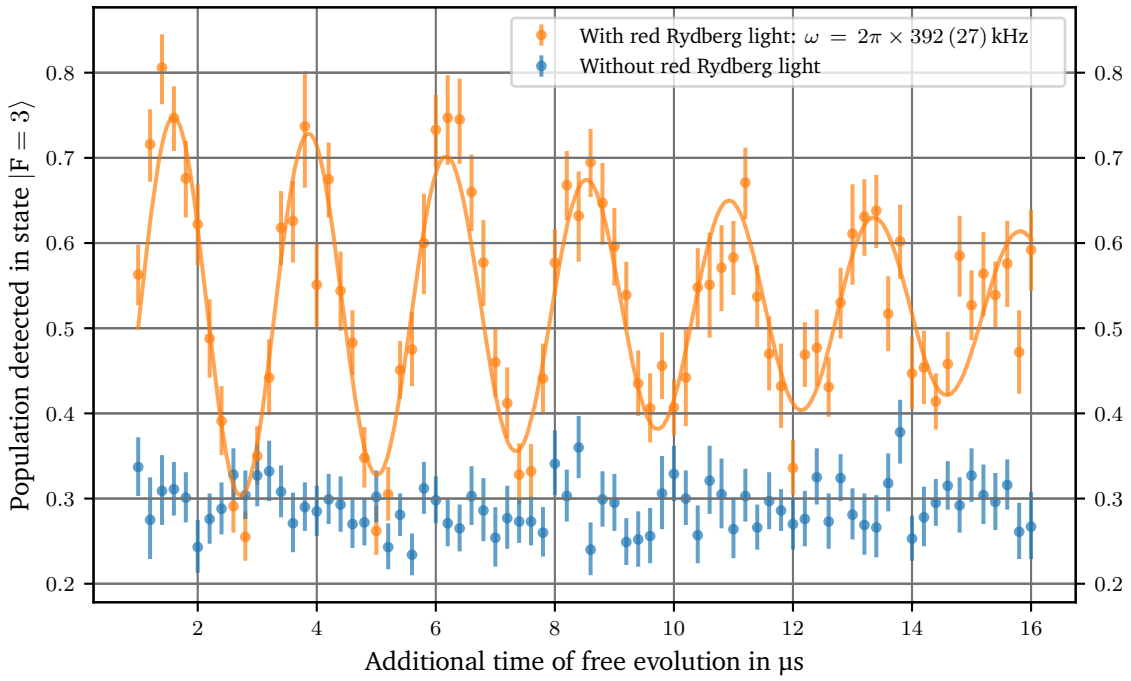

Fig. 5.17.: Ramsey oscillations between the ground states induced by the differential light shift of the red Rydberg light.

The interaction of the red Rydberg light with the qubit basis states can be measured directly with a Ramsey experiment. The pulse sequence of this experiment is shown in Fig. 5.16. Between two $\hat{R}(\pi/2, 0)$ rotations induced by the global 1-qubit gate, the red Rydberg light is irradiated for different durations. As a reference, the same measurement is performed without activating the pulse to calibrate offsets in the Ramsey frequency. The result is shown in Fig. 5.17.
As can be seen in the blue curve, the Ramsey experiment uses the free resonance well enough to suppress a phase evolution on the relevant time scales. In the yellow curve, a phase evolution with $2\pi \times 392(27)$ kHz is caused by the red Rydberg light at an optical power of 2.28 mW, measured in front of the window of the chamber.
The light is blue-detuned by $\Delta_{\mathrm{i,2}} = 2\pi \times 563.90\,\mathrm{MHz}$ to the transition $|1\rangle \leftrightarrow |5^2\mathrm{P}_{3/2}\rangle$ which means that it is red-detuned by $\Delta_{\mathrm{i,2}} - \Delta_{\mathrm{hfs}} = -2\pi \times 2471.1\,\mathrm{MHz}$ for the transition $|0\rangle \leftrightarrow |5^2\mathrm{P}_{3/2}\rangle$. In this case, the induced differential light shift $\delta^{\mathrm{induced}}$ is given by

$$\delta^{\mathrm{induced}} := \frac{\Delta E_{|1\rangle} - \Delta E_{|0\rangle}}{\hbar} \tag{5.4}$$

$$= \frac{\Omega^2_{|1\rangle \leftrightarrow |5^2\mathrm{P}_{3/2}\rangle}}{4\Delta_{\mathrm{i,2}}} - \frac{\Omega^2_{|0\rangle \leftrightarrow |5^2\mathrm{P}_{3/2}\rangle}}{4(\Delta_{\mathrm{i,2}} - \Delta_{\mathrm{hfs}})} \tag{5.5}$$

using (3.4) with the Rabi frequencies $\Omega^2_{|1\rangle \leftrightarrow |5^2\mathrm{P}_{3/2}\rangle}$, which defines the interaction between the qubit basis state $|1\rangle$ with the intermediate state, and $\Omega^2_{|0\rangle \leftrightarrow |5^2\mathrm{P}_{3/2}\rangle}$, which defines the interaction between the qubit basis state $|0\rangle$ with the intermediate state. It is worth mentioning that (3.10) would describe the differential light shift of the light driving the 1-qubit gate but not the light shift caused by the additional light field of the red Rydberg laser. A calculation on the expected differential light shift is shown in Fig. 5.18 (b). For the set detuning, a differential light shift of $h \times 382(10)$ kHz is expected which is in good agreement with the measured value. From the results of the previous section, the absolute light shift $\Delta E_{|1\rangle}$ of the $|1\rangle$-state can be extrapolated to $h \times 341(116)$ kHz. Then, the light shift of the $|0\rangle$-state can be calculated with

$$\Delta E_{|0\rangle} = \Delta E_{|1\rangle} - \hbar\delta^{\mathrm{induced}} \tag{5.6}$$

for the experiment in Fig. 5.17 to

$$\Delta E_{|0\rangle} = -h \times 51(119)\,\mathrm{kHz}. \tag{5.7}$$

In comparison with the calculations shown in Fig. 5.18, an absolute light shift of $-h \times 74(3)$ kHz is expected for the state $|\mathrm{F} = 2\rangle$ which is in good agreement with this evaluation.

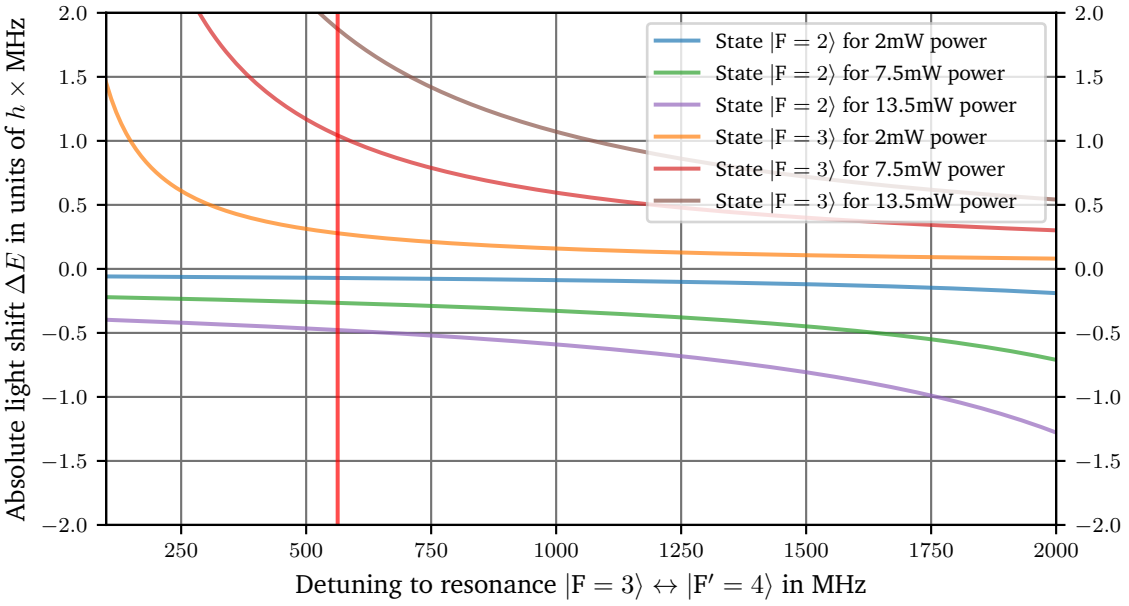

(a)

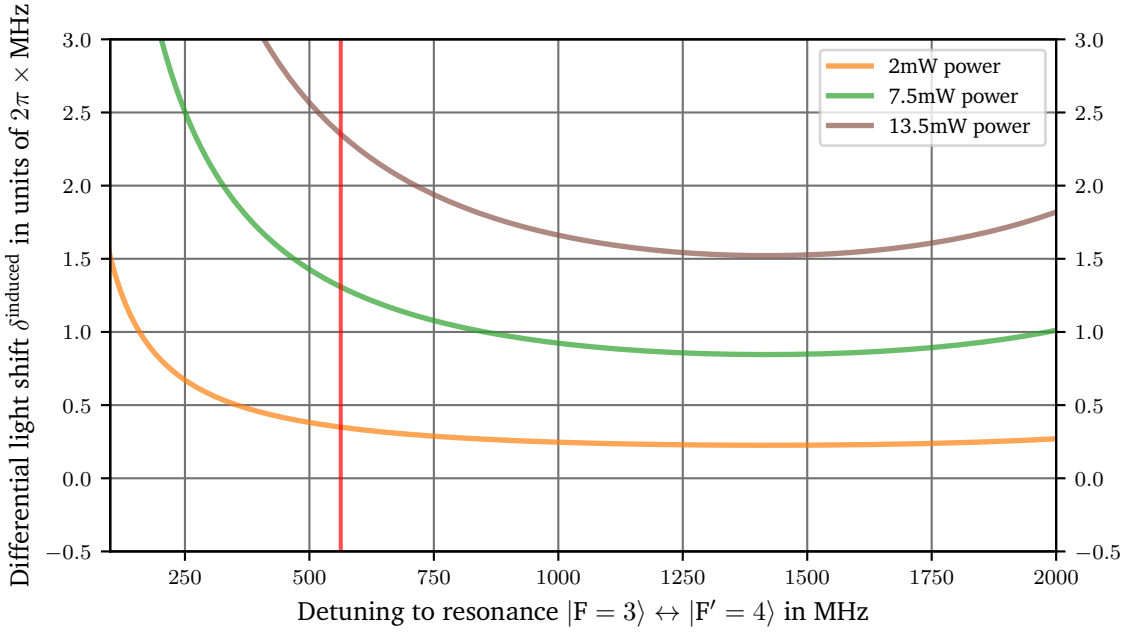

(b)

Fig. 5.18.: (a) Calculations of the scaling of the absolute light shift of the qubit basis states induced by the red Rydberg light. (b) The resulting differential light shift. Red lines indicate the detuning $\Delta_{i,2}$ used for the Rydberg excitation.

5.4. 2-qubit operations

The puzzle for the set of universal quantum gates is close to become a consistent frame but the center is still missing: The interaction itself. First, the pulse sequence for testing interactions between the qubits is shown, demonstrating the experimental control with timings down of 100 ns. This paves the way for a quantitative measurement of the blockade strength utilizing the agile frequency changes of the FPGA system (see Sec. 4.3.2). In order to prepare the CNOT operation, the differential light shifts of the red Rydberg light are calibrated. Finally, a first test of a CNOT operation is shown by the controlled inversion of the phase for a Rabi flopping of the target qubit.

5.4.1. Pulse sequence for the *H*-C_Z gate

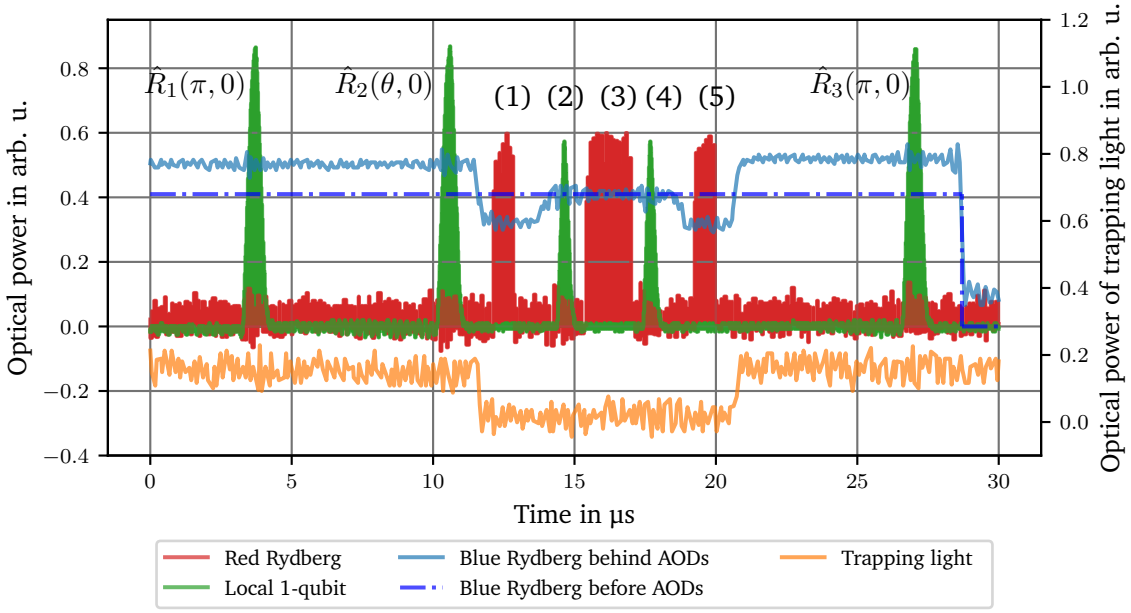

Fig. 5.19.: Experimental sequence used for gate experiments. The pulses inducing the local 1-qubit gate, the trapping light, the addressing with the blue Rydberg light, and the pulses of the red Rydberg light are shown. In order to get a feedback for the addressing of the blue Rydberg light, the signal of the fast photodiode behind the AODs shown in Fig. 4.8 is shown here. In this signal, different positions of the blue Rydberg beam are shown as different signal strengths. As an artifact, also the trapping light produces a signal on this photodiode which is visible as additional level shifts in the signal when the trapping light is switched off during the Rydberg excitation as discussed in Sec. 5.3.2. The sequence labeled with the numbers (1) - (5) in the period between 11 µs and 21 µs is the full sequence which can be used to demonstrate the H-C_Z protocol (see Fig. 3.9). Additional operations with the local 1-qubit gate in advance and after the CNOT operation are used for state preparation as discussed in the respective experiments. Additional operations with the global 1-qubit gate are possible in advance and after this sequence and are not shown here. The pulses of the light inducing the local 1-qubit gate are shorter than the bandwidth of the photodiode used for this recording. Therefore, measured pulse heights are dependent of the pulse lengths.

The gate experiments shown in this section are performed with an experimental sequence as depicted in Fig. 5.19. The signals of the light inducing the local 1-qubit gate, the trapping light, the blue Rydberg light behind and in front of the AODs, and the red Rydberg light are shown. The experiment starts with all qubits initialized in state $|0\rangle = |5^2\mathrm{S}_{1/2}, \mathrm{F} = 2, m_\mathrm{F} = 0\rangle$. The first two operations with the local 1-qubit gate allow to prepare the control qubit (first pulse at $3.3\,\mu\mathrm{s}$) and the target qubit (second pulse at $10.2\,\mu\mathrm{s}$) in the state $|1\rangle = |5^2\mathrm{S}_{1/2}, \mathrm{F} = 3, m_\mathrm{F} = 0\rangle$ individually. The time between the two pulses is given by the switching time of the AOD system for the local 1-qubit gates as described in Sec. 4.1.3. The blue light is activated before the sequence, but addresses a position outside the atom array.
The pulses labeled by the numbers (1) - (5) are the light pulses inducing the CNOT operation following the H-C_Z protocol as described in Fig. 3.9. This sequence starts with a deactivation of the trapping light. Then, state $|1\rangle$ is coupled to the Rydberg state $|r\rangle$ for the control qubit with pulse (1), inducing a ground-to-Rydberg state rotation by π. The pulse itself and its length is visible in the signal of the red Rydberg light. In the signal of the blue Rydberg light, a falling edge at $11.5\,\mu\mathrm{s}$ is visible. The falling edge is an artifact due to the trapping light that also produces a signal on this photodiode and is shut off in this moment as shown in the respective signal. Pulse (2) operates on the target qubit and performs a $\pi/2$ pulse on this qubit inducing a local $\hat{R}(\pi/2, 0)$ gate. During pulse (2), the target qubit is already addressed with the blue light to prepare a coupling to $|r\rangle$. The changed addressing is visible as a rising edge at $14\,\mu\mathrm{s}$ in the blue signal. With pulse (3), the state $|1\rangle$ is coupled to $|r\rangle$ for the target qubit and performs a 2π ground-to-Rydberg state rotation unless this operation is blockaded by the control qubit via the Rydberg blockade as described in Sec. 3.1.5. Pulse (4) is a second $\pi/2$ operation of the local 1-qubit gate inducing a local $\hat{R}(\pi/2, 0)$ gate on the target qubit. During this pulse, the control atom is addressed with the blue light, visible as a falling edge at $19\,\mu\mathrm{s}$ in the blue signal. The final coupling of state $|1\rangle$ to $|r\rangle$ for the control atom is performed by pulse (5) inducing a ground-Rydberg rotation by π.

5.4.2. Blockade strength of Rydberg interaction

For the CNOT operation, a sufficient blockade strength must be guaranteed. Based on the C_6 coefficient of $-h \times 5558.98\,\mathrm{GHz}\,\mu\mathrm{m}^6$ from Tab. 5.3, and a Rabi frequency of up to $2\pi \times 1\,\mathrm{MHz}$, a blockade radius of at least $13.3(7)\,\mu\mathrm{m}$ is calculated based on (3.28). This allows a blockade for next neighbors with a distance of $7.0(1)\,\mu\mathrm{m}$ and for diagonal neighbors at a distance of $9.9(1)\,\mu\mathrm{m}$ in this experiment. The blockade strength for the two situations are calculated following (3.27) to $47(5)\,\mathrm{MHz}$ for next neighbors and $5.9(5)\,\mathrm{MHz}$ for diagonal neighbors.
Using the fast experimental control, the frequency of the red Rydberg light can be changed with the compensation AOM on timescales of $100\,\mathrm{ns}$ by values of up to $10\,\mathrm{MHz}$. This allows the direct test of the blockade strength by exciting the control atom to the Rydberg state and testing the Rydberg excitation of a neighboring target atom with a detuned red Rydberg light. The results of such an experiment are shown in Fig. 5.20. The atom in trap (8,8) is used as control atom. By a postselection on events with a loss of this atom due to untrapped Rydberg states, shots with successful Rydberg excitation of this atom can be compared with events without excitation to the Rydberg state. The atoms in trap (9,8) as next neighbor and (9,7) as diagonal neighbor are evaluated as target atoms. Due to the near isotropic angular dependence of the van-der-Waals coefficient for pairs of $|S\rangle$-states [61], this choice of traps is expected to be representative for the interactions in the whole array.
As the blockade strength for next neighbors exceeds the scanning range of this experiment, it

is expected that no resonance is visible in the blockaded case. A suppression of the resonance by $70\,\%$ is found for the blockaded situation. This is likely due to an imperfect detection of the Rydberg excitation of the control atom and indicates an upper bound for a false-positive detection error of Rydberg atoms in this situation. In trap (8,8), atom loss occurred at a probability of $30\,\%$ without resulting in a Rydberg blockade in trap (9,8). As the typical baseline loss is only $8\,\%$, an additional loss is induced by the Rydberg light in this situation. For example, a successfully excited Rydberg atom in (8,8) leaves the blockade radius before the atom in (9,8) is excited. But this detection error is not found for the diagonal neighbor, where the suppression is better than the detection limit.
For the diagonal neighbor, a shift of the Rydberg resonance between the blockaded situation and the unblockaded situation of $5(1)\,\mathrm{MHz}$ is found. Firstly, the sign of this shift confirms the expected lift of the energy eigenvalues. But the value of the blockade strength is outside the uncertainty of the expected shift of $5.9(5)\,\mathrm{MHz}$ and could be explained by a larger mean distance of the atoms of $10.2(4)\,\mu\mathrm{m}$ instead of $9.9(1)\,\mu\mathrm{m}$ or an error in the C_6 value of more than $h \times 1000\,\mathrm{GHz}\,\mu\mathrm{m}^6$. Additionally, a broadening of the resonance is visible to a full width at half maximum (FWHM) of $4.6(20)\,\mathrm{MHz}$. Assuming this broadening to be caused by motion of the atoms, a range in the distance of the atoms (FWHM) from $(9.6 \pm 0.2)\,\mu\mathrm{m}$ to $(11.4^{+1.0}_{-0.6})\,\mu\mathrm{m}$ is calculated. The error in the distance is likely for two reasons.
The first is the spatial distribution of the atoms in the dipole traps. The trapping volume is defined by a waist of $1.45(10)\,\mu\mathrm{m}$ and a Rayleigh range of $8.3(12)\,\mu\mathrm{m}$ [39]. Especially the elongation of the trap in the **z** direction allows a larger initial distance of the atoms than defined by the pitch of the traps. This can easily explain a larger spacing of $0.3(1)\,\mu\mathrm{m}$ in the mean distance of the atoms.
The second reason is that the Rydberg experiment is performed with deactivated trapping light, resulting in a time-of-flight phase with a velocity of up to $0.08(1)\,\mu\mathrm{m}\,\mu\mathrm{s}^{-1}$ based on a temperature of $70(10)\,\mu\mathrm{K}$. With a time of flight of up to $6\,\mu\mathrm{s}$ until the target atom is excited to the Rydberg state (see Fig. 5.19), this can cause a variation of $0.46(10)\,\mu\mathrm{m}$ in a random direction. Together, the dimensions of the trapping volume and the time-of-flight phase explain a variation in the interatomic distance of $(9.8 - 10.6)\,\mu\mathrm{m}$.
The maximum of the measured distance of $(11.4^{+1.0}_{-0.6})\,\mu\mathrm{m}$ is compatible with this estimation by its lower error bound. As a worst case estimation, a variation in the distance between the two atoms of $11.4\,\mu\mathrm{m}$ would result in an error of the position of each single atoms of $0.75\,\mu\mathrm{m}$. Regarding the waists of the addressing systems of $2.2(3)\,\mu\mathrm{m}$ for light inducing the local 1-qubit and of $2.1(2)\,\mu\mathrm{m}$ for the blue Rydberg light, an error in the position of the atoms on that scale is not negligible and could cause the imperfect excitation probabilities of both systems. For the Rydberg excitation, this could mean a variation from shot-to-shot in the Rabi frequencies of up to $77\,\%$. A full evaluation of this process is given in [129].

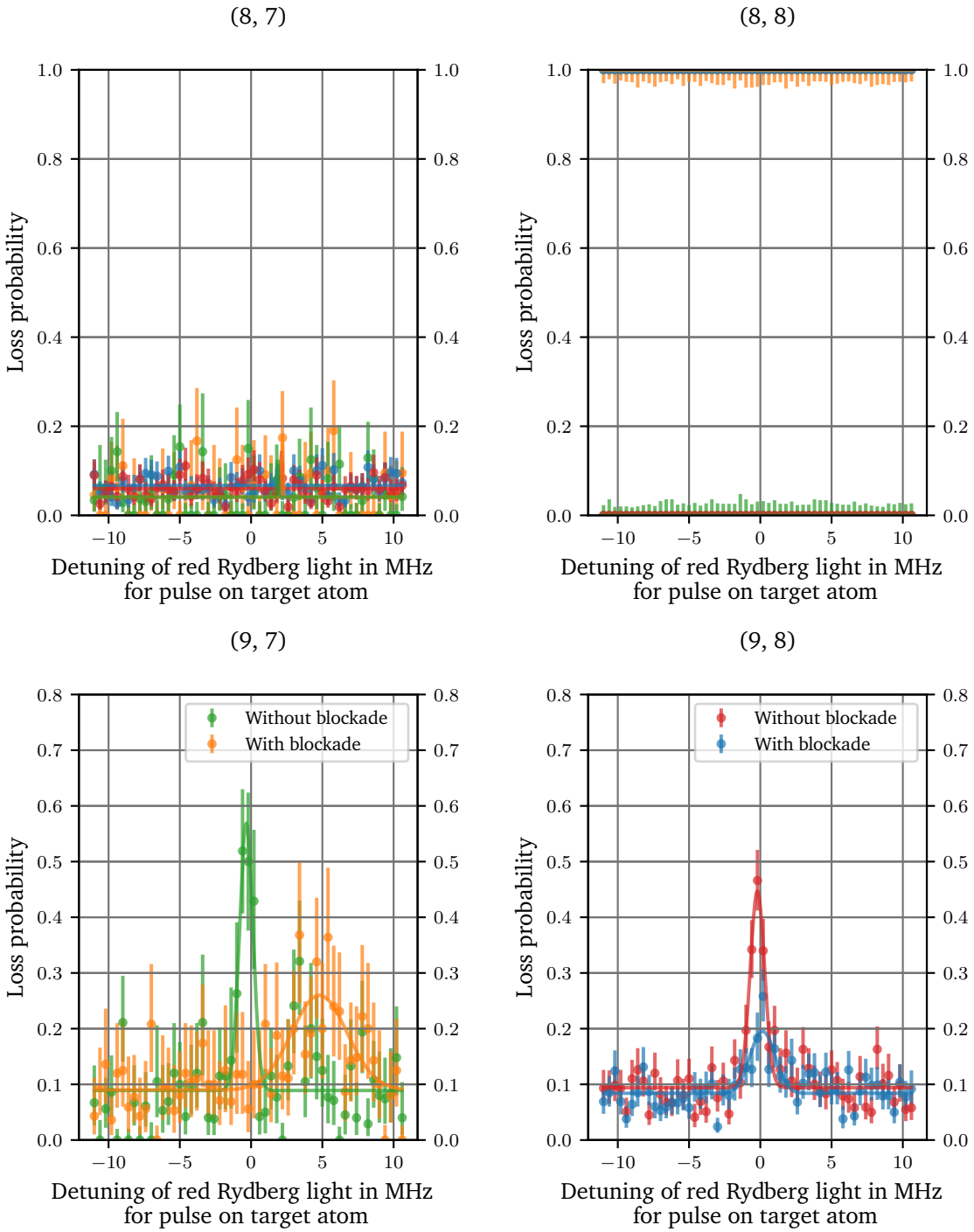

Fig. 5.20.: Direct measurement of the blockade strength of a pair of Rydberg atoms in the state $|82S_{1/2}, J = 1/2, m_J = -1/2\rangle$. The trap (8,8) serves as control atom and is excited to the Rydberg state on resonance (yellow and blue). In the next neighbor (9,8) and the diagonal neighbor (9,7), the resonance frequency is tested with detuned red Rydberg light. For the diagonal neighbor, a blockade strength of $5(1)$ MHz is found for a nominal distance of $9.9(1)$ µm. For the next neighbor, the blockade strength is outside the scanning range. For situations without blockade, the unshifted resonances are found (green and red). No crosstalk in the unaddressed trap (8,7) is found.

5.4.3. Calibration of the phase evolution of the qubit ground states in the *H*-C_Z gate sequence

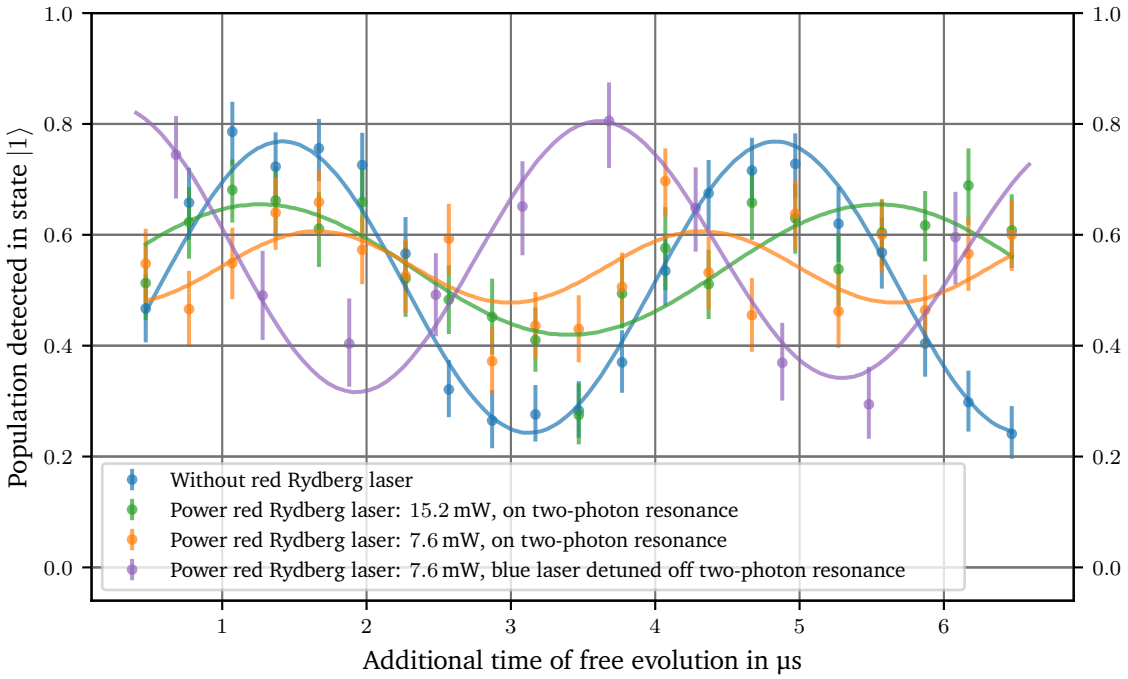

Fig. 5.21.: Measurement of the amplitude of the Ramsey experiment included in the H-C_Z gate (pulses 2 and 4). With irradiation of the 2π-Rydberg pulse (3) on resonance, the amplitude of the ground state Ramsey experiment decreases significantly (green, yellow). This is one major source of amplitude error and needs further investigation. A test with the blue Rydberg light detuned off the two-photon Rydberg resonance by 10 MHz (purple) shows that this is an issue of the Rydberg excitation for the lower power (7.6 mW) of the red Rydberg light.

Based on the successful Rydberg blockade, a H-C_Z gate can be demonstrated. This gate involves the local 1-qubit gate as discussed in Sec. 5.4.1 with $\hat{R}(\pi/2, 0)$ operations. But as these operations induce a Ramsey experiment and the red Rydberg light induces a differential light shift on the qubit basis states, a phase evolution takes place that is not intended in the gate protocol.
The $\hat{R}(\pi/2, 0)$ gates are performed on trap (9,8) and the results of the corresponding Ramsey experiments are shown in Fig. 5.21. For the light inducing the $\hat{R}(\pi/2, 0)$ gates, a detuning of 300 kHz is set in this measurement, defining the frequency of the phase evolution, whereas the pulse of the red Rydberg light adds a phase shift which is dependent on the pulse area. The evaluation shows a Ramsey experiment comparable to Sec. 5.2.3 in case that the red Rydberg light is not activated (blue). A power of $7.6(2)$ mW, corresponding to an intensity of $3.36(10) \times 10^{-6}$ mW µm^{-2}, is tested for a frequency of the blue Rydberg light that is detuned by 10 MHz to the two-photon Rydberg resonance (purple, in short: off resonance) and for a frequency that the meets the resonance (yellow, in short: on resonance). In both cases, a pulse duration of $1.25(1)$ µs is used for the red Rydberg light.
The unintended phase evolution driven by the differential light shift of the red Rydberg light is tested with the purple curve, and the intended phase shift for a successful 2π rotation of the Rydberg Rabi oscillation is tested with the yellow curve. A power of the red Rydberg light

of $15.2(4)$ mW, corresponding to an intensity $6.72(20) \times 10^{-6}$ mW µm^{-2}, is also tested (green curve) with a pulse duration of $0.88(1)$ µs used to create a 2π pulse for the excitation to the Rydberg state. This tests a phase evolution with an additional phase shift of 2π driven by the red Rydberg light.
Dominantly, a reduction of the contrast of the Ramsey oscillation is visible for operations with the Rydberg state. Whereas experiments without the red Rydberg light show oscillations with a mean of $50(5)$ % and an amplitude of $25(5)$ % (blue curve), the amplitude is reduced in experiments with red Rydberg light. With suppressed excitation to the Rydberg state due to the detuning of 10 MHz, the amplitude of the Ramsey experiment decreases slightly to $22.5(50)$ % (purple curve). On resonance, the amplitude is reduced significantly to $10(5)$ % (yellow and green curve). Additionally, a shift in the phase evolution due to the differential light shift of the red Rydberg light is visible, as expected.
Both observations indicate limits for the CNOT operation. The reduced amplitude for cases with activated red Rydberg light can be evidence for too high one-photon scattering or dephasing of the superposition state driven by this light field [133]. Therefore, a larger detuning or less intensity would allow for a better contrast of the Ramsey experiment. The differential light shift of the red Rydberg light induces a phase shift of the superposition state that is not intended in the gate sequence. The power level is chosen to reproduce the initial phase evolution with successful 2π rotation of the Rydberg Rabi oscillation as good as possible. But the dependency between the power of the red Rydberg light and the resulting pulse duration needed for the 2π rotation of the Rydberg Rabi oscillation does not allow a perfect match.
As an offset in the phase evolution could also be compensated with local 1-qubit operations, this condition is set aside. A more relevant condition is the phase shift of 2π in the wave function of the target atom between a transition to the Rydberg state and the phase evolution without transition.
This is tested with a scan over the power of the red Rydberg light and an addressing of the target trap with the blue Rydberg light as shown in Fig. 5.22 in situations where the Rydberg resonance is met and with a detuning of the blue Rydberg light of 10 MHz. As additional free parameters, the power of the blue Rydberg light and the pulse duration are varied in order to keep the 2π rotation of the Rydberg Rabi oscillation for all tested settings.
The results are shown in Fig. 5.23. A parameter set with an inversion of the state of the target qubit is found for a power of $8.9(1)$ mW. This setting is chosen for a test of the CNOT operation. Additionally, a trend towards a population in the $|5^2S_{1/2}, F = 3\rangle$ manifold is visible for higher powers of the red Rydberg light. This can be evidence for a too high scattering rate. An operation with much less power of the red Rydberg light would be preferable. But the blue Rydberg light does not reach high enough values to compensate for the missing power of the red Rydberg light.

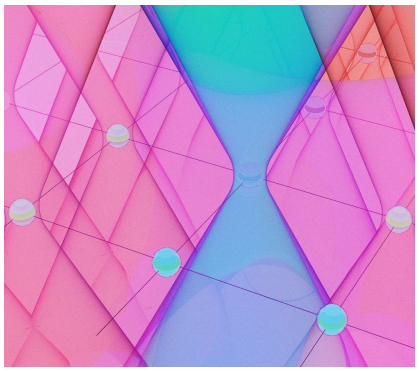

Fig. 5.22.: Addressing of trap (9,8) with the blue Rydberg light (blue) and trap (9,8) with the light inducing the 1-qubit gate (green). Trapping light is drawn in red, the red Rydberg light is drawn in pink. Light of traps in the foreground is not drawn for a clear perspective.

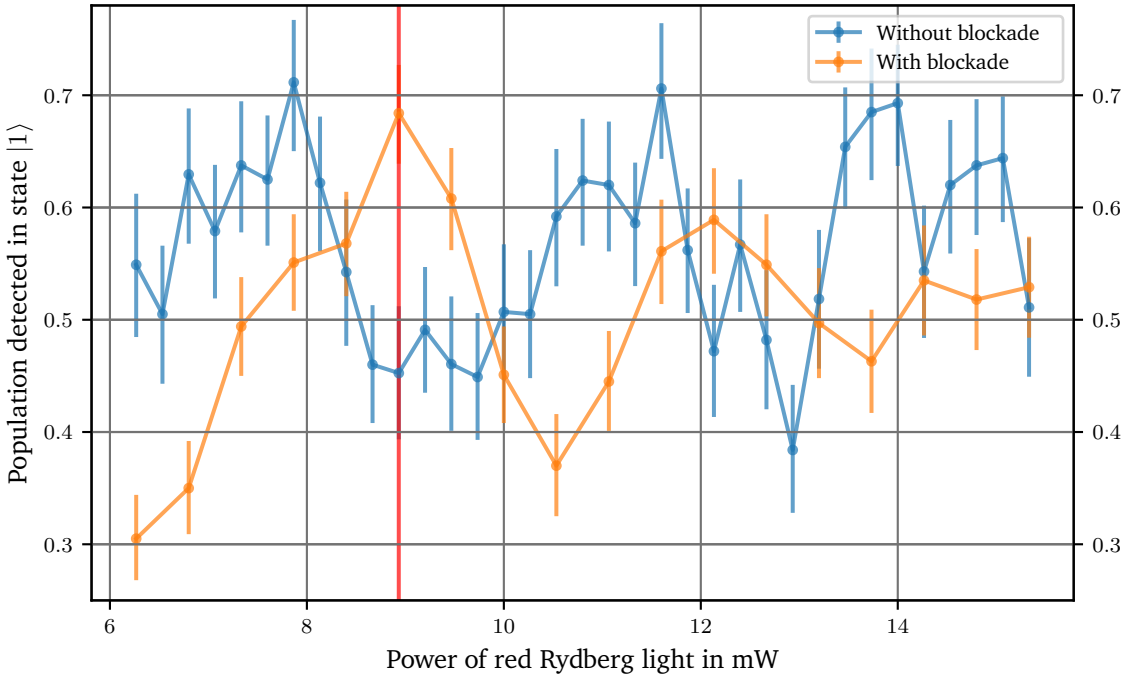

Fig. 5.23.: Measurement using different powers of the red Rydberg light to find a setting with a phase shift of π in the state population between the evolution of the ground states without excitation to the Rydberg state (blue) and with excitation to the Rydberg state (yellow). The red line at a power of $P = 8.9(1)$ mW highlights the power used for the test of the CNOT operation.

5.4.4. Test of the CNOT operation

For the test of the CNOT operation, the H-C_Z sequence as discussed in Sec. 5.4.1 is executed with the modification that the pulse (5) is left out. This avoids to de-excite the control atom from the Rydberg state, allowing for a postselection for events where the control atom is lost. A successful excitation of the control atom with pulse (1) is expected in these cases. If the control atom is prepared in $|1\rangle$ with operation $\hat{R}_1(\pi, 0)$, it must be transferred to the state $|0\rangle$ at the end of the sequence to avoid false-positive losses of the control atom. This can be achieved with the $\hat{R}_3(\pi, 0)$ gate on the control atom shown in Fig. 5.19 as the last operation of the local 1-qubit gate.
The CNOT operation is tested with various initial states of the target qubit. This is achieved by the gate operation $\hat{R}_2(\theta, 0)$ on trap (9,8) with a scan of the rotation angle θ by varying the pulse duration of the inducing light field. While the target qubit is prepared in various initial states, the control qubit in trap (8,8) is prepared in the state $|c\rangle = |1\rangle$ or $|c\rangle = |0\rangle$. Depending on this preparation, a Rydberg excitation of the control qubit is expected (for $|c\rangle = |1\rangle$) or not (for $|c\rangle = |0\rangle$). With this sequence, the logic states $|00\rangle$, $|01\rangle$, $|10\rangle$, $|11\rangle$ (see Sec. 3.1.6 for the nomenclature) are tested as part of these settings. Due to the differential light shift of the red Rydberg light discussed in the previous section, the outcome is expected to be shifted by a phase offset. Depending on the state of the target qubit, the Rydberg blockade occurs for the population in the initial state $|11\rangle$.
The result of this experiment is shown in Fig. 5.24 (a). Two Rabi oscillations with Rabi frequen-

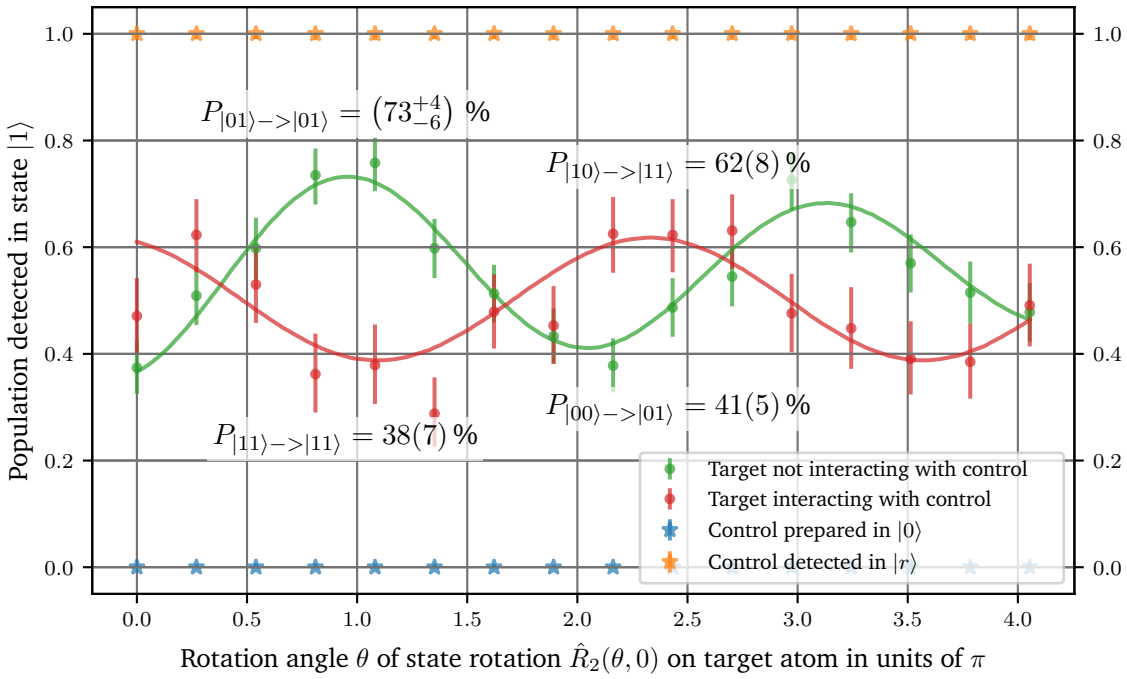

(a)

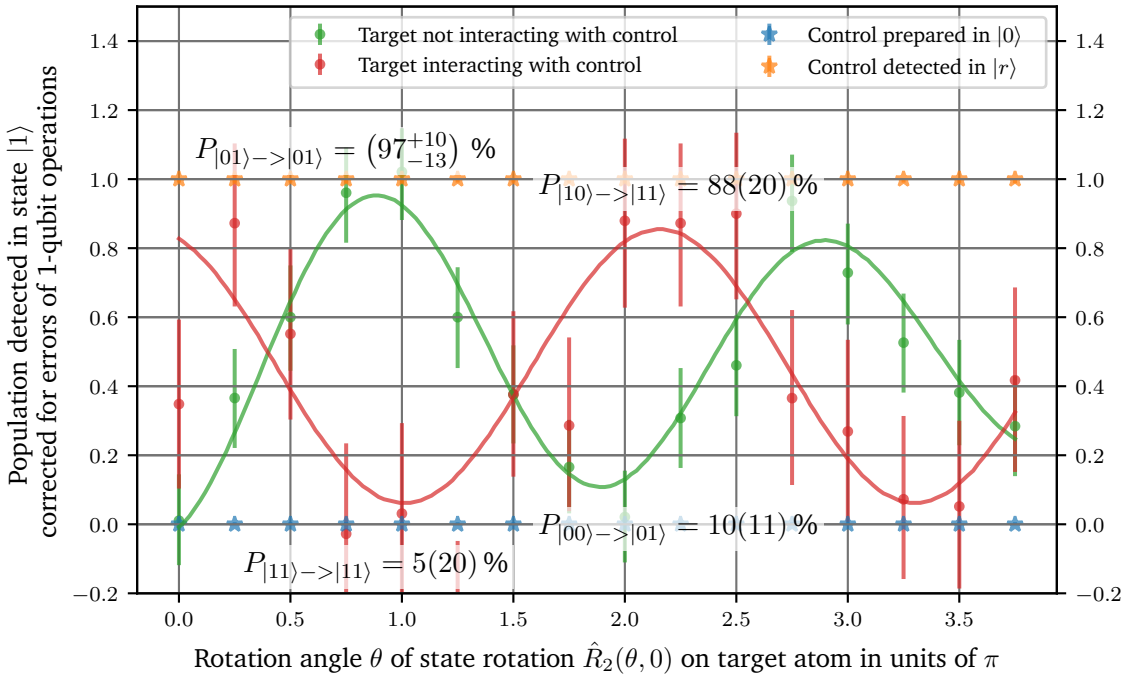

(b)

Fig. 5.24.: (a) Test of a CNOT operation. A Rabi flopping is induced with the local 1-qubit gate on the target qubit (blue dots). Depending on the state in (8,8) (stars), the state prepared in trap (9,8) is inverted (yellow dots). The data is postselected to events with the desired outcome of the control qubit. (b) The same data corrected for known errors in the 1-qubit operations.

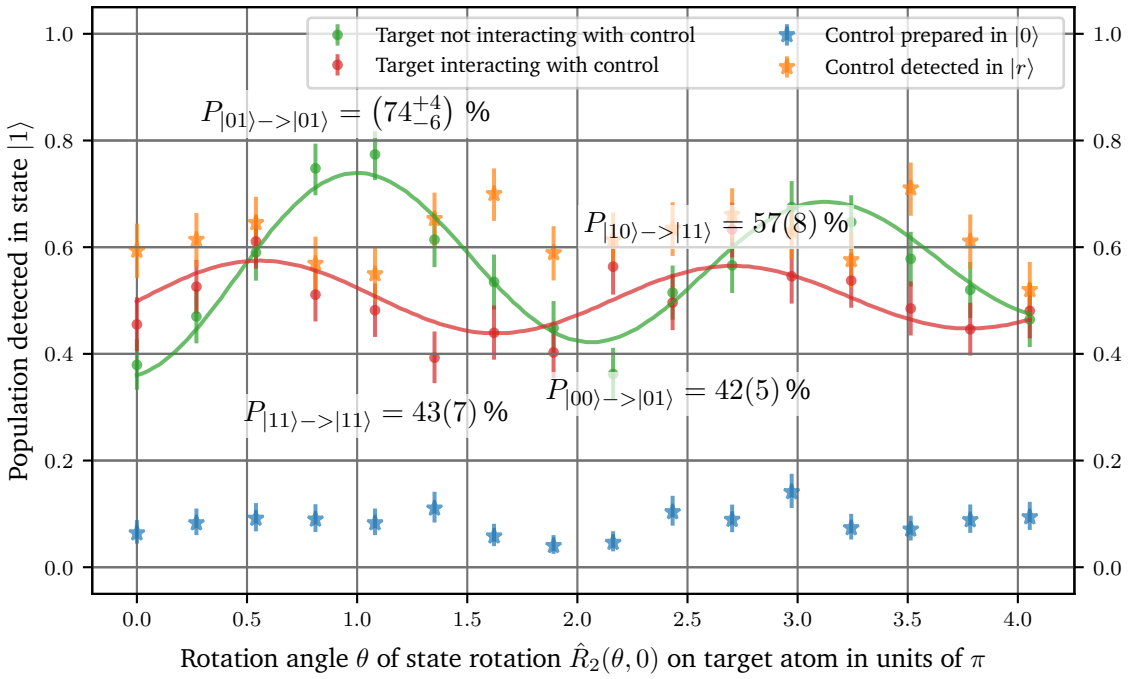

Fig. 5.25.: Without postselection, the test of the 2-qubit operation shows a clear result only for the case that does not intend an interaction between the target and the control qubit (green). Due to the low probabilities for a successful excitation of the control qubit to the Rydberg state (yellow stars), the postselection is required for the detection of an interaction (red).

cies of $1.22(5)$ MHz ($|c\rangle = |0\rangle$) and $1.05(10)$ MHz ($|c\rangle = |1\rangle$) are found. These frequencies match to the expected Rabi frequencies induced by the local 1-qubit gate, see Sec. 5.2.2. As intended, an inversion of the final state of the target qubit can be induced by the state of the control qubit. The oscillation of the case $|c\rangle = |0\rangle$ starts close to a minimum, whereas the situation $|c\rangle = |1\rangle$ starts close to a maximum. The offsets of the phases indicate the influence of the differential light shift of the red Rydberg light. Following the standard logic of a CNOT gate (see Fig. 3.8 (c)), the opposite outcome would be expected: The state of the target qubit is inverted unless the control is in state $|1\rangle$. For this logic, the situation would start in a maximum corresponding to a mapping $|0\rangle \rightarrow |1\rangle$. In the experiments performed here, only $\hat{R}(\theta, 0)$ gates (or X gates) are used, where the H-C_Z protocol proposes H gates ($H = Z_{\pi/2} X_{\pi/2} Z_{\pi/2}$). Due to the lack of fast Z gates, the result of the experiments does not match the outcome of the H-C_Z protocol. Nevertheless, this logic can be realized by choosing a power of the red Rydberg light near 6 mW, based on the parameters for the differential light shift of the red Rydberg light shown in Fig. 5.23. The controllable logic of the CNOT operation in this system is an interesting feature that should be further investigated.
A challenge of this operation are the low success rates. This starts with the excitation probability of the control atom to the Rydberg state. Without the postselection, the outcome of the operation is not identified. The errors on the control qubit are given by the site-selective state preparation with the local 1-qubit gate as shown in Fig. 5.5. If the Rydberg excitation is intended, only $80\,\%$ of the events start with the control atom prepared in state $|1\rangle$. The excitation to the Rydberg state is limited to a mean probability of $65\,\%$, resulting in only $52\,\%$

probability for a control atom in the Rydberg state.
Therefore, the postselection is required for the identification of these cases. For cases with intended interaction between control and target qubit, the shots are postselected for an initial occupation of both traps and atom loss in the trap of the control qubit after the operation. In average over the whole measurement, only $49(4)$ % of the executed shots satisfy the conditions of the postselection for this case. For cases with no intended interaction between control and target qubit, the shots are postselected for an initial occupation of both traps and no atom loss in the trap of the control qubit after the operation. In average over the whole measurement, $87(4)$ % of the executed shots satisfy the condition of the postselection for this case. In total, $973(5)$ events are taken into account for the experiments with intended interaction and $1662(12)$ events are taken into account for the experiments without intended interaction.
Also the Rydberg excitation of the target qubit suffers from low excitation probabilities of 65 %. Moreover, the low contrast of Ramsey experiments using the local 1-qubit gate and the red Rydberg light is the most severe impact. The amplitude of a Ramsey oscillation induced with the local 1-qubit gate is limited to band between 20 % and 80 % as shown in Fig. 5.9. For an off-resonant irradiation of the Rydberg light, a Rabi flopping with a mean of $55(5)$ % and an amplitude of $20(5)$ % is possible as shown in Fig. 5.23. For a resonant irradiation of the Rydberg light with a 2π ground-to-Rydberg state rotation, a Rabi flopping with a mean of $52.5(5)$ % and an amplitude of $17.5(3)$ % is possible.
Due to the low amplitudes of the respective operations, the fitted curves are tested regarding their significance with a Monte-Carlo simulation. Rabi oscillations assuming an error range of ± 100 % for the parameters of the two fitted Rabi oscillation are compared to the data points regarding the χ^2 error of an orthogonal distance regression. From $100\,000$ combinations, only in $0.15(5)$ % of the tested Rabi oscillations reach a similar or better χ^2 error than the shown curves. So, the fitted curves can be accepted within a 3σ confidence interval.
Assuming that the phase evolution is compensated by a 1-qubit gate afterwards (or by H gates), the minima and maxima of the fitted curves are interpreted as the outcomes of the operation as noted in Fig. 5.24 (a). As the limits of the 2-qubit operation are mainly given by errors in the 1-qubit operations with the local 1-qubit gate and the 1-qubit ground-to-Rydberg state rotations, these errors are corrected using the mean values and amplitude from respective Rabi oscillations without an interaction. The resulting outcomes of the operation are shown in Fig. 5.24 (b). Asymmetric error bounds originate from the calculation following the Clopper-Pearson statistics [134, 135, 136] and are given explicitly if the difference between upper and lower bound is larger than 1 %.
Following these numbers, a truth table of the operation can be created. As the result of the operation is projected on the state $|1\rangle$, only probabilities $P_{|ct\rangle->|c1\rangle}$, $c,t \in \{0,1\}$ are directly measured in the experiment. The corresponding probabilities for a projection on state $|0\rangle$ $\left(P_{|ct\rangle->|c0\rangle},\ c,t \in \{0,1\}\right)$ are calculated following

$$P_{|ct\rangle->|c0\rangle} \ = \ 1 - P_{|ct\rangle->|c1\rangle}, c,t \ \in \{0,1\}\,. \tag{5.8}$$

The corresponding truth table is visualized in Fig. 5.26.
The probabilities larger than 85 % indicate that the interaction between the two qubits is not a limitation but the operations on the single qubits as discussed above. A special case is the input of a $|10\rangle$ state which reaches a probability of only $62(8)$ % for the expected outcome $|11\rangle$. On the one hand, this is caused by the maxima of the yellow curve in Fig. 5.24 which do not reach as high values as the maxima of the blue curve. On the other hand, this point is evaluated for the preparation by a $\hat{R}_2(2\pi, 0)$ rotation of the target atom which includes higher dephasing due to the rotation by 2π. The differential light shift of the red Rydberg light does

not allow to use the natural version without a rotation.
As a conclusion, a restricted (i. e. postselected) CNOT operation could be demonstrated the first time in this experiment and shows a clear interaction between the single qubits via the Rydberg blockade. The main causes for errors are identified in the operations on the single qubits regarding the operations on the ground states as well as the excitation to the Rydberg state. Possible reasons are identified in drifts occurring on timescales longer than 60 min as discussed in Sec. 5.3.5 and varying distances between the atoms and a varying overlap of the laser beams used for the addressing and the atoms as indicated in Sec. 5.4.2. This gives a starting point for future developments.

Tab. 5.6.: Truth table of outcomes of the restricted (i. e. postselected) CNOT operation. Bold printed numbers are read out from Fig. 5.24 (a) and from Fig. 5.24 (b) for the values with errors from 1-qubit operations excluded. Probabilities for projection on state $|0\rangle$ are calculated from $P_{|ct\rangle->|c1\rangle}, c, t \in \{0, 1\}$ as $1 - P_{|ct\rangle->|c1\rangle}$.

Output / Input	$\|00\rangle$ Min: $25(5)$ % Max: $65(5)$ %	$\|01\rangle$ Min: $35(5)$ % Max: $75(5)$ %	$\|10\rangle$ Min: $30(5)$ % Max: $65(5)$ %	$\|11\rangle$ Min: $35(5)$ % Max: $70(5)$ %
$\|00\rangle$	$59(5)$ %	$\mathbf{41(5)}$ %	-	-
1-qubit errors excluded	$90(11)$ %	$\mathbf{10(11)}$ %	-	-
$\|01\rangle$	$\left(27^{+6}_{-4}\right)$ %	$\left(\mathbf{73^{+4}_{-6}}\right)$ %	-	-
1-qubit errors excluded	$\left(3^{+13}_{-10}\right)$ %	$\left(\mathbf{97^{+10}_{-13}}\right)$ %	-	-
$\|10\rangle$	-	-	$38(8)$ %	$\mathbf{62(8)}$ %
1-qubit errors excluded	-	-	$12(20)$ %	$\mathbf{88(20)}$ %
$\|11\rangle$	-	-	$62(7)$ %	$\mathbf{38(7)}$ %
1-qubit errors excluded	-	-	$95(20)$ %	$\mathbf{5(20)}$ %

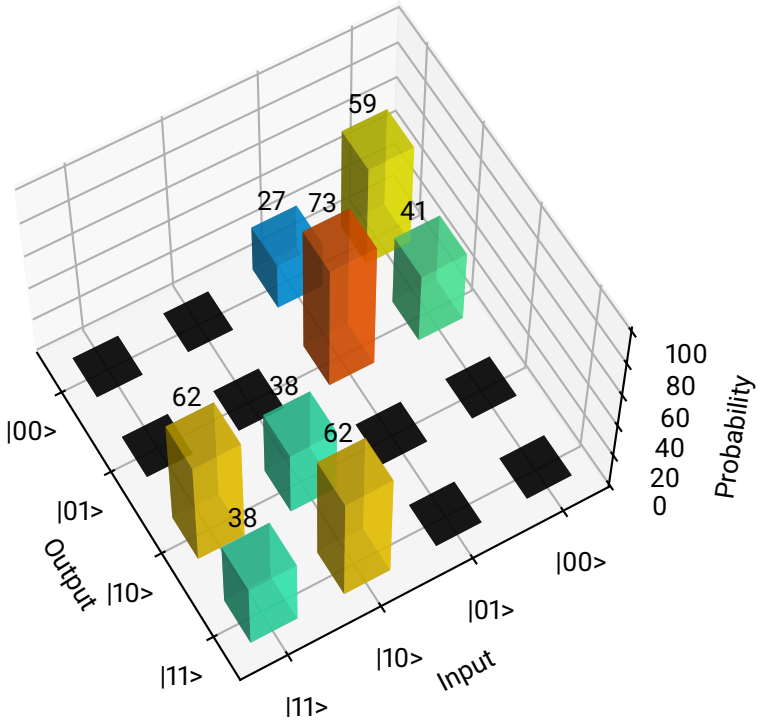

(a)

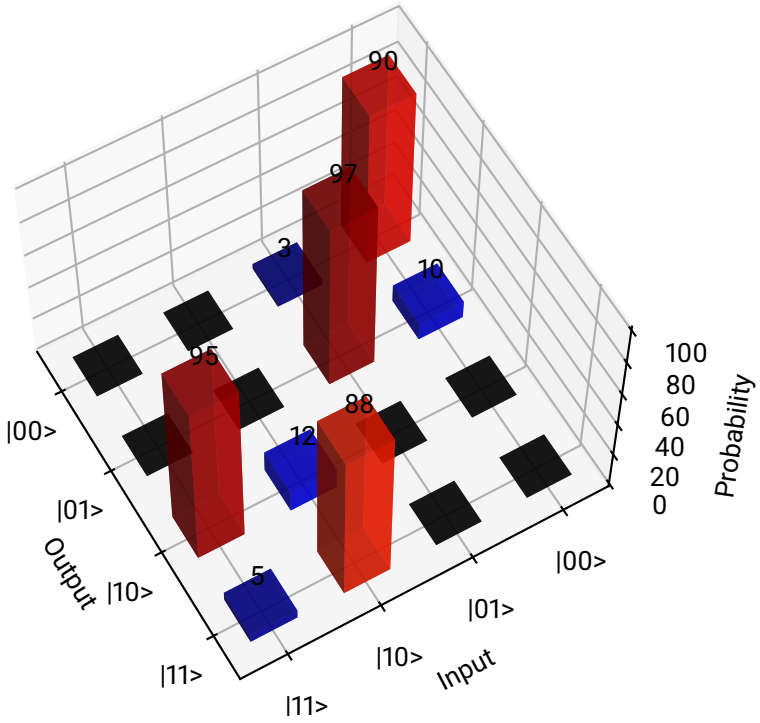

(b)

Fig. 5.26.: (a) Visualization of the truth table of the restricted (i. e. postselected) CNOT operation with probabilities extracted from the fits in Fig. 5.24 (a). (b) The same data corrected for errors of 1-qubit operations extracted from the fits in Fig. 5.24 (b) as explained in the text. Black bars indicate configurations that are not tested due to the required postselection.

5.5. Conclusion

This chapter showed the operations required for a CNOT gate. Operations on the qubit basis states are demonstrated regarding globally addressed rotations on all atoms in the array on the one hand and rotations and virtual-Z rotations single-site addressed on individual qubits. The excitation of individual atoms to Rydberg states is demonstrated with an effective Rabi frequency of up to $1.0(1)$ MHz resulting from on-resonance Rabi frequencies of $\Omega_1 = 2\pi \times 55(21)$ MHz (red Rydberg light) and $\Omega_2 = 2\pi \times 12(3)$ MHz (blue Rydberg light). The application of an optical phase-locked loop in both laser systems for the red and the blue Rydberg laser has been demonstrated and gives perspective on a future evaluation of errors and drift in the experiment that limit the results on averaging times longer than 1 h. Using the OPLL, the Rydberg blockade could be demonstrated and the blockade strength is tested. The blockade strength is measured to be 20 % smaller than expected from the calculation. Though, the van-der-Waals coefficient of $h \times -5559$ GHz µm^6 can be accepted as an error in the position of the atoms of only $0.34(14)$ µm or 3 % in the absolute position can explain this deviation. The broadening of the Rydberg resonance in the blockaded case gives perspective to future investigations for improvements of the experiment. Using the Rydberg blockade, a restricted (i. e. postselected) CNOT operation on one trap site could be demonstrated. The scaling of this operation to other trap sites is only a governed by calibration and measurement time but directly possible with the given setup.
All measurements suffer from low success probabilities. The Ramsey experiments performed with single traps show results in a band between 20 % and 80 % detection in the upper qubit basis state. This is the major error that is also present in the CNOT operation. The Rydberg excitation shows a maximum detected probability of 65 %. Though a small error for the detection of a Rydberg state is included in this number as discussed in [39], the required postselection for measurements with the Rydberg blockade indicate that the probability for a Rydberg-Rydberg interaction is dominated by a probability for a single excitation of 75 %.
These limitations are the major limit for the demonstration of gates in this experiment. Though both success rates need to be improved in order to show quantum computation, the implementation of a CNOT protocol that decouples the 2-qubit gate from the 1-qubit gate success rates would be a promising alternative. The Levine-Pichler gate sequence [32] using optimal control [137] is a perspective for this task.

6. Demonstration of quantum sensing

The universal and coherent control over quantum mechanical states in an array of individual atoms allows for many other applications than quantum computing. One of these applications is quantum sensing as demonstrated in [138]. Whereas the clock states are used for the demonstration of gate operations because of their weak interaction with the environment, the choice of states with quantum numbers $m_\mathrm{F} \neq 0$ allows the interaction with the environment on purpose. This is used for the demonstration of a magnetic field sensor.
In this chapter, the differences to the experiments shown so far, regarding the used configuration of laser systems and magnetic fields, are described first. Then, the results of the Ramsey spectroscopy used for the magnetic field sensing are shown for one example. Next, the magnetic resolution and sensitivity of the sensor are discussed. Finally, the result for a measurement of the spatial distribution of a quadrupole field is shown.

6.1. Experimental setup for quantum sensing

For the demonstration of quantum sensing in the Quips-B experiment, a configuration of laser beams and magnetic fields as shown in Fig. 6.1 is used. As a global spectroscopy on all atoms simultaneously is sufficient for quantum sensing, as long as a site-resolved detection is performed, a spectroscopy beam is irradiated along the **x** direction with a waist at the atom plane of $170(20)$ µm, avoiding the use of the high-NA objective. This reduces aberrations in the optical beam path. The **x** direction allows to use a two-photon transition via the $|5^2\mathrm{P}_{3/2}\rangle$ manifold as light along this direction does not point towards the EMCCD camera. This light is produced with a system of two phase-locked ECDLs similar to the system described in Sec. 4.1.1 but with lasers operating at $780\,\mathrm{nm}$ and a detuning of $\Delta_{\mathrm{i},1} = -2\pi \times 9\,\mathrm{GHz}$ to the D2 line of ^{85}Rb [139].
The setup of magnetic fields is shown in detail in Fig. 6.2 (a). Following the direction of the spectroscopy beam, the quantization field B_q is also set in the **x** direction as marked with the red arrows. The field is generated with the coils shown in red color aligned with the **x** direction. These coils are operated in Helmholtz configuration carrying the current I_q. The magnetic field strength of this field is set to $283(1)$ µT and can be altered in steps of $10(1)$ nT, using a 4 1/2 digit voltage source in current mode (Hewlett-Packard, HP6626) which controls the current I_q. Tests with these step sizes can be used for a direct evaluation of the resolution of magnetic field sensing.
Additionally to the quantization field, a pair of coils in anti-Helmholtz configuration induces a test field $\mathbf{B}_\mathrm{t}$ set by the counter-propagating currents I_t. These coils are aligned along the **z** direction and generate the quadrupole field that is used for the MOT. The atom plane is located in the center between both pairs of coils such that the atoms experience the homogeneous part of the quantization field and a part of the test field close to the zero-crossing of its magnetic field strength.
The two fields allow the demonstration of two types of experiments. The first experiment tests the magnetic field resolution δB by an analysis of the quantization field without the activation of the test field. The second experiment tests the capabilities of measuring the spatial distri-

bution of the test field.
The experimental cycle for both experiments is drawn in Fig. 6.2 (b). The parameters used for the optical dipole traps are listed in Tab. 6.1. The experiment starts with an array of individual atoms as described in Sec. 3.4 and a first fluorescence image serving as the reference image. After imaging, the traps are ramped down to a trap depth of $k_\mathrm{B} \times 0.2\,\mathrm{mK}$.

Then the state preparation is performed via interrupted optical pumping using π-polarized light resonant to the transition $|5^2\mathrm{S}_{1/2}, \mathrm{F} = 3, m_\mathrm{F} = 0\rangle \leftrightarrow |5^2\mathrm{P}_{3/2}, \mathrm{F}' = 3, m_{\mathrm{F}'} = 0\rangle$ in combination with a repumping at the transition $|5^2\mathrm{S}_{1/2}, \mathrm{F} = 2, m_\mathrm{F} = 0\rangle \leftrightarrow |5^2\mathrm{P}_{3/2}, \mathrm{F}' = 3, m_{\mathrm{F}'} = 0\rangle$. Starting from a population with a major fraction in the state $|5^2\mathrm{S}_{1/2}, \mathrm{F} = 3, m_\mathrm{F} = -3\rangle$, a fraction of $30\,\%$ is transferred into the state $|5^2\mathrm{S}_{1/2}, \mathrm{F} = 3, m_\mathrm{F} = -1\rangle$. This state is chosen because it shows the highest preparation rate of all magnetically sensitive states excluding $|m_\mathrm{F} = -3\rangle$ which is not accessible with the two-photon process. The measurement is performed using a Ramsey experiment of the superposition of states $|\uparrow\rangle = |5^2\mathrm{S}_{1/2}, \mathrm{F} = 3, m_\mathrm{F} = -1\rangle$ and $|\downarrow\rangle = |5^2\mathrm{S}_{1/2}, \mathrm{F} = 2, m_\mathrm{F} = -1\rangle$.
A Ramsey experiment is created by two $\pi/2$ pulses of the spectroscopy beam separated by a time of free precession T. In this experiment, precession times of up to $200\,\mu\mathrm{s}$ are used to characterize the sensor. The time steps are chosen to a resolution of $2\,\mu\mathrm{s}$. Then, the result of the Ramsey experiment is determined by a state projection using the same technique as described in Sec. 3.3 with a beam counter-propagating the spectroscopy beam. Finally, the trap depth is

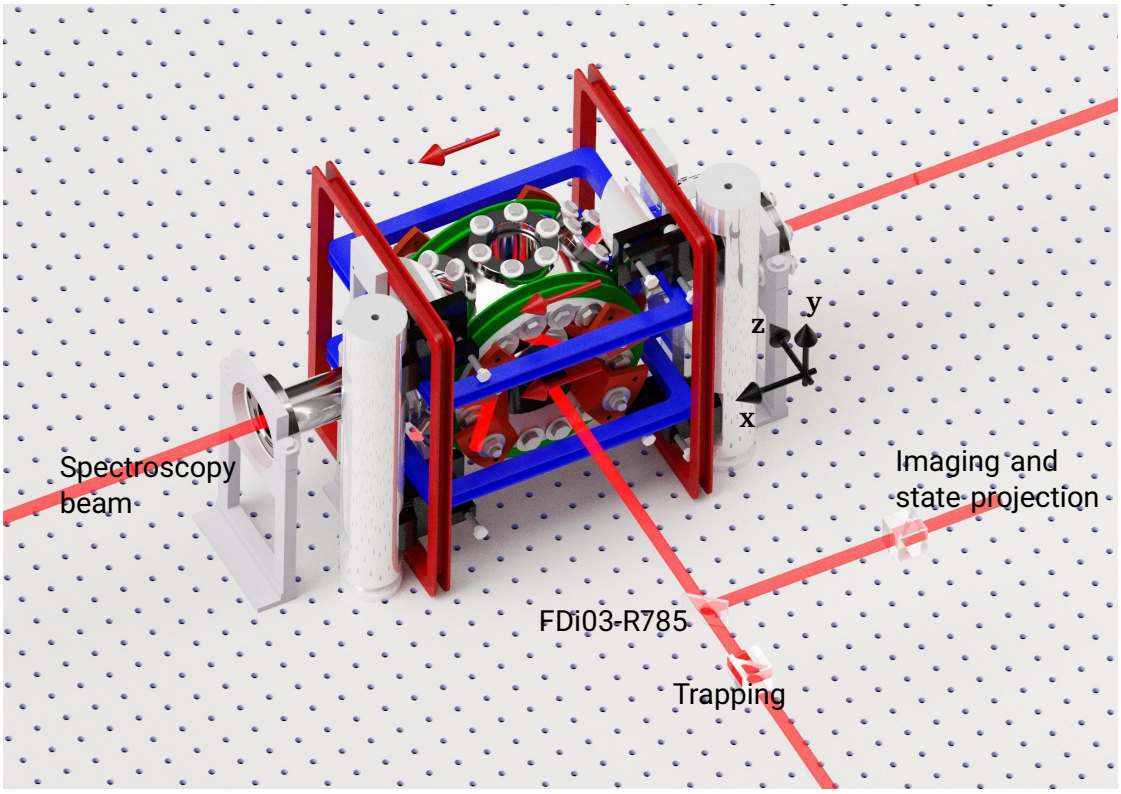

Fig. 6.1.: Render graphic of the vacuum chamber with a schematic visualization of the most import beams: The trapping light superimposed with the beam path for imaging and state projection is drawn in the front; The spectroscopy beam propagates from left to right along the $-\mathbf{x}$ direction. The magnetic field coils drawn in red induce a homogeneous magnetic field indicated by the red arrows.

ramped up for a second image used for the evaluation of atom loss induced by the state projection. For magnetic sensing, an array of 18×15 trap sites with a pitch of $7.0(2)$ µm is evaluated.

Tab. 6.1.: Parameters of trapping light used in the different steps of the experimental cycle used for the demonstration of quantum sensing. The given power is the total laser power used for the generation of the trap array. The trap depth is the calculated trap depth of the central trap.

Stage in experimental cycle	Wavelength of trapping light in nm	Power of trapping light in W	Trap depth in units of $k_B \times$ mK
Loading of traps	796.5	0.79	1.4
Time of free evolution	796.5	0.11	0.2

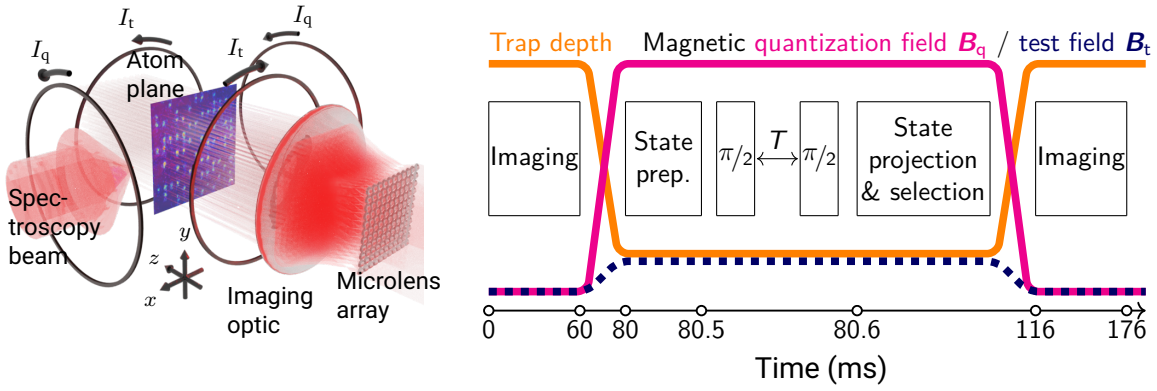

(a) (b)

Fig. 6.2.: (a) Configuration of magnetic fields used for the demonstration of the magnetic field sensor. The quantization field along the **x** direction is induced by currents I_q co-propagating through a pair of coils in Helmholtz configuration. The test field is induced by counter-propagating currents I_t through a pair of coils in anti-Helmholtz configuration oriented along the **z** direction. (b) Scheme of the experimental cycle showing the major steps of imaging, state preparation, Ramsey spectroscopy and state projection. The trap depth and the magnetic field strengths of the quantization field and of the test field are drawn over time, both not to scale.

6.2. Globally addressed Ramsey spectroscopy

For the evaluation of the magnetic field resolution δB, an array of 3 x 3 atoms is sorted and the influence of two different magnetic field strengths on the phase evolution of the atoms is tested. From the phase evolution, quantified by the Ramsey period T_R or Ramsey frequency $\omega_R = 2\pi/T_R$, the magnetic field strength at the location of each individual atom can be calculated on the basis of the Zeeman effect (3.30). A set magnetic field B in first order shifts the transition

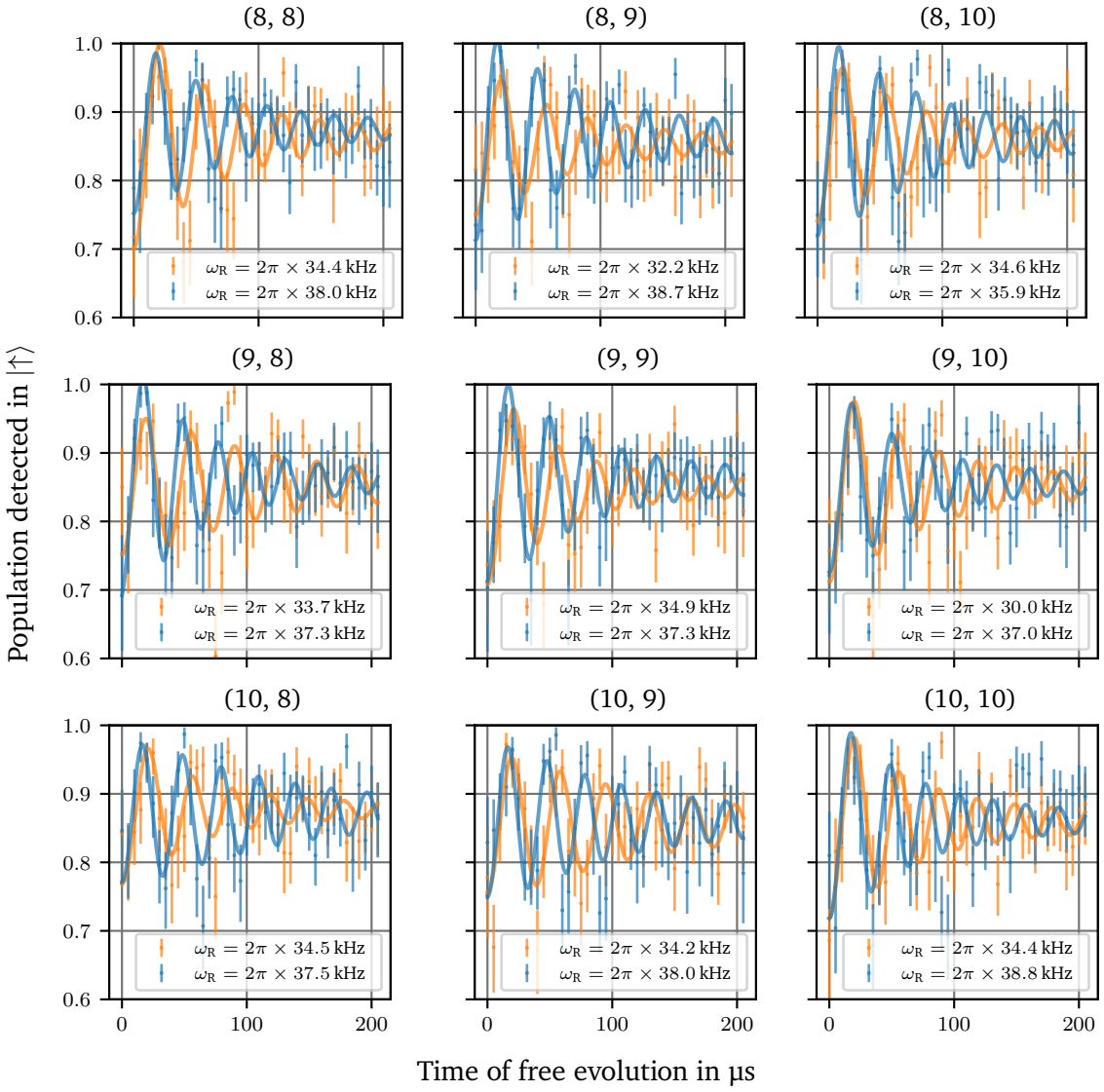

Fig. 6.3.: Site-resolved Ramsey experiments used for magnetic field sensing. The external magnetic field is tested for $283(1)$ µT (blue) and $500(10)$ nT less (yellow). With full measurement time, all individual traps show a clear discrimination between the two settings of the magnetic field in agreement with the magnetic field resolution of $\delta B = 98(29)$ nT for the full averaging time of 6.4×10^4 s.

frequency proportionally following [43]

$$\Delta E_{|\uparrow\rangle|\downarrow\rangle} = \hbar \, 9.2777(3) \, \frac{\text{kHz}}{\mu\text{T}} \, |\mathbf{B}| \, . \tag{6.1}$$

The result of the Ramsey experiments is shown in Fig. 6.3. As magnetic field strengths, the standard value used with this pair of coils of $283(1)$ µT is used and compared to a setting that is supposed to create a field strength that is smaller by $500(10)$ nT. For both settings of the magnetic field strength, a $1/e$ amplitude damping of $T_2^* = 100(32)$ µs with a range of $(65 - 159)$ µs over the array is found. As these traps are located in the center of the array, the damping due to the trapping light is slightly higher than for outer traps. In the mean over the

whole array (18 x 15 traps), a damping of $T_2^* = 118(33)$ µs is found.
Over a period of 100 µs, two frequencies with a difference of 5 kHz build up a phase shift of π. A frequency resolution of at least 5 kHz is therefore expected for this measurement principle. The used step size of 2 µs is chosen to measure a frequency range from $(0 - 500)$ kHz. Within this range of frequencies, a Ramsey frequency is chosen that allows to identify a range of acceleration (or retardation) of the Ramsey frequency corresponding to the range of energy shifts induced by the magnetic field strength. A Ramsey frequency of 37.6 ± 0.3 kHz is set for the standard magnetic field strength by an appropriate detuning Δ_{12} relative to the two photon resonance, resulting in a range of $(35.9 - 38.8)$ kHz over the array. With this choice, energy shifts in the range of $-\hbar \times 25$ kHz to $\hbar \times 460$ kHz could be resolved.
As shown in Fig. 6.3, the step of $500(10)$ nT shifts the Ramsey frequencies from a mean of 37.6 ± 0.3 kHz for the standard magnetic field to 33.7 ± 0.5 kHz and a range of $(30.0 - 34.9)$ kHz. This corresponds to a mean frequency difference of 3.9 ± 0.8 kHz, corresponding to a phase shift of only $0.78 \times \pi$ which is a slightly better resolution than the estimation of a minimum phase difference of $1 \times \pi$ calculated above.

6.3. Resolution of the magnetic field sensor

The damping and the shot noise of the data resulting from the Ramsey spectroscopy (see i. e. Fig. 6.3) limit the resolution of the Ramsey frequency. Whereas the damping of the Ramsey oscillations is set by the experimental setup, especially regarding the scattering rate of the trapping light, the shot noise scales with the number of samples. This is quantified with the Allan variance (AV) [140, 141]. For the calculation of the AV, the measured data points a_i with $i = 1, 2, ...N$ are binned into non-overlapping time slots k with highest value K:

$$\underbrace{a_{(1)},\ a_{(2)}, \dots\ a_{(m)}}_{k=1},\ \underbrace{a_{(m+1)},\ a_{(m+2)}, \dots\ a_{(2m)}}_{k=2}\ \cdots\ \underbrace{\cdots\ a_{((K-1)\,m-1)},\ a_{(N)}}_{k=K}. \tag{6.2}$$

With m samples in one time slot, the average $\overline{a}\,[k]$ of the single results in this time slot k is

$$\overline{a}\,[k] \;=\; \frac{1}{m}\sum_{i=1}^{m} a_{((k-1)m+i)} \tag{6.3}$$

for all $k = 1, 2, 3, \dots K$. For data sampled on a constant frequency f, the number of points in one slot can also be labeled with their sampling times $t_k(j) = ((k-1)\frac{\tau}{K} + j\frac{t}{m})$:

$$\underbrace{a_{t_1(1)},\ a_{t_1(2)}, \dots\ a_{t_1(m)=\tau/K}}_{k=1},\ \underbrace{a_{t_2(1)},\ a_{t_2(2)}, \dots\ a_{t_2(m)=2\tau/K}}_{k=2}\ \cdots\ \underbrace{\cdots\ a_{t_K(m-1)},\ a_{\tau}}_{k=K} \tag{6.4}$$

with the sampling time t for one slot. This duration is directly proportional to the averaging time τ following $t = \tau/K$. For each cluster, the average $\overline{a}_\tau\,[k]$ can be defined up to a specific averaging time τ with

$$\overline{a}_\tau\,[k] \;=\; \frac{K}{\tau\, f}\sum_{i=1}^{m} a_{(k-1)\frac{\tau}{K}+i\frac{t}{m}}. \tag{6.5}$$

Then, the AV up to the averaging time τ is defined by

$$\sigma_A^2(\tau) \;=\; \frac{1}{2(K-1)}\sum_{k=1}^{K-1}\left(\overline{a}_\tau\,[k+1] - \overline{a}_\tau\,[k]\right)^2. \tag{6.6}$$

The Allan deviation σ_A is the square root of its variance. Due to the scaling of the Allan variance with $(2(K-1))^{-1}$, the number of time slots K should not be chosen too high to avoid too small sample sizes in each slot. Nevertheless, a sufficient number of slots needs to be evaluated to compare the averages of enough time slots. The optimum number of time slots can be found numerically by minimizing σ_A for each averaging time τ.
An evaluation of the Allan deviation for the data shown in the blue curves in Fig. 6.3 is shown in Fig. 6.4 (a). For averaging times τ larger than 3×10^4 s, the Allan deviation for the results summed over the array of 3 x 3 traps decreases below 1 µT in a sharp edge.
This behavior is explained by an analysis of the Allan deviations of the individual traps shown in Fig. 6.4 (b). For each trap, the Allan variation is nearly constant for short averaging times and drops below 1 µT for an individual averaging time. To the knowledge of the author, this is not a systematic error of single trap sites but rather a statistical effect caused from the fitting of the Ramsey frequency to the data points as shown in Fig. 6.3. The nearly flat line for short averaging times can be explained by too noisy data that do not allow the identification of one

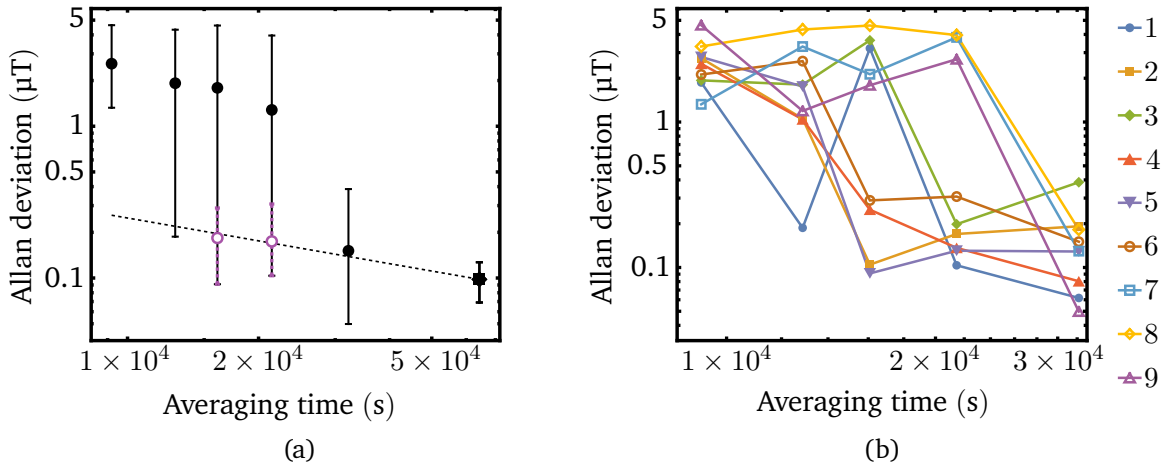

Fig. 6.4.: (a) Analysis of the Allan deviation for the measurement of the magnetic field strength extracted from the average of the Ramsey experiments in Fig. 6.3. The data is binned to analyze the convergence of the measurement towards the value for the full averaging time. The points in purple are concluded from the analysis of the single traps shown in (b). There, the Allan deviation is plotted for each of the nine traps separately showing a plausible result for some traps already for shorter averaging time. The purple points are the mean values of the results for traps 2, 4, 5, and 6 for the two respective time bins. The traps are indexed from left to right, line-by-line starting from the top left corner of the 3 x 3 array.

dominant frequency. The Allan deviation therefore does not decrease with longer measurement time until a dominant frequency is fitted. Taking only those results into account, that dropped below a deviation of 1 µT, the type of noise of this sensor can be estimated using the extrapolation in Fig. 6.4 (a). The linearly decreasing Allan variation in the log-log plot is a sign of white noise dominating the result of the sensor on these timescales [111]. The slope of this extrapolation corresponds to the sensitivity of $25\,\mu\mathrm{T}/\sqrt{\mathrm{Hz}}$, taking into account that from the total averaging time only a fraction of 2.3×10^{-8} corresponds to the time of free precession [142].

6.4. Measurement of external fields

The capability of measuring the spatial variation of an external magnetic field is demonstrated with the test field. A self-calibrating cycle is used by measuring the quantization field together with and without the test field. For each trap, two Ramsey spectroscopies are performed, of which one measures the Ramsey frequency $\omega_{\mathrm{R,ref}}$ describing the quantization field and the other measures the Ramsey frequency ω_{R} probing the geometric sum of the quantization field and the test field following

$$\left|\mathbf{B}_{\mathrm{ges}}\right| = \sqrt{(B_{\mathrm{q},x}+B_{t,x})^2+(B_{t,y})^2+(B_{t,z})^2},\quad B_{\mathrm{q},x}\gg B_{\mathrm{t},x},B_{\mathrm{t},y},B_{\mathrm{t},z}, \tag{6.7}$$

$$\approx B_{\mathrm{q},x}+B_{\mathrm{t},x}. \tag{6.8}$$

As the quantization field is the dominating field for all traps, only the **x** component of the test field $B_{\mathrm{t},x}$ gives a significant contribution in the geometric sum as it is oriented in the direction of the quantization field. The two Ramsey frequencies ω_{R} and $\omega_{\mathrm{R,ref}}$ calculated from the

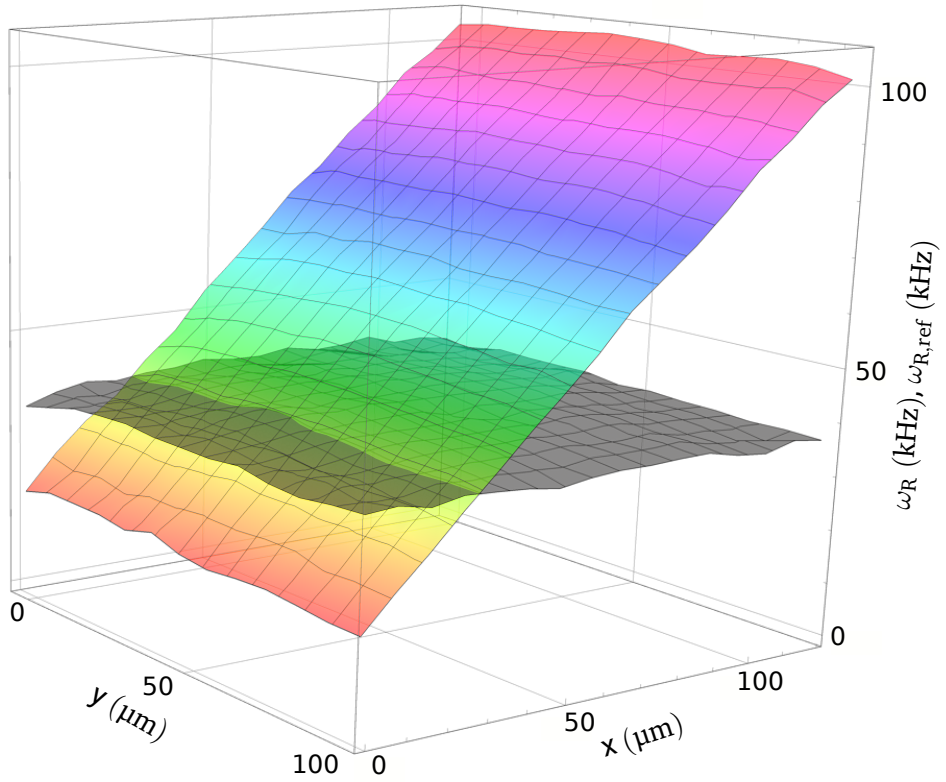

Fig. 6.5.: Three-dimensional visualization of the measured Ramsey frequencies induced by the quantization fields (gray) and the quadrupole field together with the quantization field (colored). A superposed linear slope induced by the quadrupole field along the **x**-axis is visible in the colored surface together with a slight curvature induced by the variation of the differential light shift induced by the trapping light in both measurements.

spectroscopies for these two situations are shown in Fig. 6.5. The trap positions are converted into spatial dimensions using the separation of the traps of $7.0(2)\,\mu\text{m}$. This spans up the size of the sensor of $119\,\mu\text{m} \times 98\,\mu\text{m}$ (18 × 15 pixel).
The gray plane shows the calibration measurement with the quantization field alone. A slight variation over the sensor size is visible and is due to the variation of the differential light shift induced by the trapping light. With the activated test field, the Ramsey frequencies show a linear variation over the **x** direction. Higher values than for the quantization field alone are measured for **x**-positions larger than $25\,\mu\text{m}$. Following (6.8), this corresponds to a contribution of the test field in the direction of the quantization field. For smaller **x**-positions, the measured Ramsey frequencies are smaller than for the quantization field alone. This corresponds to an opposite polarity of this component of the test field compared to the quantization field.
From the differences of the Ramsey frequencies $\Delta\omega_{\mathrm{R}(x,y)}$ following

$$\Delta\omega_{\mathrm{R}(x,y)} = \omega_{\mathrm{R}}(x,y) - \omega_{\mathrm{R,ref}}(x,y) \tag{6.9}$$

the magnetic field strength of the **x** component of the test field can be calculated using (6.1). Following

$$B_{\mathrm{t},x}(x,y) = \frac{\Delta\omega_{\mathrm{R}(x,y)}}{9.2777(3)\,\frac{\mathrm{kHz}}{\mu\mathrm{T}}} \tag{6.10}$$

the measured differences in the Ramsey frequency $\Delta\omega_{\mathrm{R}(x,y)}$ are transformed into the magnetic field strength. The resulting magnetic field strength of the **x** component of the test field $B_{\mathrm{t},x}(x,y)$ is shown in Fig. 6.6. As only the **x** component of the test field gives a signif-

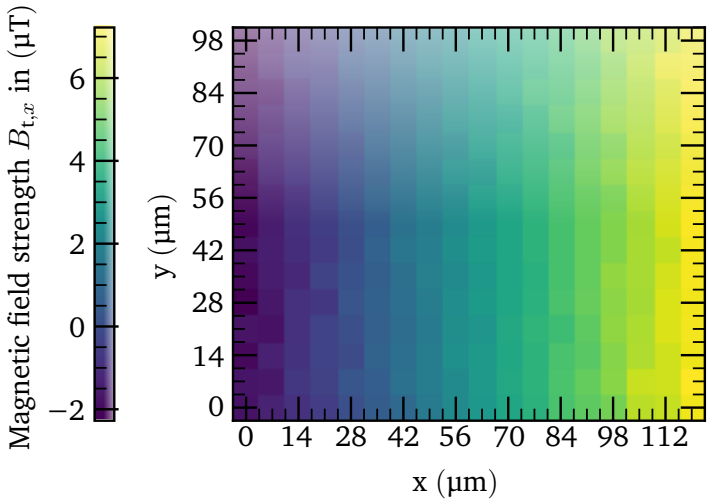

Fig. 6.6.: Evaluation of the magnetic field strength of the **x** component of the test field showing a range of -2µT to 7 µT.

icant contribution to the Ramsey spectroscopy, the 15 traps along the **y** axis are supposed to deliver identical values. From the statistics of these traps, the mean uncertainty of the frequency differences can be calculated. Over the full sensor size, the uncertainty amounts to $2\pi\times0.91(27)$ kHz. This demonstrates a magnetic field resolution δB of $98(29)$ nT.
The measured component of the quadrupole field shows a linear slope over the sensor size of $77.3(4)$ nT µm^{-1} over a range of -2µT to 7 µT. The linear slope of this component of the quadrupole field corresponds to the expectation to this field. As this field is used for the MOT, the zero-crossing is supposed to be located inside the atom array in order to achieve a good overlap of the MOT and the dipole trap array. For the **x** component of the field, this can be confirmed by this measurement. A measurement of the zero crossing for the other two components of the quadrupole field would give a starting point for further optimizations of the experiment.
The spatial resolution of this measurement is $7.0(2)$ µm. Tests with one atom in a movable optical tweezer showed the possibility of using this technique for a finer spatial sampling with a maximum resolution of $1.3(4)$ µm. These results are reported in detail in [61].

6.5. Conclusion

An array of 18 × 15 individual atoms has been demonstrated to act as a spatially resolved magnetometer with magnetic field resolution δB of $98(29)$ nT. This could be verified using a defined step of the quantization field of $500(10)$ nT which could be well resolved with a measurement time of 6×10^4 s. One component of a magnetic quadrupole field could be probed with results in a range of -2µT to 7 µT and a spatial resolution of $7.0(2)$ µm. Using a movable tweezer, the spatial resolution can be improved to $1.3(4)$ µm. Separating the time used for the

generation of the atom array from the time of free evolution used in the Ramsey experiments, a sensitivity of $25\,\mu\mathrm{T}/\sqrt{\mathrm{Hz}}$ is calculated.
This first demonstration of quantum sensing in this experiment opens the door for much more advanced operations. A straight-forward optimization can be achieved by using the techniques for gate operations presented in the previous chapters in this measurement scheme. Using the Raman-assisted pumping, the $|\mathrm{F} = 2, m_\mathrm{F} = -1\rangle$ state could be prepared with nearly $90\,\%$ probability. This would allow to reduce the sampling time by nearly two thirds. Additionally, the light inducing the Ramsey experiment here has a wavelength of $780\,\mathrm{nm}$. Using the same techniques with light at a wavelength of $795\,\mathrm{nm}$ gave evidence for longer decoherence times than used here. Furthermore, an orientation of the quantization field along the **z** direction would allow the measurement of one more component of the quadrupole field, giving more evidence for an optimum positioning of the MOT in this experiment. By turning the magnetic field axis from shot to shot, the direct measurement of both components could be demonstrated. As the initial state preparation is demonstrated for both axis and is defined only by the orientation of the light inducing the operations on the qubit basis states for the Raman-assisted pumping, only the setup of beam lines for $795\,\mathrm{nm}$ in both directions, the **x** and **z** direction would be required for this demonstration.

7. Discussion and future perspectives

In the course of this thesis, the versatile use of neutral atoms in optical tweezer arrays has been demonstrated in the context of quantum sensing and quantum computing. Using the sensibility of $m_\mathrm{F} = -1$ states, a magnetic field sensor with unique properties such as a magnetic resolution of $\delta B = 98(29)\,\mathrm{nT}$ and a spatial resolution down to one micrometer has been demonstrated [138]. For the same system, the first steps with gate operations on neutral atoms has been taken regarding 1-qubit operations and 2-qubit operations. The key to the demonstration of both types of gates was the alignment of the quantization field along the **z** direction. New optical systems have been implemented to the experiment in order to combine all subsystems required for the 2-qubit operation.
Regarding the 1-qubit operation, the operation is implemented on the D1 line of ^{85}Rb, allowing this light to be irradiated along the **z** direction. Therefore, a new laser system of phase-locked ECDLs at a wavelength of $795\,\mathrm{nm}$ [89] is built. The single-site addressing of the local 1-qubit gate is realized by a system of AODs moving a tightly focused laser spot at any position of the atom array. With this system, rotations around two axes of the Bloch sphere have been demonstrated in this thesis for arbitrary angles θ and ϕ, corresponding to a $\hat{R}(\theta, \phi)$ gate operation.
The combination of these gate operations with a site-specific Rydberg excitation allows the demonstration of a H-C_Z gate. For this task, a system for agile frequency synthesis and experimental control, based on a versatile FPGA platform, has been improved [108], allowing for the fast control of acousto-optic devices and light pulses. A new system for the addressing of individual sites in the atom array with the blue Rydberg light is set up, using AODs as highly efficient and fast addressing system. This has been one key for the demonstration of the site-selective Rydberg excitation. With a quantitative understanding of the properties of Rydberg atoms, the LIAD effect, that has limited this experiment for years, could be kept under control. A novel technique of optical phase-locking of lasers to the light transmitted through an ULE cavity completed the capabilities for reliable experiments with Rydberg atoms.
This thesis firstly demonstrated the application of all requirements for a CNOT operation in the Quips-B experiment. Using all these techniques, a restricted (i. e. postselected) CNOT operation could be demonstrated at an arbitrary position in the atom array. The result of this demonstration gives rise to many optimizations needed in order to demonstrate quantum computation and to improve the capabilities of quantum sensing. Some of these are named in the following.

7.1. Optimization of magnetic field sensing

The magnetic field sensing with the states $|\mathrm{F} = 2, m_\mathrm{F} = -1\rangle$ and $|\mathrm{F} = 3, m_\mathrm{F} = -1\rangle$ was demonstrated before the implementation of the Raman-assisted pumping. Using the Raman-assisted pumping, the preparation of the $|\mathrm{F} = 2, m_\mathrm{F} = -1\rangle$ state could be improved to close to $90\,\%$. This would allow to perform the shown measurements in less than a third of the time than in the presented sequence. Additionally, the magnetic field along the **z** direction could by tested, providing more information about the zero-crossing of the quadrupole field used for the MOT.

7.2. Optimization of the traps

In the neutral atom community, many new techniques for the creation and scaling of optical tweezer arrays have been developed in the recent years which give prospects to traps that offer a more stable operation and less scattering. With the used microlens arrays, a larger detuning of the trapping light would offer a much longer T_1 depolarization time and less differential light shift. In the regime of a detuning of $50\,\mathrm{nm}$, a scaling with δ^{-4} is expected and would allow an even larger depolarization time [79].
But not only the parameters of the dipole traps can be developed further. Another approach is the utilization of dark-spot arrays, storing the atoms in blue detuned traps. Demonstrations of such "bottle beams" have already shown a cloud of trapped atoms [143] and also trap arrays [144].

7.3. Optimization of the 1-qubit operation

The 1-qubit operations show a large potential for optimization which is already ongoing. A new laser system allowing for adaptions of the phase of the beat note of the two light fields inducing the 1-qubit gate on the timescale of nanoseconds has been developed [145] in order to achieve virtual-Z rotations on much shorter timescales than demonstrated here. This would allow the preparation of arbitrary quantum states of the individual atoms only limited by the switching time of the AOD system. The preparation of an array of 5 x 5 atoms within $100\,\mu\mathrm{s}$ can be expected. Additionally, a fast control over this phase would allow the execution of H gates, which is required for establishing the correct outcome of the CNOT gate.
Another progress could be achieved with a laser system optimizing the Raman-assisted pumping scheme with the ability of fast frequency jumps as described in Sec. 4.1.2. This would allow to reduce the time for state initialization by an order of magnitude.

7.4. Optimization of the Rydberg excitation

The observation of a shift of the Rydberg resonance after pulses of light at short wavelengths allowed to gain control over these shifts. An estimation using the polarizability of the Rydberg atoms is consistent with the explanation, that a LIAD effect produces electric fields in the science chamber. But though the shift of the resonance is under control on timescales resolvable with the experiment, fast fluctuations cannot be excluded. In order to avoid electric charge on the vacuum windows, a coating with indium tin oxide on the inside is recommended for setups for experiments with Rydberg atoms. This technique has been applied successfully in the Rydberg experiment described in [146].
Though huge progress could be achieved regarding the phase noise of the Rydberg lasers, the improvement for the Rydberg excitation falls short of the expectations. The Rydberg excitation is still limited to probabilities of $75\,\%$ on long averaging times. The reasons for this need further investigation. One possible explanation is that the positions of the addressing system of the blue Rydberg light and the atoms show too much variation [129]. This would also explain the low performance of the local 1-qubit operation. A straightforward test of this hypothesis is to use a larger spot size of the blue Rydberg light or of the light inducing the 1-qubit gate. Nevertheless, single-site addressed operations bear complex dynamics regarding the fidelity of quantum operations as shown in [129].

7.5. Optimization of the 2-qubit operation

The test of the 2-qubit operation showed very low success rates which are mainly due to the errors of the 1-qubit operations and the Rydberg excitation. But regarding the gate operation itself, the differential light shift of the red Rydberg light is a fault that needs to be eliminated for a stable operation. The compensation of differential light shifts is possible as shown in [147] and the optical access in the laser system is already prepared. It is a straightforward step to implement this feature.
The test of the 2-qubit operation suffers additionally from a lack of fast Z gates. With a fast manipulation of the phase of the light inducing the 1-qubit gate, H gates can be used in the CNOT sequence as intended in the H-C_Z protocol.
But even with this implementation, the gate sequence itself can be optimized. As discussed in recent work, the Levine-Pichler gate is a more promising protocol that avoids many of the error sources limiting this work. Especially, this gate protocol decouples the errors of the 1-qubit gate from the errors of the 2-qubit gate as it does not rely on operations on the qubit basis states. Furthermore, the time needed for switching from one qubit to another is eliminated as both qubits are excited to the Rydberg state at the same time. Typically, this is performed using a DMD. But due to the inherent cancellation of frequency offsets of the AOD system for addressing diagonal neighbors with the blue Rydberg light shown here, this system in-principle allows the demonstration of this protocol, too. With the implementation of a multi-tone signal for the AODs (f_3, f_4) and a phase operation in the frequency controlling the red compensation AOM (f_5), this gate protocol is within the scope of this experiment.

7.6. Outlook towards scaling into 3D

The Talbot planes, created automatically by the microlens array used for the creation of dipole traps, offer an ideal starting point for the scaling of this system into three dimensions. Additionally, the imaging of multiple planes of a three-dimensional array of atoms has already been demonstrated [148]. A short discussion about the option of using the third dimension is added because this seems to be very promising for a further scaling of qubits.
The main reason why this is not intended in this thesis is the problem of a fast adaption of an optical focus. As stated for the addressing of different qubits, a switching time on the order of $1\,\mu s$ is desired. Even if this limit is raised towards $10\,\mu s$, there is no optical element to the knowledge of the author that would allow to switch the optical focus of the camera or of the single-site addressed light beams within this time span.
There could be an intermediate region in timings where multiple layers of atom planes could be used sequentially and independently from each other so that the timing limit would not necessarily be given by the decoherence time but by the lifetime of the trapped atoms. Nevertheless, the integration of such a technique in a fashion that is compatible with the DiVincenzo criteria is beyond the scope of this thesis. To name one example, the globally addressed state projection could not be used in such a scenario as this light needs to be applied within the decoherence time but would automatically project the states of all atoms in all planes. A starting point for using the Talbot planes not only for storing atoms but to use these atoms for quantum information processing would be a state projection in individual Talbot planes. This would be a further demonstration of the scalability of platforms based on neutral atoms in optical dipole traps created by microlens registers.

A. List of publications

D. Schäffner, T. Schreiber, F. Lenz, M. Schlosser, and G. Birkl, *Quantum Sensing in Tweezer Arrays: Optical Magnetometry on an Individual-Atom Sensor Grid*, PRX Quantum **5**, 010311 (2024).

B. Supervised theses

Bachelor theses

Moritz Domack
Ansteuerung eines AODs mit einem selbst entwickelten Multi-Tone Frequenzgenerator
September 2021

Nathan Fuchs
Charakterisierung eines programmierbaren 'AWGs' für zeitkritische Quantenexperimente
November 2022

Justus Götzinger
Phasengelockter ECDL bei 795 nm mit Stromquelle im Laserkopf
September 2022

Master thesis

Fabian Lenz
Zustandspräparation und Rydberg-Wechselwirkung einzeln adressierter Atome
Mai 2021

Jan Lautenschläger
Initiale Zustandspräparation und Einzelplatzadressierung bei 795nm in einem 2D neutralen Atomgitter
October 2022

Moritz Domack
Single-site addressed state-manipulation and Rydberg excitation on neutral atoms as building blocks for a CNOT gate
December 2023

Simon Bickel
Ramanlaser für Ein-Qubit-Quantengatter: Entwicklung eines Hochleistungssystems mit geringem Phasenrauschen
March 2024

Justus Götzinger
Untersuchung der Fehlerquellen bei 2-Qubit Operationen
December 2024

Bibliography

[1] R. P. Feynman, *Simulating physics with computers*, *International Journal of Theoretical Physics* **21**, 467–488 (1982).

[2] F. Arute, K. Arya, and R. Babbush et al., *Quantum supremacy using a programmable superconducting processor*, *Nature* **574**, 505–510 (2019).

[3] A. Morvan, B. Villalonga, et al., *Phase transitions in random circuit sampling*, *Nature* **634**, 328–333 (2024).

[4] Y. Kim, A. Eddins, S. Anand, K. X. Wei, E. van den Berg, S. Rosenblatt, H. Nayfeh, Y. Wu, M. Zaletel, K. Temme, and A. Kandala, *Evidence for the utility of quantum computing before fault tolerance*, *Nature* **618**, 500–505 (2023).

[5] D. P. DiVincenzo, *The Physical Implementation of Quantum Computation*, *Fortschritte der Physik* **48**, 771–783 (2000).

[6] T. Monz, D. Nigg, E. A. Martinez, M. F. Brandl, P. Schindler, R. Rines, S. X. Wang, I. L. Chuang, and R. Blatt, *Realization of a scalable Shor algorithm*, *Science* **351**, 1068–1070 (2016), eprint: https://www.science.org/doi/pdf/10.1126/science.aad9480.

[7] S. J. Evered, D. Bluvstein, M. Kalinowski, S. Ebadi, T. Manovitz, H. Zhou, S. H. Li, A. A. Geim, T. T. Wang, N. Maskara, H. Levine, G. Semeghini, M. Greiner, V. Vuletić, and M. D. Lukin, *High-fidelity parallel entangling gates on a neutral-atom quantum computer*, *Nature* **622**, 268–272 (2023).

[8] A. Lengwenus, J. Kruse, M. Volk, W. Ertmer, and G. Birkl, *Coherent manipulation of atomic qubits in optical micropotentials*, *Applied Physics B* **86**, 377–383 (2006).

[9] D. Ohl de Mello, D. Schäffner, J. Werkmann, T. Preuschoff, L. Kohfahl, M. Schlosser, and G. Birkl, *Defect-Free Assembly of 2D Clusters of More Than 100 Single-Atom Quantum Systems*, *Phys. Rev. Lett.* **122**, 203601 (2019).

[10] M. Saffman, I. I. Beterov, A. Dalal, E. J. Páez, and B. C. Sanders, *Symmetric Rydberg controlled-Z gates with adiabatic pulses*, *Phys. Rev. A* **101**, 062309 (2020).

[11] H. Levine, A. Keesling, A. Omran, H. Bernien, S. Schwartz, A. S. Zibrov, M. Endres, M. Greiner, V. Vuletić, and M. D. Lukin, *High-Fidelity Control and Entanglement of Rydberg-Atom Qubits*, *Phys. Rev. Lett.* **121**, 123603 (2018).

[12] P. Scholl, M. Schuler, H. J. Williams, A. A. Eberharter, D. Barredo, K.-N. Schymik, V. Lienhard, L.-P. Henry, T. C. Lang, T. Lahaye, A. M. Läuchli, and A. Browaeys, *Quantum simulation of 2D antiferromagnets with hundreds of Rydberg atoms*, *Nature* **595**, 233–238 (2021).

[13] T. M. Wintermantel, M. Buchhold, S. Shevate, M. Morgado, Y. Wang, G. Lochead, S. Diehl, and S. Whitlock, *Epidemic growth and Griffiths effects on an emergent network of excited atoms*, *Nature Communications* **12** (2021).

[14] M. Schlosser, D. O. de Mello, D. Schäffner, T. Preuschoff, L. Kohfahl, and G. Birkl, *Assembled arrays of Rydberg-interacting atoms*, *Journal of Physics B: Atomic, Molecular and Optical Physics* **53**, 144001 (2020).

[15] N. Šibalić, J. Pritchard, C. Adams, and K. Weatherill, *ARC: An open-source library for calculating properties of alkali Rydberg atoms*, *Computer Physics Communications* **220**, 319–331 (2017).

[16] T. H. Maiman, *Stimulated Optical Radiation in Ruby*, *Nature* **187**, 493–494 (1960).

[17] S. Chu, J. E. Bjorkholm, A. Ashkin, and A. Cable, *Experimental Observation of Optically Trapped Atoms*, *Phys. Rev. Lett.* **57**, 314–317 (1986).

[18] E. L. Raab, M. Prentiss, A. Cable, S. Chu, and D. E. Pritchard, *Trapping of Neutral Sodium Atoms with Radiation Pressure*, *Phys. Rev. Lett.* **59**, 2631–2634 (1987).

[19] A. F. Linskens, I. Holleman, N. Dam, and J. Reuss, *Two-photon Rabi oscillations*, *Phys. Rev. A* **54**, 4854–4862 (1996).

[20] I. Mourachko, D. Comparat, F. de Tomasi, A. Fioretti, P. Nosbaum, V. M. Akulin, and P. Pillet, *Many-Body Effects in a Frozen Rydberg Gas*, *Phys. Rev. Lett.* **80**, 253–256 (1998).

[21] J. P. Dowling and G. J. Milburn, *Quantum technology: the second quantum revolution*, *Philosophical Transactions of the Royal Society of London. Series A: Mathematical, Physical and Engineering Sciences* **361**, 1655–1674 (2003).

[22] A. W. Harrow and A. Montanaro, *Quantum computational supremacy*, *Nature* **549**, 203–209 (2017).

[23] J. Preskill, *Quantum Computing in the NISQ era and beyond*, *Quantum* **2**, 79 (2018).

[24] I. Quantum, *Development & Innovation Roadmap* (2024), URL: https://www.ibm.com/quantum/assets/IBM_Quantum_Development_&_Innovation_Roadmap.pdf (visited on 10/15/2024).

[25] L. Pause, L. Sturm, M. Mittenbühler, S. Amann, T. Preuschoff, D. Schäffner, M. Schlosser, and G. Birkl, *Supercharged two-dimensional tweezer array with more than 1000 atomic qubits*, *Optica* **11**, 222–226 (2024).

[26] J. Zeiher, R. van Bijnen, P. Schauß, S. Hild, J.-y. Choi, T. Pohl, I. Bloch, and C. Gross, *Many-body interferometry of a Rydberg-dressed spin lattice*, *Nature Physics* **12**, 1095–1099 (2016).

[27] I. S. Madjarov, A. Cooper, A. L. Shaw, J. P. Covey, V. Schkolnik, T. H. Yoon, J. R. Williams, and M. Endres, *An Atomic-Array Optical Clock with Single-Atom Readout*, *Phys. Rev. X* **9**, 041052 (2019).

[28] D. Schrader, I. Dotsenko, M. Khudaverdyan, Y. Miroshnychenko, A. Rauschenbeutel, and D. Meschede, *Neutral Atom Quantum Register*, *Phys. Rev. Lett.* **93**, 150501 (2004).

[29] S. Ma, A. P. Burgers, G. Liu, J. Wilson, B. Zhang, and J. D. Thompson, *Universal Gate Operations on Nuclear Spin Qubits in an Optical Tweezer Array of ^{171}Yb Atoms*, *Phys. Rev. X* **12**, 021028 (2022).

[30] Y. Wang, A. Kumar, T.-Y. Wu, and D. S. Weiss, *Single-qubit gates based on targeted phase shifts in a 3D neutral atom array*, *Science* **352**, 1562–1565 (2016), eprint: https://www.science.org/doi/pdf/10.1126/science.aaf2581.

[31] M. Schlosser, S. Tichelmann, D. Schäffner, D. Ohl de Mello, M. Hambach, J. Schütz, and G. Birkl, *Scalable Multilayer Architecture of Assembled Single-Atom Qubit Arrays in a Three-Dimensional Talbot Tweezer Lattice*, *Phys. Rev. Lett.* **130**, 180601 (2023).

[32] H. Levine, A. Keesling, G. Semeghini, A. Omran, T. T. Wang, S. Ebadi, H. Bernien, M. Greiner, V. Vuletić, H. Pichler, and M. D. Lukin, *Parallel Implementation of High-Fidelity Multiqubit Gates with Neutral Atoms*, *Phys. Rev. Lett.* **123**, 170503 (2019).

[33] L. Isenhower, E. Urban, X. L. Zhang, A. T. Gill, T. Henage, T. A. Johnson, T. G. Walker, and M. Saffman, *Demonstration of a Neutral Atom Controlled-NOT Quantum Gate*, *Phys. Rev. Lett.* **104**, 010503 (2010).

[34] A. J. Daley, J. Ye, and P. Zoller, *State-dependent lattices for quantum computing with alkaline-earth-metal atoms*, *The European Physical Journal D* **65**, 207–217 (2011).

[35] N. Schine, A. W. Young, W. J. Eckner, M. J. Martin, and A. M. Kaufman, *Long-lived Bell states in an array of optical clock qubits*, *Nature Physics* **18**, 1067–1073 (2022).

[36] N. C. Brown and K. R. Brown, *Comparing Zeeman qubits to hyperfine qubits in the context of the surface code:* $^{174}Yb^{+}$ *and* $^{171}Yb^{+}$, *Phys. Rev. A* **97**, 052301 (2018).

[37] A. Keselman, Y. Glickman, N. Akerman, S. Kotler, and R. Ozeri, *High-fidelity state detection and tomography of a single-ion Zeeman qubit*, *New Journal of Physics* **13**, 073027 (2011).

[38] W. Demtröder, *Atoms, Molecules and Photons : An Introduction to Atomic-, Molecular- and Quantum Physics* (2018), URL: https://doi.org/10.1007/978-3-662-55523-1.

[39] D. Ohl de Mello, *Rydberg interactions in a defect-free array of single-atom quantum systems*, PhD thesis, Technische Universität Darmstadt (2020).

[40] L. Isenhower, *Demonstration of Rydberg blockade and a neutral atom CNOT gate*, PhD thesis, University of Wisconsin-Madison (2010).

[41] V. I. Yudin, A. V. Taichenachev, C. W. Oates, Z. W. Barber, N. D. Lemke, A. D. Ludlow, U. Sterr, C. Lisdat, and F. Riehle, *Hyper-Ramsey spectroscopy of optical clock transitions*, *Phys. Rev. A* **82** (2010).

[42] K.-N. Schymik, S. Pancaldi, F. Nogrette, D. Barredo, J. Paris, A. Browaeys, and T. Lahaye, *Single Atoms with 6000-Second Trapping Lifetimes in Optical-Tweezer Arrays at Cryogenic Temperatures*, *Phys. Rev. Appl.* **16**, 034013 (2021).

[43] D. A. Steck, *Rubidium 85 D Line Data*, Available online at http://steck.us/alkalidata (revision 2.3.3, 28 May 2024) (2024).

[44] *Performance Sheet X-13699*, PS iXon Ultra ISSUE 1, Rev. 2, Andor Technology Ltd. (2014).

[45] S. Kuhr, W. Alt, D. Schrader, I. Dotsenko, Y. Miroshnychenko, W. Rosenfeld, M. Khudaverdyan, V. Gomer, A. Rauschenbeutel, and D. Meschede, *Coherence Properties and Quantum State Transportation in an Optical Conveyor Belt*, *Phys. Rev. Lett.* **91**, 213002 (2003).

[46] M. P. A. Jones, J. Beugnon, A. Gaëtan, J. Zhang, G. Messin, A. Browaeys, and P. Grangier, *Fast quantum state control of a single trapped neutral atom*, *Phys. Rev. A* **75**, 040301 (2007).

[47] A. Fuhrmanek, R. Bourgain, Y. R. P. Sortais, and A. Browaeys, *Free-Space Lossless State Detection of a Single Trapped Atom*, *Phys. Rev. Lett.* **106**, 133003 (2011).

[48] M. J. Gibbons, C. D. Hamley, C.-Y. Shih, and M. S. Chapman, *Nondestructive Fluorescent State Detection of Single Neutral Atom Qubits*, *Phys. Rev. Lett.* **106**, 133002 (2011).

[49] A. G. Radnaev, W. C. Chung, M. Saffman, and T. W. N. et al., *A universal neutral-atom quantum computer with individual optical addressing and non-destructive readout* (2024), arXiv: 2408.08288 [quant-ph].

[50] M. A. Nielsen and I. L. Chuang, *Quantum Computation and Quantum Information: 10th Anniversary Edition*, Cambridge University Press (2010).

[51] D. D. Yavuz, P. B. Kulatunga, E. Urban, T. A. Johnson, N. Proite, T. Henage, T. G. Walker, and M. Saffman, *Fast Ground State Manipulation of Neutral Atoms in Microscopic Optical Traps*, *Phys. Rev. Lett.* **96**, 063001 (2006).

[52] T. M. Graham, Y. Song, J. Scott, C. Poole, L. Phuttitarn, K. Jooya, P. Eichler, X. Jiang, A. Marra, B. Grinkemeyer, M. Kwon, M. Ebert, J. Cherek, M. T. Lichtman, M. Gillette, J. Gilbert, D. Bowman, T. Ballance, C. Campbell, E. D. Dahl, O. Crawford, N. S. Blunt, B. Rogers, T. Noel, and M. Saffman, *Multi-qubit entanglement and algorithms on a neutral-atom quantum computer*, *Nature* **604**, 457–462 (2022).

[53] D. D. Yavuz, P. B. Kulatunga, E. Urban, T. A. Johnson, N. Proite, T. Henage, T. G. Walker, and M. Saffman, *Fast Ground State Manipulation of Neutral Atoms in Microscopic Optical Traps*, *Phys. Rev. Lett.* **96**, 063001 (2006).

[54] C. Knoernschild, X. L. Zhang, L. Isenhower, A. T. Gill, F. P. Lu, M. Saffman, and J. Kim, *Independent individual addressing of multiple neutral atom qubits with a micromirror-based beam steering system*, *Applied Physics Letters* **97**, 134101 (2010).

[55] I. Beterov, E. Yakshina, D. Tretyakov, V. Entin, N. Al'yanova, K. Mityanin, A. Faruk, and I. Ryabtsev, *Implementation of one-qubit quantum gates with individual addressing of two rubidium atoms in two optical dipole traps*, *Quantum Electronics* **51**, 464–472 (2021).

[56] J. H. Lee, E. Montano, I. H. Deutsch, and P. S. Jessen, *Robust site-resolvable quantum gates in an optical lattice via inhomogeneous control*, *Nature Communications* **4** (2013).

[57] F. Liu, C. Wang, L. Li, and L. Chen, *Long-term and wideband laser intensity stabilization with an electro-optic amplitude modulator*, *Optics & Laser Technology* **45**, 775–781 (2013).

[58] M. Saffman, *Quantum computing with atomic qubits and Rydberg interactions: progress and challenges*, *Journal of Physics B: Atomic, Molecular and Optical Physics* **49**, 202001 (2016).

[59] L. Pause, *A New Setup for Scaling Up Microlens-Based Individual-Atom Quantum Processors*, PhD thesis, Technische Universität Darmstadt (2023).

[60] I. I. Ryabtsev, I. I. Beterov, D. B. Tretyakov, V. M. Entin, and E. A. Yakshina, *Doppler- and recoil-free laser excitation of Rydberg states via three-photon transitions*, *Phys. Rev. A* **84**, 053409 (2011).

[61] D. Schäffner, *Interacting Neutral Atoms in a Scalable Platform of Optical Tweezers for Quantum Computation and Sensing*, PhD thesis, Technische Universität Darmstadt (2022), viii, 109 Seiten.

[62] H. Metcalf and P. van der Straten, *Laser Cooling and Trapping*, Springer New York (2001).

[63] R. Grimm, M. Weidemüller, and Y. B. Ovchinnikov, *Optical Dipole Traps for Neutral Atoms*, in: edited by B. Bederson and H. Walther, **42**, Advances In Atomic, Molecular, and Optical Physics, Academic Press (2000), 95–170.

[64] A. J. Dunning, *Coherent Atomic Manipulation and Cooling : Interferometric Laser Cooling and Composite Pulses for Atom Interferometry* (2015), URL: https://doi.org/10.1007/978-3-319-21738-3.

[65] M. Fewell, *Adiabatic elimination, the rotating-wave approximation and two-photon transitions*, *Optics Communications* **253**, 125–137 (2005).

[66] R. Loudon, *The Quantum Theory of Light*, OUP Oxford (2000).

[67] P. Krantz, M. Kjaergaard, F. Yan, T. P. Orlando, S. Gustavsson, and W. D. Oliver, *A quantum engineer's guide to superconducting qubits*, *Applied Physics Reviews* **6**, 021318 (2019), eprint: https://pubs.aip.org/aip/apr/article-pdf/doi/10.1063/1.5089550/16667201/021318_1_online.pdf.

[68] J. Bakos, *AC stark effect and multiphoton processes in atoms*, *Physics Reports* **31**, 209–235 (1977).

[69] S. Kuhr, W. Alt, D. Schrader, I. Dotsenko, Y. Miroshnychenko, A. Rauschenbeutel, and D. Meschede, *Analysis of dephasing mechanisms in a standing-wave dipole trap*, *Phys. Rev. A* **72**, 023406 (2005).

[70] S. Burgardt, S. B. Jäger, J. Feß, S. Hiebel, I. Schneider, and A. Widera, *Measuring the environment of a Cs qubit with dynamical decoupling sequences*, *Journal of Physics B: Atomic, Molecular and Optical Physics* **56**, 165501 (2023).

[71] C. H. Chow, B. L. Ng, and C. Kurtsiefer, *Coherence of a dynamically decoupled single neutral atom*, *J. Opt. Soc. Am. B* **38**, 621–629 (2021).

[72] M. Schlosser, *Bereitstellung und kohärente Kontrolle von Einzel-Atom-Quantensystemen in zweidimensionalen Quantenregistern*, PhD thesis, Technische Universität Darmstadt (2014).

[73] Leybold Didactic GmbH, *Observing the normal Zeeman effect in transverse and longitudinal configuration*, Hürth (2005).

[74] A. Derevianko, P. Kómár, T. Topcu, R. M. Kroeze, and M. D. Lukin, *Effects of molecular resonances on Rydberg blockade*, *Physical Review A* **92** (2015).

[75] R. Löw, H. Weimer, J. Nipper, J. B. Balewski, B. Butscher, H. P. Büchler, and T. Pfau, *An experimental and theoretical guide to strongly interacting Rydberg gases*, *Journal of Physics B: Atomic, Molecular and Optical Physics* **45**, 113001 (2012).

[76] C. S. Adams, J. D. Pritchard, and J. P. Shaffer, *Rydberg atom quantum technologies*, *Journal of Physics B: Atomic, Molecular and Optical Physics* **53**, 012002 (2019).

[77] T. F. Gallagher, *Rydberg Atoms*, Cambridge University Press (1994).

[78] T. Scheiber, *Preparation of initial Zeeman levels and single-site selective Rydberg excitations in a Neutral Atom Quantum Processor*, Master-Thesis, TU Darmstadt (2023).

[79] R. A. Cline, J. D. Miller, M. R. Matthews, and D. J. Heinzen, *Spin relaxation of optically trapped atoms by light scattering*, *Opt. Lett.* **19**, 207–209 (1994).

[80] D. A. Steck, *Rubidium 87 D Line Data*, Available online at http://steck.us/alkalidata (revision 2.3.3, 28 May 2024) (2024).

[81] J. Werkmann, *Control Systems and Optical Tweezers for Quantum Information Processing*, Master-Thesis, TU Darmstadt (2018).

[82] M. Mittenbühler, *Reactive Real-Time Synthesis of Multiple Tweezers for Parallelized Atom Transport*, Master-Thesis, TU Darmstadt (2024).

[83] Thorlabs, Inc., *Shortpass Dichroic Mirrors / Beamsplitters: TC12APC-780* (2024), URL: https://www.thorlabs.com/newgrouppage9.cfm?objectgroup_id=5124 (visited on 09/22/2024).

[84] *Matisse C User's Guide*, 56A12621B, Version 1.2.2, Sirah Lasertechnik GmbH (2021).

[85] L. Pause, T. Preuschoff, D. Schäffner, M. Schlosser, and G. Birkl, *Reservoir-based deterministic loading of single-atom tweezer arrays*, *Phys. Rev. Res.* **5**, L032009 (2023).

[86] T. Gollerthan, *Beyond the 10000-Tweezer Barrier: Progress Towards Large-Scale Quantum Computers with Neutral Atoms*, Master-Thesis, TU Darmstadt (2023).

[87] A. Laskin and al, *Refractive field mapping beam shaping optics: important features for a right choice*, *Proc. of ICALEO* (2010).

[88] J. Wen, Y. Zhang, and M. Xiao, *The Talbot effect: recent advances in classical optics, nonlinear optics, and quantum optics*, *Adv. Opt. Photon.* **5**, 83–130 (2013).

[89] J. Götzinger, *Phasengelockter ECDL bei 795 nm mit Stromquelle im Laserkopf*, Bachelor Thesis, TU Darmstadt (2022).

[90] T. Preuschoff, *Laser Technologies for Applications in Quantum Information Science*, PhD thesis, Technische Universität Darmstadt (2023), vi, 154 Seiten.

[91] A. Alberti, W. Alt, R. Werner, and D. Meschede, *Decoherence models for discrete-time quantum walks and their application to neutral atom experiments*, *New Journal of Physics* **16**, 123052 (2014).

[92] W. Alt, *An objective lens for efficient fluorescence detection of single atoms*, *Optik* **113**, 142–144 (2002).

[93] *Tools for infrared and Raman spectroscopy*, in: *Infrared and Raman Spectroscopy*, John Wiley & Sons, Ltd (1995), chapter 3, 63–188, eprint: https://onlinelibrary.wiley.com/doi/pdf/10.1002/9783527615438.ch03.

[94] *Certificate of Compliance*, IN22020214-1, Foctek Photonics, Inc (2022).

[95] Thorlabs, Inc., *Shortpass Dichroic Mirrors / Beamsplitters: DMSP650L* (2024), URL: https://www.thorlabs.com/newgrouppage9.cfm?objectgroup_id=9240 (visited on 09/22/2024).

[96] IDEX Health & Science LLC., *Individual Optical Filters* (2024), URL: https://www.idex-hs.com/store/products/semrock_optical_filters/individual_optical_filters/1?dichroic_beamsplitters=Long-pass&semrock_filter_families=RazorEdge%C2%AE+Raman+Filters (visited on 09/22/2024).

[97] Kimball Physics, *MCF600-SphOct-F2C8* (2023), URL: https://www.kimballphysics.com/wp-content/uploads/2023/02/MCF_Spherical_Octagon_2023_0222.pdf (visited on 09/22/2024).

[98] A. J. Sattler, *Planung und Aufbau eines Experiments zur Manipulation einzelner neutraler Atome*, Master-Thesis, TU Darmstadt (2008).

[99] Edmund Optics GmbH, *polarisierender Strahlteilerwürfel für Laserlinien* (2024), URL: https://www.edmundoptics.de/document/download/355512 (visited on 09/22/2024).

[100] K. L. Corwin, S. J. M. Kuppens, D. Cho, and C. E. Wieman, *Spin-Polarized Atoms in a Circularly Polarized Optical Dipole Trap*, *Phys. Rev. Lett.* **83**, 1311–1314 (1999).

[101] *785 nm laser BrightLine single-edge λ/10 flatness dichroic beamsplitter*, FDi03-r785-26x36, IDEX Health & Science LLC. (2016).

[102] *Ultrafast MSM Photodetectos G4176 Series (GaAs) G7096 Series (InGaAs)*, Hamamatsu (2003).

[103] T. Preuschoff, *GitHub repository TU-Darmstadt-APQ/HMC439_Phase-Frequency_Detector* (2022), URL: https://github.com/TU-Darmstadt-APQ/phase-frequency_detector (visited on 09/22/2024).

[104] Red Pitaya, *"Swiss Army Knife for Engineers"* (2018), URL: https://www.redpitaya.com/ (visited on 09/22/2024).

[105] *DTSXY AO DEFLECTORS 1-axis/2-axis*, AA OPTO-ELECTRONIC (2018).

[106] M. E. Wilkinson and K. S. Shahid, *Optics Review*, University of Iowa (2006).

[107] M. Domack, *AOD based 2D-addressing system for Raman excitation on a neutral atom lattice*, Studienarbeit, TU Darmstadt (2023).

[108] M. Domack, *Single-site addressed state-manipulation and Rydberg excitation on neutral atoms as building blocks for a CNOT gate*, Master-Thesis, TU Darmstadt (2023).

[109] L. Li, W. Huie, N. Chen, B. DeMarco, and J. P. Covey, *Active Cancellation of Servo-Induced Noise on Stabilized Lasers via Feedforward*, *Phys. Rev. Appl.* **18**, 064005 (2022).

[110] T. Preuschoff, P. Baus, M. Schlosser, and G. Birkl, *Wideband current modulation of diode lasers for frequency stabilization*, *Review of Scientific Instruments* **93** (2022).

[111] P. Baus, *Current Drivers and Control Electronics for the Laser Spectroscopy of Highly Charged Ions*, PhD thesis, Technische Universität Darmstadt (2024), 239 Seiten.

[112] QUBIG GmbH, *PM7-NIR - Series* (2024), URL: https://www.qubig.com/products/electro-optic-modulators_eom/phase-modulators_pm/pm-free-space_pm-bulk/pm7-nir (visited on 09/22/2024).

[113] S. Bickel, *Frequenzstabilisierung eines Rydberg-Lasersystems mittels Pound-Drever-Hall-Verfahren*, Studienarbeit, TU Darmstadt (2023).

[114] *SSG3000X Series RF Generator*, Siglent Technologies Co.LTD (2019).

[115] *Wavelength Meter Angstrom WS 8*, High Finesse GmbH (2020).

[116] DILAS Diodenlaser GmbH, *TA-0780-2000 Tapered Amplifier for MOPA Setups* (2018), URL: http://dilas.com/assets/media/products/DILAS_TA-0780-2000.pdf (visited on 11/22/2018).

[117] *AOMO 3200-121 SMB-2*, 99-48146-11, Rev. E, Crystal Technology, Inc (2001).

[118] Jenoptik GmbH, *Integriert-optische Lichtmodulatoren von Jenoptik* (2024), URL: https://www.jenoptik.de/produkte/optoelektronische-systeme/lichtmodulation/integriert-optische-modulatoren-iom (visited on 09/22/2024).

[119] T. Preuschoff, *GitHub repository TU-Darmstadt-APQ/PDH_Photodiode* (2022), URL: https://github.com/TU-Darmstadt-APQ/PDH_photodiode (visited on 09/22/2024).

[120] T. Preuschoff, *GitHub repository TU-Darmstadt-APQ/PDH-module* (2022), URL: https://github.com/TU-Darmstadt-APQ/PDH-module (visited on 09/22/2024).

[121] Thorlabs, Inc., *Shortpass Dichroic Mirrors / Beamsplitters: DMSP900* (2024), URL: https://www.thorlabs.com/newgrouppage9.cfm?objectgroup_id=9240 (visited on 09/22/2024).

[122] Thorlabs, Inc., *Photodiodes* (2024), URL: https://www.thorlabs.com/newgrouppage9.cfm?objectgroup_id=285&pn=FGA01 (visited on 09/22/2024).

[123] *Low Pass Filter SLP-5+ 50 ΩDC to 5 MHz*, M153690, Rev.D, Mini-Curcuits (2024).

[124] M. Saffman, X. L. Zhang, A. T. Gill, L. Isenhower, and T. G. Walker, *Rydberg state mediated quantum gates and entanglement of pairs of neutral atoms*, *Journal of Physics: Conference Series* **264**, 012023 (2011).

[125] Analog Devices, Inc, *1 GSPS, 14-Bit, 3.3 V CMOS Direct Digital Synthesizer* (2018), URL: https://www.analog.com/media/en/technical-documentation/data-sheets/ad9910.pdf (visited on 09/22/2024).

[126] P. T. Starkey, C. J. Billington, S. P. Johnstone, M. Jasperse, K. Helmerson, L. D. Turner, and R. P. Anderson, *A scripted control system for autonomous hardware-timed experiments*, *Review of Scientific Instruments* **84**, 085111 (2013), eprint: https://pubs.aip.org/aip/rsi/article-pdf/doi/10.1063/1.4817213/14786066/085111_1_online.pdf.

[127] M. Domack and P. Baus, *GitHub repository TU-Darmstadt-APQ/FPGA-DDS-connector_main* (2024), URL: https://github.com/TU-Darmstadt-APQ/FPGA-DDS-connector_main (visited on 09/22/2024).

[128] J.-N. Schmidt, *Two-photon Rydberg excitation and analysis of an atom-loss detection scheme for atoms in dipole-trap arrays*, Master-Thesis, TU Darmstadt (2017).

[129] K. Gillen-Christandl, G. D. Gillen, M. J. Piotrowicz, and M. Saffman, *Comparison of Gaussian and super Gaussian laser beams for addressing atomic qubits*, *Applied Physics B* **122** (2016).

[130] L. Kohfahl, *Two-Photon Rydberg Excitation of Neutral Atoms in Optical Dipole-Trap Arrays*, Master-Thesis, TU Darmstadt (2017).

[131] C. Klempt, T. van Zoest, T. Henninger, O. Topic, E. Rasel, W. Ertmer, and J. Arlt, *Ultraviolet light-induced atom desorption for large rubidium and potassium magneto-optical traps*, *Phys. Rev. A* **73**, 013410 (2006).

[132] B. Mamat, C. Sheng, X. He, J. Hou, P. Xu, K. Wang, J. Zhuang, M. Wei, M. Liu, J. Wang, and M. Zhan, *Mitigating noise of residual electric fields for single Rydberg atoms with electron photodesorption* (2024), arXiv: 2312.02597 [physics.atom-ph].

[133] J. Götzinger, *Untersuchung der Fehlerquellen bei 2-Qubit-Operationen*, Master Thesis, TU Darmstadt (2024).

[134] F. Lenz, *Zustandspräparation und Rydberg-Wechselwirkung einzeln adressierter Atome*, Master-Thesis, TU Darmstadt (2021).

[135] M. Thulin, *The cost of using exact confidence intervals for a binomial proportion*, *Electronic Journal of Statistics* **8**, 817–840 (2014).

[136] C. J. Clopper and E. S. Pearson, *The use of confidence or fiducial limits illustrated in the case of the binomial*, *Biometrika* **26**, 404–413 (1934), eprint: https://academic.oup.com/biomet/article-pdf/26/4/404/823407/26-4-404.pdf.

[137] M. M. Müller, T. Pichler, S. Montangero, and T. Calarco, *Optimal control for Rydberg quantum technology building blocks*, *Applied Physics B* **122** (2016).

[138] D. Schäffner, T. Schreiber, F. Lenz, M. Schlosser, and G. Birkl, *Quantum Sensing in Tweezer Arrays: Optical Magnetometry on an Individual-Atom Sensor Grid*, *PRX Quantum* **5**, 010311 (2024).

[139] M. Werner, *Kohärente Manipulation von kalten Atomen mit phasenstabilisierten Lasersystemen*, Master-Thesis, TU Darmstadt (2017).

[140] D. W. Allan, *Should the classical variance be used as a basic measure in standards metrology?*, *IEEE Transactions on Instrumentation and Measurement* **IM-36**, 646–654 (1987).

[141] K. Draganová, F. Kmec, J. Blažek, D. Praslička, J. Hudák, and M. Laššák, *Noise Analysis of Magnetic Sensors Using Allan Variance*, *Acta Physica Polonica A* **126**, 394–395 (2014).

[142] J. F. Barry, J. M. Schloss, E. Bauch, M. J. Turner, C. A. Hart, L. M. Pham, and R. L. Walsworth, *Sensitivity optimization for NV-diamond magnetometry*, *Rev. Mod. Phys.* **92**, 015004 (2020).

[143] D. Pfeiffer, L. Lind, J. Küber, F. Schmaltz, A. Turpin, V. Ahufinger, J. Mompart, and G. Birkl, *Trapping of Bose-Einstein condensates in a three-dimensional dark focus generated by conical refraction*, *Phys. Rev. A* **108**, 053320 (2023).

[144] P. Huft, Y. Song, T. M. Graham, K. Jooya, S. Deshpande, C. Fang, M. Kats, and M. Saffman, *Simple, passive design for large optical trap arrays for single atoms*, *Physical Review A* **105** (2022).

[145] S. Bickel, *Ramanlaser für Ein-Qubit-Quantengatter: Entwicklung eines Hochleistungssystems mit geringem Phasenrauschen*, Studienarbeit, TU Darmstadt (2024).

[146] L. Beguin, *Measurement of the van der Waals interaction between two Rydberg atoms*, PhD thesis, Institut d'Optique (2014).

[147] M. Schlosser, A. Lengwenus, and G. Birkl, *Synchronization of atomic quantum systems in multi-site optical trapping potentials (unpublished)*.

[148] K. D. Nelson, X. Li, and D. S. Weiss, *Imaging single atoms in a three-dimensional array*, *Nature Physics* **3**, 556–560 (2007).

Danksagung

Die Vervollständigung dieser Arbeit wäre nicht möglich gewesen ohne eine Reihe von Personen, denen ich hier ausdrücklich (aber nicht ausschließend) danken möchte.
An erster Stelle danke ich Herr Prof. Birkl für die Chance, eine Promotion in seiner Arbeitsgruppe zu absolvieren. In diesem Zuge wurde mir ein über viele Jahre entwickeltes Experiment anvertraut, um aktuellen Fragen der Quantenphysik nachzugehen. Besonderer Dank ergeht in diesem Zusammenhang auch an Dominik, Daniel und last-but-not-least Malte für den Aufbau, die Übergabe und die wissenschaftliche Betreuung am Experiment. Eine besondere Freude war es für mich, mit Lars, Tilman, Dominik, Ludwig und Patrick zusammenzuarbeiten. Diesen guten Jahren der Zusammenarbeit in wertschätzender Kollegialität werde ich mich noch oft entsinnen. Ohne Patricks großartiges Fotoequipment sähen viele Darstellungen des Experiments als Foto oder 3D Scan nicht halb so gut aus! Der Text und zahlreiche Abbildungen sähen ebenfalls nicht halb so gut aus ohne die unermüdlichen Anregungen von Patrick und Martin. Danken möchte ich auch Prof. Walther, zum einen für die einprägsamen Vorlesungen und zum anderen für die Übernahme des Zweitgutachtens trotz Ihrer zahlreichen offiziellen Aufgaben.
Als meine größten Erfolge während der Promotion zähle ich die Betreuung der Bachelor- und Masterstudenten, die mir immer ein besonderes Anliegen und Freude waren und an denen ich persönlich und wissenschaftlich wachsen konnte. In diesem Zuge danke ich Fabian, ohne dessen fleißige Programmierarbeit das Magnetfeldpaper kaum möglich gewesen wäre. Besonders gefreut haben mich die „Wiederholungstäter“ Moritz und Justus, die gleich doppelt als Bachelor- und Masterabschluss ihr Vertrauen in meine Betreuung gesetzt haben und ohne deren kompetente Hilfe viele Systeme nie fertiggestellt worden wären. Vielen Dank an Justus für die zahlreichen Justagen an ECDLs während der Bachelorzeit, die Operationen mit 795nm ermöglicht haben, die zuvor außer Reichweite erschienen. Vielen Dank an Moritz für AOD-Ansteuerung, Einzelplatzadressierung und besonders die stetige Demonstration, dass ich mich mehr mit Programmierung auseinandersetzen musste. Ehe ich Justus erneut für seine Masterzeit danken kann, gilt mein Dank Jan, der mir eine sehr große Stütze am Experiment war und ohne dessen ausgiebige Wartung das Experiment seinerzeit vermutlich auseinandergefallen wäre (mindestens im übertragenen Sinne). Dein Name gehört auf den Lasertisch graviert, für den jeder Zentimeter dem Labor abgerungen werden musste! Dank auch an Nathan für das Durchquälen durch eine API, die einfach noch nicht reif für die Welt war. Zum Schluss noch Dank an meine letzten Masterstudenten Simon und Justus. Vielen Dank an Simon, für die produktive Arbeit an Lasersystemen, die ihre besten Zeiten hoffentlich noch vor sich haben. Und zuletzt nochmal Dank an Justus, der die spannendste und schwierigste Zeit mit mir durchlebt hat und sich dabei von plötzlichen Kurswechseln und unerwarteten Erkenntnissen nicht hat aus der Bahn werfen lassen!
Jedem der vorweggenannten Personen kann ich die Projekte aufzählen, mit denen sie diese Arbeit möglich gemacht haben. Bei meiner Familie ist die Liste unzählbar, angefangen von den großartigen Möglichkeiten, die ihr mir seit dem Schulalter eröffnet habt, bis zur Unterstützung mit Finanzen, Arbeitsplatz und leckerem Essen in der Schlussphase.
Danke, Martina und Jürgen!

Für ihre unerschütterliche Unterstützung in der Schlussphase danke ich ganz besonders meiner Fanny. Dich zu kennen und um mich zu wissen, ist ein großes Glück, auch wenn das Labor und die Dissertation uns bis jetzt einige Zeit geraubt haben. Ich freue mich darauf, mit Dir gemeinsamen Abenteuern entgegenzugehen.

Erklärungen laut Promotionsordnung

§ 8 Abs. 1 lit. c PromO

Ich versichere hiermit, dass die elektronische Version meiner Dissertation mit der schriftlichen Version übereinstimmt.

§ 8 Abs. 1 lit. d PromO

Ich versichere hiermit, dass zu einem vorherigen Zeitpunkt noch keine Promotion versucht wurde. In diesem Fall sind nähere Angaben über Zeitpunkt, Hochschule, Dissertationsthema und Ergebnis dieses Versuchs mitzuteilen.

§ 9 Abs. 1 PromO

Ich versichere hiermit, dass die vorliegende Dissertation – abgesehen von den in ihr ausdrücklich genannten Hilfen – selbstständig verfasst wurde und dass die „Grundsätze zur Sicherung guter wissenschaftlicher Praxis an der Technischen Universität Darmstadt“ und die „Leitlinien zum Umgang mit digitalen Forschungsdaten an der TU Darmstadt“ in den jeweils aktuellen Versionen bei der Verfassung der Dissertation beachtet wurden.

§ 9 Abs. 2 PromO

Die Arbeit hat bisher noch nicht zu Prüfungszwecken gedient.

Darmstadt, 13.11.2024

T. Schreiber